UNIVERSITÀ DEGLI STUDI DI TRIESTE

XXI CICLO
DEL DOTTORATO DI RICERCA IN
FISICA

Measurement of transverse spin effects in COMPASS on a polarised proton target

Settore scientifico-disciplinare
FISICA NUCLEARE E SUBNUCLEARE (FIS/04)

ANNO ACCADEMICO 2007/2008

Dottorando
Stefano Levorato

Coordinatore del collegio dei docenti
prof. Gaetano Senatore

Tutore
prof. Franco Bradamante

Relatore
prof. Franco Bradamante

Correlatrice
dott.ssa Silvia Dalla Torre

Contents

Chapter 1

Introduction

1.1 Preface

Investigations of the spin structure of the nucleon are best performed by measuring double spin asymmetries in the deep inelastic scattering (DIS) of polarised leptons (electrons or muons) on polarised proton and neutron targets. These measurements allow the spin-dependent structure functions $g_{1,2}(x)$ for the proton and for the neutron to be extracted.
The COMPASS (Common Muon and Proton Apparatus for Structure and Spectroscopy) experiment was proposed as a fixed-target experiment at CERN in 1996 to investigate the spin structure of the nucleon and the existence of exotic hadrons (hybrids and glueballs). The experiment was approved in 1997, and the construction of the state-of-the art detectors lasted 5 years. The 2005 year-long break provided the opportunity to carry out important upgrades to the COMPASS spectrometer, and the configuration is now very close to the one first envisaged. The first years of running have in the meantime already shed important light on our understanding of the spin of the proton and the neutron. Using a polarised deuteron target, a total of about 30 billion events were put on tape in 2002, 2003, 2004, and 2006. Many important results have already been obtained and published and many more will come out. Contrary to several theoretical speculations, the contribution of the gluons to the spin of the nucleon has been shown to be rather small, less than 20% of $\hbar$, and the fraction of the nucleon spin carried by the quarks has been measured to be 30%, with a few % error.
Moreover, to completely specify the quark structure of the nucleon, the transverse distribution functions must be added to the momentum and helicity ones. Transversity functions are chiral-odd and so absent in inclusive DIS processes, the usual source of information on the nucleon partonic structure. They can be extracted from the spin asymmetries measured in the cross section of semi inclusive DIS (SIDIS) between leptons and transversely polarised nucleons, in which a hadron is also de-

tected in the final state.
Different mechanisms have also been suggested as possible causes of spin asymmetries in the SIDIS cross section.
Within the statistics, all the asymmetries measured at COMPASS on a transversely polarised deuterium target in the years 2002, 2003 and 2004 are compatible with zero. Taking into account the results from HERMES for a proton target and those of BELLE on $e^+ + e^- \rightarrow hadrons$ it can be only concluded that cancellation effects between protons and neutrons come into play.
It is therefore of the greatest importance to measure transversity spin effects on a proton target: half of 2007 COMPASS data taking has been dedicated to collect events on a transversely polarised proton target, and the result of the analysis are the subject of this thesis.
My PhD work started in 2006, when the upgrade project of the RICH-1 of the COMPASS spectrometer had already been started: I have dedicated nearly half of my PhD time to the *hardware* studies for this detector, investigating several aspects of the upgraded RICH-1. The last part of my PhD has been devoted to the analysis of the data collected during the 2007 transverse run. This thesis is so organised as to describe both these activities.
After a short introduction to the physics of COMPASS and the description of the spectrometer, the RICH-1 upgrade project is presented within the performed laboratory activities. Also the preliminary results of the performances of the new RICH-1 are illustrated. The focus then moves on the analysis of the data, and taking advantage of the upgraded RICH-1, the Collins and the Sivers asymmetries, extracted from the data collected during the transverse run of 2007, are presented both for unidentified and identified hadrons.

1.2 The spin structure of the nucleon

In the investigation of the structure of the nucleon, the question about the origin of the nucleon spin is still not completely solved [1]. For a nucleon polarised along the direction of the incoming lepton (longitudinal polarisation), the contribution of the spin of the partons, the constituents of the nucleon, is given by the first moments of the helicity distributions. These distribution are the difference of the numbers of partons with their spins aligned and antialigned with the nucleon spin in a frame in which the nucleon has a very large momentum (infinite momentum frame) and the direction of its spin is aligned to its momentum. In the naïve quark parton model the partons are identified with the quarks and their spins add up to yield the total nucleon spin. However, measurements at CERN, SLAC and DESY yielded helicity distributions of all quarks of less than 30% [2].
In quantum chromodynamics the interaction of quarks is described by the exchange

of gluons, the gauge bosons of the strong interaction. These gluons dress the quarks in the nucleon with a sea of virtual quark antiquark pairs and gluons. Besides the spin of the gluons, also the orbital angular momenta of quarks and gluons can contribute to the nucleon spin in addition to the spin of the quarks. To date, indirect and direct measurements of the gluon helicity distribution gave only vague information about its size and a direct measurement of the orbital angular momenta is not possible so far.
Not only the helicity distribution but also the distributions of the transverse spin of the constituents can reveal information about the structure of the nucleon. In contrast to the helicity distribution, the transversity distribution is defined for a nucleon with spin transverse to its direction of motion. As in the case of a longitudinal nucleon spin, the transversity distribution is the difference of the numbers of partons with their spins aligned and antialigned to the nucleon spin. Both helicity and transversity distributions are defined in the infinite momentum frame. Since rotations and Lorentz boost do not commute, helicity and transversity distributions are expected to be different. In addition, helicity conservation forbids contributions from the gluon to the transversity distribution in the nucleon. It has been shown that three distribution functions (unpolarised, helicity and transversity) are necessary to fully describe the quark structure of the nucleon at the twist-two level.
The notion of transversity in hadron physics has been with us now for over a quarter of a century. However, for much of that time, transversity has remained an intangible and remote object, of interest principally to only few theoreticians. In recent years transversity and transverse spin effects in general have grown as both theoretical and experimental areas of active research. This increasing attention, while initially riding to some extent in the wake of the famous proton-spin crisis, has now matured into a thriving field with a driving force of its own. The ever-growing bulk of data on asymmetries in collisions involving transversely polarised hadrons now demands a more solid and coherent theoretical basis for its description. Indeed, it now appears rather clear that transversity and other closely related properties play a significant role in generating such phenomena.

1.3 A short history of DIS experiments[1]

The first measurements of polarised electron-proton scattering were performed at SLAC in the 1980's by the E80 and E130 Collaborations, and yielded results that were consistent with the expectation. The comparison with the Bjorken sum rule was and is particularly important, but could not be performed at the time as the SLAC experiments did not measure the neutron. Derived as early as 1966 using current algebra tools, this sum rule relates the difference of the first moments of g_1 for the proton and the neutron to $\frac{G_A}{G_V}$, that is, to fundamental constants of the weak interaction. A breakthrough occurred when the European Muon Collaboration

(EMC) at CERN extended these measurements to a much larger kinematic range. Using a polarised muon beam with an energy 10 times higher than at SLAC, and the largest solid polarised target ever built (about 2 l), in 1988 the collaboration reported a significant violation of the Ellis-Jaffe sum rule for the proton. In the context of the quark-parton model this implied that the total contribution of the quark spins to the proton spin is small, a major surprise that soon came to be known as the "spin crisis". Soon after, the Spin Muon Collaboration (SMC) experiment was proposed to CERN, with the aim of improving the measurement of g_1 for the proton and performing the same measurement with a polarised deuteron target. SMC soon achieved a major accomplishment with the first measurement of g_1 for the deuteron in 1992. The result, when combined with the EMC result, was in agreement with the Bjorken sum rule, and implied that the Ellis-Jaffe sum rule was also violated for the neutron. So it was already safe to conclude in 1992 that the spin crisis was a well-established phenomenon for both the proton and the neutron, and that it occurred within the boundaries given by the Bjorken sum rule. The SMC experiment also provided another important result, determining for the first time the separate contributions of the valence and sea quarks to the nucleon spin via semi-inclusive DIS measurements. Given the large range in x covered by the measurement, the polarised quark distributions could be integrated to obtain the first momenta: Δu_v, Δq_v and $\Delta \bar{q}$. The polarisation of the strange sea could not be accessed as this requires full particle identification, which the SMC spectrometer could not provide. Several experiments at SLAC (E143, E154, E155, E155x), and more recently HERMES at HERA [3], have confirmed the results from EMC and SMC on the structure functions g_1. The HERMES Collaboration has also recently reported first results on the strange sea polarisation. All these measurements accurately determine $\Delta\Sigma$, the contribution of both valence and sea quark spins to the nucleon spin, to be only 30%. However it was already clear in the mid-1990's that a better understanding of nucleon spin structure demanded separate measurements of the missing contributions, i.e. the gluon polarisation $\Delta G/G$ and the orbital angular momentum of both the quarks and the gluons. In particular, several theoretical analyses suggested a large contribution ΔG as a solution to the spin crisis. Progress required a new experimental approach, namely semi-inclusive DIS with the identification of the hadrons in the current jet, because the determination both of Δq and $\Delta \bar{q}$ and of ΔG requires a flavor-tagging procedure to identify the struck parton. A suggestion to isolate the photon-gluon fusion (PGF) process and measure ΔG directly had been put forward several years previously, and implied measuring the cross-section asymmetry of open charm in DIS. A new experiment, with full hadron identification and calorimetry, therefore seemed to be necessary. At the same time, transversity, an interesting new physics case for semi-inclusive DIS measurements, was also developing rapidly. Today transversity is a big issue and is a major part of the programme of many experiments. Originally the idea was much debated in the

US, where it was largely responsible for the Spin Project at the Relativistic Heavy Ion Collider (RHIC) at Brookhaven. In Europe two proposal were put forward in 1993, one at DESY (HERMES) and one at CERN (HELP). The HERMES proposal was accepted, while the HELP one was not. At CERN however the physics case was not given up, and together with the measurement of ΔG, it became one of the important goals laid down in the proposal for a new experiment, COMPASS[4]. The COMPASS two-stage spectrometer, with particle identification and calorimetry, and the capability to handle a muon beam rate of $10^8 s^{-1}$, was proposed for hall 888 at CERN, after completion of the SMC experiment. Submitted in March 1996, the proposal was fully approved in October 1998 with the first physics run in 2002.

Chapter 2

Polarised DIS, an overview.

2.1 Introduction

Deep Inelastic lepton-hadron Scattering has played a seminal role in the development of the present understanding of the substructure of "*elementary*" particles. The discovery of the Bjorken scaling in the late 1960s provided the critical impetus for the idea that nucleons contain point-like constituents and the subsequent invention of the parton model. DIS continued to play an essential role in the period of gradual linking of partons and quarks, in the discovery of the existence of missing constituents, later identified as gluons, and in the confluence of all the different "ingredients" into a dynamical theory of quarks and gluons: QCD.
Polarised DIS, involving the collision of a longitudinally polarised lepton beam on a polarised target (either longitudinally or transversely) provides a different, complementary and equally important insight into the structure of the nucleon. Whereas ordinary DIS probes simply the number density of partons with a fraction x of the momentum of the parent hadron, polarised DIS can partly answer the more sophisticated question about the number density of parton with a given x and given spin polarisation, in a hadron of definite polarisation.
The transverse structure of the nucleon is investigated in COMPASS via semi inclusive deep inelastic scattering of muons off a transversely polarised target.
In section 2.2 the general formalism of DIS will be introduced and structure function interpretation within the naïve parton model will be object of section 2.3. Transversity will be introduced in section 2.7. The complete cross section formula for polarised SIDIS process will be investigated in section 2.7.1 and the structure function containing the Collins and Sivers terms will be introduced. Finally section 2.7.2 and 2.7.3 will describe how the Collins and the Sivers asymmetries are measured in COMPASS.

2.2 Deep Inelastic Scattering

Polarised deep inelastic experiments involve scattering a high energy charged lepton beam off a nucleon target at large momentum transfer squared. The lepton beam is longitudinally polarised while the nucleon target could be either longitudinally or transversely polarised. Consider the process:

$$\ell(k,s) + N(P,S) \rightarrow \ell(k^{'},s^{'}) + X \tag{2.1}$$

depicted in figure 2.1 in one photon exchange approximation, in which the nucleon structure breaks up and generates a final hadronic state X. While the lepton pho-

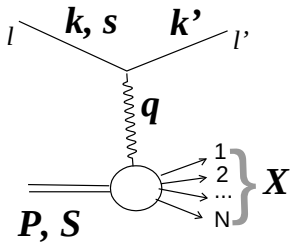

Figure 2.1: Deep Inelastic Scattering process.

ton vertex is described by perturbative QED, the internal QCD structure of the proton implies that the photon proton interaction is described in terms of various structure function. Since polarised deep inelastic scattering experiment, as well as COMPASS, have so far all been performed using a fixed target we specialise in the target rest frame. The 4-momentum of the initial nucleon in the laboratory frame is $\mathbf{P}$=(M, $\overrightarrow{0}$), with M the nucleon mass. $\mathbf{k}$=(E, $\overrightarrow{k}$) is the 4-momentum of the of the incident lepton with mass m which is scattered through an angle θ to emerge in the final state with 4-momentum $\mathbf{k}$=($E^{'}$, $\overrightarrow{k^{'}}$). The exchanged photon carrying momentum $q_\mu = k_\mu - k^{'}_\mu$ scatters from a polarised nucleon with momentum P_μ and mass M and spin S_μ.
The photon nucleon scattering is characterised by the two invariants $Q^2 = -q^2$ and $\nu = \mathbf{p}\cdot\mathbf{q}/M$ where $\nu = (E - E^{'})$ in the target rest frame. The Bjorken variable x is defined by the ratio $x = Q^2/2M\nu$. The squared momentum transfer Q^2 is a measure of the spatial resolution of the reaction: in DIS it is large enough to resolve the inner structure of the nucleons. In the specific case of COMPASS Q^2 ranges between 1 and 100 $(GeV/c)^2$.
For inclusive scattering the final state hadrons X are not detected, that is we sum

over all accessible hadronic final states and scattered lepton spins and measure the inclusive cross section.
For semi-inclusive deep inelastic scattering processes a particular hadron in the final state is tagged. This hadron carries memory of the struck parton and bring information about the distribution of quarks, anti-quarks and gluons carrying different momenta and spin of the nucleon.
The differential cross-section to find the scattered lepton in a solid angle $d\Omega$ with energy in the range $(E^{'}, E^{'} + dE^{'})$ can be written [5]

$$\frac{d^2\sigma}{d\Omega dE^{'}} = \frac{\alpha^2}{2Mq^4}\frac{E^{'}}{E}L_{\mu\nu}W^{\mu\nu} \tag{2.2}$$

where α is the fine structure constant and $L_{\mu\nu}$ and $W^{\mu\nu}$ are respectively the leptonic and hadronic tensor. Both tensor can be split into symmetric (S) and antisymmetric (A) parts under μ,ν interchange and, after summing over the spin of the final lepton they take the form:

$$\begin{aligned} L_{\mu\nu}(k, s; k^{'}) &= 2[L^S_{\mu\nu}(k; k^{'}) + iL^A_{\mu\nu}(k, s; k^{'})] \\ W_{\mu\nu}(q; P, S) &= W^S_{\mu\nu}(q; P) + iW^A_{\mu\nu}(q; P, S) \end{aligned} \tag{2.3}$$

where the leptonic tensor is given by QED and the hadronic tensor, $W_{\mu,\nu}$ which contains the strong interaction dynamics can be written in terms of four scalar inelastic form factor, $W_{1,2}$ and $G_{1,2}$, functions of at most of q^2 and $P \cdot q$. Putting 2.3 in equation 2.2 one finds:

$$\frac{d^2\sigma}{d\Omega dE^{'}} = \frac{\alpha^2}{Mq^4}\frac{E^{'}}{E}[L^{(S)}_{\mu\nu}W^{\mu\nu(S)} - L^{(A)}_{\mu\nu}W^{\mu\nu(A)}] \tag{2.4}$$

Note that only the antisymmetric part of $W^{\mu\nu(A)}$ depends on the nucleon's spin and that the cross section 2.4 is independent of the nucleon spin if the lepton is unpolarised[5].
The spin-independent inelastic form factors $W_{1,2}$ and the spin-dependent ones $G_{1,2}$, which can be measured experimentally, are written in terms of scaling functions $\mathcal{F}_{1,2}$ and $g_{1,2}$

2.2.1 Scaling and polarised deep inelastic scattering: measurement of g_1 and g_2

In high Q^2 deep inelastic scattering the structure functions exhibit approximate scaling, that is:

$$MW_1(\nu, Q^2) \to \mathcal{F}_1(x) \tag{2.5}$$
$$\nu W_2(\nu, Q^2) \to \mathcal{F}_2(x) \tag{2.6}$$
$$\frac{\nu}{M} G_1(\nu, Q^2) \to g_1(x) \tag{2.7}$$
$$\frac{\nu^2}{M^2} G_2(\nu, Q^2) \to g_2(x) \tag{2.8}$$
$$\tag{2.9}$$

The structure functions $\mathcal{F}_1, \mathcal{F}_2, g_1, g_2$ are to a very good approximation independent of Q^2 and depend only on x, the small logarithmic Q^2 dependence is determined by QCD evolution. Let $\uparrow\downarrow$ denote the longitudinal polarisation of the lepton beam. For a longitudinally polarised nucleon target (with spin denoted by $\Uparrow\Downarrow$) the unpolarised and polarised cross-sections are:

$$\left(\frac{d^2\sigma}{d\Omega dE'}^{\uparrow\Uparrow} + \frac{d^2\sigma}{d\Omega dE'}^{\uparrow\Downarrow}\right) = \frac{\alpha^2}{4E^2 \sin^4 \frac{\theta}{2}} \left[2 \sin^2 \frac{\theta}{2} \mathcal{F}_1(x, Q^2) + \frac{M}{\nu} \cos^2 \frac{\theta}{2} \mathcal{F}_2(x, Q^2)\right] \tag{2.10}$$

and

$$\left(\frac{d^2\sigma}{d\Omega dE'}^{\uparrow\Uparrow} - \frac{d^2\sigma}{d\Omega dE'}^{\uparrow\Downarrow}\right) = \frac{4\alpha^2}{M\nu} \frac{E'}{Q^2 E} \left[(E + E' \cos\theta) g_1(x, Q^2) - 2xM g_2(x, Q^2)\right] \tag{2.11}$$

For a target polarised transversely to the lepton beam the spin dependent part for the differential cross section is:

$$\left(\frac{d^2\sigma}{d\Omega dE'}^{\uparrow\Rightarrow} - \frac{d^2\sigma}{d\Omega dE'}^{\uparrow\Leftarrow}\right) = \frac{4\alpha^2}{M\nu} \frac{E'^2}{Q^2 E} \sin\theta \left[g_1(x, Q^2) - \frac{2E}{\nu} g_2(x, Q^2)\right] \tag{2.12}$$

In the unpolarised scattering (see eq. 2.10), where we have the average over the target polarisation, the antisymmetric part of $W_{\mu\nu}$ vanishes and we measure the form factor $\mathcal{F}_{1,2}(x, Q^2)$. The $\mathcal{F}_{1,2}$ structure functions parametrise the deviation from the cross section for the scattering of spin 1/2 particle of a point-like constituent, corresponding respectively to the electric and magnetic form factor in lepton nucleon scattering. $\mathcal{F}_1$ form factor is connected to $\mathcal{F}_2$ via the Callan-Gross relation $2x\mathcal{F}_1(x) = \mathcal{F}_2(x)$. The knowledge of $\mathcal{F}_2$ is shown in figure 2.2.
The two form factor $g_1(x, Q^2)$ and $g_2(x, Q^2)$ contribute to the cross section in the

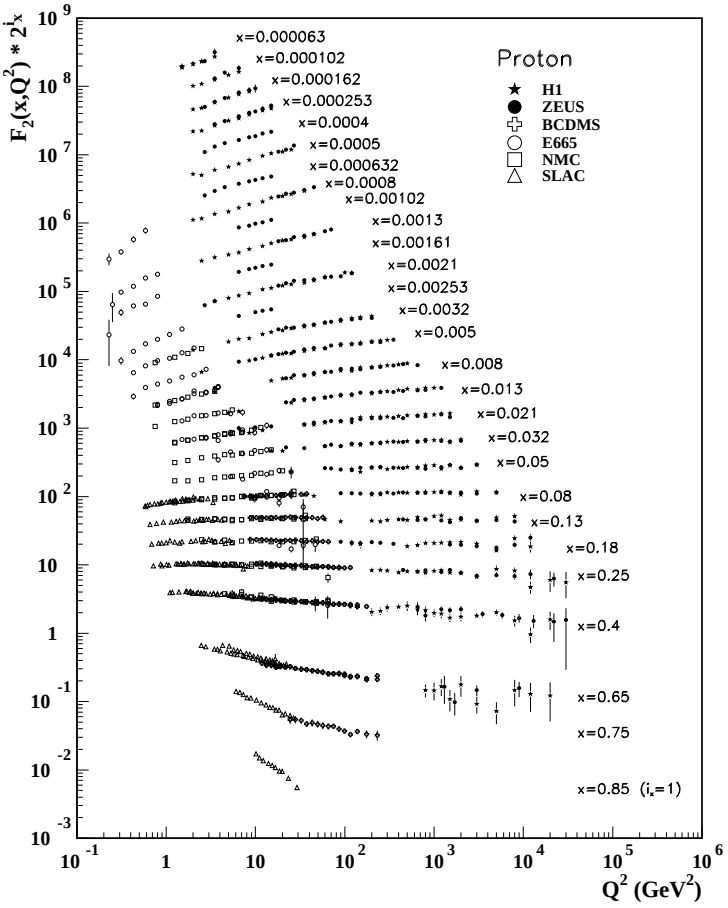

Figure 2.2: The proton structure function $\mathcal{F}_2^p$ measured in electromagnetic scattering of positrons on protons (experiments ZEUS[6] and H1[7]) at HERA, for $x > 0.00006$, and for electrons (SLAC[8]) and muons (BCDMS[9], E665[10], NMC[11]) on a fixed target. Statistical and systematic errors added in quadrature are shown. The data are plotted as a function of Q^2 in bins of x. For clarity, $\mathcal{F}_2^p$ has been multiplied by 2^{i_x}, where i_x is the number of the x bin, ranging from $i_x = 1$ ($x = 0.85$) to $i_x = 28$ ($x = 0.000063$). The figure has been taken from [12].

product of $W^{\mu\nu(A)}$ and the antisymmetric part of $L^{\mu\nu}$. They can be measured only with a polarised nucleon target and a polarised lepton beam. The quantity which is experimentally measured is the longitudinal spin-spin asymmetry:

$$A_{||} \equiv \frac{d\sigma^{\uparrow\Downarrow} - d\sigma^{\uparrow\Uparrow}}{d\sigma^{\uparrow\Downarrow} + d\sigma^{\uparrow\Uparrow}} \tag{2.13}$$

so the measurement of $A_{||}$ tells about the combination of g_1 and g_2 and not on the single function independently. Because of the relative magnitude of the coefficients of g_1 and g_2 in equations 2.11 and 2.12 respectively, g_2 contribution is suppressed in 2.11 with respect to g_1 of a factor M/E. For this reason $A_{||}$ provides essentially a direct measurement of the polarised structure function g_1. For transverse polarised target this kinematic suppression is missing, meaning that transverse polarisation is vital to measure g_2. In this case the measured quantity to access g_2 is the asymmetry of longitudinally polarised leptons on a transversely polarised target:

$$A_{\perp} \equiv \frac{d\sigma^{\rightarrow\Downarrow} - d\sigma^{\rightarrow\Uparrow}}{d\sigma^{\rightarrow\Downarrow} + d\sigma^{\rightarrow\Uparrow}} \tag{2.14}$$

The measurement of $A_{\perp}$ allows to extract information on the combination of g_1 and g_2. The general approach is to obtain information on g_2 relying on the result of $A_{||}$ for g_1.

2.3 The naïve parton model interpretation of $g_{1,2}$

In this section the parton-model expression for $g_{1,2}$ will be briefly derived. In the kinematic region of DIS the structure functions behave as function of x alone, Q^2 dependence is in fact observed only as a logarithmic variation $\sim ln(Q^2)$. This scaling property inspired Feynman to deduce the parton model of the nucleon in which the latter is visualised as being composed of point-like constituents identified with partons.
In an *infinite momentum frame* the nucleon can be considered as made up of fast moving constituents (partons), collinear with the nucleon, and the collision with the projectile is treated in an impulse approximation, as if the constituents were free particle. The deep inelastic cross-section is then the incoherent sum over elastic lepton quark-parton scattering, moreover since partons are considered as free all interactions between themselves and the target remnants are neglected.
In the parton model the deep inelastic structure function are written as:

$$\mathcal{F}_1(x) \overset{Callan\ Gross}{=} \frac{1}{2x}\mathcal{F}_2(x) = \frac{1}{2}\sum_q e_q^2\{q+\bar{q}\}(x) \tag{2.15}$$

and the polarised structure function g_1 is:

$$g_1(x) = \frac{1}{2}\sum_q e_q^2 \Delta q(x). \tag{2.16}$$

Here e_q denotes the electric charge of the struck quark and

$$\{q+\bar{q}\}(x) = (q^{\uparrow}+\bar{q}^{\uparrow})(x) + (q^{\downarrow}+\bar{q}^{\downarrow})(x) \tag{2.17}$$

$$\Delta q(x) = (q^{\uparrow}+\bar{q}^{\uparrow})(x) - (q^{\downarrow}+\bar{q}^{\downarrow})(x) \tag{2.18}$$

denotes the spin-independent (unpolarised) and spin dependent quark parton distributions (PDs) which measure the distribution of quark momentum and spin in the proton. $\bar{q}^{\downarrow}(x)$ is so interpreted as the probability of finding an antiquark with a fraction x of momentum of the parent nucleon and with its spin in the opposite direction of the target nucleon. When the momentum fraction x is integrated out, the first moment of the unpolarised PD measure the number of valence quarks in the proton:

$$\int_0^1 dx(u-\bar{u})(x) = 2 \tag{2.19}$$

$$\int_0^1 dx(d-\bar{d})(x) = 1 \tag{2.20}$$

$$\int_0^1 dx(s-\bar{s})(x) = 0 \tag{2.21}$$

for the up, down and strange quark respectively. The quantity

$$\Delta q = \int_0^1 dx \Delta q(x) \tag{2.22}$$

is interpreted as the fraction of the nucleon spin which is carried by quarks and anti-quarks of flavor q.
In the naïve parton model $g_1(x)$ has a clear unambiguous probabilistic interpretation, much more the result is not sensitive to the quark mass.
Quite the opposite happens for $g_2(x)$ where transverse spin is relevant, in the framework of the parton model in fact, it is not possible to obtain a reliable calculation for the second spin structure function: $g_2(x)$ has a non trivial parton interpretation and vanishes without the effect of quark transverse momentum.
It is useful to rewrite the expression for $g_1(x)$ in terms of linear combinations of quark densities which have specific transformation properties under the group of flavour $SU(3)_F$:

$$\Delta q_3 = (\Delta u - \Delta\bar{u}) - (\Delta d - \Delta\bar{d}) \tag{2.23}$$

$$\Delta q_8 = (\Delta u - \Delta\bar{u}) + (\Delta d - \Delta\bar{d}) - 2(\Delta s - \Delta\bar{s}) \tag{2.24}$$

$$\Delta\Sigma = (\Delta u - \Delta\bar{u}) + (\Delta d - \Delta\bar{d}) + (\Delta s - \Delta\bar{s}) \tag{2.25}$$

These three quark densities transform respectively as the third component of an isotopic spin triplet, the eighth component of an $SU(3)_F$ octet, and a flavour singlet. Then:

$$g_1^P(x) = \frac{1}{9}\left[\frac{3}{4}\Delta q_3(x) + \frac{1}{4}\Delta q_8(x) + \Delta\Sigma(x)\right] \tag{2.26}$$

$$g_1^N(x) = \frac{1}{9}\left[-\frac{3}{4}\Delta q_3(x) + \frac{1}{4}\Delta q_8(x) + \Delta\Sigma(x)\right] \tag{2.27}$$

and the first moments

$$\Gamma_1^P = \int_0^1 g_1^P(x)dx = \frac{1}{9}\left[\frac{3}{4}a_3 + \frac{1}{4}a_8 + a_0\right], \quad \Gamma_1^N = \int_0^1 g_1^N(x)dx = \frac{1}{9}\left[-\frac{3}{4}a_3 + \frac{1}{4}a_8 + a_0\right] \tag{2.28}$$

where

$$a_3 = \int_0^1 \Delta q_3(x)dx \quad a_8 = \int_0^1 \Delta q_8(x)dx \quad a_0 = \int_0^1 \Delta\Sigma(x)dx \equiv \Delta\Sigma\ . \tag{2.29}$$

In the previous expressions a_3 and a_8 are measures of the proton matrix elements of an $SU(3)$ flavor octet of quark axial-vector currents.

$$\left\langle P,S|J_{5\mu}^j|P,S\right\rangle = Ma_jS_\mu \qquad j = 1,.....8 \tag{2.30}$$

where

$$J_{5\mu}^j = \bar{\psi}\gamma_\mu\gamma_5\left(\frac{\lambda_i}{2}\right)\psi, \tag{2.31}$$

while a_0 is the hadronic matrix element of a flavour singlet axial current $J_{5\mu}^0$. Here the λ_i are the usual Gell-Mann matrices and ψ is a column vector in flavor space $\psi^T = (\psi_u, \psi_d, \psi_s)$. To the extent that flavor $SU(3)$ is a global symmetry of the strong interactions the non singlet octet will be conserved currents, and this will lead to the a_j $(j = 1, ...8)$ being independent of Q^2. The singlet axial current is not conserved as a consequence of the axial anomaly so that $a_0 = a_0(Q^2)$. Now what is remarkable is that the octet of the axial-vector currents is precisely the set of currents that controls the weak β-decays of the neutron and of the spin 1/2 hyperons. Consequently a_3 and a_8 can be expressed in terms of two parameters F and D measured in hyperon β-decay.

$$\begin{array}{l} a_3 = F + D \equiv g_A = 1.2573 \pm 0.0028 \\ \frac{1}{\sqrt{3}}a_8 = \frac{1}{3}(F - D) = 0.193 \pm 0.008 \end{array} \tag{2.32}$$

It follows that the measurement of Γ_1^p in polarised DIS can be interpreted via equation 2.28 as a measurement of a_0.

2.4 The spin crisis

The EMC[13] collaboration provided in 1998 the first moments of g_1^P over such a large x-range that it was possible to evaluate accurately its firs moment Γ_1^P. The original data from EMC are shown in figure 2.3 their measured value was:

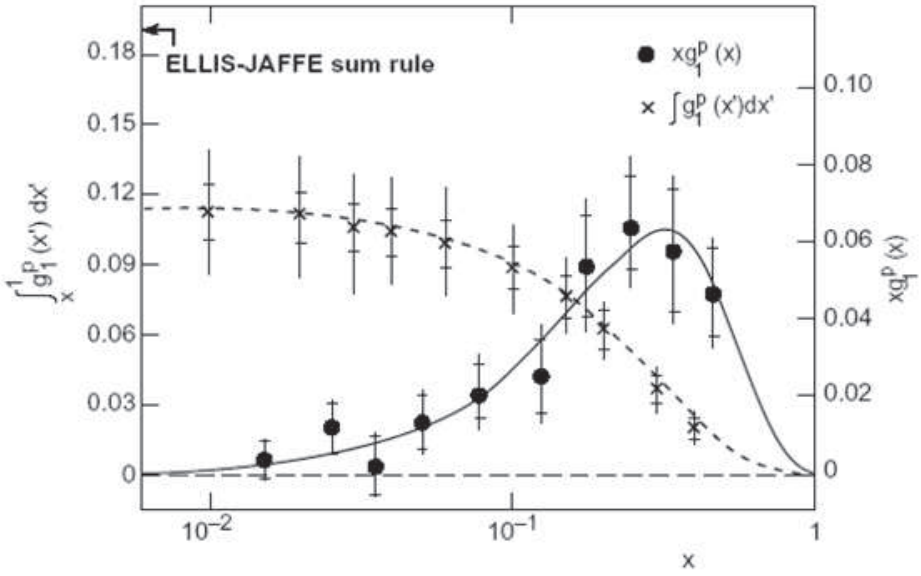

Figure 2.3: $xg_1^P(x)$ (circles) and $\Gamma_1^P = \int_x^1 g_1^P(\tilde{x})d\tilde{x}$ (crosses) resulting from the measurement by the EMC collaboration in 1988. The expected value from the Ellis-Jaffe sum rule for the first moment of the proton is indicated by the arrow.

$$\Gamma_1^P = 1.123 \pm 0.013 \pm 0.019 \tag{2.33}$$

where the first is the statistical error, the second the systematic one respectively. Using the known value of a_3 and a_8, the EMC could estimate a_0,

$$a_0^{EMC} = 0.12 \pm 0.17. \tag{2.34}$$

In the reasonable assumptions that one can neglect in the nucleon spin budget the contribution of $\Delta s = \Delta\bar{s}$ of the strange quark (this hypothesis is at the basis of the Ellis-Jaffe sum rule), one has

$$\Delta\Sigma^{EMC} = a_0^{EMC} = 0.12 \pm 1.17 \ . \tag{2.35}$$

This result is at variance with our theoretical prejudice.
In the naïve parton model the nucleon is simply an ensemble of free, parallel moving quarks with no orbital angular momentum, and the nucleon state is a superposition of free quarks. Now given the physical significance of the number densities $q_\pm(x)$ discussed in 2.3 the integral $\Delta\Sigma$ is just twice the expectation value of the sum of the z-components of the quark and anti-quark spins, i.e.

$$a_0 = \Delta\Sigma = 2\langle S_z^{quarks}\rangle \tag{2.36}$$

which implies that $a_0 = 1$ is expected. The EMC experiment result, a_0 compatible with zero, provoked a crisis in the parton model which came to be known as "the spin crisis".

2.5 The parton model in QCD: sum rules

The treatment in section 2.3 was proposed before the formulation of QCD, and does not take into account the presence of the gluon field and the interaction between quarks and gluons. When interaction comes into play Bjorken scaling is broken and the main effect is that the parton densities get replaced by Q^2-dependent densities $\Delta q(x, Q^2)$, whose Q^2-dependence or evolution can be handled perturbatively. The first moment of the proton can then be written as:

$$\begin{array}{l} \Gamma_1^p(Q^2) \equiv \int_0^1 dx g_1^p(x, Q^2) \\ = \frac{1}{12}\left[(a_3 + \frac{a_8}{\sqrt{3}})E_{NS}(Q^2) + \frac{4}{3}a_0(Q^2)E_S(Q^2)\right] \end{array} \tag{2.37}$$

where the non-singlet and singlet coefficients function have the expansion:

$$\begin{array}{l} E_{NS}(Q^2) = 1 - \frac{\alpha_s}{\pi} - \left(\begin{array}{c} 3.58 \\ 3.25 \end{array}\right)\left(\frac{\alpha_s}{\pi}\right)^2 ... \\ E_S(Q^2) = 1 - \frac{\alpha_s}{\pi} - \left(\begin{array}{c} 1.10 \\ -0.07 \end{array}\right)\left(\frac{\alpha_s}{\pi}\right)^2 ... \end{array} \tag{2.38}$$

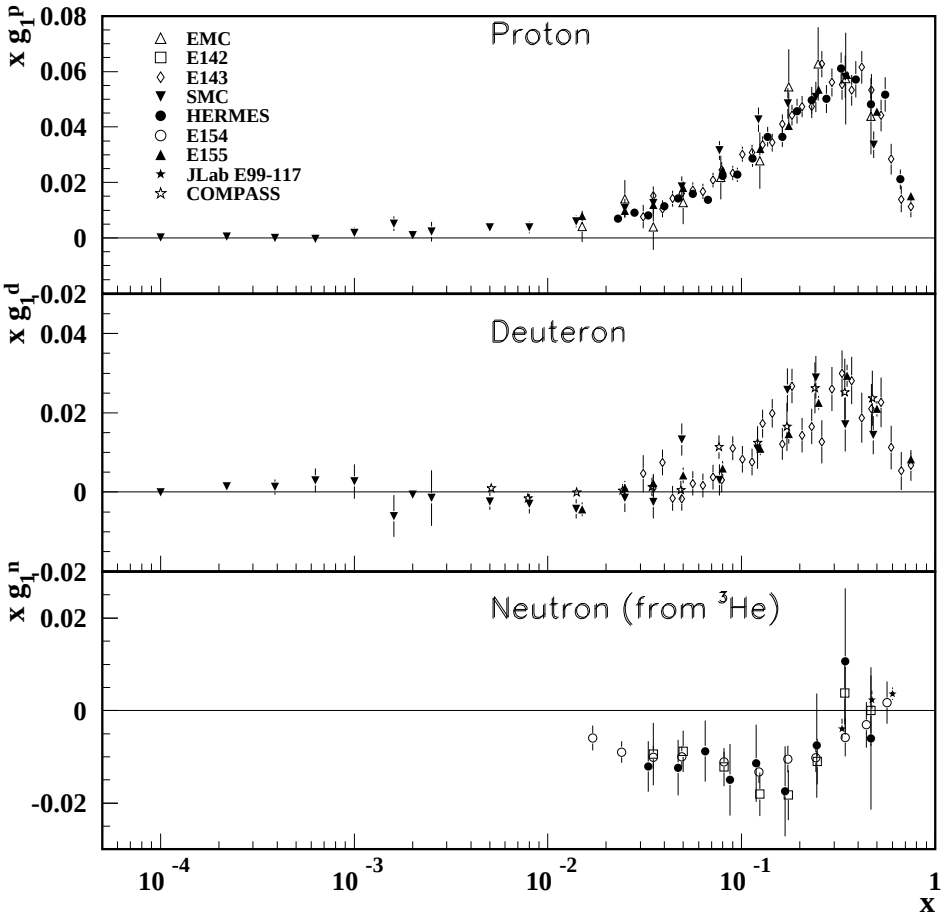

Figure 2.4: The spin-dependent structure function $xg_1(x)$ of the proton (top), deuteron (middle), and neutron (bottom) measured in deep inelastic scattering of polarised electrons/positrons: E142[14] ($Q^2 \sim 0.3{-}10$ GeV^2), E143[15] ($Q^2\sim 0.3 - 10$ GeV^2), E154[16] ($Q^2\sim 1 - 17$ GeV^2), E155[17] ($Q^2\sim 1 - 40$ GeV^2), JLab E99-117[18]($Q^2\sim 2.71 - 4.83$ GeV^2), HERMES[19] ($Q^2\sim 0.8 - 20$ GeV^2) and muons: EMC[13] ($Q^2\sim 1.5 - 100$ GeV^2), SMC[20] ($Q^2\sim 0.01 - 100$ GeV^2), COMPASS[21] ($Q^2\sim 1 - 100$ GeV^2), shown at the measured Q^2 (except for EMC data given at $Q^2 = 10.7$ GeV^2 and E155 data given at $Q^2 = 5$ GeV^2). Statistical and systematic errors are added in quadrature. The figure has been taken from [12].

where $\alpha_s = \alpha_s(Q^2)$ is the running QCD coupling, and the upper and lower number corresponds to taking either three flavors of quark or four flavors if one includes the charm quark.

The determination of the first moment of the proton is not straightforward, firstly since extrapolation of the data using $g_1(x, Q^2)$ have to be made in the region $x = 0$ and $x = 1$ in calculating the integral and secondly because the data at different x-values correspond to different ranges of Q^2. It is worth to note that in going from the case of the proton to a neutron a_8 and a_0 remain unchanged while a_3 changes sign. Consequently one has the *Bjorken sum rule*:

$$\int_0^1 dx \left[g_1^p(x, Q^2) - g_1^n(x, Q^2)\right] = \frac{g_A}{6} E_{NS}(Q^2) \tag{2.39}$$

This equation is considered to be a very fundamental result since it can be derived independently from the parton model framework. The measurement of Γ_1^p by the EMC[13] and of Γ_1^n by SMC[20] allowed for a first consistent check of this sum rule obtained using the known value of a_3. Currently the right hand side is known with great accuracy and much effort has gone into trying to test it: up to now it seems to be well satisfied by the data.
Adding the the assumption $\Delta s = \Delta \bar{s} = 0$ it results $a_0 = \sqrt{3} a_8$ and eq. 2.37 reads:

$$\Gamma_1^{p,n} = \frac{1}{12} a_3 \left\{ \pm 1 + \frac{5}{\sqrt{3}} \cdot \frac{a_8}{a_3} \right\} \tag{2.40}$$

which is known as the Ellis-Jaffe sum rule[1].
The Γ_1^p measured from EMC indicated a large violation of the Ellis-Jaffe sum rule, implying that the assumption $\Delta s = \Delta \bar{s} = 0$ had to be released. Even more important the value of a_0 extracted from the Γ_1^p turned out to be consistent with zero and, as stressed in the previous section, led to a *crisis in the parton model*.
The present value of $\Gamma_1^p(Q^2)$ at Q^2=10 $(\mathrm{GeV}/c)^2$ has been measured by many experiments and lies in the range

$$0.130 \leq \Gamma_1^p(Q^2 = 10(GeV/c)^2) \leq 0.142 \tag{2.41}$$

which leads to

$$0.22 \leq a_0(Q^2 = 10(GeV/c)^2) \leq 0.34. \tag{2.42}$$

a value still considered as disturbingly small.

2.6 QCD improved parton model: corrections and evolution

In the previous sections it has been seen that although gluons do not interact directly with the virtual photon, they mediate the strong interaction giving rise to QCD

[1]The $\pm$ sign corresponds to the proton or neutron case respectively.

corrections to the quark-parton model. In a QCD improved parton model the PDFs depend upon Q^2 in a way which is calculable. When Q^2 is increased the resolution of the probe is increased too: what appeared a quark at a given scale at a different one may appear as a quark surrounded by a clouds of $q\bar{q}$ pairs (the sea quark) and gluons, so the number of resolved parton is increased. In QCD this is described by the splitting functions P_{qq}, P_{qg}, P_{gq}, and P_{gg} where P_{gg} for instance corresponds to the possibility of a gluon to emit a gluon. The Q^2 evolution of the PDFs is described by the DGLAP equations and if they are known at a certain scale they can be computed (evoluted) at any other scale using DGLAP equations.
The $SU(3)$ singlet axial current conservation, valid for massless quarks, in QCD is no longer valid. There exists a non zero anomalous contribution that induces a gluon contribution. Including the anomaly effect the expression between a_0 and $\Delta\Sigma$ becomes different from the naïve parton model one:

$$a_0(Q^2) = \Delta\Sigma - 3\frac{\alpha_s(Q^2)}{2\pi}\Delta G(Q^2) \tag{2.43}$$

This results has the fundamental implication that *the small measured value of* a_0 *from the EMC collaboration does not necessary imply that* $\Delta\Sigma$ *is small.* The contribution of quark and anti-quark to the nucleon spin can be cancelled out by the anomalous gluonic part. Moreover the added term in equation 2.43 does not vanish at large Q^2 where $\alpha_s(Q^2) \rightarrow\ 0$ because $\Delta G(Q^2)$ can be shown to grow in precise the right way to compensate the decrease of $\alpha_s(Q^2)$[5]. A measurement of ΔG is necessary, both for itself and as an element of the spin puzzle; taking into account this new contribution, eq. 2.36 can be written as:

$$S_z = \frac{1}{2} = \frac{1}{2}\Delta\Sigma + \Delta G + \langle L_z \rangle, \tag{2.44}$$

where the possible contribution from the gluons and quarks orbital angular momentum, $\langle L_z \rangle$ have also been included. A direct measurement of ΔG is one of the most important measurements at COMPASS, and is part of the scientific program of other polarised semi-inclusive deep inelastic scattering experiments as HERMES and of high energy polarised pp scattering experiments at RHIC.

2.7 Transversity

There are three species of twist two quark distributions in QCD. These are the spin independent distributions $q(x)$, measured in the unpolarised structure functions F_1 and F_2, the spin dependent quark distribution $\Delta q(x)$, measured in g_1 and the transversity distributions $\Delta_T q(x)$ denoted also as $\delta q(x)$ and $h_1^q(x)$ [22]. All these PDFs have to be considered to fully describe the quark spin composition of the nucleon. The third distribution was introduced first in 1979 by Ralston and Soper [23],

but only in the nineties it was the subject of an intense theoretical activity, when it was rediscovered by Artru and Mekhfi [24] and by Jaffe and Ji [25]. In the same time, on the experimental side, first proposals [26, 27] to measure transversity were put forward. In recent years new theoretical [25, 28] and experimental efforts [29, 30] have been devoted to explore the transverse spin and momentum structure of the nucleon. This concerns in particular the investigations of the chiral-odd transversely polarised quark distribution function. In parton language its interpretation is clear[31]: considering a nucleon moving along the z direction and polarised along a transverse direction with respect to z, $\Delta_T q(x)$ counts the quark with flavor q, momentum fraction x and their spin parallel to the spin of the nucleon minus the number anti-parallel. That is $\Delta_T q(x) = q^{\uparrow}(x) - q^{\downarrow}(x)$ measures the distribution of partons with transverse polarisation in a transversely polarised nucleon. In a helicity basis, transversity corresponds to the helicity flip structure shown in figure 2.5 therefore it can not be measured in inclusive DIS due to the helicity conservation in QCD processes. However with another hadron in the initial state, *e.g.* Drell-Yan Scattering [23], or in the final state, *e.g.* semi-inclusive deep-inelastic [32] scattering, the transverse structure of the nucleon can be accessed without suppression by a hard scale and, at leading twist one can measure the product of $\Delta_T q$ with another distribution or fragmentation function.
If quark moved non relativistically the nucleon δq and Δq would be identical since rotation and Euclidean boost commute and a series of boosts and rotation can convert a longitudinally polarised nucleon in a transversely polarised one at infinite momentum. The difference between δq and Δq is so related to the relativistic character of quark motion in the nucleon.
Little is presently known about the shape of the transversity distributions. However

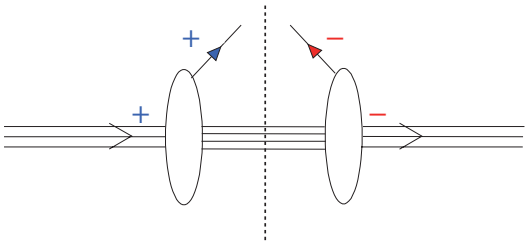

Figure 2.5: Transversity in helicity basis.

some general properties can be deduced from QCD arguments. The spin distributions δq and Δq have opposite charge conjugation operator: Δq is C-even whereas δq is C-odd. Also transversity is chiral odd. The spin quark and the gluon helicity mix under Q^2 evolution. In contrast there is no analogue of gluon transversity

so δq evolves without mixing like a non singlet PDF. Under QCD evolution the moments $\int_0^1 dx x^n \delta q(x, Q^2)$ decrease with increasing Q^2. In leading order QCD the transversity distributions are bound by the Soffer's inequality:

$$\left|\delta q(x, Q^2)\right| \leq \frac{1}{2}\left[q(x, Q^2) + \Delta q(x, Q^2)\right]. \tag{2.45}$$

2.7.1 A way to measure transversity: SIDIS processes.

As mentioned in section 2.7 a possible way access transversity is via Semi Inclusive Deep Inelastic Scattering reactions. Based on the general principles of quantum field theory it can be shown in a model independent way that the cross-section of the SIDIS process

$$\ell(k) + N(P) \rightarrow \ell(k') + h(P_h) + X \tag{2.46}$$

can be factorised into a hard photon-quark scattering process and parton distribution functions describing the distribution of quarks in the target and fragmentation functions describing the fragmentation of a quark into the observed hadron. Within this approach the cross section formula for hadron produced in the current fragmentation region of SIDIS can be written as

$$d\sigma^{lN \rightarrow l'hX} = \sum_q q \cdot d\sigma^{lq \rightarrow l'q'} \cdot D_q^h \tag{2.47}$$

The term $d\sigma^{lq \rightarrow l'q'}$ is the hard part of the scattering, q functions are the parton distribution function while D_q^h are the fragmentation functions which relate the probability of a quark to produce a hadron h. Symmetry arguments reduce the number of fragmentation functions: due to $SU(2)$ symmetry $D_u^{\pi^+} = D_{\bar{d}}^{\pi^-}$ and $D_{\bar{d}}^{\pi^+} = D_{\bar{u}}^{\pi^-}$ and due to charge conjugation $D_{\bar{d}}^{\pi^-} = D_{\bar{d}}^{\pi^+}$. The fragmentation function $D_u^{\pi^+}$ is said to be *favoured* since it corresponds to the production of a $\pi^+ = u\bar{d}$ from a u quark, similarly $D_u^{\pi^-}$ is said *unfavoured*. In the so called *gamma-nucleon system* (GNS, fig. 2.6) where the virtual photon direction defines the z axis, and the xz plane is the lepton scattering plane (defined by the initial and final lepton momenta), the polarised semi-inclusive DIS cross section depends on the azimuthal angle ϕ_h of the produced hadron with respect to the scattering plane, as well as on the azimuthal angle of the target nucleon spin, ϕ_S. Assuming single photon exchange, and in case

of spinless final state hadrons, the cross section reads [33]:

$$\frac{d\sigma}{dx\,dy\,d\phi_S\,dz\,d\phi_h\,dP_T^{h\,2}} =$$
$$\frac{\alpha^2}{xyQ^2}\,\frac{y^2}{2\,(1-\zeta)}\left(1+\frac{\gamma^2}{2x}\right)\Bigg\{F_{UU,T}+\zeta\,F_{UU,L}+\sqrt{2\,\zeta(1+\zeta)}\,\cos\phi_h\,F_{UU}^{\cos\phi_h}$$
$$+\zeta\cos(2\phi_h)\,F_{UU}^{\cos 2\phi_h}+\lambda_e\,\sqrt{2\,\zeta(1-\zeta)}\,\sin\phi_h\,F_{LU}^{\sin\phi_h}$$
$$+S_\parallel\left[\sqrt{2\,\zeta(1+\zeta)}\,\sin\phi_h\,F_{UL}^{\sin\phi_h}+\zeta\sin(2\phi_h)\,F_{UL}^{\sin 2\phi_h}\right]$$
$$+S_\parallel\lambda_e\left[\sqrt{1-\zeta^2}\,F_{LL}+\sqrt{2\,\zeta(1-\zeta)}\,\cos\phi_h\,F_{LL}^{\cos\phi_h}\right]$$
$$+S_\perp\Bigg[\sin(\phi_h-\phi_S)\left(F_{UT,T}^{\sin(\phi_h-\phi_S)}+\zeta\,F_{UT,L}^{\sin(\phi_h-\phi_S)}\right)$$
$$+\zeta\,\sin(\phi_h+\phi_S)\,F_{UT}^{\sin(\phi_h+\phi_S)}+\zeta\,\sin(3\phi_h-\phi_S)\,F_{UT}^{\sin(3\phi_h-\phi_S)}$$
$$+\sqrt{2\,\zeta(1+\zeta)}\,\sin\phi_S\,F_{UT}^{\sin\phi_S}+\sqrt{2\,\zeta(1+\zeta)}\,\sin(2\phi_h-\phi_S)\,F_{UT}^{\sin(2\phi_h-\phi_S)}\Bigg]$$
$$+S_\perp\lambda_e\Bigg[\sqrt{1-\zeta^2}\,\cos(\phi_h-\phi_S)\,F_{LT}^{\cos(\phi_h-\phi_S)}+\sqrt{2\,\zeta(1-\zeta)}\,\cos\phi_S\,F_{LT}^{\cos\phi_S}$$
$$+\sqrt{2\,\zeta(1-\zeta)}\,\cos(2\phi_h-\phi_S)\,F_{LT}^{\cos(2\phi_h-\phi_S)}\Bigg]\Bigg\}; \qquad (2.48)$$

where λ_e is the helicity of the lepton beam, $S_\parallel$ and $S_\perp$ are respectively the projection of the target polarisation in the plane parallel or transverse with respect to the photon direction, and the ratio ζ of longitudinal and transverse photon flux is given by:

$$\zeta=\frac{1-y-\frac{1}{4}\gamma^2y^2}{1-y+\frac{1}{2}y^2+\frac{1}{4}\gamma^2y^2}, \qquad (2.49)$$

where $\gamma=\frac{2Mx}{Q}\sim 0$, and will be neglected in the following. The 18 structure functions F depend on x, Q^2, z and $P_T^{h\,2}$[2]; the first and second subscript indicate

[2] P_T^h is the transverse momentum of the final state hadron with respect to the photon direction, while p_T^h is the transverse momentum of the final state hadron with respect to the fragmenting quark direction

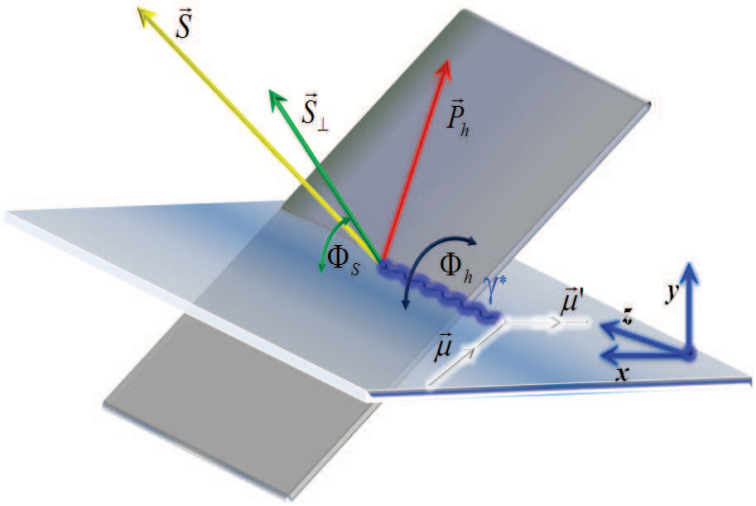

Figure 2.6: Definition of the Gamma Nucleon System, the xz plane is defined by the incoming and scattered lepton, the z axis is defined by the photon direction.

the respective polarisation of beam and target (U=unpolarised, L=longitudinal, T=transverse), whereas the third subscript in $F_{UU,T}$, $F_{UU,L}$ and $F_{UT,T}^{\sin(\phi_h-\phi_S)}$, $F_{UT,L}^{\sin(\phi_h-\phi_S)}$ specifies the polarisation of the virtual photon. The superscript in the structure functions indicates the different azimuthal modulation in ϕ_h and ϕ_S. Equation 2.48 shows that of the eighteen structure functions, eight depend on the target transverse polarisation. Due to the different azimuthal modulations of each term, it is possible to build cross section asymmetries and extract each term from the data. Out of the eight transverse structure functions of eq. 2.48, four can be expressed via leading twist PDFs:

$$F_{UT}^{\sin(\phi_h+\phi_S)} = \mathcal{C}\left[-\frac{\hat{h}\cdot\vec{p}_T}{M_h} h_1 H_1^\perp\right] , \tag{2.50}$$

$$F_{UT,T}^{\sin(\phi_h-\phi_S)} = \mathcal{C}\left[-\frac{\hat{h}\cdot\vec{k}_T}{M} f_{1T}^\perp D\right] , \tag{2.51}$$

$$F_{UT}^{\sin(3\phi_h-\phi_S)} = \mathcal{C}\left[\frac{2\left(\hat{h}\cdot\vec{k}_T\right)\left(\vec{k}_T\cdot\vec{p}_T\right)+\vec{k}_T^2\left(\hat{h}\cdot\vec{p}_T\right)-4\left(\hat{h}\cdot\vec{k}_T\right)^2\left(\hat{h}\cdot\vec{p}_T\right)}{2M^2M_h} h_{1T}^\perp H_1^\perp\right] , \tag{2.52}$$

$$F_{LT}^{\cos(\phi_h-\phi_S)} = \mathcal{C}\left[\frac{\hat{h}\cdot\vec{k}_T}{M} g_{1T} D\right] ; \tag{2.53}$$

where $\hat{h} = \vec{P_T^h}/|P_T^h|$.

Equation 2.50 is related to the Collins effect (section 2.7.2); the $\delta q(x)$ PDF is the TMD transversity, defined as:

$$h_1(x, k_T^2) = h_{1T}(x, k_T^2) - \frac{k_T^2}{2M^2} h_{1T}^{\perp}(x, k_T^2); \tag{2.54}$$

this unintegrated PDF is related to the transversity distribution introduced in section 2.7 via:

$$\Delta_T q(x) = h_1(x) \int d^2\vec{k}_T h_1(x, k_T^2) \ . \tag{2.55}$$

The fragmentation function $H_1^{\perp}$ appearing in eq. 2.50 is the Collins fragmentation function, describing the spin-dependent part of the fragmentation of a transversely polarised quark.

Eq. 2.51 describes the so called Sivers effect, that will be explained in section 2.7.3. The Sivers function $f_{1T}^{\perp}$ is convoluted with the unpolarised fragmentation function D.

The structure functions in eq. 2.52 and 2.53 give access to the PDFs $h_{1T}^{\perp}$ and the chiral even g_{1T}, convoluted with $H_1^{\perp}$ and D respectively.

The other four transverse structure functions in eq. 2.48 are twist-3 contributions, and have no simple interpretation in the parton model.
The terms that have received more attention both from the experimental and from the theoretical side, are the Collins and Sivers modulations, that will be described in the following.

2.7.2 The Collins mechanism

In SIDIS off transversely polarised nucleons the Collins mechanism is responsible for a modulation in the azimuthal distribution of the produced hadrons. The measurable asymmetry is due to the combined effect of $\Delta_T(q)$ and a chirally-odd fragmentation function (FF) $H_1^{\perp}$ which describes the spin-dependent part of the hadronisation of a transversely polarised quark. At leading twist, the existence of such a naively T-odd FF arising from final state interaction effects, was predicted by Collins [32] and is now generally known as the Collins FF.

In the fragmentation of transversely polarised quarks it is responsible for a left-right asymmetry which is due to a correlation between the spin of the fragmenting quark and the transverse momentum $\vec{p}_T^{\,h}$ of the produced hadron with respect to the quark direction. $H_1^{\perp}$ can be defined considering the distribution of hadrons produced from quarks with opposite polarisation [34]:

$$N_{h/q\uparrow}(z, \vec{p}_T) - N_{h/q\downarrow}(z, \vec{p}_T) = \frac{|\vec{p}_T|}{M_h} sin(\Phi_h - \Phi_{S'}) H_1^{\perp}(z, {p_T^h}^2) \ . \tag{2.56}$$

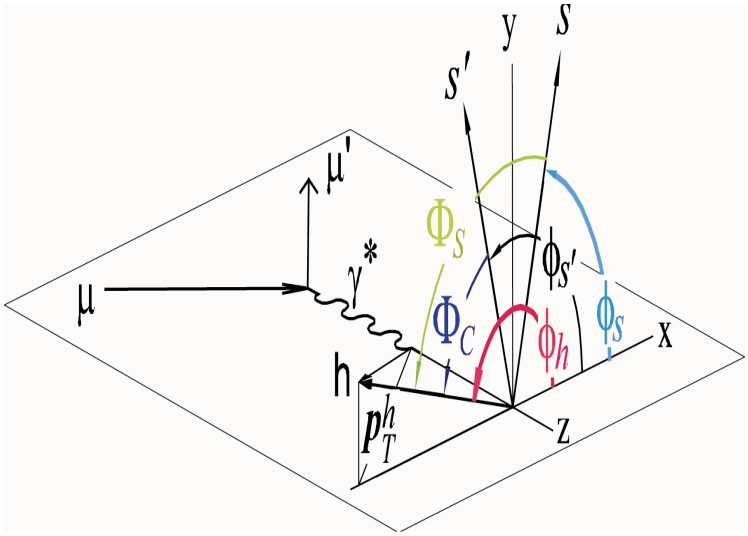

Figure 2.7: Definition of the azimuthal angle Φ_h of the transverse momentum P_T^h of the outgoing hadron and of the azimuthal angle Φ_S of the transverse spin vector $\vec{S}$ of the target nucleon.

In a gamma nucleon reference system (GNS) (see fig. 2.7), in which the z-axis coincides with the virtual photon direction and the x-z plane is the lepton scattering plane, the Collins angle is defined as $\Phi_C = \Phi_h + \Phi_S - \pi = \Phi_h + \Phi_{S'}$. Here Φ_h is the azimuthal angle of the transverse momentum of the outgoing hadron and Φ_S is the azimuthal angle of the transverse spin vector $\vec{S}$ of the target nucleon. By comparing the cross sections on oppositely polarised target nucleons one obtains the transverse single spin asymmetry:

$$A_T^h \equiv \frac{d\sigma(\vec{S}_\perp) - d\sigma(-\vec{S}_\perp)}{d\sigma(\vec{S}_\perp) + d\sigma(-\vec{S}_\perp)} = S_\perp \cdot D_{NN} \cdot A_{Coll} \cdot \sin\Phi_C \ . \tag{2.57}$$

The Collins asymmetry is

$$A_{Coll} = \frac{\sum_q e_q^2 \cdot x \cdot \Delta_T q(x) \cdot \Delta_T^0 D_q^h(z, {P_T^h}^2)}{\sum_q e_q^2 \cdot x \cdot q(x) \cdot D_q^h(z, {P_T^h}^2)} \ , \tag{2.58}$$

where

$$D_{NN} = \frac{1-y}{1-y+y^2/2} \tag{2.59}$$

is the transverse spin transfer coefficient from the initial to the struck quark [28] and

$$\Delta_T^0 D(z, {p_T^h}^2) = -\frac{|\vec{p}_T|}{M_h} H_1^\perp(z, {p_T^h}^2). \tag{2.60}$$

is the Collins Fragmentation Function. As evident from eq. 2.58, the Collins asymmetry gives access to the transversity distribution function.

2.7.3 The Sivers mechanism

An entirely different mechanism was suggested by Sivers [35] to explain a spin asymmetry in the cross-section of SIDIS of leptons off transversely polarised nucleons. Sivers conjecture was the possible existence of a correlation between the transverse momentum $\vec{k}_T$ of an unpolarised quark in a transversely polarised nucleon and the nucleon polarisation vector. Considering the number density of unpolarised quarks in opposite transversely polarised nucleons, the Sivers function can be defined as:

$$\begin{aligned} \mathcal{P}_{q/N\uparrow}(x,\vec{k}_T) - \mathcal{P}_{q/N\downarrow}(x,\vec{k}_T) &= \mathcal{P}_{q/N\uparrow}(x,\vec{k}_T) - \mathcal{P}_{q/N\uparrow}(x,-\vec{k}_T) && (2.61) \\ &= -\frac{|\vec{k}_T|}{M} S_\perp \sin(\phi_S - \phi_q)\, f_{1T}^\perp(x,k_T^2)\,. && (2.62) \end{aligned}$$

where the Sivers angle, $\Phi_S = \Phi_S - \Phi_h$ is the relative azimuthal angle between the target spin $\vec{S}_\perp$ and the quark transverse momentum $\vec{k}_T$, and the $f_{1T}^\perp(x,k_T^2)$ is the Sivers function. Again, comparing the cross sections on oppositely polarised target nucleons, the transverse spin asymmetry results

$$A_T^h \equiv \frac{d\sigma(\vec{S}_\perp) - d\sigma(-\vec{S}_\perp)}{d\sigma(\vec{S}_\perp) + d\sigma(-\vec{S}_\perp)} = S_\perp \cdot A_{Siv} \cdot \sin\Phi_S\ , \tag{2.63}$$

where the Sivers asymmetry

$$A_{Siv} = \frac{\sum_q e_q^2 \cdot x \cdot \Delta_0^T q(x, P_T^{h\,2}/z^2) \cdot D_q^h(z)}{\sum_q e_q^2 \cdot x \cdot q(x, P_T^{h\,2}/z^2) \cdot D_q^h(z)} \tag{2.64}$$

is revealed as a $\sin\Phi_S$ modulation in the number of produced hadrons (see equation 2.63) and

$$\Delta_0^T q(x,k_T^2) \;=\; -\frac{|\vec{k}_T|}{M}\, f_{1T}^T(x,k_T^2)\,. \tag{2.65}$$

is the Sivers TMD function.

2.7.4 Collins an Sivers asymmetries, present status.

Despite the problem that the lowest order QCD cross sections yield zero for asymmetries involving either an initially transversely polarised hadron or the production of a transversely polarised final state hadron in an unpolarised collision, experimentally

there is a huge amount of data showing large asymmetries or large polarisations both in elastic and semi inclusive reactions. The most dramatic examples are the Λ hyperons polarisation in unpolarised collisions of a 300 GeV proton beam on different targets (Be and p) at FERMILAB[36] (see fig. 2.8 left side) and during the '90s, the E704 [37] collaboration result. The E704 Collaboration collected single spin asymmetries data for pp and $p\bar{p}$ collisions using secondary polarised proton antiproton beams for different produced hadrons (π and Λ). As shown in figure 2.8 (right side) they measured very large single spin asymmetries, up to 30-40% in inclusive pion production in the large x_f region, both for polarised proton and antiprotons beams colliding on hydrogen target. Large transverse single spin asymmetries have also been observed in recent data from STAR collaboration at RHIC in proton proton collision at centre of mass energy of $\sqrt[2]{s}$=200 GeV [38]. Higher twist contribution

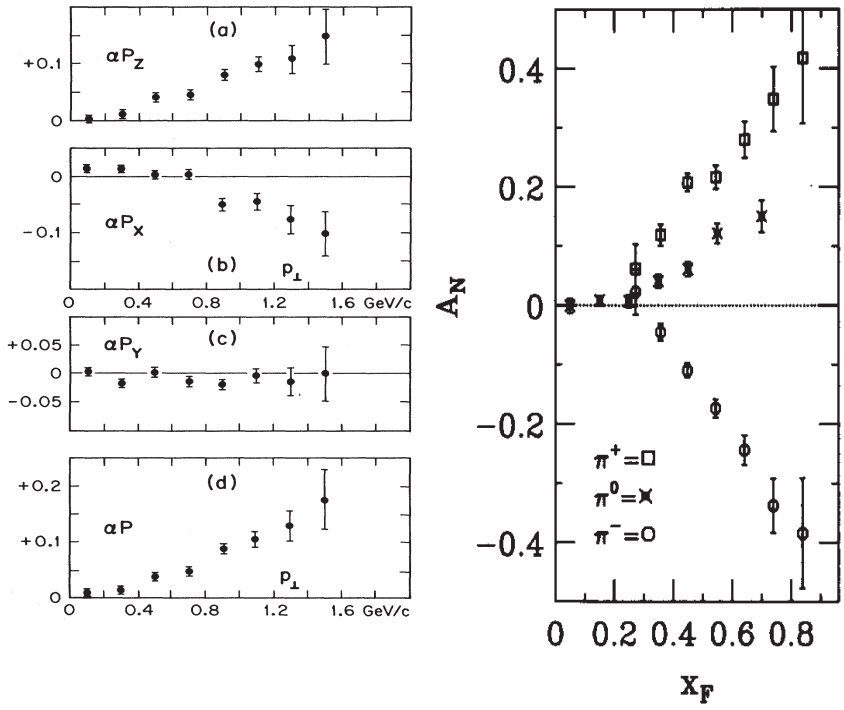

Figure 2.8: Left: Λ polarisation measured for inclusive production from proton-Beryllium scattering at FERMILAB [36]. Right: asymmetries in the inclusive production of pions using a polarised proton beam at FERMILAB [37].

from quark gluon correlations may be important[39]: recent PHENIX data [40] on $pp^{\uparrow} \rightarrow \pi^0 X$ at mid-rapidity has been interpreted to suggest a small gluon Sivers function [41]. The BRAHMS collaboration has also measured a significant non-zero asymmetries in forward charged pion production at 200 GeV/c as well as 62.4 GeV/c

momentum [42].
More in detail both the COMPASS and HERMES experiments have carried out several sets of azimuthal asymmetries measurement in SIDIS processes of leptons off transversely polarised target. The HERMES experiment has taken measurements of charged and neutral pion and charged kaons production in *ep* scattering with transverse target polarisation. This data has been analysed for possible contributions from the Collins and the Sivers effect. The azimuthal distribution of the final state pions with respect to the virtual photon axis is expected to carry information about transversity through the Collins mechanism and about intrinsic transverse momentum in the proton through the Sivers effect. In this analysis the transverse single spin asymmetries amplitude are written as:

$$\begin{aligned} A^{Collins} &\propto |\vec{s}_t| \sin(\phi + \phi_s) \frac{\sum_q e_q^2 \Delta_T q(x) H_1^{\perp,q}(z)}{\sum_q e_q^2 q(x) D_q^\pi(z)} \\ A^{Sivers} &\propto |\vec{s}_t| \sin(\phi - \phi_s) \frac{\sum_q e_q^2 f_{1T}^{T,q} D_q^\pi(z)}{\sum_q e_q^2 q(x) D_q^\pi(z)} \end{aligned} \tag{2.66}$$

Here ϕ is the angle between the lepton direction and the $(\gamma^*\pi)$ plane, ϕ_s the angle between the lepton direction and the transverse target spin. The projections of the two terms with different azimuthal angular dependence suggest that both the Collins and Sivers effect are present in the data (figure 2.9).
The preliminary results including *all the available statistics* (2002-2005 data) have been presented at the DIS07 and Hadron 2007 conferences [43, 44] and are shown as a function of x, z and P_T^h in fig. 2.9. The HERMES measurement of non zero single spin asymmetries on a proton target confirms that the Sivers and Collins effects are real effects, and that the transversity PDF is different from zero (the first evidence was already given by HERMES Collaboration in 2004 [43]). The kinematic region covered by the HERMES experiment is bound by the following constraints: $W^2 > (10\ \mathrm{GeV}^2/\mathrm{c}^4)$, $Q^2 > 1\ (\mathrm{GeV/c})^2$, $0.1 < y < 0.85$, $0.2 < z < 0.7$, $0.023 < x < 0.4$. The Sivers asymmetries are measured to be positive for π^+ and consistent with zero for π^-, moreover for K^+ the asymmetry signal is greater that the corresponding pion one, while for K^- is compatible with zero. The Collins asymmetries are positive for π^+ and negative and comparable in magnitude for π^-. For positive kaons the Collins asymmetry is comparable with the corresponding positive pion. For negative kaons the signal has the same strength but opposite sign with respect to negative pions. For neutral pions (not displayed) the Sivers asymmetry is positive and similar in strenght to the π^+ one, for Collins it is found statistically compatible with zero. With the positive and neutral pion asymmetries the HERMES collaboration has performed an important consistency check for the isospin symmetry of the π triplet, which has to hold both for the Collins and Sivers case[44]:

$$\langle \sin(\Phi_S \pm \Phi_h) \rangle_{UT}^{\pi^+} + \mathcal{C} \cdot \langle \sin(\Phi_h \pm \Phi_S) \rangle_{UT}^{\pi^-} - (1 - \mathcal{C}) \cdot \langle \sin(\Phi_h \pm \Phi_S) \rangle_{UT}^{\pi^0} = 0 \tag{2.67}$$

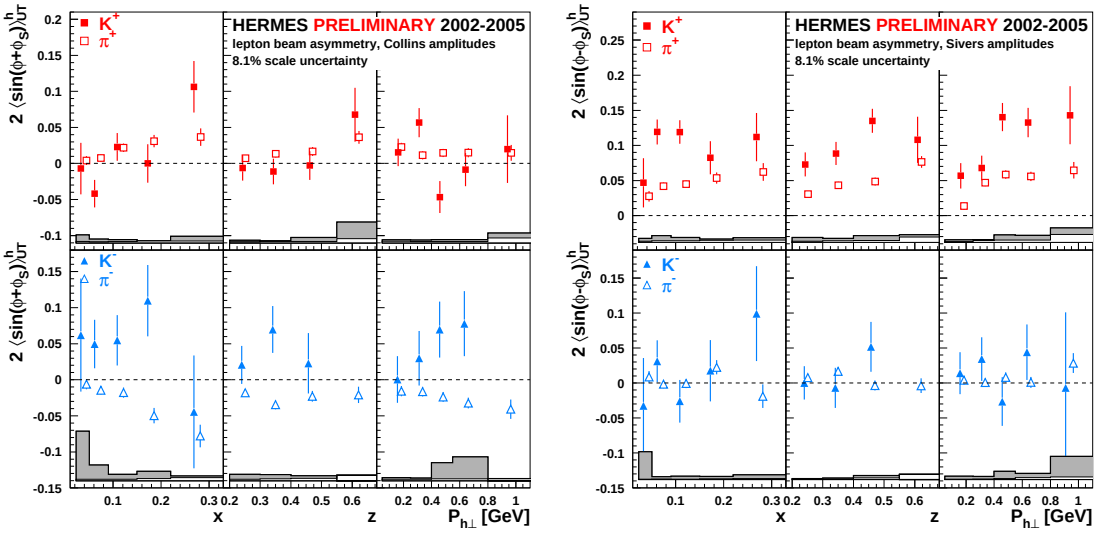

Figure 2.9: Collins amplitudes (left column) and Sivers amplitudes (right column) for charged kaons (closed symbols) and charged pions (open symbols) as function of x, z and P_T^h from HERMES experiment [43].

where $C = \sigma_{UU}^{\pi^-} \Big/ \sigma_{UU}^{\pi^+}$ is the ratio of the unpolarised cross section for negative and positive pion production. The extracted amplitudes for neutral pions, compatible with zero for Collins and slightly positive for the Sivers case present a magnitude intermediate compared to the corresponding ones for π^+ and π^-, fulfilling the isospin relation 2.67.
The COMPASS Collaboration has measured for the first time the Sivers and Collins asymmetries using a transversely polarised deuteron target. The kinematic range covered is: $W > 5$ GeV/c^2, $Q^2 > 1$ (GeV/c)^2, $0.1 < y < 0.9$, $z > 0.2$, $0.003 < x < 0.3$, $P_T^h > 0.1$ GeV/c. The results on the *entire collected statistics* for unidentified hadrons are shown in fig. 2.10[45]. Clearly from the figure 2.10 it results that all the measured asymmetries are small, if any, and compatible with zero. This trend already characterised the published data of the 2002 run [46], and is confirmed by full data sample result with considerably improved precision. The smallness of the transverse spin effects in the deuteron and the comparison with models and fits were

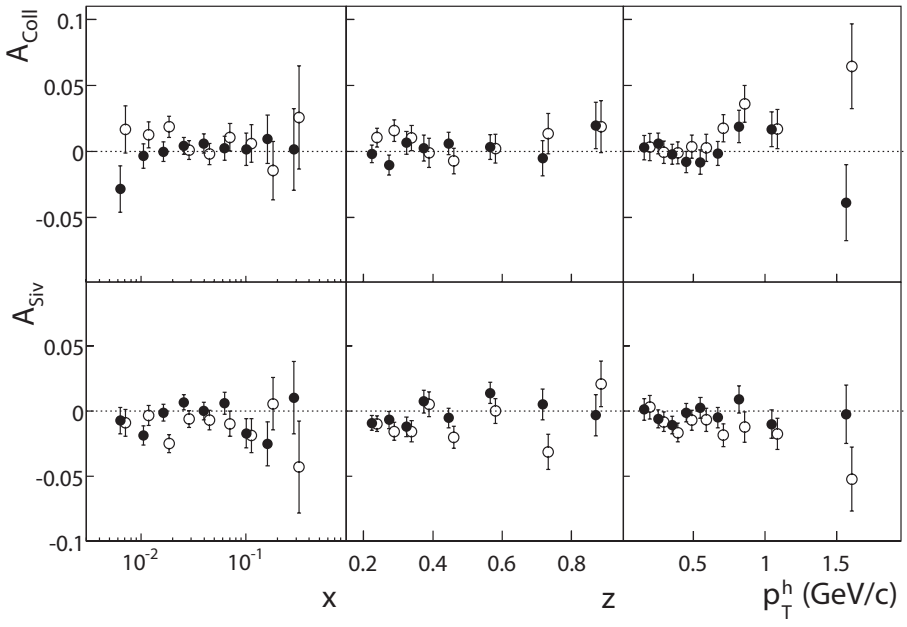

Figure 2.10: Overall results for Collins asymmetry (top) and Sivers asymmetry (bottom) against x, z and P_T^h for positive (full circles) and negative hadrons (open circles) from 2002, 2003, and 2004 data. Error bars are statistical only. In all the plots the open circles are slightly shifted horizontally with respect to the measured value.

explained via the opposite sign contribution for the u and d distributions, causing cancellations on the asymmetries of an isoscalar target, very much like in the helicity case. Still, it was not obvious that they would have been so small.
The same data set is used also to extract the asymmetries on charged identified hadrons as π and K using the RICH-1 detector as illustrated in figure 2.11. All the measured asymmetries are small also in this case. In all the previously illustrated figures only the statistical errors are shown, since systematic errors have been evaluated to be considerably smaller than statistical ones[30].

Collins and Sivers effect: extraction models

The study of the single transverse spin asymmetries has always preserved a deep interest of some theoreticians group, interest which was renewed when a statistically significant experimental data sample recently became available.
On the theoretical side there exist several approaches to understand the SSA.
The first example is given by the work of Vogelsang and Yuan [47], who using the QCD factorisation approach at small transverse momentum, could fit with simple

parametrisation the Collins and Sivers functions to the HERMES data. Then using the informations from the fits they compared their prediction to the COMPASS result. The fits demonstrated to work well and to be consistent with the COMPASS asymmetries. Moreover their analysis allowed also to predict the SSA for various processes in pp collision at RHIC.
A slightly different approach was adopted by the group of Efremov, Goeke and Schweitzer[48, 49], for the Collins function their possible theoretical understanding is discussed in the framework of QCD-induced factorisation approach but using for the transversity distribution function the predictions from the chiral quark-soliton model (χQSM) to give quantitative estimates for the experimental asymmetries. For the Sivers case they resorted to a Gaussian distribution of transverse parton momenta in the Sivers function.
Despite the models are different and the different theoretical constraints the results from the two groups are in good agreement showing that the model dependence effects should be small.
The third group of Anselmino [50] has obtained a crucial improvement towards the successful extraction of the Collins and Transversity functions using the two independent measurement of the BELLE data in which the convolution of two Collins FF is involved, and the SIDIS experimental data of HERMES and COMPASS.
Due to the existing collaboration with the group of Anselmino and the participation to the same PRIN[3], in this thesis their model will be described with more details.

Collins case

The naive expectations can be worked out for the pion asymmetries [45]. Formula 2.58 simplifies considerably by neglecting the sea contribution and considering only the valence x-region, i.e. the region where the HERMES and COMPASS data overlap, and the HERMES data show non-zero values. Assuming: $D_u^{\pi^+} = D_d^{\pi^-} = D_1$, $D_d^{\pi^+} = D_u^{\pi^-} = D_2$, $\Delta_T^0 D_u^{\pi^+} = \Delta_T^0 D_d^{\pi^-} = \Delta_T^0 D_1$, $\Delta_T^0 D_d^{\pi^+} = \Delta_T^0 D_u^{\pi^-} = \Delta_T^0 D_2$, and using eq. (2.58), one gets for a deuteron target

$$A_{Coll}^{d,\pi^+} \simeq \frac{\Delta_T u_v + \Delta_T d_v}{u_v + d_v} \frac{4\Delta_T^0 D_1 + \Delta_T^0 D_2}{4D_1 + D_2} \; A_{Coll}^{d,\pi^-} \simeq \frac{\Delta_T u_v + \Delta_T d_v}{u_v + d_v} \frac{\Delta_T^0 D_1 + 4\Delta_T^0 D_2}{D_1 + 4D_2}. \tag{2.68}$$

The fragmentation term is known to be different from zero: detailed studies have been performed using the high statistics data sample of the BELLE experiment, which has measured asymmetries through the process ($e^+e^- \to h_{pairs}$) where the Collins fragmentation function enters. The BELLE results supports a finite Collins asymmetry[51]. The data of HERMES suggest that $\Delta_T^0 D_1 \simeq -\Delta_T^0 D_2$. The smallness of both the π^+ and π^- Collins asymmetries measured on the deuteron is an

[3]PRIN 2006, Studio di effetti di spin Transverso nel nucleone

indication that $\Delta_T u_v \simeq -\Delta_T d_v$. [52, 43, 45].
A first global analysis which combined the 2002−2004 HERMES pion Collins asymmetries, the COMPASS results for non-identified hadrons, and the BELLE data has allowed to extract the Collins functions and, for the first time, the transversity distributions for the u and d quark [50]. The global analysis result shows that the transversity distribution has opposite sign for u and d quarks, and that the magnitude of $\Delta_T u$ is larger than that of $\Delta_T d$, while they are both significantly smaller than the corresponding Soffer bound.
Very recently, the inclusion of the new HERMES 2002−2005 data, the latest BELLE data[57] and the COMPASS asymmetries on the identified pion and kaon sample [58] has allowed a new extraction[53] of transversity.
The transversity distribution functions $\Delta_T u(x, k_t)$ and $\Delta_T d(x, k_t)$ as resulting from the latest fit are plotted as a function of x and k_t in fig. 2.12. For comparison, the Soffer bound is also shown. The shaded area corresponds to the uncertainty in the parameter values. In the same manner, in fig. 2.13, the resulting Collins functions $\Delta^N D_{fav}(z, P_T^h)$ and $\Delta^N D_{unf}(z, P_T^h)$ are plotted as a function of z unintegrated over $d^2\mathbf{P_T^h}$ and normalised to twice the unpolarised fragmentation functions and as a function of P_T^h. The Collins functions from Efremov *et a.* [55] and Vogelsang *et al.*[47] are superimposed as dashed and dotted lines (left panels), and the corresponding positivity bound are plotted.
It is worth to notice that while the HERMES data alone constrain the transversity distribution of u quarks, the addition of COMPASS data to the fit allows to better constrain the transversity distribution function of d quarks although the COMPASS measured azimuthal asymmetry is very small, the inclusion of these data significantly contributes to the extraction of the transversity distribution.
Looking at the identified kaon sample (see fig. 2.11) also this case shows small asymmetries. The neutral kaon sample is smaller in size by a factor of about 3 with respect to the charged kaons, and the error bars start being large. The COMPASS data do not exhibit the large difference between K^+ and π^+ asymmetries seen by HERMES. Very much like for the $\pi^\pm$ case, cancellations are expected between u and d quarks when using the isoscalar deuteron target. Therefore the smallness of the COMPASS kaon asymmetries suggests that the sea quark contributions to the asymmetries are small or that the Collins function is small.
New data on the azimuthal asymmetry for K production, possible from COMPASS, can shed new light in outlining the importance of the sea quark transversity distributions and the size of the Collins function, thanks also to the extended x phase space accessible. It is clear that the kaon data provide a unique handle on the s-quark implying the necessity of a full global analysis including pions and kaons.
More quantitative information, in particular for the s-quark distributions, could be obtained introducing the measurements with the data extracted from the 2007 transversely polarised proton target run at COMPASS.

Thanks to the global fit analysis it is possible to predict the asymmetries on proton target at COMPASS. The Comparison with the preliminary result from the 2007 run will be illustrated and discussed in chapter 7.

Sivers case

Also in this case it is useful to consider the expressions one obtains for A_{Siv} in the hypothesis that all hadrons are pions. Again, the simplified analysis is restricted to the valence region. Neglecting the sea contribution (i.e. $\Delta_0^T\bar{q} = \Delta_0^T s = 0$ and $\bar{q} = s = 0$ at all x) and assuming $D_u^{\pi^+} = D_d^{\pi^-} = D_1$ and $D_d^{\pi^+} = D_u^{\pi^-} = D_2$, on a proton target, from eq. (2.63) one gets for π^+ [45]:

$$A_{Siv}^{p,\pi^+} \simeq \frac{4\Delta_0^T u_v D_1 + \Delta_0^T d_v D_2}{4u_v D_1 + d_v D_2} \tag{2.69}$$

and for π^- [45]:

$$A_{Siv}^{p,\pi^-} \simeq \frac{4\Delta_0^T u_v D_2 + \Delta_0^T d_v D_1}{4u_v D_2 + d_v D_1}\,. \tag{2.70}$$

Assuming $D_2 \simeq 0.5 D_1$, $d_v \simeq 0.5 u_v$[59], the previous expressions become

$$A_{Siv}^{p,\pi^+} \simeq \frac{\Delta_0^T u_v}{u_v} \tag{2.71}$$

and

$$A_{Siv}^{p,\pi^-} \simeq \frac{2\Delta_0^T u_v + \Delta_0^T d_v}{2.5 u_v} \tag{2.72}$$

respectively. Since the Sivers asymmetries for π^- as measured by HERMES is about zero, in this very simplified treatment it follows that

$$\Delta_0^T d_v = -2\Delta_0^T u_v\,. \tag{2.73}$$

For a deuteron target the Sivers asymmetries can be written as

$$A_{Siv}^{d,\pi^+} \simeq \frac{\Delta_0^T u_v + \Delta_0^T d_v}{u_v + d_v} \tag{2.74}$$

and

$$A_{Siv}^{d,\pi^-} \simeq \frac{\Delta_0^T u_v + \Delta_0^T d_v}{u_v + d_v} \tag{2.75}$$

which implies $A_{Siv}^{d,\pi^+} \simeq A_{Siv}^{d,\pi^-}$. The approximatively zero Sivers asymmetries for positive and negative hadrons observed in COMPASS require

$$\Delta_0^T d_v \simeq -\Delta_0^T u_v\,, \tag{2.76}$$

a relation which is also obtained in some models.
Anselmino *et al*[59] have performed a global analysis of the data to extract the Sivers DF using HERMES and COMPASS deuteron data (prior 2007). Thanks to the reduced error bars and hadron separation in both the HERMES and COMPASS last published sets of experimental data, a better determination of the u and d flavour Sivers distribution functions and, most importantly, a first insight into the sea and strange contributions to the Sivers functions is possible. In the global fit the COMPASS data on K^0 [58] are not included.
Figure 2.14 shows the Sivers distribution functions for u, d and s flavours as determined by the simultaneous fit of HERMES and COMPASS deuteron data. Using the Sivers functions, determined through the global fit in [59], the predictions for other transverse single spin asymmetries $A_{UT}^{\sin(\phi_h - \phi_S)}$ can be performed. In particular the comparison of the prediction with the measured asymmetries at COMPASS on a proton target, extracted from the 2007 run will be discussed in chapter 7.

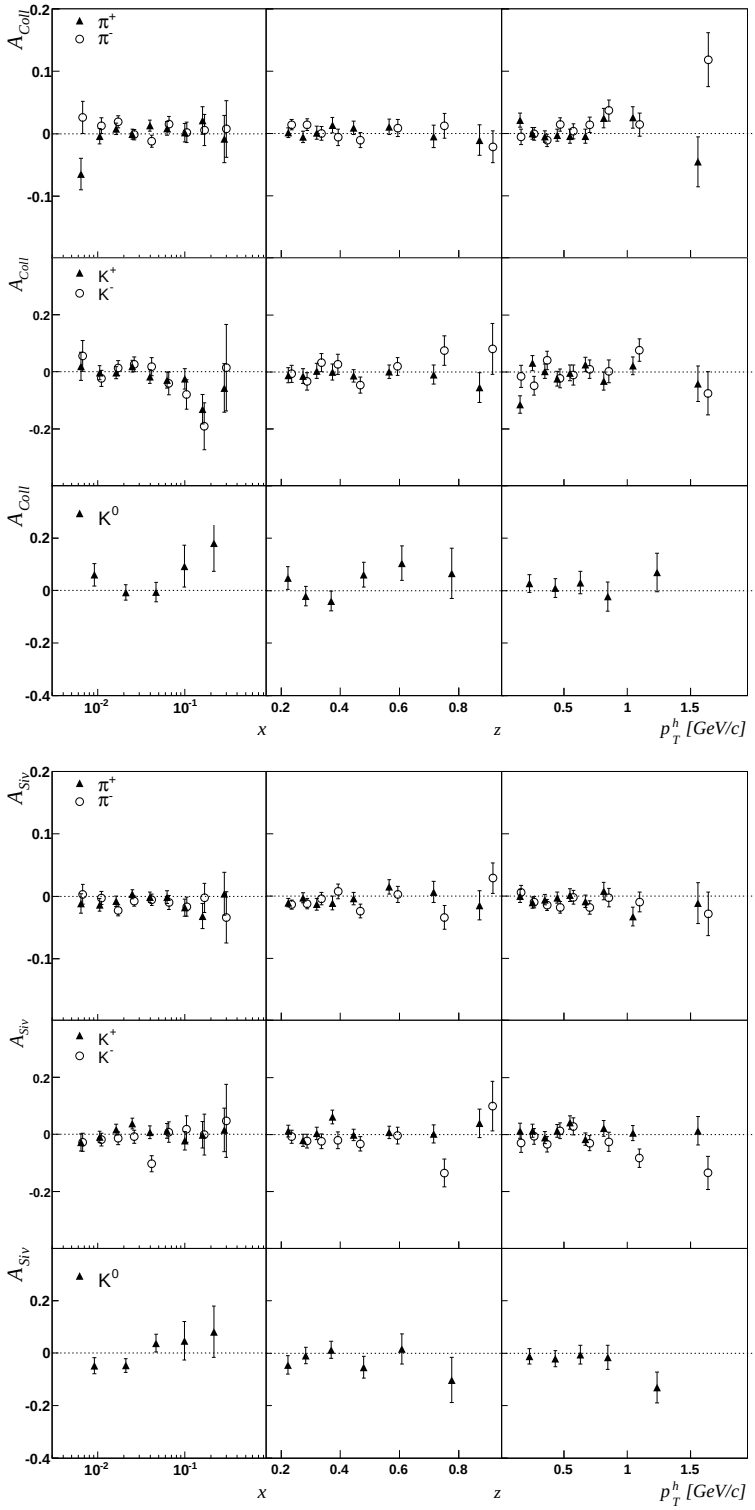

Figure 2.11: Collins asymmetry (top) and Sivers asymmetry (bottom) against x, z and P_T^h for charged pions and kaons from 2003–2004 data, and K^0 from 2002–2004 data. Error bars are statistical only.

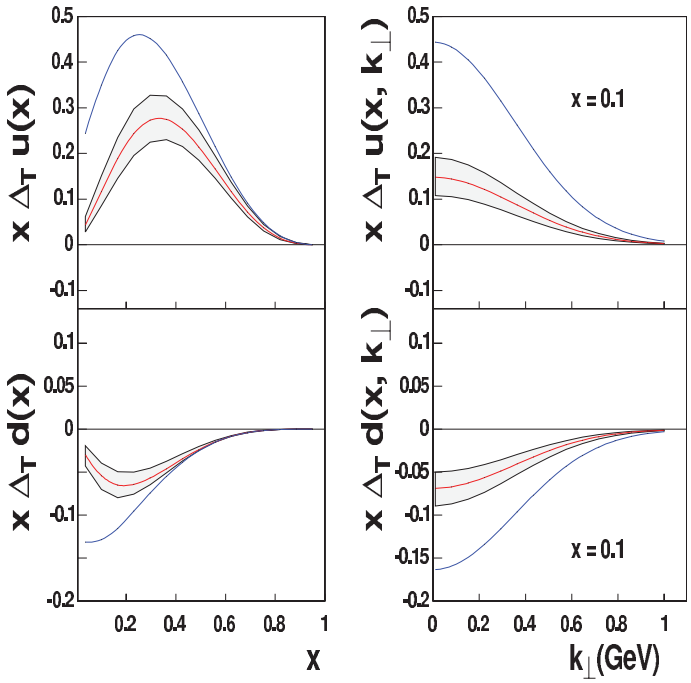

Figure 2.12: The transversity distribution functions for u and d quarks extracted from the the latest prediction of Anselmino *et al.*[53]. On the left side, $x\,\Delta_T u(x)$ (upper plot) and $x\,\Delta_T d(x)$ (lower plot) are shown as functions of x and $Q^2 = 2.4$ GeV^2. For comparison, as bold blue line, the Soffer bound is shown [54]. On the right the unintegrated transversity distributions, $x\,\Delta_T u(x, k_t)$ (upper plot) and $x\,\Delta_T d(x, k_t)$ (lower plot), as functions of k_t at a fixed value of x are illustrated. The k_t dependence has been chosen to be the same as that of the unpolarised distribution functions. It is plotted in order to show its uncertainty (shaded area), due to the uncertainty in the determination of the free parameters. Figures from [53].

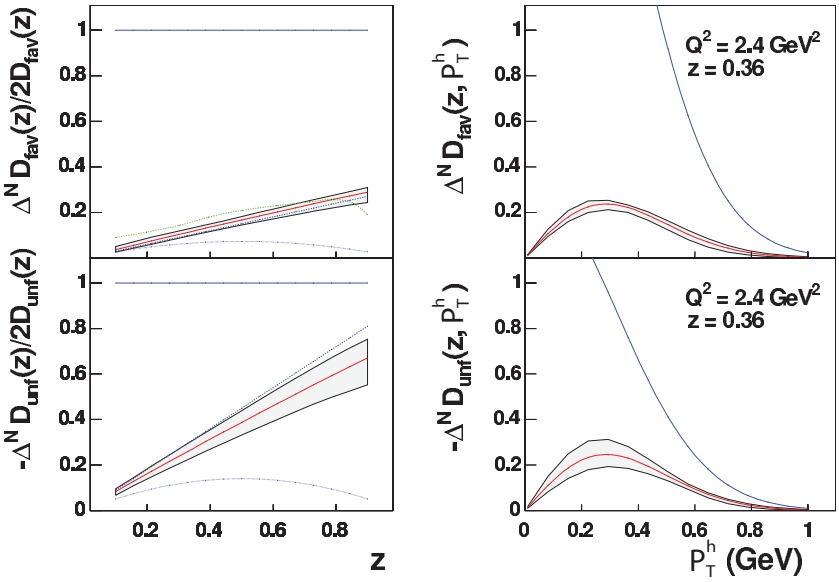

Figure 2.13: Favoured and unfavoured Collins fragmentation functions from the prediction of Anselmino *et al.*[53]. In the left panel the z dependence of the P_T^h integrated Collins functions is shown normalised to twice the corresponding unpolarised fragmentation functions; The results of other groups [55] (dashed line), [47] (dotted line) and [56] (green line) are plotted too. In the right panel the P_T^h dependence of the Collins functions is shown at a fixed value of z. The Q^2 value is 2.4 GeV^2, in which the Q^2 evolution of $\Delta^N D$ is taken identical to the D one. The positivity bound $|\Delta^N D_{h/q^\uparrow}(z, P_T^h)| \leq 2D_{h/q}(z, P_T^h)$ (upper lines) is shown.

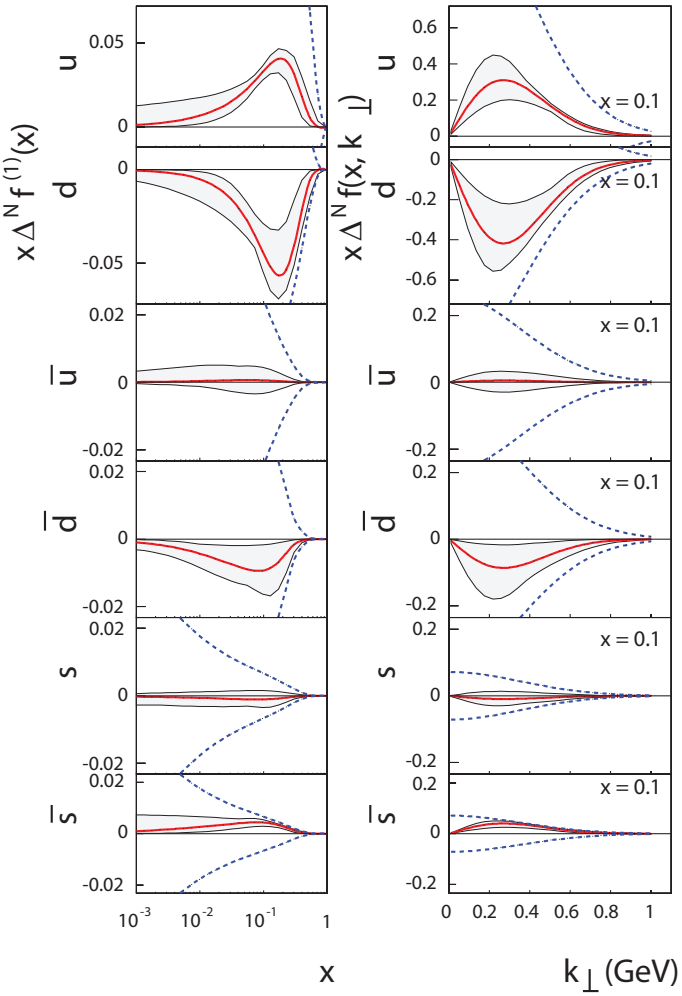

Figure 2.14: The Sivers distribution functions for u, d and s flavours as determined by the simultaneous fit of HERMES and COMPASS. On the left panel, $x\,\Delta^N f^{(1)}(x)$, is shown as a function of x for each flavour. Similarly, on the right panel, the Sivers distribution $x\,\Delta^N f(x, k_t)$ is shown as a function of k_t at a fixed value of x for each flavour. The highest and lowest dashed lines show the positivity limits $|\Delta^N f| = 2f$.Figure from [59].

Chapter 3

The COMPASS spectrometer

3.1 Introduction

The Common Muon and Proton Apparatus for Structure and Spectroscopy COMPASS is a high rate, fixed target experiment at the Super Proton Synchrotron SPS of the European Centre for Nuclear Research CERN. Initiated with the proposal of 1996, COMPASS is born from combination of two competing collaborations, CHEOPS and HMC, that shared similar demands to the experimental apparatus but addressing different physics topics, both focusing around structure and spectroscopy of hadrons. The aim of the COMPASS is to study in detail the nucleon spin structure via a high energy muon beam and to perform hadron spectroscopy via a hadron beam. From the first year of beam (2002) till 2007 only the muon beam has been used, except a short data taking pilot run with a hadron beam in 2004. At the moment (2008) COMPASS has started its hadron program with a π,K,p beam. Data used to extract the Collins and the Sivers asymmetries here presented, have been collected during the last muon beam year (2007) with a NH_3 polarised target. After 2004 the spectrometer has undergone two major upgrades: they are the new target SC solenoid magnet with a increased geometrical acceptance and the tree cell setup for the target material, and the RICH-1 upgrade with the substitution of the central photodetection system with Multi Anode PhotoMulTipliers and a new Front End electronic for the outer part. In the following paragraphs the apparatus will be shortly described, the various detection technique will be described too. The RICH-1 upgrade will be matter of the next chapter.

3.2 The COMPASS layout

The COMPASS physics program imposes specific requirements to the experimental setup which are: large angle and momentum acceptance, including the request to

track particles scattered at extremely small angles, precise kinematic reconstruction of the events together with efficient particle identification and good mass resolution. Operation at high luminosity imposes capabilities of high beam intensity and counting rates, high trigger rates and huge data flows. To cope these requirements the spectrometer is organised in a two stage spectrometer setup: tree different parts can be distinguished. The first part includes the detectors upstream of the target, which measures the incoming beam particles. The second and the third part of the setup are located downstream of the target, and extend over a total length of 50 m. These are the large angle spectrometer and the small angle spectrometer, respectively. The use of two spectrometers for the outgoing particles is a consequence of the large momentum range and the large angular acceptance requirements. The Large Angle Spectrometer (LAS), has been designed to ensure 180 mrad polar acceptance. It is built around the SM1 magnet, which is preceded and followed by telescopes of trackers. SM1 is a dipole magnet located 4m downstream of the target centre. The main component of the field goes from top to bottom. Its field integral was measured to be 1.0 T m and corresponds to a deflection of 300 mrad for particles with a momentum of 1 GeV/c. The bending due to the field allows for momentum measurement. The information from the RICH-1 detector, placed just after SM1 is used in combination with the momentum measurement to perform particle identification. Particles than travel through the gaseous volume of the RICH reaching the electromagnetic and hadronic calorimeters.
The small angle spectrometer detects particle at small angles ($\pm$30mrad) and large momenta of $5GeV/c$ and higher. The structure is very similar to the SAS: its central element is the 4m long SM2 magnet, located 18 m downstream the target centre and preceded and followed by telescope of trackers. SM2 is a rectangular shape dipole magnet with a gap of $2 \times 1\ m^2$ and a total field integral of 4.4 T m for its nominal current of 4000 Amperes. As for SM1 the main component of the field is in the vertical direction. The downstream part of the SAS includes electromagnetic and hadronic calorimeters and a muon filter. A second muon filter is positioned at the downstream end of the spectrometer.
The flexibility required by the broad spectrum of the COMPASS physics program has been implemented by mounting huge setup elements on rails, allowing them to be positioned at variable distances from the experimental target: the RICH, the first hadron calorimeter, the first muon filter, the second analysing magnet and the trackers fixed to it can move longitudinally on rails.

3.3 The M2 beam line

The muon beam is derived from a very intense primary proton beam, extracted from the CERN SPS at 400 GeV/c momentum, that impinges on a Beryllium target with

500 mm thickness (T6). Thinner targets can be selected for lower flux, if required. The nominal proton flux available for COMPASS is $1.2{\cdot}10^{13}$ protons during 4.8 s long spills, within a 16.8 s long SPS cycle. A section of six acceptance quadrupoles and a set of three dipoles select a high pion flux within a momentum band of up to $\pm 10\%$ around a nominal momentum up to 225 GeV/c and within a geometrical acceptance of about $3\pi\mu$sr. The pions are transported along a 600m long channel, consisting of regularly spaced alternately focusing and defocusing quadrupoles. Along this channel a fraction of the pions decay into a muon and a neutrino. Both pions and a large fraction of the muons produced in the decays are transported until the muons are focused and the hadrons are stopped in a hadron absorber. Before entering the experimental hall, the μ momentum (nominal value 160 GeV/c) is measured by the Beam Momentum Station (BMS), consisting of a bending magnet and six hodoscope stations located downstream and upstream the magnet. Four stations are made of horizontal strips of different pitch in order to cope with the different flux in the regions around the beam axis; two stations are made of scintillating fibres with 2 mm of diameter. The time resolution achieved by the system is around 0.3 ns; the reconstruction efficiency of each beam track is around 93% and the momentum resolution is better than 1%. After the BMS, the muons are focused on the polarised target. The incoming muon flux is of the order of $2{\cdot}10^{8}$ muons per SPS cycle. The beam is also accompanied by a large halo, composed of muons outside the beam-line acceptance: the "near" halo, in the region within 15 cm from the beam line, accounts for $\sim$16% of the beam intensity, while the "far" halo accounts for about 7%.

3.4 The polarised Target

Taking profit of the long SPS shutdown in 2005, as already mentioned, an important upgrade project of the spectrometer has been carried on. One of the most important changes in the setup is the substitution of the SMC target solenoid with the superconducting solenoid with larger geometrical acceptance ± 180 mrad (was ± 75 mrad). The new solenoid provides a field homogeneity of $\pm 4{\cdot}10^{-5}$ over the target region. The target configuration has been changed into three cells, instead of the two used until 2004, and a new microwave cavity has been installed too. The COMPASS muon program aims to measure cross section asymmetries $\Delta\sigma/2\sigma$ where $\Delta\sigma$ is the difference between the cross sections of a given process for two different spin configurations and σ the spin averaged cross section. The corresponding observable counting rate asymmetry is $A_{obs} = (P_\mu \cdot PT \cdot f \cdot (\Delta\sigma/2\sigma))$, where P_μ and PT are the beam and target polarisations respectively, and f the fraction of polarisable material inside the target. The use of a polarised target is thus mandatory and, in addition the factors PT and f must be made as large as possible in order to optimise the sta-

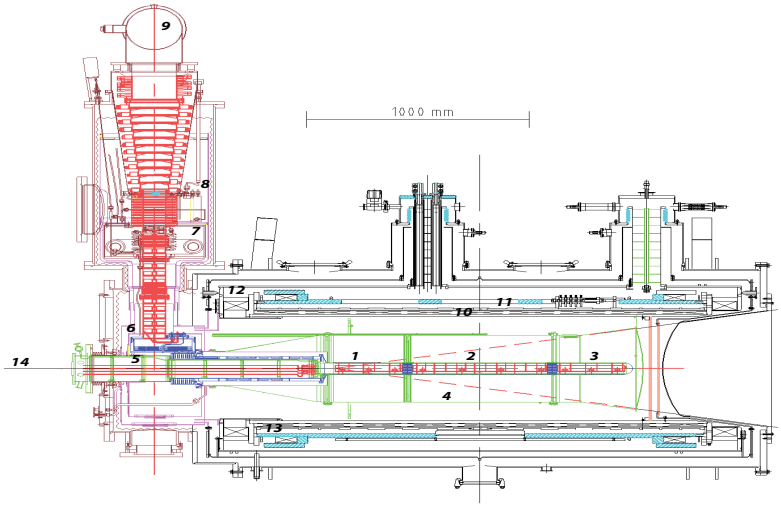

Figure 3.1: Side view of the COMPASS polarised target: upstream target cell 1, central 2 and downstream target cell 3 inside mixing chamber, microwave cavity 4, target holder 5, still or ^{3}He evaporator 6, ^{4}He evaporator 7, ^{4}He liquid/gas phase separator 8, ^{3}He pumping port 9, solenoid coil 10, correction coils 11, end compensation coil 12, dipole coil 13, muon beam entrance 14. The tree halves of the microwave cavity are separated by a thin microwave stopper.

tistical significance of the results. Furthermore, due to the limited muon flux, a solid state polarised target, much thicker than those commonly used in electron beams, is required. While electron spins can be aligned in a magnetic field and give rise to a large polarisation at equilibrium for a low enough temperature, only a negligible nuclear spin polarisation can be reached. Therefore, solid state polarised targets rely on dynamic nuclear polarisation (DNP)[60] which transfers the electron polarisation to the nuclear spins by means of a microwave field. This process requires a material containing some amount of paramagnetic centres, a temperature below 1 K and a strong and homogeneous magnetic field. During 2006 and previous data taking years Deuterated Lithium (^6LiD) has been chosen as isoscalar target while during 2007 Ammonia target (NH_3) has been used. ^6LiD allows to reach a high degree of deuteron polarisation ($\geq$40%) and has a very favourable composition. ^6LiD can be considered to a good approximation as a spin-0 ^{4}He nucleus and a deuteron, the fraction of polarisable material f is of the order of 0.35, taking into account also the He content in the target region. The irradiated ammonia (NH_3), which has been used as polarised proton target, has a less favourable composition (f $\sim$ 0.15) but can be polarised to a higher degree ($\geq$80%). Spin asymmetries are measured using a target divided in tree cells which are exposed to the same beam flux but polarised

in opposite alternated directions. In order to cancel acceptance effects which could mask the physics asymmetries, the spin directions must be frequently inverted by rotating the solenoid field in the longitudinal target configuration, rebuilding the polarisations with opposite microwave frequencies in the transverse target polarisation case. The COMPASS polarised target (see fig.3.1) has been designed to meet these requirements. The superconducting solenoid produces a 2.5 T magnetic field along the beam direction. Sixteen corrections coils are used to obtain an axial homogeneity better than 20 ppm in a volume 1500 mm long, and 50 mm in diameter. The transverse holding field of 0.42 T is produced by a dipole coil and deviates at most by 10% from its nominal value inside the target volume. The $^3He/^4He$ dilution refrigerator is filled with liquid helium from the gas/liquid phase separator (see Fig. 3.1, (8)). The cold gas from the separator cools down the outer and inner vertical and horizontal thermal screens around the dilution refrigerator at nominal temperatures of 80 K and 4 K, respectively. The incoming $^3He/^4He$ gas is also cooled with cold gas from the separator. Needle valve controlled lines are used to fill the ^4He evaporator (see Fig. 3.1, (7)) with liquid helium and to cool the microwave cavity (see Fig. 3.1,(4)). The nominal operation temperatures of the cavity and the ^4He evaporator are 3 K and 1.5 K, respectively. A microwave cavity (Fig. 3.16,(3)) similar to the one previously used by SMC was built. The amount of unpolarised material along the beam was minimised by reducing the thickness of the microwave stopper, and by modifying the downstream end window. The 30, 60 and 30 cm long target cells (see Fig.3.1 ,(1),(2),(3)) have a diameter of 4 cm and are separated by 10 cm. The cells are made of a polyamide mesh in order to improve the heat exchange between the crystals and the liquid helium. They are fixed in the centre of an aramid fibre epoxy tube, which itself is fixed to the target holder isolation vacuum tube (see Fig. 3.1, (5)). The target cells are filled with ^6LiD or NH_3 crystals of 2,4 mm size; the volume between the target material crystals is filled with a mixture of liquid $^3He/^4He$. The target mass in each target cell depends on the packing factor (between 0.49 and 0.54) achieved during the filling. Each cell contains five NMR coils used for the local monitoring of the polarisation. The target material is polarised via dynamic nuclear polarisation, obtained by irradiating the paramagnetic centres with microwaves at a temperature of about 200 mK. During transverse data taking the target material is kept in frozen spin mode below 90 mK and the spin direction is maintained by the 0.42 T transverse dipole field. The polarisation is reversed by exchanging the microwave frequencies of the tree cells. The relaxation rate in frozen spin mode is $(0.4 \div 1.0)$ %.

3.5 Tracking

The tracking system of COMPASS comprises many tracking stations, distributed over the entire length of the spectrometer. Each tracking station consists of a set of detectors of the same type, located at approximately the same z-coordinate along the beam. In a station, the trajectory of a charged particle is measured in several projections transverse to the beam direction in order to reduce ambiguities. Due to the large overall acceptance of the spectrometer, the region to be covered by the detectors is large and the requirements for the tracking change with the distance from the beam axis. Near the beam axis region, detectors should stand high particle flux and they must provide good timing and position resolution; in the region far from the beam axis, the particle flux is less intense and the requirements for the detectors can be relaxed. In this way three main tracking detector types can be identified: the very small, small and large area trackers.

3.5.1 Very Small area tracker

The Very Small Area Trackers (VSAT) cover the beam region up to a radial distance of 2,5 - 3 cm. The very high rate of beam particles in this area, up to about $10^5 s^{-1} mm^{-2}$ in the centre of the muon beam requires excellent time or position resolution of the corresponding detectors in order to identify hits belonging to the same track in a highly crowded environment. Scintillating fibres (SciFi) and silicon microstrip detectors fulfil this task.
The scintillating fibres have a diameter between 0.5 and 1 mm; each station is made by different planes in order to measure more than one projection. In each plane several layers, shifted one with respect to the other, are used in order to avoid low efficiency zones. Hits belonging to different tracks can be assigned to the corresponding track by time correlation only. Time correlation is also used to link the incoming muon with the scattered muon track, as well as with the trigger and the information from the beam momentum station. For the muon program, a total of eight SciFi detector stations are used. The obtained time resolution ranges between 350 ps and 450 ps for the central regions of the various detector planes with a detection efficiency above 99%.
The silicon microstrip detectors are made of a wafer 300μm thick n-type with an active area of 5×7 cm^2. The 1280 readout strips on the n-side are perpendicular to the 1024 readout strips on the p-side so that with one wafer two-dimensional position information can be obtained. Two detectors make up one silicon station. They are mounted back-to-back on a fibre-glass frame such that one detector measures the horizontal (X) and vertical (Y) coordinates of a particle trajectory, while the other is rotated around the beam axis by 5°, providing two additional projections (U,V). The average spatial resolution is about 10 μm, time resolution is about 2.5 ns.

3.5.2 Small area tracker

The intermediate region at a radial distance of 2.5 cm to 30 - 40 cm is covered by the Small Area Trackers (SAT), and is the domain of micropattern gas detectors. Two novel devices MicroMegas and GEM detectors are employed for the first time in a large-scale particle physics experiment. These detectors combine high rate capability and good spatial resolution over fairly large sizes.
The MicroMegas (Micromesh Gaseous Structure) detector is based on a parallel plate electrode structure and a set of parallel microstrips for readout. The presence of a metallic micromesh separates the gaseous volume into two regions: a conversion gap where the ionisation takes place and the resulting primary electrons drift in a moderate field ($\sim$1 kV/cm over 3.2 mm), and an amplification region where a higher field (50 kV/cm over 100μm) produces an avalanche which results in a large number of electron/ion pairs (see Fig. 3.3). The field configuration near the mesh is such that most of the ions from the avalanche are captured by the mesh and do not drift back into the conversion gap: ions drift over a maximum distance of 100μm and the width of the signal induced cannot exceed the drift time over that distance, that is about 100 ns. The fast evacuation of positive ions combined with the reduced transverse diffusion of the electrons and the high granularity of the detector result in a high rate capability. The detector has an active area of 40$\times$40 cm^2, with a detection efficiency of 97%, 9 ns time resolution and 90 μm spatial resolution.
The GEM consists of a 50μm thin Polyamide foil with Cu cladding on both sides, into which a large number of micro-holes (about $10^4 = cm^2$, diameter 70 μm) has been chemically etched using photolithographic techniques. A potential difference of several 100V is applied across the foil, avalanche multiplication of primary electrons drifting into the holes is achieved when the foil is inserted between parallel plate electrodes of a gas filled chamber. Suitable electric fields extract the electrons from the holes on the other side of the foil and guide them to the next amplification stage or to the readout anode (see fig. 3.3). The electron cloud emerging from the last GEM induces a fast signal on the readout anode, which is segmented in two sets of 768 strips with a pitch of 400 μm each, perpendicular to each other and separated by a thin insulating layer. The detector active area is of 31$\times$31 cm^2. The detection efficiency, time and space resolution are 97%, 12 ns and 70 μm respectively. Both Micromegas and GEM detectors have central dead zones with 5 cm diameter.

3.5.3 Large area tracker

The reduced flux in the outermost regions, covered by the Large Area Tracker allows the use of detectors such as drift chambers, straw tube chambers, and multiwire proportional counters.
Three identical drift chambers (DC) are installed in COMPASS. Their design was

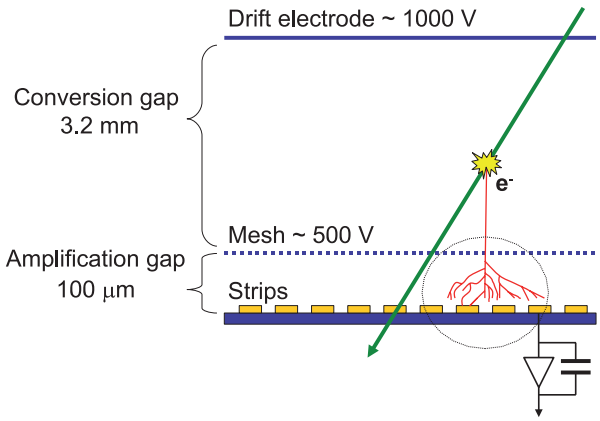

Figure 3.2: Schematic view of the MicroMegas. The conversion and the amplification regions are separated by a metallic micromesh; in the conversion gap the ionisation process takes place, and a moderate field of 1 KV/cm produces the drift of the primary electrons. A higher field of 50 KV/cm in the second region (100 μm gap) produces an avalanche resulting in many e^-/ions pairs. The electrons are then collected by the anode segmented in microstrips.

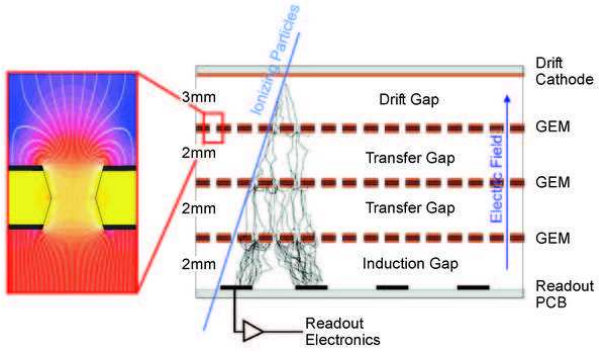

Figure 3.3: Schematic view of the GEM detectors. The gas-filled region between two parallel plate electrodes is divided by three 50 μm thin Polyamide foils with a very large number of holes ($\sim 10^4/\mathrm{cm}^2$). A Cu cladding on both sides of the foil allow the application of a potential difference of several hundreds of volts; when the primary electrons pass through the holes, multiplication avalanche occurs, and then the electrons are guided to another amplification stage or to the readout anode, formed by two sets of perpendicular strips.

optimised for operation upstream of the first dipole magnet (SM1), where the total particle flux through the chamber is higher by almost a factor of three compared

to the downstream side due to the low-energy background which is bent away by the magnet. One DC is installed upstream, and two DCs downstream of the SM1 magnet. All three DCs have an active area of 180 $\times$ 127 cm^2 with a central dead zone of 30 cm diameter, fully covering the acceptance of the target magnet upstream as well as downstream of SM1. The spatial resolution of a DC is 190 μm. As part of the spectrometer upgrade, due to the larger geometrical acceptance, from 2006 downstream SM1 a new Drift Chamber (DC4) was installed and put into operation. Characterised by the same construction parameters of the other DCs but with increased dimensions bringing the active area from 1200 to 2000 mm.
To provide tracking for charged particles detected in the COMPASS SAS a system of six large area drift chambers is used. Each chamber has an active area of 500 $\times$ 250 cm^2; the spatial resolution has been evaluated in $\sim$500 μm.
Straw tube drift chambers are used for the tracking of charged particles produced at large scattering angles (15 $\div$ 200 mrad) in the Large Area Tracking section (LAT) of COMPASS downstream of the first spectrometer magnet. In total 12440 straw tubes are assembled into 15 detectors. Each detector has an active area of about $9m^2$ with a a central dead zone of 20 $\times$ 20 cm^2. In order to measure three projections of a particle trajectory, one station consists of three detectors, one with vertical, one with horizontal and one with inclined straw tubes. The detectors with inclined straws are rotated by 10° with respect to the vertical ones. For one straw detector (two layers), the average resolution is 190μm.
The tracking of particles at large radial distances to the beam in the SAS is mainly based on a system of multiwire proportional chambers (MWPC). A total of 34 wire layers, corresponding to about 25000 detector channels, is installed and operational. The active area is of 178$\times$120 cm^2, while the distance between anodic wires is 2 mm, allowing a spatial resolution of 1.6 mm. The diameters of their insensitive central zones increase along the beam line from 16 to 22 cm before SM2, from 50 cm to 100 cm in the last spectrometer part.

3.6 Muon identification

The muon identification is performed by two detector systems, one in the LAS and one in the SAS part. Both systems are made of a set of tracking stations and a hadron absorber followed by a second set of tracking stations covering large surfaces ($\sim$4$\times$2 m^2). Muon Wall 1 uses 8+8 stations of aluminium Mini Drift Tubes (MDT) with square cross section, measuring two projections and the absorber is a 60 cm long iron block. Muon Wall 2 employs 6+6 planes of drift tubes measuring three projections and a 2.4m long concrete block. The MW1 averaged tracking efficiency per plane is typically 91%, while for MW2 it is between 81 and 84%.

3.6.1 Rich Wall

A new large-size (4.86×4.22 m^2) tracking station (Rich Wall), is positioned downstream of RICH-1, directly in front of the ECAL1 electromagnetic calorimeter. It consists of eight layers of MDT modules. Mechanically, the Rich wall detector is similar to one station of Muon Wall 1. The tracking planes are alternated to converter layers made of a sandwich of three plates (steel/lead/steel), resulting in a total converter thickness of about 3 radiation lengths. The Rich wall tracker station performs a twofold function in the COMPASS spectrometer. First, it measures the particle trajectories downstream of the RICH, thus allowing a better reconstruction of the particle trajectories in the RICH volume. Second, it acts as preshower for the ECAL1 electromagnetic calorimeter, thus improving the spatial resolution of the calorimeter itself.

3.7 Calorimetry

3.7.1 Hadron calorimeters

The COMPASS spectrometer is provided of two hadron calorimeters positioned before the Muon Wall detectors. They are used both for the hadron energy measurement and for trigger purposes in semi inclusive muon scattering events. HCAL1 has a modular structure, each module consisting of 40 layers of iron and scintillator plates, 20mm and 5mm thick respectively, amounting to 4.8 nuclear interaction lengths. The hadron calorimeter 2 (HCAL2) takes the form of a matrix of 22 × 10 modules, arranged on a mobile platform. The overall thickness of the counters is 5 nuclear interaction lengths for pions and 7 for protons. The linearity of the energy response is of the order of a few percents for both calorimeters over different energy ranges: 0-25 GeV for HCAL1 and 10-100 GeV for HCAL2. The energy resolution can be parametrised as:

- HCAL1 σ/E =59.4%/$\sqrt{E}\otimes$ 7.6% for pions;
- HCAL2 σ/E =65%/$\sqrt{E}\otimes$ 5% for pions;

where E is expressed in GeV.

3.7.2 Electromagnetic calorimeters

An electromagnetic calorimeter (ECAL1), with overall dimensions of 4.0×2.91m^2 is assembled and positioned upstream of the HCAL1 hadronic calorimeter. The ECAL1 calorimeter is formed by blocks of lead glass of different size: centrally 576 blocks of 38.2 × 38.2 mm^2, in the intermediate region 580 blocks of 75 × 75mm^2

and the most external region is equipped with 320 blocks with dimensions of 143 × 143mm^2. It allows measurements of reaction channels with the production of low energy prompt photons and/or neutral pions.
The electromagnetic calorimeter ECAL2 in the SAS part of the COMPASS spectrometer consists of 2972 lead glass modules with 38×38×450 mm^3 dimensions amounting to 16 radiation lengths. A high energy gamma ray (or electron) incident on ECAL2 develops an electromagnetic shower inside the lead glass. The electrons and positrons from a shower emit Cherenkov light on their way through the glass. The amount of Cherenkov light is proportional to the energy deposited in each counter. Each lead glass block is viewed at one end by a PMT. Linearity response is better than 1% until 40 GeV; the energy and spatial resolutions have been measured as:

- σ/E =5.5%/$\sqrt{E}\otimes$ 1.5%;
- σ_x =6 mm/$\sqrt{E}\otimes$ 0.5 mm;

with E in GeV.

3.8 Triggering

The trigger system is used to perform several tasks: select event candidates in a high rate environment with a decision time below 500 ns and minimum dead time, provide an event time reference and generate the signals for the analog to digital converters, finally to trigger the readout of detectors and front end electronics. The setup for the muon beam is designed for an as large kinematic acceptance in Q^2 as possible ranging from $Q^2 \sim 0$ to the maximum allowed by kinematics. A large range in the muon energy loss is required too. The trigger system is based on fast hodoscope signals, energy deposits in calorimeters and a veto system (see fig. 3.4). Depending on the kinematics of the reactions different elements are combined to form the trigger signal. Due to the high rate in the central region of the spectrometer the hodoscope is segmented in four subsystems consisting of two hodoscope stations each, the inner (H4I, H5I), the ladder (H4L,H5L) , the middle (H4M, H5M) and the outer system (H3O, H4O). Events belonging to the kinematics regime with $Q^2 \gtrsim 0.5$ GeV/c^2 are mainly triggered by using the scattered muon information only. The muons are measured in two horizontal scintillator hodoscopes in order to determine the projection of the muon scattering angle in the non-bending plane and to check its compatibility with the target position (vertical target pointing). To suppress events due to halo muons, a veto system is added to the trigger system. For the quasi-real photon regime (low Q^2) the target pointing technique can not be used since muon scattering angles are close to zero. These events are selected by measuring the energy loss with two vertical scintillator hodoscopes using the bending

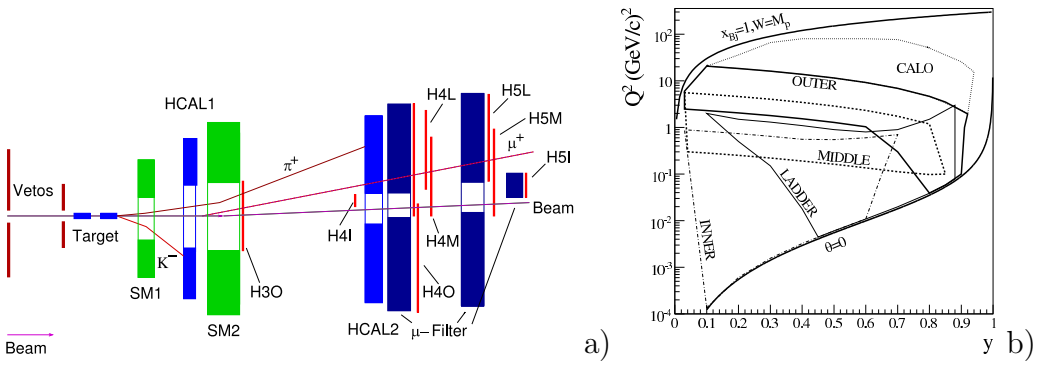

Figure 3.4: a) Schematic view of the location of the trigger components in the setup; b) The range in y and Q^2 for the four hodoscope trigger subsystems and the standalone calorimeter trigger.

of the muon track in the spectrometer magnets. At these small angles there are several background processes such as elastic scattering of target electrons, elastic and quasi-elastic radiative scattering of target nuclei and beam halo contributing to the scattered muon signal. To overcome this difficulty the trigger system requires energy clusters in the hadronic calorimeter, which are absent in the background processes. Thus, the quasi-real photon trigger consists of two parts, a trigger on the energy loss by measuring the deflection of the scattered muon in the two spectrometer magnets and a calorimetric trigger selecting hadron energy clusters above a threshold (see fig. 3.4). Together with hodoscope triggers, also a standalone calorimeter trigger is used to cover regions of high Q^2 that cannot be covered by the outer trigger as the scattered μ is outside hodoscopes acceptance. A standalone calorimeter trigger signal is generated if a minimum energy deposit in the calorimeter is left.

3.9 Data Acquisition

The main characteristics of the COMPASS data acquisition system are parallelism and buffering in order to cope the high rate of the trigger system and readout electronics. The COMPASS experiment consists of approximately 1400 single detector elements and 250,000 electronic channels. The readout electronics has been adopted to cope with an event size of 35 KByte at a trigger rate about 10 kHz for the muon beam. This is done by a pipelined and dead-time free readout scheme. The architecture of the DAQ system in COMPASS is chosen to be very flexible and expandable to allow for upgrades and modifications. The digitised data from several front-end devices are transferred to distributed readout driver modules named COMPASS Accumulate, Transfer and Control Hardware (CATCH) [61, 62] or GEm

SIlicon Control and Acquisition (GeSiCA) [63]. The main task of these readout driver modules are a fast readout of the front-end boards and the local subevent building at data rates of up to 160 MByte/s. In parallel, the Trigger Control System (TCS) [63] provides the trigger signals, time synchronisation and an information on event identification to the CATCH and GeSiCA. The TCS also distributes a reference clock needed for precise time measurement and provides additional means of control like artificial triggers for calibration. The trigger signals from the TCS are transferred via the CATCH to all connected front-end boards. At the beginning of a data taking run the CATCH initialises all connected front-end boards. The GeSiCA works similar to the CATCH, but is optimised for the readout of GEM and Silicon detectors. Through optical fibres (S-link) [64] the data collected from CATCH or GeSiCA are then transferred to readout buffer PCs (ROB). The ROBs store the received data on PCI cards called spillbuffers. The regrouping and event building of the data streams is supported by those spillbuffers. These allow to make use of the break in the SPS accelerators duty cycle to reduce the sustained data rate to a third of the onespill rate (4.8/16.8s). For further processing the information of each subevent in the ROBs, which do not contain the full information from all detectors, are transferred via three Gigabit Ethernet switches to the event builder (EB) computers. The subevents arriving from different ROBs are combined together forming the complete event blocks, which include the data of all detectors. The finalised and filtered events in the EBs are asynchronously transferred through the network via a dedicated Gigabit Ethernet switch to the CERN central data recording system, where they are temporarily stored on disk, before they get migrated to the tapes of the CERN Advanced STORage system [64] (CASTOR).

3.10 Event reconstruction

The huge amount of data (about 350TB/y) collected by the experiment requires the availability of sufficient computing power to reconstruct the events at a rate comparable to the data acquisition rate. The required CPU power is estimated to be 200k SPECint2000 units[65], which are provided currently by 200 Linux Dual-CPU PCs out of the CERN shared batch system. Event reconstruction is performed by a fully object oriented program, CORAL[66], with a modular architecture and written in C++. The input of the reconstruction software is represented either by the raw data collected by the experiment or Monte Carlo data. The data files produced by the COMPASS acquisition software contain the raw information from the detectors, digitised by the front-end electronics. Two initial processing phases are needed to prepare the input to the track finding algorithm. In the first phase, called decoding, the information on the fired detector channel (either wire, pad, or cell, depending on the detector type) is extracted from the raw data. In the second phase, called clus-

tering, detector channels that are fired by the same particle are grouped together. The result of the reconstruction phase (track parameters, vertexes, calorimeter clusters, PID probabilities, detector hit patterns, etc.) is stored in output ROOT trees, called mini Data Summary Tapes (mDST), that are distributed to home computing centres and serve as input for all the physics data analysis. The data reduction factor between the input raw data and the output mDSTs is about 100. Large DST files, storing the detector digits and clusters in addition to the tracking, vertex, and PID information are also created and kept at CERN on tape.

Chapter 4

The upgrade of COMPASS RICH-1

4.1 Introduction

During the years 2001-2004, photon detection with RICH-1 has been performed by Multi Wire Proportional Chambers (MWPCs) equipped with CsI photo-cathodes [67]. Some characteristic features of these photon detectors and of its associate front-end read-out electronics (sec. 4.2.4) limits the RICH-1 performance in the COMPASS environment, reducing the efficiency in particular for particles scattered at small angles and introducing some dead-time in the experiment data acquisition. To overcome these limitations, the photon detection system of the RICH-1 counter has been upgraded. In the peripheral region, which amounts to 75% of the active surface, the photon detectors are unchanged since the level of uncorrelated background is not very large. The read-out, however, is now based on a new system [68] with the APV chip [69] with negligible dead-time and improved time resolution. The central photon detection area (25% of the active surface) is both highly populated by uncorrelated background images with photon rates up to 1MHz per channel and it includes the large majority of the high momentum hadron images, as these particles are scattered at small angles. The uncorrelated background signals can be rejected by pushed time resolution, while good Cherenkov angle resolution is the handle for effective identification of high momentum hadrons. These requisites, together with high rate capability, are at the base of the main design criteria of the new photon detection system. This system is now in operation since the 2006 data taking.
The organisation of the chapter is as follows: section 4.2 describes the RICH-1 detector before the upgrade, while from section 4.3 the upgrade project is presented.

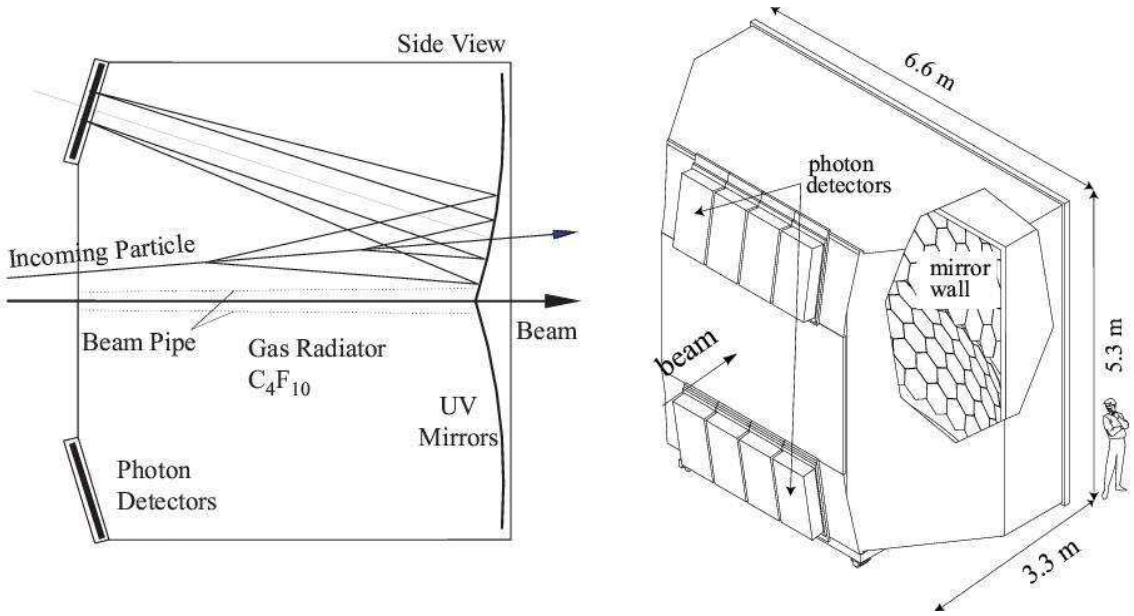

Figure 4.1: COMPASS RICH-1: principle and artistic view.

4.2 RICH-1 description

The RICH-1 [70] detector is a large size Ring Imaging Cherenkov operating in COMPASS since 2001. The request to cover a wide momentum range for particle identification, from a few GeV/c up to 60 GeV/c, has suggested the use of a gaseous radiator, C_4F_{10}, in order to achieve good resolution also in the high momentum domain. The overall length of the radiator vessel ($\sim$3 m), has been chosen in order to have a large number of photons emitted from particles crossing the vessel. The transverse dimensions are also very large, to match the overall spectrometer acceptance ($\pm$250 mrad in the horizontal plane and $\pm$180 mrad in the vertical plane). The detector dimensions and the requirement of a minimal amount of material in the spectrometer acceptance, dictated the final geometry (see fig. 4.1): two spherical mirror surfaces reflect the photons and focus them on 8 MWPCs with CsI photocathodes located outside the spectrometer acceptance.

4.2.1 Gas and gas system

The RICH-1 radiator vessel has a length of $\sim$3 m and a volume of about 80 m^3. C_4F_{10} has been chosen as radiator due to its very low chromaticity ($dn/dE \sim 5 \cdot 10^{-5}$ at 7 eV) and a refractive index ($n - 1 = 0.0015$ for 7 eV photons) that allows hadron identification from Cherenkov threshold till momenta near to 60 GeV/c; the

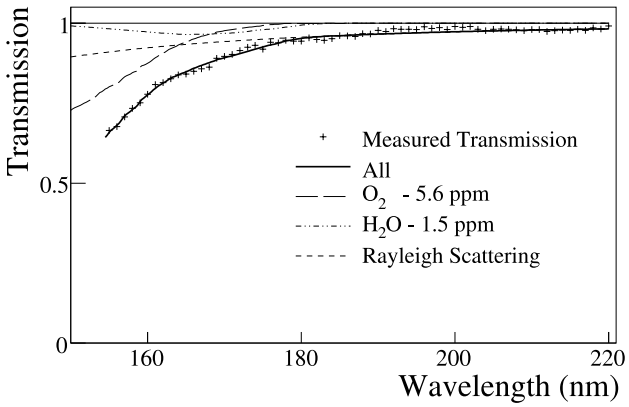

Figure 4.2: Typical UV light transmission through 1.87 m of C_4F_{10}, as measured online during data taking (crosses). The solid curve is a fit to the data. The main contributions to the UV light absorption are also shown.

Cherenkov threshold for π, K and p are respectively 2.5, 9.5 and 17 GeV/c.

RICH-1 operates in the VUV wavelength domain, since the CsI quantum efficiency is different from zero only below 200 nm; therefore the radiator transparency to VUV photons is mandatory for RICH-1 operation. Since the photons are absorbed from impurities as water vapour and O_2, the level of contamination in the radiator gas is kept below 3 ppm with a dedicated gas system [71]. The system covers also other different tasks: it is used to fill the radiator gas and to recover it in the storage tank, it avoids gas stratification inside the vessel and controls the radiator pressure in order to avoid mechanical stress to the thin vessel surfaces in the acceptance region and to the photodetector windows. Good transparency of the radiator, stable over months, was achieved since 2002 data taking. Figure 4.2 shows a typical transmission curve in the VUV domain, with the main contributions to the VUV light absorption: Rayleigh scattering, O_2 and H_2O.

In order to absorb the photons emitted from beam muons, that would cause a prohibitive amount of background photons, a 10 cm diameter pipe filled with Helium is positioned inside the vessel around the beam axis.

4.2.2 Mirror system

The RICH-1 optical system [72] relies on two large surfaces of spherical mirrors with radius of curvature of 6.6 m. The curvature centres of the surfaces are located at ± 1.6 m distance from the beam axis, therefore the photon image is focused outside the spectrometer acceptance, where the photodetectors are located (fig. 4.1). Since the focusing surfaces are spherical, the geometrical aberration causes a small

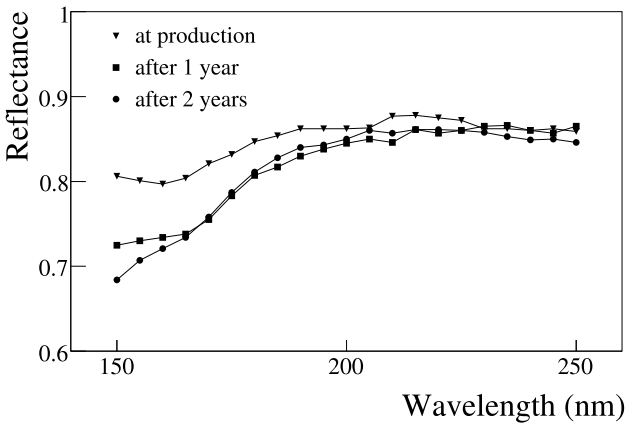

Figure 4.3: Measured reflectance for a typical mirror element. The measurements have been performed shortly after production, 1 year and 2 years later.

deformation of the image formed on the detector plane surfaces.

The reflecting surfaces cover an area of $\sim$21 m^2 and are made of 116 pentagonal or hexagonal mirrors (fig. 4.4); the dead zones between adjacent mirrors correspond to a 4% loss of reflecting surface. To limit the multiple scattering of particles crossing the detector, the mirrors are very thin: they are made of 7 mm of borosilicate glass coated with a layer of UV reflecting material ($\sim$ 80 nm of Al). Another layer of 30 nm MgF_2 protects the Al surface material from water vapour and O_2 contamination. The total material is about 5.5% of radiation length. The reflectance of the mirror system is above 80% in the 160-200 nm wavelength range (fig. 4.3). Mirrors are suspended to nodal points of a net-like mechanical structure (fig. 4.4). The nodal points lay on a spherical surface and allow an angular adjustment of each mirror position with 0.1 mrad precision.

4.2.3 Photon detectors

The photon detection system comprises 8 large-size MWPCs (576$\times$ 1152 mm^2) with CsI photocathodes [73]. The chambers are operated with CH_4 gas, transparent to VUV photons. A quartz window separates the methane from the radiator; pressure gap is avoided maintaining the photodetector gas pressure at atmospheric pressure. Each chamber has the photocathode surface segmented in 72×72 pads of 8×8 mm^2; these dimensions determine the spatial resolution of the detector. The distance between anode and cathode is 2 mm. The geometrical structure of the detectors is shown in fig. 4.5.

The CsI film on the segmented cathode is 500 nm deep, and it has a non zero quantum efficiency in the VUV domain only (fig. 4.6). The CsI photoconverter


a)

b)

Figure 4.4: a) Picture of the reflecting surfaces of the spherical mirrors; b) mechanical support structure of the mirror surfaces (mirror rear side).

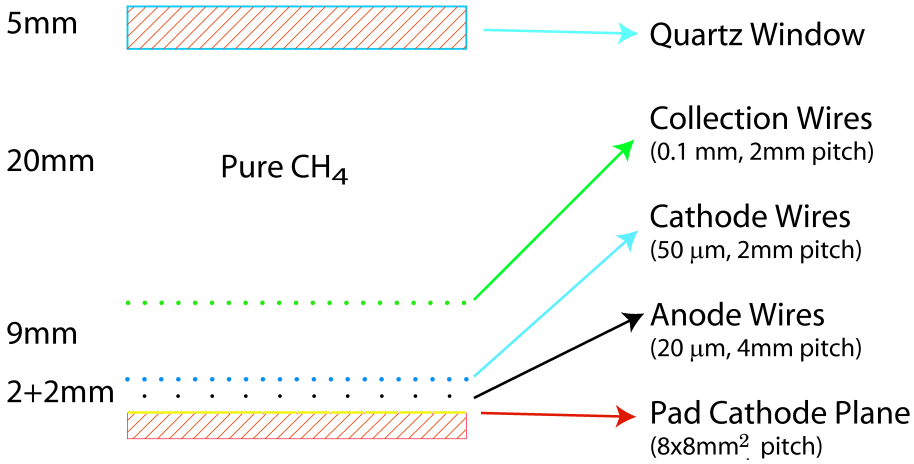

Figure 4.5: Schematic of the RICH-1 photon detector scheme.

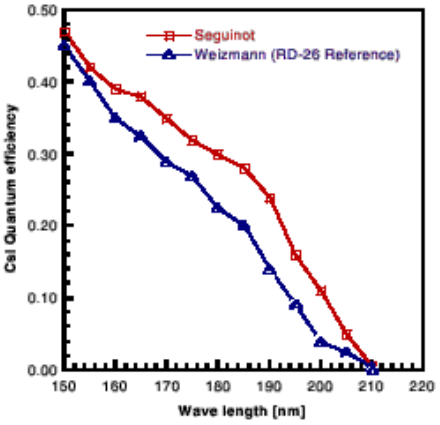

Figure 4.6: CsI quantum efficiency measured in vacuum as a function of the wavelength [76, 77].

has been chosen since it is the only photon converter material stable in gaseous environment. Because of the presence of the CsI layer, photon detectors can exhibit electrical instabilities which are related to the high voltage and to the particle flux [74]; nevertheless great care in the mechanical construction of the MWPC and uniformity of the anode wire tension allowed to reach gain up to $5{\cdot}10^4$.

4.2.4 Readout system

The Cherenkov effect is characterised by the emission of few photons, 3 orders of magnitude below a scintillation process. This results in signals in the MWPC generated by single photo-electrons: the amplitude spectra for these signals is described by Polya functions, that can be approximated by an exponential curve for low multiplication values ($\sim 5{\cdot}\ 10^4$). It is therefore mandatory to have a readout system with reduced electronics noise and precise control of the effective threshold setting; in COMPASS RICH-1 this is obtained by using a modified version of the Gassiplex chip [78] and adjusting the threshold for each readout channel independently. Gassiplex has optimum matching with the detector signal, even if it has some intrinsic limitations: in particular an effective dead time of 3 μs, resulting from the time required for baseline restoration after the release of the track-and-hold signal. The large number of RICH-1 electronic channels (82944) correspond to $\sim$ 40% of the total number of COMPASS electronic channels. To reduce the data flow, empty channels are suppressed at the front end stage and only the amplitude signals above threshold are read out and stored in local FIFO arrays. Data are then transmitted with optical fibres to the general acquisition system at a rate of 40 MB/s.

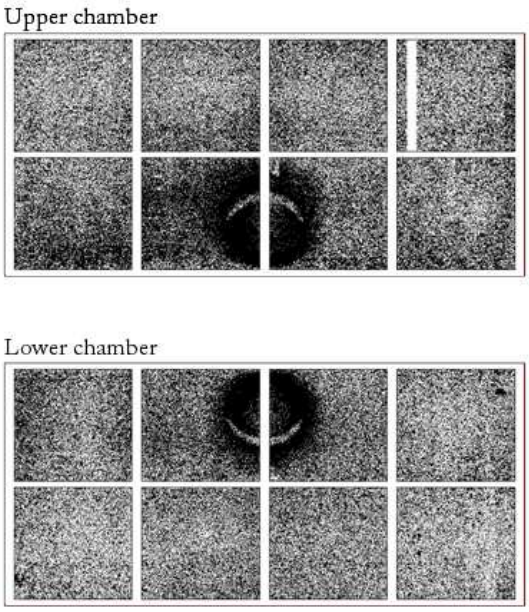

Figure 4.7: Overlap of event images, the central part is completely saturated by the photons generated by the beam halo.

4.3 The motivation of the upgrade

Taking advantage of beam stop at CERN in year 2005a major upgrade has been performed on the RICH-1 detector. This topic is illustrated in the next sections.

4.3.1 RICH-1 performances

The basic parameters characterising the detector performances are the mean number of detected photons: 14 per particle at saturation, the single photon resolution on the measured Cherenkov angle: 1.2 mrad at saturation, the global resolution on the measured Cherenkov angle: 0.6 mrad at saturation, a PID efficiency larger than 95% for Cherenkov angles larger than 30 mrad and a 2-σ π-K separation at 43 GeV/c [70, 71, 72, 73, 74, 75].
In spite of these remarkable figures characterising RICH-1, there are some performance limitations. The presence of the CsI photoconverter imposes to operate the MWPCs at a rather low gain (below 5×10^4) to guarantee their electrical stability. The first stage of the electronics read-out system is based on a modified version of the front end Gassiplex chip [78], amplifying and shaping the signal with a rather long integration time (0.5-1 ms) to compensate for the reduced gain. The typical noise figure obtained is 1100 electrons equivalent. The low gain, the integration time and an effective threshold at 3-3.5 times the noise level, result in a detection efficiency for single photoelectrons, which ranges around 70%. The Gassiplex integration time acts as a detector memory: each event image collected by the photon detectors includes the information of uncorrelated background events. Due to the nature of the background, the related rings cluster in the central region of the photon detectors (see fig. 4.7). The high level background limits both the RICH-1 efficiency and the resolution. The efficiency drops for very forward scattered particles, due to the combination of two effects, namely the high level background images present in the central photon detector region and due to photon losses: part of the Cherenkov photons generated by the forward scattered particles are lost due to the central dead zones of RICH-1, present to screen the photon detectors from the photons generated by the non interacting beam. The background also limits the RICH-1 resolution in the measured Cherenkov angle. In fact, single photon resolution does not scale with the number of detected photons to give the resolution obtained making use of all the detected photon in a ring: the actual resolution is almost a factor of two worse due to the signal dilution caused by the presence of the high level background.

4.4 The new photon detection system of the central region of COMPASS RICH-1

The new photon detectors of COMPASS RICH-1 [136] are based on the use of Multi Anode Photo Multiplier Tubes (MAPMTs) as active elements. MAPMTs, intrinsically fast and with sub-ns time resolution, are read out via a digital system based on highly sensitive amplifier-discriminators and high resolution Time to Digital Converters (TDCs) [79]. The choice of a digital system matches well the MAPMT characteristics: the spread amplitude spectrum provided by this photon detector (sec. 5.5.5) would make photon counting via amplitude measurement poorly effective. These photon detectors are more extensively studied in chapter 5. The MAPMTs are coupled to individual telescopes of fused silica lenses to enlarge the effective detection area. A compact setup with negligible dead zones and able to ensure both light and gas tightness has been obtained with an accurate design, construction and assembly of the mechanical components of the setup. MAPMTs coupled to lens telescopes have already been successfully employed for single photon detection in the HeraB RICH counter [80]. They have been proposed as one of the options for photon detection in LHCb RICHes [81]. Our approach is characterised by some novel features:

- the photon wavelength domain is extended to the UV range, obtained thanks both to the use of MAPMTs with UV extended window, that allow to convert photons down to 200 nm wavelength, and to the choice of telescopes formed by quartz lenses;

- the demagnification parameter of the telescopes coupled to each MAPMT is large; this makes it possible to get a ratio between the entrance window of each telescope and the photocathode surface larger than 7; this parameter, coupled to an accurate arrangement of the MAPMT and lens mechanical supports, allow both to save on the number of MAPMT required, and to obtain a dead zone fraction of $\sim$2% only;

- the read out is performed by a system providing a high sensitive front-end stage, resulting in a high efficiency detection of the single photoelectron, sub-ns time resolution to minimise the background due to uncorrelated events and to fully exploit the MAPMT time resolution, and high rate capabilities, as required by the high luminosity of the COMPASS experiment.

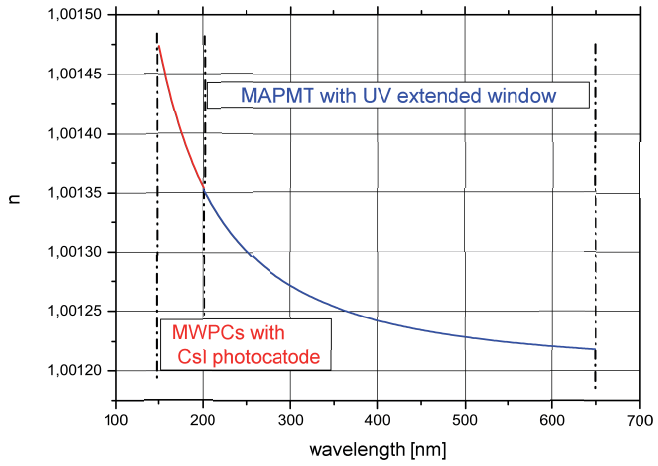

Figure 4.8: C_4F_{10} refractive index versus light wavelength. The wavelength ranges of effective quantum efficiency for the MWPCs with CsI photocathodes and for MAPMTs with extended UV glass windows are indicated.

4.4.1 Number of detected photons and resolution considerations

The main motivations for the upgrade, as said (sec. 4.3), are to obtain high rate capability and to decrease the background level down to a negligible level. Concerning the resolution in the measured Cherenkov angle, the goal is to recover the figure spoiled by the background presence, namely to get an r.m.s. of $\sim$0.3 mrad.

Comparing photon detection with MWPCs equipped with CsI photocathodes (i), to the photon detection performed with MAPMTs (ii), two major differences have to be taken into account. The converted Cherenkov photons have wavelengths spanning different ranges, which results in a different effective refractive index value of the radiator gas (fig. 4.8) and in a different chromatic dispersion. Folding the refractive index evolution with the Cherenkov spectrum and the detector quantum efficiency, the resulting dispersion of the refractive index has an r.m.s of 30×10^{-6} for (i), and 46×10^{-6} for (ii). Concerning the number of detected photons, taking into account the Cherenkov spectrum, the quantum efficiency and the photoelectron conversion efficiency, the number of detected photons per active surface unit is about 4 times larger for (ii) then for (i), opening the possibility of detecting a larger number of photons per ring using the MAPMTs.

A larger number of detected photons can compensate for the resolution worsening caused by an enlarged effective pixel size. The MAPMTs photocathode size and pixel size are fixed, but the use of an optical system in front of the MAPMT can enlarge the effective size of the cathode surface and, correspondingly, of the pixel.

This approach has several advantages:

- it makes possible to recover for the intrinsic dead zone between adjacent MAPMTs, due to the external MAPMT dimension,
- enlarging even more the distance between adjacent MAPMTs, it is possible to reduce the number of MAPMTs needed, making the project economically affordable,
- averaging the chromatic dispersion over a larger number of detected photon it is possible to recover for the increased chromatic effect,
- a larger number of detected photons is an important handle to increase the RICH-1 efficiency for those images, for which the number of photons is reduced, namely at very small scattering angle, due to the dead zones at RICH centre, and for particles with momenta near to the threshold of the Cherenkov emission.

The effective pixel size cannot be enlarged excessively. In fact, if the pixel size becomes too large, the probability of having more converted photons impinging on the same pixel becomes important. Using a digital read-out system, this corresponds to an effective reduction in the number of detected photons. On the base of these considerations, an effective pixel size of about 12×12 mm^2 has been chosen. Assuming no dead areas between the effective active surface of adjacent MAPMTs and the characteristics of the photomultipliers used (Sec. 5.4.2), this result in a MAPMT pitch of $\sim$5 cm, corresponding to the need of 576 MAPMTs to instrument the central region of COMPASS RICH-1.

4.4.2 Orientation and acceptance of the lens telescope

The needs concerning orientation and angular acceptance of the lens telescope have been determined with Monte Carlo studies. The requirements can be partially different according to the physics process considered. As reference, the most challenging physics channel for the RICH-1 performance within the COMPASS research program, has been used: the detection of the decay channels $D^0 \rightarrow K^- \pi^+$ and $\bar{D}^0 \rightarrow K^+ \pi^-$. A sample of these events has been generated using AROMA [82] and traced along the COMPASS spectrometer with Geant 3.21 [83], making use of COMGEANT [84], the dedicated interface to Geant developed in order to simulate the performance of the COMPASS spectrometer. The orientation of the optical telescope axis and its angular acceptance, defined as the angular range for which the photon acceptance is larger than 50%, for the final telescope design have so been fixed. The optimal telescope orientation was fixed at 5.5 degrees for the horizontal projection and 23.5 degrees for the vertical one. The design of the lens telescope [85]

has been performed using ZEMAX[1]. The wavelength distribution was weighted with the Cherenkov spectrum and the effective quantum efficiency of the MAPMTs and the requirements concerning the effective pixel size and MAPMT pitch coming from the overall project design (sec. 4.4.1) are taken into account. Two constrains come from the existing COMPASS spectrometer set-up. The total telescope length cannot exceed 15 cm, due to the reduced space available upstream of RICH-1 in the COMPASS spectrometer. The MAPMT has to be oriented at an angle respect to the telescope entrance axis, a feature needed for compatibility with the existing MWPCs that remain as peripheral photon detectors: the telescope has to be a non-axial system. To match the requirements, the telescope has to include a field lens followed by a concentrator, for a total of 4 lens surfaces; this basic scheme is derived from the one used for HeraB RICH [86], with a major modification: the field lens has to include a wedge element to get the needed non axial telescope architecture. As a consequence, we have chosen to have the second face of the field lens planar. The optimal architecture has been selected according to the following criteria:

- maximise the photon acceptance,
- minimise the image distortions,
- taking into account the production and cost aspects.

The architecture adopted is shown in detail in Fig. 4.9. The equation describing the aspheric surface is

$$z = \frac{\rho^2/R}{1+\sqrt{1-\rho^2/R^2}} + \alpha\rho^4 \tag{4.1}$$

where z is the coordinate along the surface axis and ρ is the distance from the axis; the parameters defining the surface are the radius of curvature R and the aspherical 4^{th} coefficient α. The telescope parameters are given in table 4.1. The fraction of photons lost by reflection in the telescope has been estimated for the effective Cherenkov photon spectrum: 14.4%, and the spectrum of photons lost by reflection is peaked around 300 nm. For this reason a single layer MgF_2 coating has been applied. The layer thickness has to be chosen so to minimise the reflection at 300 nm. It is so possible to reduce the fraction of photons lost by refraction by a factor of two, namely to increase the number of detected photons by 8.4%. Both the telescope lenses are coated with a single layer of MgF_2.

4.4.3 Lens production

The lens drawings for production (figs. 4.11 and 4.12) have been obtained merging the optical design with those details that allow to assembly the telescopes and their

[1]ZEMAX Development Corporation, 3001 112th Avenue NE, Suite 202 Bellevue, WA 98004-8017 USA

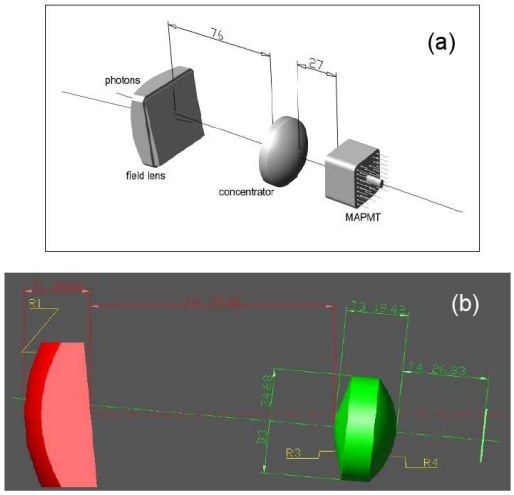

Figure 4.9: The final design of the telescope; (a) artistic view; (b) side view (parameters are quoted in table 4.1.

parameter	value
R_1 (mm)	54.937
R_2 (mm)	20.696
R_3 (mm)	-24.964
$\alpha \times 10^5$ (mm^{-3})	-6.13884
T_1 (mm)	20.813
T_2 (mm)	75.805
T_3 (mm)	19.420
T_4 (mm)	26.835
D_3 (mm)	34.68

Table 4.1: Telescope parameters.

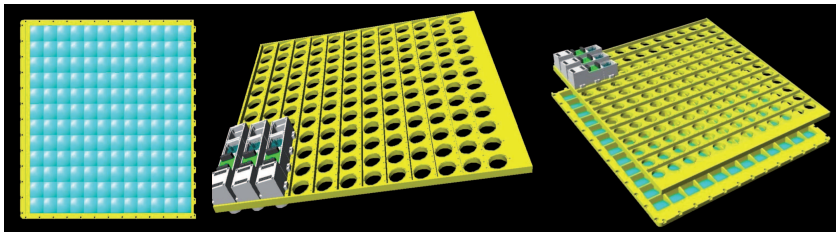

Figure 4.10: The three frames that assembled together form one of the mechanical structures of the four quadrants; (a) the field lens frame, (b) the concentrator lens frame housing the aspherical lenses, (c) the two previous described frames coupled. The concentrator lens frame is enclosed in the Armco holder, described in figure 5.5, to which MAPMTs are fixed by screws.

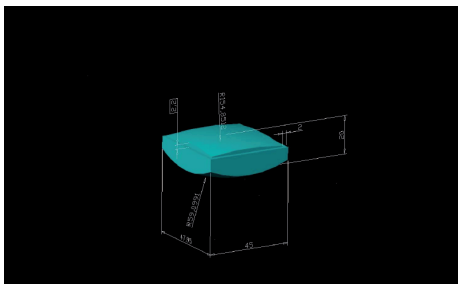

Figure 4.11: Drawing of the field lens.

mechanical supports (see figure 4.10).

576 field lenses and 576 concentrator are needed for the complete project. The material used is fused silica, type Corning 7980, standard grade F5 by Corning[2].

4.4.4 Quality Checks for the lens telescope

A setup for the optical quality assessment has been designed and built, to be used for the quality control of the quartz lenses at production and to check the telescopes mounting, after assembling them. The test system is based on the Hartmann method [87] and it is suitable for the optical checks of a large number of lenses and telescopes. The principle of the Hartmann technique (fig. 4.13 is based on the use of a mask with a regular array of holes, placed at the pupil of the optical system to be tested. A parallel beam illuminates through the mask the optical system. The image of the spots corresponding to the holes are collected at a defocusing position see figure 4.13.

[2]Corning Incorporated, One Riverfront Plaza, Corning, NY 14831 USA

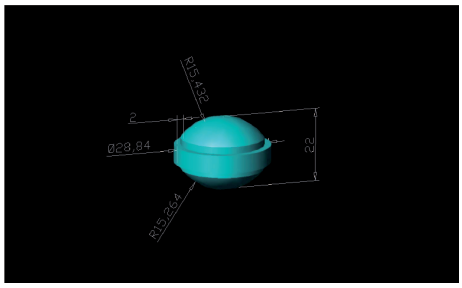

Figure 4.12: Drawing of the concentrator lens.

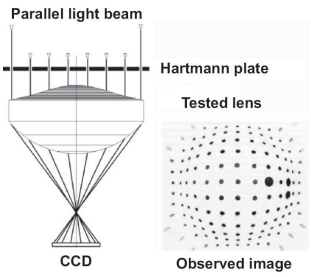

Figure 4.13: Scheme of the principle and observed image of the Hartmann validation test for the condenser (aspheric) lens.

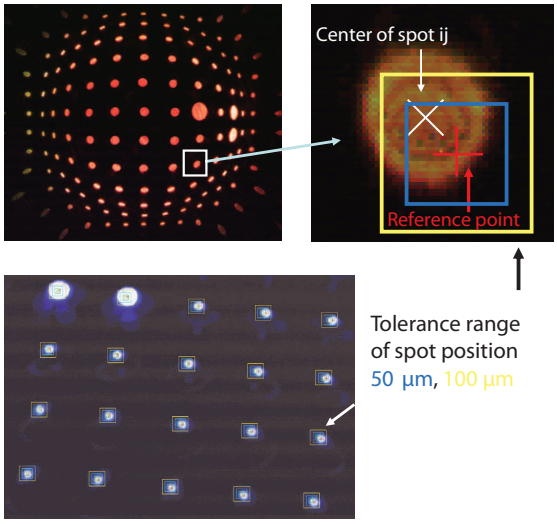

Figure 4.14: A typical image collected with the Hartman setup. The zoom of a spot is shown. The comparison between the spot position in the image and the expected position for the ideal optical object is also shown. The accepted tolerance for the optical object can be translated in an area around the ideal position: if the actual spot is contained in this area, the optical distortions are within tolerances.

The shape of the wavefront can be deduced from the spot image: the aberrations of the optical system can be determined, comparing the reconstructed wavefront with the ideal one. The differences between the actual image and the ideal one are analysed. The set of orthogonal Zernika polynomia are used and the coefficients multiplying the first 14 elements in the series are determined. Each of them is related to a specific optical distortion. A typical image is shown in fig. 4.14.

4.5 The new electronic read out

The read-out system for the MAPMTs is based on the MAD4 preamplifier discriminator and the high resolution dead-time free F1 TDC. The electronic scheme, illustrating the signal path-chain, is displayed in figure 4.15. The read-out system is free from cable connections to minimise the electrical noise, and to obtain a very robust setup. The elements of the chain will be now described.

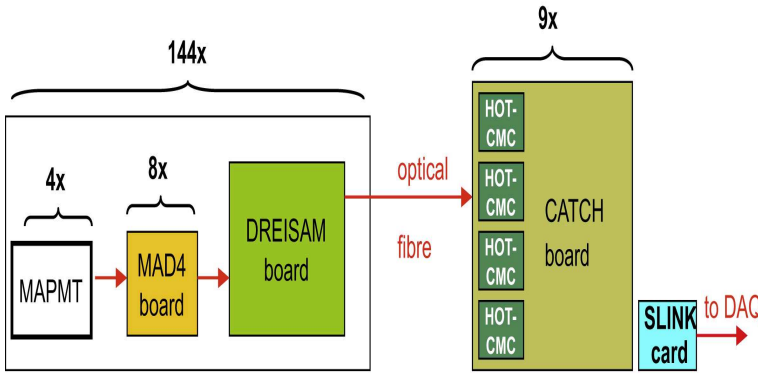

Figure 4.15: Electric scheme summarising the electronic signal path: 1) discrimination 2) preamplification followed by 3) digital conversion.

4.5.1 The MAD chip

The main task of the front-end board is to amplify the signals from the MAPMT, to discriminate them and send the differential LVDS signals to the digital board. The MAD4 chip is a full custom ASIC in Bi-CMOS technology developed by the I.N.F.N - Sezione di Padova for the muon drift tubes of the CMS barrel [88]. An integrated circuit includes four channels. Each channel features a charge preamplifier with fixed gain (3.35 mV/fC), a simple shaper with baseline restorer, a comparator, a programmable one-shot to shape the digital output and a LVDS driver. A resistive voltage divider is implemented on the MAD4 board itself in order to attenuate by a factor of 2.4 the MAPMT output signal before the preamplification stage, thus avoiding a preamplifier saturation for very large signals. At the preamplifier output, the signal shape is formed by a shaper: a low gain integrator with a small time constant has the non-inverting input pin connected to the preamplifier, while the inverting pin allows to put this stage inside the feedback loop of a low offset Operational Transconductance Amplifier (OTA), thus implementing a baseline restorer. The quiescent level of the baseline is set externally to a fixed voltage VREF common to the four OTAs. The output of this stage is then directly connected to the non-inverting input of a fully differential discriminator. The discriminator is provided with an external threshold common to all the four channels. A logical shaper, the one-shot, follows the comparator stage, allowing a width adjustment of the standard differential LVDS output from 20 to 200 ns. In our application, the width is externally fixed to 40 ns by pin W_{CTRL}, common to the four channels.
Services to the MAD4 boards are provided by the roof board: power, threshold setting and input/output data transfer from and to the digital board. Each Roof board is directly connected to eight MAD4 boards and a digital board.

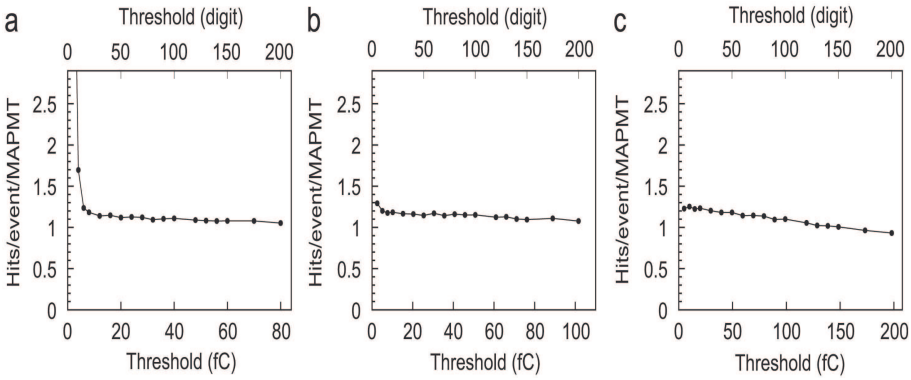

Figure 4.16: Typical threshold curves with three different DAC resolutions. Error bars are smaller than the symbols dimensions.

Front end tests

Several exercises have been performed to determine the design of the input partition optimised in terms of signal attenuation, granularity of the threshold setting, and minimum noise and cross-talk level. A resistive voltage divider with an attenuation factor of 2.4 has been chosen for the final layout. Before selecting the resistive voltage divider scheme, various layouts with capacitive dividers have been widely tested but finally excluded due to a slightly higher cross-talk level observed at high rates. Typical threshold curves with three different DAC resolutions are displayed in figure 4.16 . In the second plot, corresponding to the final design, there is a wide range of values for threshold setting outside the noise and cross-talk region with negligible photo-electron losses. Due to the high rate environment, the maximum rate sustainable is a parameter of extreme importance. The test performed showed that the MAD4 is capable to sustain an event rate up to 1 MHz per channel as illustrated in figure 4.17.

4.5.2 The digital F1 board

The digital element of the RICH-1 read-out system is the DREISAM front-end board (see fig. 4.18). It is equipped with eight F1 TDC chips [89] and reads out four MAPMTs. In total, there are 144 DREISAM boards for the read-out of the entire central part of the RICH-1 detector. The data are digitised on the DREISAM boards and transferred via optical links to HOT-fibre CATCH Mezzanine Card (HOT-CMC) boards. Each HOT-CMC receives inputs from four optical links. The HOT-CMC is a mezzanine board, which is plugged into the common read-out driver of the COMPASS experiment: The COMPASS Accumulate, Transfer and Control Hardware (CATCH) [84, 89]. On the CATCH, data from four HOT-CMC boards

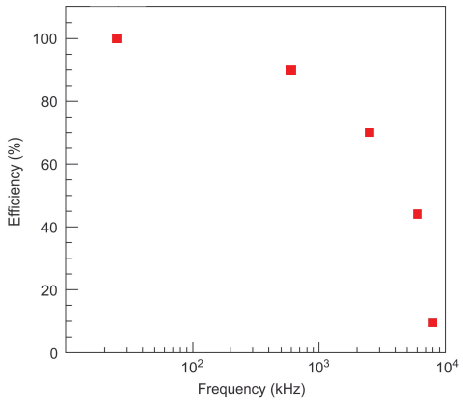

Figure 4.17: Measured MAD4 efficiency versus single photo-electron rate. Error bars are smaller than the symbols dimensions

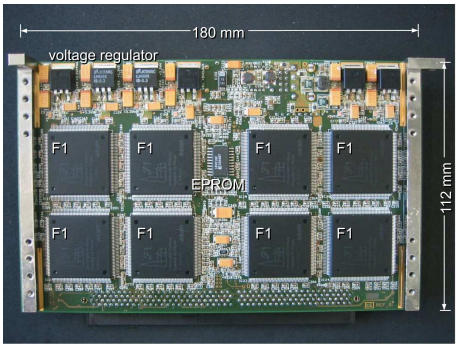

Figure 4.18: Front side of the DREISAM board: The eight F1 TDCs can be seen in the lower part of the board. On both sides of the board aluminium bars for mechanical fixation are visible.

are merged and sent out via S-LINK [90] modules to read-out PCs of the COMPASS data acquisition system [84]. For the RICH-1 read-out the F1 board gives a time unit of 108.3 ps for the measurement [91].
The performance of the DREISAM board was studied in a laboratory setup. For this purpose, LVDS signals were generated in a 1:64 NIM-LVDS converter. An adapter board transfers the data to the input of the DREISAM board. The maximum trigger and input data rates as well as the time jitter of the TDC measurement have been tested. The DREISAM board has been tested at trigger rates up to 100 kHz. The maximum data input rate on each of the 64 input channels can be 10 MHz. A time jitter of less than 35 ps RMS for every individual channel versus a reference TDC was measured [92].

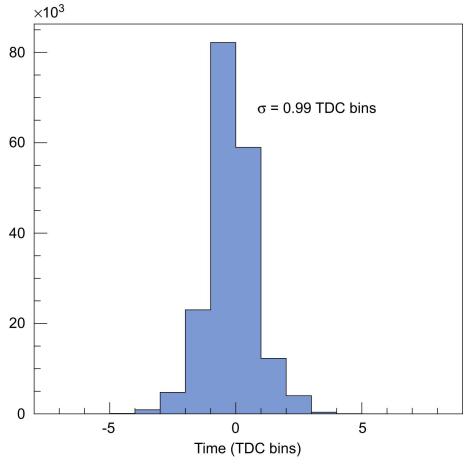

Figure 4.19: Time spectrum of the electronic chain (MAD4+Roof+DREISAM). 1 TDC bin corresponds to 108.3 ps.

Time resolution

The time resolution of the read-out system has been measured from the time difference of the signals of two MAD4 boards plugged on the same DREISAM board, getting a measurement of the time jitter due to the electronics only, without the contribution of the MAPMT. In figure 4.19 the time spectrum obtained is shown. The time resolution of the read-out electronics system is $\frac{110}{\sqrt{2}} \cong 75ps$. To evaluate the overall time resolution of the photon detector the MAPMT was included in the read-out chain. A laser head consisting of a laser diode and collimating optic generates optical pulses of a width of $\lesssim$ 45ps . These pulses are sent through an optical filter and $300\mu m$ pinhole onto the MAPMT photo-cathode. The distribution of the MAPMT signal times in response to single photons relative to the trigger time gives the total jitter of the complete read-out system: MAPMT, MAD4 board, Roof board, DREISAM board and the optical fibre, which distributes the clock signal to the TDC. The time spectrum is shown in figure 4.20. The central peak has a width of $\sigma = 320ps$. In addition, there is a tail of later signals related to photons impinging on the photo-cathode close to the border between two neighboured channels [92].

4.5.3 Cross talk

The cross-talk between neighbouring channels has been determined by illuminating an isolated MAPMT pixel by a laser diode through a small pin hole of about $300\mu m$ diameter, and measuring the number of hits in the other channels. The results of the measurements are shown in figure 4.21. The measured cross-talk level for thresholds above 10 fC is well below 10^{-3} for all channels and therefore negligible.

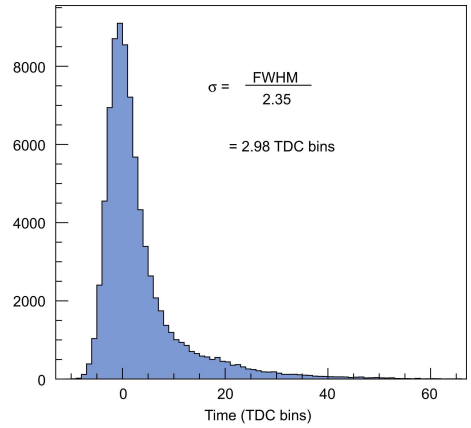

Figure 4.20: Full chain time spectrum. 1 TDC bin corresponds to 108.3 ps.

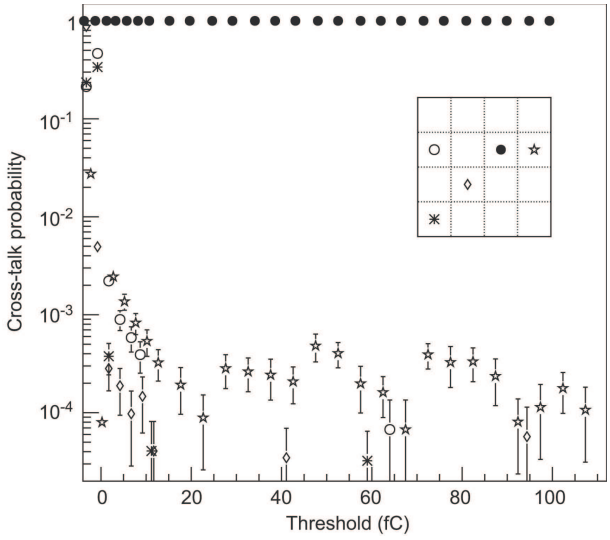

Figure 4.21: Cross-talk measurement: hit rates of the illuminated reference pixel (closed circle) and in different neighbouring channels, each normalised to the reference pixel.

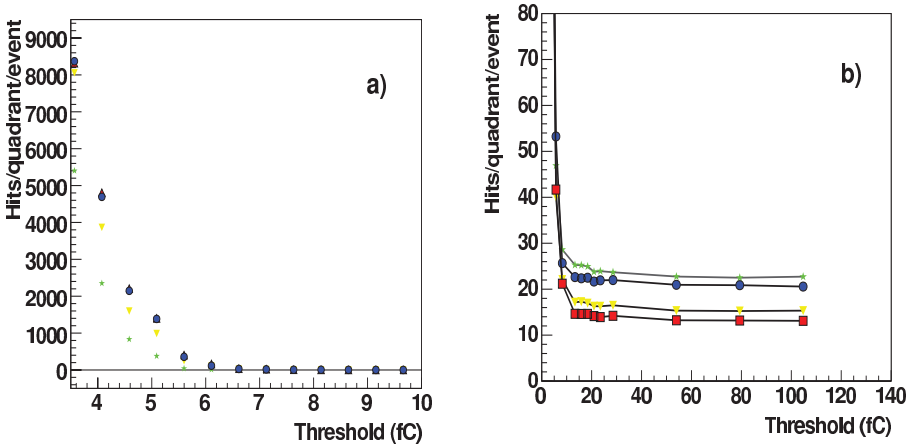

Figure 4.22: Threshold curves for the four quadrants. (a) Beam off (b) beam on; the different plateau levels correspond to different particle rates in the different detector quadrants (time window: 100 ns). Error bars are smaller than the symbols dimensions

4.5.4 Noise and cross-talk in real environment

The electronics noise has been measured channel by channel in the real environment with beam off, in order to find the correct threshold over noise value for each MAD4 chip. In figure 4.22 a), the obtained threshold curves for the four quadrants are shown: The noise level is lower than 7 fC, like in the laboratory studies. To evaluate the cross-talk level, another threshold scan has been performed with beam on for threshold values above noise level. The obtained threshold curves are shown in fig. 4.22 (b. The cross-talk level is negligible above 35 fC. The distribution of the thresholds set during the 2006 run for each MAD4 chip is finally shown in fig. 4.23.

4.6 Performances of the RICH-1 after the upgrade.

RICH-1 has been fully characterised in both the old and the upgraded version, determining in operative conditions all the relevant observables: the number of detected photons, the angular resolution and the PID efficiency. The number of signal photons at saturation, namely for $\cos\theta_{Cherenkov} = 1/n$, has been evaluated through a fit of the number of photons per ring as a function of the Cherenkov angle, using a function of the type $N_0 \sin^2(\theta_{Ch})$ [93]. The number of detected photons at saturation is around 14 before the RICH-1 upgrade and, after the upgrade, in the peripheral regions, while it has increased up to 56 (fig. 4.24) in the upgraded RICH,

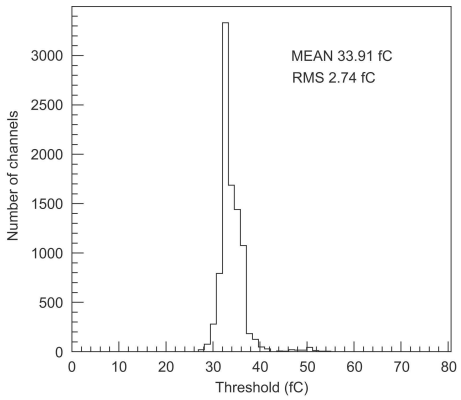

Figure 4.23: Distribution of the final threshold setting.

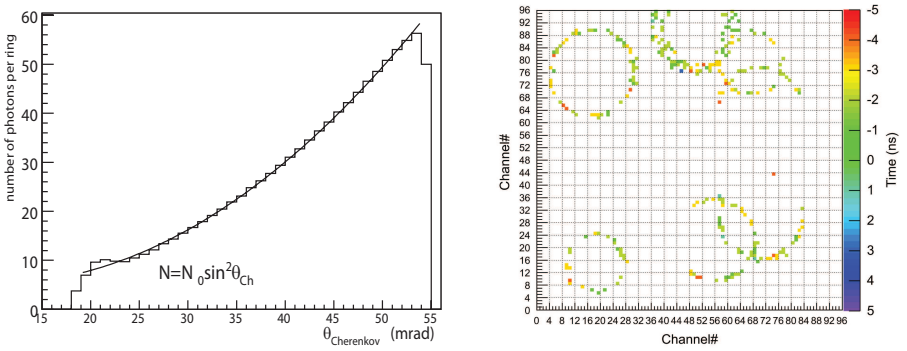

Figure 4.24: Left: number of photons per ring as a function of the Cherenkov angle, for rings detected in the MAPMT part only; the curve is a fit with a function of the type $N_0 \sin^2(\theta_{Ch})$. The number of photons at saturation after background subtraction is around 56. Right: example of hadron Cherenkov rings in a single event.

central regions. The single photon resolution σ_θ is evaluated from the width of the distribution $\theta_{ph,i} - \theta_\pi$, where $\theta_{ph,i}$ is the Cherenkov angle of a photon belonging to the ring and θ_π is the angle for the pion mass hypothesis. The Cherenkov angle is obtained as the average value of all the single photon angles resulting: $\theta_{Ch} = \sum_{i=1}^{N} \theta_{ph,i}/N$, the single ring resolution is so $\sigma_{ring} = \sigma_\theta/\sqrt{N}$ [94]. In RICH-1 before the upgrade, the mean value of the resolution is around 1.2 mrad, while the resolution on the ring angle is around 0.6 mrad. The two numbers do not scale with the square root of the number of detected photons per ring due to the large background contribution in each reconstructed ring, diluting the signal. After the upgrade,

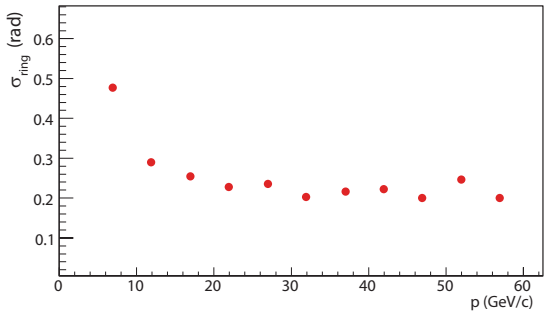

Figure 4.25: Standard deviation of the $\theta_{ring} - \theta_\pi$ distribution, for particles identified as pions, as a function of the particle momentum; ring detected in the MAPMT detector only.

the single photon resolution in the central part is around 2 mrad, while the ring angular resolution is less than 0.3 mrad (fig. 4.25); the almost complete scaling of the ring resolution with the number of photons is due to the fact that the background contribution per ring is small. The PID efficiency has been evaluated selecting with kinematics criteria a sample of exclusively produced ϕ mesons; the sample has a purity of about 90%. The efficiency has been evaluated separately for K^+ and K^-, using the positive or negative track coming from the ϕ decay. In fig. 4.26 and 4.27 the K efficiency is shown as a function of the particle polar angle, both for the old and for the upgraded RICH. The curve corresponding to the old RICH shows clearly that the efficiency increases at large polar angle, since at small angles it is limited due to the presence of an important background coming from the muon beam halo. The strong suppression of the background can be appreciated also looking to the time spectrum of a whole quadrant of the MAPMT detector part in data taking (see fig.4.28). It shows a peak with a sigma of about 1 ns corresponding to the Cherenkov photons created by particles in the triggered physics events. The width of the peak is determined by the different geometrical path lengths of the photons in one Cherenkov ring travelling from the particle track via the mirrors to the photon detection system. The pushed time resolution of the photon detection system itself and the read-out electronics, measured to be 320 ps (see sec. 4.5.2) allows an extremely good background to signal separation. The impact of the upgrade on the RICH efficiency is clearly visible from the corresponding efficiency curve: also at small polar angle the efficiency is above 90%.
The effect of the improved efficiency and purity can be appreciated in the comparison of the reconstructed mass spectra, obtained combining the measured momentum and the RICH information, for 2004 data and 2006 data in figure 4.29.

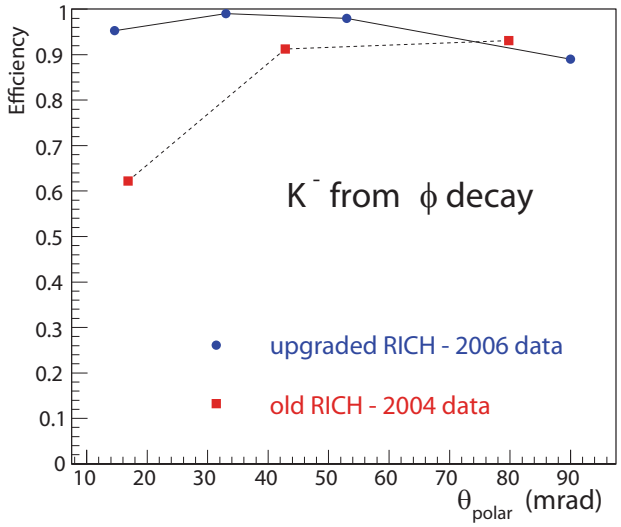

Figure 4.26: PID efficiency for K^-, evaluated on a sample of particles from ϕ decay, as a function of the particle polar angle. The two sets of data points correspond to the old and to the upgraded versions of RICH-1. The error bars are not drawn since smaller than the symbols used, for the last point, where the error is maximum, the relative error ranges between 2 and 3 %.

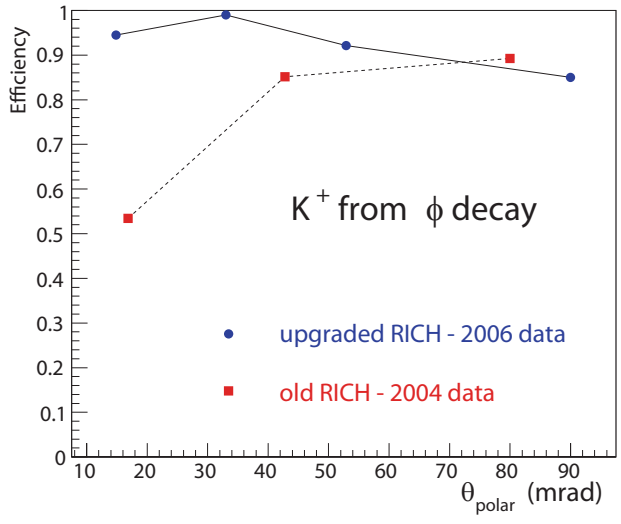

Figure 4.27: Same as fig. 4.26, for K^+

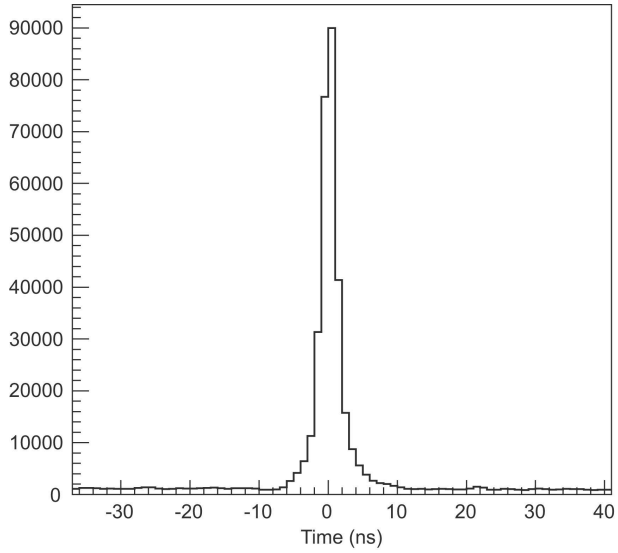

Figure 4.28: Time spectrum of a whole quadrant of the MAPMT detector part in data taking is displayed. It shows a peak with a sigma of about 1 ns corresponding to the Cherenkov photons created by particles in the triggered physics events.

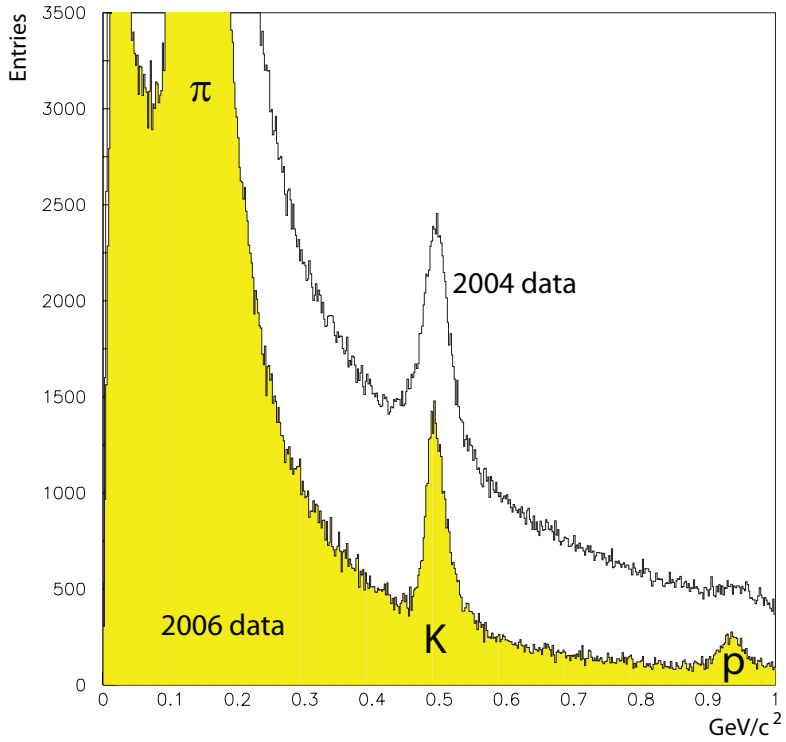

Figure 4.29: Mass spectra obtained combining the momentum measured by the COMPASS spectrometer and the RICH information, before (2004 data) in white and after in yellow the RICH upgrade (2006 data). The pion, the kaon peak and the proton peak are visible. The strong background suppression is evident.

Chapter 5

The Multi Anode PhotoMulTipliers (MAPMT) for the upgrade of COMPASS RICH-1

The possibility to identify charged particles by detecting the feeble glow emitted when they move through a medium with a velocity greater than the local phase velocity of light, was already pointed out by Cherenkov who discovered this phenomenon, in 1937[95]. The appearance of photomultipliers (PMTs) allowed to develop a variety of powerful devices, known as *Cherenkov counters*, which enabled several experiments to achieve remarkable physics results. The measurement of the Cherenkov angle via the direct imaging of the emitted photons, although conceptually simple, was indeed so demanding in the various practical aspects to require almost seventeen years before becoming a reality.
The accomplishment achieved in the '90s by the groups involved in the construction of the large volume devices of the OMEGA, DELPHI and SLD experiments[96] made the Cherenkov ring imaging technique an experimental toolkit, nowadays largely used in nuclear and sub-nuclear physics as well as in astroparticle physics experiments around the world. Its capabilities are still unmatched among the current alternative technologies especially when a high particle separation is required by the physics objectives, as shown by the outstanding discoveries made in the field of the B physics[97].

5.1 The photomultiplier tube

Photodetectors or light sensors can be broadly divided by their operating principles into three main categories: external photoelectric effect, internal photoelectric effect and thermal types based. The external photoelectric effect is the phenomenon

in which electrons are emitted from a metal or a semiconductor surface, placed in vacuum, when light impinges on it. Photomultiplier (PMT) tubes make use of this external photoelectric effect. Recently also devices based on external photoelectric effect in gaseous atmosphere have been operated [67].
The photoelectric effect was discovered in 1887 by Herts[98] through experiments exposing a negative electrode to ultraviolet radiation and in the next year 1888 the effect was conclusively confirmed by Hallwacks[99]. In 1889, Elster and Geiter[100] reported the photoelectric effect induced by visible light striking an alkali metal (sodium-potassium). Since then, a variety of experiments on photoemission have been performed. As a result, the concept proposed by Einstein[101] in 1905 "*Photoemission is a process in which photons are converted in free electrons*" has been proved and accepted.
In 1929 a compound photocathode made of Ag-O-Cs (the so-called S-1) was discovered by Koller[102] and Campbell[103]: this photocathode showed photoelectric sensitivity about two order of magnitude higher than the previously used materials, achieving high sensitivity in the visible to the near infrared region. Since then various photocathode materials have been used and tested including bi-alkali photocathodes for the visible region, multi-alkali photocathodes with high sensitivity extending to the infrared region and alkali halide intended for ultra violet detection[104, 105, 106, 107]. In addition, photocathodes using compound semiconductors such as GaAs[108, 109, 110, 111, 112, 113] and InGaAs[114, 115] have been developed and put into practical use. These photocathodes have a negative electron affinity structure and offer high sensitivity from the UV through the near infrared region. It was only 1935 when the phenomenon of photoemission (the photoelectric effect) was combined with secondary emission that the photomultiplier was created. The first report on a secondary emissive surface was made by Austin et *al*[116] in 1902. Since that time research into secondary emissive surfaces (secondary electron emission) has been carried out to achieve higher electron multiplication. It was 1935 when Iams et *al*[117] succeeded in producing a photomultiplier tube with a photocathode combined with a single stage dynode: the device consisted of a semicylindrical photocathode, a secondary emitter mounted on the axis, and a collector grid surrounding the secondary emitter. The tube had a gain of about eight. In the following 1936 Zworykin at *al*[118] developed a PMT with multiple dynode stage setup. This tube enabled electron to travel inside the tube combining the effect of a magnetic and electric static field. In 1939 Zworykin and Rajchmann[119] developed an electrostatic focusing type photomultiplier tube, which is the the basic structure of the currently used PMT. The requirement of high gain led to improve the geometrical structure of the PMT as obtained by Morton in 1949[120] and in 1956[121]. The dynode structure was so intensively studied, leading to a variety of dynode systems including circular cage, linear focused and box grid types.

5.2 The detection of single photoelectrons

A single photon detector requires a certain amplification mechanism, as noiseless as possible, which generates a secondary pulse of electrons consisting of at least some thousands electrons per primary generated electron. If the pulse itself is short in time, the resulting instantaneous current can be quite large and the pulse becomes easy detectable by additional electronics. Both MWPCs coupled to CsI and MAPMTs which are used in COMPASS are members of this family. When a photon is capable of releasing an electron from the photocathode, the electron gets accelerated by a rather strong electric field releasing secondary electrons; according to the electrostatic field applied, different gain can be achieved. In COMPASS the instabilities of the MWPCs force them to operate at low gain $\sim 5 \cdot 10^4$. In MAPMTs on the contrary, the set of multiplication stages allow to reach an average amplification of the order of 10^6 or more. This, among the other differences, (time resolution, spatial resolution), is of the utmost importance. Looking at figure 5.1 this aspect becomes clear. A simple Montecarlo using GARFIELD [122] has been used to obtain the normalised photo-electron distribution shown in figure 5.1. The x axis is proportional to the charge collected. The four different plots represents the distribution of photo-electrons in case of different gain values from $\sim 10^4$ (up left plot) till $\sim 10^6$ (down right plot). The red coloured part is the cut on the signal for an applied theoretical threshold of 0.5. It is clear that in the low gain case setting the threshold to reject noise signals is always critical, finally resulting in a limited photo-electron detection efficiency. Any minimal change of it would result in very different effective efficiency of the detector. Moving to higher gain results in the modification of the distribution shape. For a gain $\sim 10^6$ (down right) the threshold setting does not result in a critical task allowing a good photoelectron detection efficiency and stable behaviour of the detector. A remark is also necessary: due to the normalisation imposed the mean of the distribution is always 1. For higher gain, in the real case the mean value of the distribution shifts to greater values, and the now arbitrary choice of 0.5 as threshold becomes even less critical. The up-grade of RICH-1 has been designed so to take advantage as much as possible of the high gain MAPMTs and of the low noise electronic, resulting in a extremely stable and performing detector.

5.2.1 A model for the PMT response.

There has been considerable investigation of the detection statistics of PMT based systems under the assumption that the PMT is an ideal photon counter [123]. The photo-multiplication process, however, is itself a random process, and the fluctuations in the photomultiplier gain will affect the performance of the systems itself.
For this reason the output statistics of photomultiplier tubes is investigated with

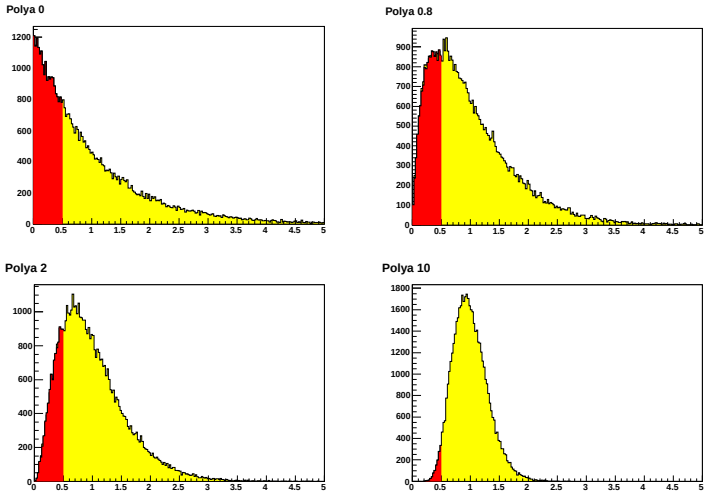

Figure 5.1: Different output spectra for electron multipliers detector for different gain values, the first spectrum (top left) corresponds to a gain $\sim 10^4$, the last (bottom right) to a gain of $\sim 10^6$. The red shadowed area corresponds to cut on the signal for a hypothetical threshold of 0.5. At low gain the threshold setting is much more critical than in the high gain case. For the definition of the x axis see text.

particular attention to parameters, as gain per stage, and how they affect the performance of the photon detector.
The transmitter will be an ideal laser whose output is gated on and off in conjunction with the binary information to be transmitted. Each pulse interval has a duration of T seconds. Let's now consider as receiver a photomultiplier tube followed by a charge storage device such as a capacitor. The total charge (q_T) accumulated in an appropriately synchronised T_s interval is then used to determine whether or not a pulse was sent. Let q_{th} be the threshold value of the accumulated charge. If $q_T \geq q_{th}$ it is assumed that a pulse was sent and if $q_T \leq q_{th}$ it is assumed that no pulse was sent. The quantity q_T is selected to minimise the probability of error. It is convenient to use

$$q_T = n_e \cdot e \tag{5.1}$$

where n_e is number of electrons accumulated in T_s and e is the charge of an electron. Also let $n_{th} = \frac{q_{th}}{e}$ then the detection as previously described is mathematically equivalent to comparing n_e with n_{th}. The photo multiplication process, however, is itself a random process and there are two different causes for n, being random.
Firstly, the number of photoelectrons ejected from the primary photosensitive surface of the photomultiplier is a random variable; secondly, the gain of the photomultiplier is a random quantity which varies for each initial photoelectron.
This can be summarised writing

$$n_e = \sum_{i=1}^{m} A_i \tag{5.2}$$

where A_i is the photomultiplier gain for the i^{th} initial photoelectron and m is the number of initial photoelectrons ejected from the photosurface in the T-s pulse interval. It will be assumed that all the electrons reach the anode during the T-s interval and edge-of-the-pulse interval effects will be ignored.
It is also assumed the photomultiplier is operating in a non saturated condition and hence the A_i are assumed to be statistically independent random variables. Each of the A_i, however, are assumed to have the same probability distribution. In order to obtain a probability distribution for n_e, equation 5.2 will be used within the statistical independence of A_i. In such way

$$p(n_e) = \sum_{m} F_m(n_e) p_0(m) \tag{5.3}$$

where $p_0(m)$ is the probability distribution for m the number of initial photoelectrons, and where $F_m(n_e)$ is given by the convolutions:

$$F_{n_e}(m) = P_A(A_l) * P_A(A_2) * ....P_A(A_m) \tag{5.4}$$

and $p_A(A_i)$ is the probability distribution for the photomultiplier gain. Since all the $p_A(A_i)$ are the same, F, is m-1 fold self-convolution of $p_A(A_i)$. Let $Q_A(s)$ be the generating function for $p_A(A_i)$ and $Q_n(s)$ be the generating function for $p(n_e)$, then

$$Q_{n_e}(s) = \sum_m [\mathrm{Q_A(s)}]^{\mathrm{m}} \cdot p_0(m) \tag{5.5}$$

The form of the generating function used in the followings is given by

$$Q(s) = \sum_m p(m)(1-s)^m \tag{5.6}$$

These formulas will now be used to obtain the output statistics for a multistage PMT. In order to obtain a specific result for the probability distribution for $p(m)$ it is necessary to choose a mathematical model for the gain of each of the PMT stage. In recent years the Polya distribution has received considerable attention as the gain per stage probability distribution [124],[125],[126]. This distribution includes as limiting cases the Poisson distribution and Furry distribution which have been observed in practice, and it has been used with some success to describe the effects of inhomogeneities in PMT stage surfaces [124]. The Polya distribution is given by [124]:

$$p(n_1) = \frac{\mu^{n_1}}{n_1!}(1+b\mu)^{-n_1-(1/b)} \prod_{i=1}^{n_1-1}(1+ib) \tag{5.7}$$

where $p(n_1)$ is the probability distribution for the number of secondary electrons generated at a PMT stage by a single incident electron. The corresponding generating function of the form of 5.6 is given by

$$Q(s) = [1+b\mu s]^{1/b} \tag{5.8}$$

and the mean and the variance of n_1 are given by:

$$\langle n \rangle = \mu\sigma_{n_1} = \mu^2 b + \mu \tag{5.9}$$

In the limit that $b \to 0$, $p(n_l)$ becomes a Poisson distribution and in the limit that $b \to 1$, $p(n_1)$ becomes a Furry distribution. Here b we bill call the "Polya b-parameter". It has been shown [124] that the deviation of b from zero may be caused by non uniformity of gain across the surface of a single stage of the PMT. The following notation will be used: let $p_k(n)$ be the probability distribution for the total number of electrons after k PMT stages, and $Q_k(s)$ be the associated generating function. Then from 5.6 one obtains

$$Q_k(s) = \sum_m [Q(\mu_k, b_k, s)]^m p_{k-1}(m) \tag{5.10}$$

where

$$Q(\mu_k, b_k, s) = [1 + b_k \cdot \mu_k \cdot s_k]^{1/b_k} \tag{5.11}$$

and p_k is the gain of the k^{th} stage, and b_k is the Polya b-parameter for the k^{th} stage. Equation 5.10 may then be expressed in the following form:

$$Q_k(s) = \sum_m \left[1 + \left(\frac{b_k}{m}\right)(m_{\mu_k})s\right]^{-(m/b_k)} p_{k-1}(m) \tag{5.12}$$

Thus $Q(\mu_k, b_k, s)^m$ part of 5.10 leads to a Polya distribution with (m_{μ_k}) in place of μ and b_k/m in place of b. The probability distribution for the number of electrons after k stages is then given by

$$p_k(n) = \sum_m \left[\frac{m}{b_k}(1 + b_k\mu_k)^{-(m/b_k)} \left(\frac{b_k\mu_k}{1 + b_k\mu_k}\right)^n \cdot \frac{\Gamma\left(\frac{m}{b_k} + n\right)}{\Gamma\left(\frac{m}{b_k} + n\right)\Gamma(n+1)} p_{k-1}(m)\right] \tag{5.13}$$

Thus if one knows the initial photoelectron distribution $p(m)$, one can obtain the probability distribution for the number of electrons after k stages by repeated use of 5.13. In the case of single electron emission

$$p_0(n_1) = \begin{cases} 1, & if \quad n_1 = 1 \\ 0, & otherwise \end{cases} \tag{5.14}$$

It should be noted that 5.13 does not require each stage to be identical. The equation just derived for the output statistic will be used for the analysis of the MAPMT response in the following of the chapter.

5.3 The use of photomultipliers tube in Ring Imaging Cherenkov

RICH detectors based on vacuum photon detectors deserve a special mention for their great potentialities when a fast response is required for applications in high-luminosity experiments associated with spatial resolution finally allowing to combine both these informations. The commercially available MAPMTs have a performance that perfectly match the requirement to detect and measure the position of single photons and assure a much higher number of detected photons, thus allowing a significant increase of the separation power.
The shift of the photon detector bandwidth from the UV to the visible spectrum has played an extremely important role for the evolution of the RICH technique. The

shift of the photon detector energy detection towards the visible Cherenkov spectrum simplifies the detector construction allowing the use of common and cheaper materials, since the requirements on the optical properties of the media are less demanding in the visible than in the UV band. It allows a much wider choice of radiators (silica aerogel in particular) and improves the detector performance: larger factor of merit, as a consequence of the larger detector bandwidth, smaller angular resolution because of the reduced chromatic aberration, and higher rate capability.
The visible light sensitive photon detectors to be employed are based on vacuum photon sensor with a semi-transparent bi(tri)-alkali photocathode and subsequent charge amplification via secondary emission (PMTs and MAPMTs). Very recently new PMTs, characterised by unprecedented Quantum Efficiency (QE) have been commercialised by Hamamatsu. The new bi-alkali photocathode allows to reach QE values of $\sim 45\%$[127].
Experiments with RICH detectors equipped with PMTs have obviously been operated since the early times tanks to their availability, simplicity, robustness and high rate capability. An example is the experiment SELEX[128] at FERMILAB using almost 3000 PMTs, and more recently the experiments PHENIX[129] at RHIC-BNL, BABAR[130] at SLAC and HERMES[131] at DESY. Large arrays of PMTs are also largely employed in the astrophysics experiments as KAMIOKANDE[132] and AMANDA [133]. In the last decade multianode PMTs developed by Hamamatsu and Photonis, characterised by a finer granularity than *standard* PMTs for image reconstruction, were used in the experiment HERA-B [134] at DESY and from 2006 in COMPASS[84].
There are several reason that make MAPMTs very attractive for RICH detector applications tanks to several advantages: they are easy to use, robust and compact. They offer also the advantage of providing many channels with a single HV common power supply which helps to reduce the cost of the detector construction. Moreover the efficient system of electron multiplication provides an excellent signal-to-noise ratio and high gains thus alleviating any specific demand or constrain on the front-end readout electronics. The pushed time resolution of the photon detection system itself makes them suitable to be operated in a very crowded counting rate environment.
They present however severe limitations: they are expensive devices, a fact which prevents them to be used in the coverage of very wide surfaces, which is an intrinsic limitation for RICH counters when wide photodetection areas are employed.
A possible way to solve this problem has been exploited by the HERA-B RICH counter that used a two-lens demagnification system focusing the Cherenkov light onto the 18×18 mm^2 pad matrix. A lens system has been though also for LHCb in case of MAPMTs use instead of HPD. A similar system has been used in COMPASS for the upgrade of the RICH-1 detector, as described in 4.4.2.
The LHCb experiment is the first and, for the time being, the only one experiment

to use HPDs as RICH photon detector. Due to the fact that the desired momentum range for pion/kaon separation cannot be spanned by a single radiator, two focused RICH detectors with three radiators are employed. Photons are detected via an array of HPDs located on each side of the RICH detector. The large fraction of active area (82%) of the cross-focused HPDs, alleviates the need for a lens system when close-packing the devices. After successfully performing comprehensive tests on pre-series HPDs, the mass production has started and the tubes so far delivered are fully functional. The HPDs readout electronics, accounting to about 340000 channels totally for both counters, developed in 0.25 m CMOS IBM rad-hard technology (up to 30 kRad), is bump bonded to the silicon sensors and implemented in the vacuum envelopes. It will run at 40 MHz clock to be compatible with the LHC bunch-crossing frequency.

5.4 The multianode photomultiplier tubes for the upgrade of COMPASS RICH-1

5.4.1 History of Hamamatsu

Hamamatsu Photonics was established in 1953. In 1959 Hamamatsu marketed side-on photomultiplier tubes with a Sb-Cs photocathode, which have been widely used in spectroscopy. Hamamatsu also developed and marketed side-on photomultiplier tube with an Ag-Bi-O-Cs photocathode in 1962. This photocathode had higher sensitivity in the red region of spectrum than that of the Sb-Cs photocathode, making them best suited for spectroscopy in those days. Head-on photomultiplier tubes with an Sb-Cs photocathode were put on the market in 1965 while in 1969 photomultiplier tubes were equipped with a multi-alkali (Na-K-Cs-Sb) photocathode.
Then, in 1974 a new side-on photomultiplier tube that achieved much higher sensitivity in the red to near infrared region was produced. Since that time, Hamamatsu has continued to develop and produce a wide variety of photomultiplier tubes. The current product line ranges in size from the world's smallest 3/8-inch tubes to the world's largest 20-inch hemispherical tubes.

5.4.2 R7600-3 M16 MAPMT

Due to the stringent requirements for the RICH-1 upgrade project, among the whole set of PMT available the R7600-03-M16 type by Hamamatsu has been chosen to detect single photons at high rates, with fast response and in a wide photon wavelength range.

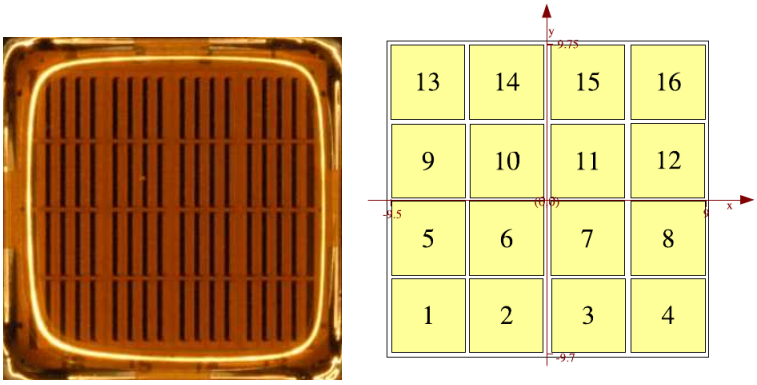

Figure 5.2: Left: front view of the MAPMT entrance window, the 4×4 anodic structure can be recognised. The thinner substructures are given by the dynodes. Right: coordinate system used to identify the 16 MAPMT anodes.

The R7600-3 M16 PMT[127] is Multi Anode PMT with bi-alkali photocathode. The 16 pixels (4mm × 4mm) are arranged on an 4×4 square grid. These pixels are separated from each other by a pitch of 0.26 mm. Focusing electrodes run over the pixels which guide the photoelectrons into the dynode structure.
The high current amplification and high S/N ratio of this particular photomultiplier tube is due to the use of a low-noise electron multiplier system which amplifies electrons by a cascade secondary emission process: each pixel has two identical dynode chains associated with it which terminate in a single anode pad. The electron multiplier for the R7600-3 M16 consists of 12 stages of dynodes. The metal channel dynode has a compact dynode construction which delivers high-speed response due to a space between each dynode stage that is much smaller than other types of conventional dynodes. The metal channel dynode is also ideal for position sensitive measurement.
The characteristics of this PMT type, provided by Hamamatsu, are summarised in table 5.1.
The MAPMTs delivered were asked to fulfil several requirements: No misalignment between the internal grid end the external case of the MAPMT, gain uniformity between the anodes better than 3 : 1, dark current 20 minutes after the power up lower than 2nA per channel. These checks are described in section 5.6.

Part Number	R7600-03-M16
Type	Square
Size	26mm
Active Diameter/L	18mm
Active Height	18mm
Minimum λ	300nm
Maximum λ	650nm
Peak Sensitivity	420nm
Cathode Radiant Sensitivity	72mA/W
Window	Borosilicate
Cathode Type	Bialkali
Cathode Luminous Sensitivity	80mA/lm
Cathode Blue Sensitivity Index	8.5
Anode Luminous Sensitivity	280A/lm
Gain (850 V)	3.50E+06
Dark current after 30 minutes	0.8nA
Rise Time	0.83ns
Transit Time	10.9ns
Transit Time Spread	0.3ns
Number of Dynodes	12
Number of Elements (X)	4
Number of Elements (Y)	4
Type	Pixilated(Pixilated or PSD)
Pixel Size	4 x 4(mm^2)
Pixel Pitch	0.26 (mm)

Table 5.1: Basic nominal characteristics of the R7600-M13 16-channel photomultiplier produced by Hamamatsu Photonics [135].

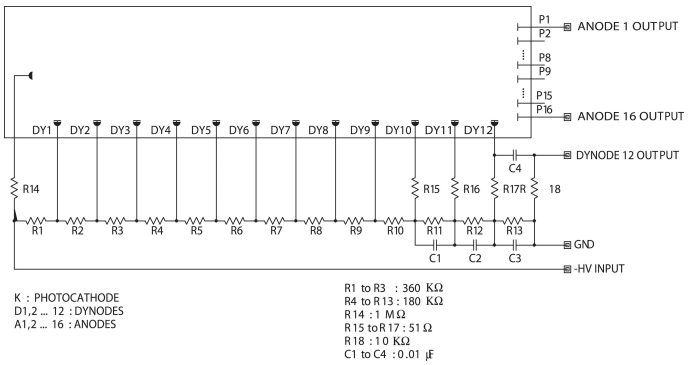

Figure 5.3: HV divider scheme adopted for the final installation of the R7600-M13 PMT.

5.5 The characterisation of the multianode photomultiplier tubes for the upgrade of COMPASS RICH-1

A complete study and characterisation of the MAPMTs behaviour and response is a mandatory step in order to fix several set-up variables like HV, noise threshold and to reach a accurate understanding of the response of the upgraded detector. For the large majorities of these characterisation studies, a few channel read out and data acquisition system with an architecture similar to the one used at the COMPASS experiment (see section 4.5) has been used in the Trieste INFN laboratories.

5.5.1 HV Divider

The interstage voltage for the dynodes for this specific photomultiplier tube is supplied by voltage-divider circuits consisting of series connected resistors. A schematic diagram of the adopted voltage-divider circuit is illustrated in figure 5.3. The final PCB board is non-standard since it has been produced to match specific geometrical requirements. The electric scheme based on the Hamamatsu specification has been used. There exist a relation between the incident light intensity and the output current of a photomultiplier tube obtained using a particular voltage-divider circuit: deviation from ideal linearity can occur. This is caused by an increase in dynode voltage due to the redistribution of the voltage loss between the last few stages, resulting in an apparent increase in sensitivity. As the input light intensity is increased, the anode output current begins to saturate near the value of the current flowing through the voltage divider. To verify that the voltage divider circuit for the power distribution to the MAPMT electrodes is able to ensure good efficiency of sin-

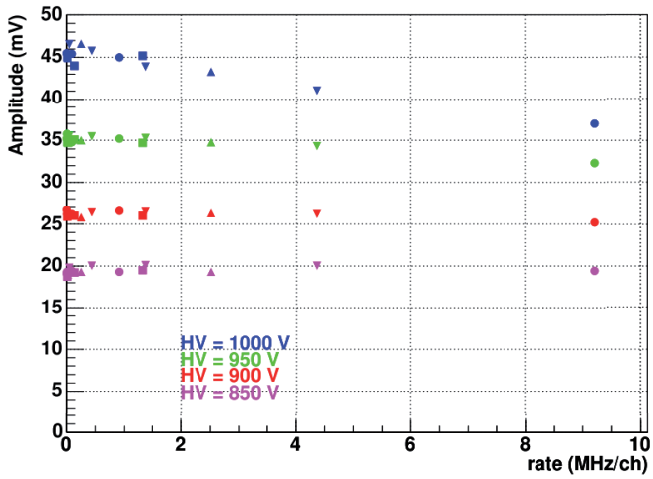

Figure 5.4: Signal amplitude as function of the photon rate (MHz) for different powering voltages of the MAPMT, no sensible signal reduction up to 5 MHz is detectable except for the highest HV value.

gle photo-electron detection also at high rates the standard configuration proposed by Hamamatsu for these MAPMTs[135] has been tested in laboratory and test beam studies. No MAPMT gain reduction is observed up to single photo-electron rates larger than 5 MHz per anode[136] as illustrated in figure 5.4, where the MAPMT signal amplitude is measured as function of the photon rate for different high voltages.

5.5.2 Magnetic Shielding

The photomultiplier tubes are extremely sensitive to magnetic fields and exhibit output variations even from very feeble fields. A special magnetic shield case has been designed specifically to protect the R7600-M13 photomultiplier tube from the influence of the SM1 magnet field: the fringe field intensity in the MAPMT region is at most 20 mT. In the COMPASS case Nikelated Armco, a soft iron material that has a high permeability has been chosen. The shielding structure, obtained as a compromise between the shielding effect and the weight of the device, results of two main building blocks, a squared rectangular case enclosing the MAPMT and an extra cylindrical structure which complete the closure of the magnetic field lines and acts also as lens holder. During the laboratory tests magnetic fields up to 40 mT have been generated via an Helmoltz coil[1] with an internal diameter of 26 cm, a total length 24 cm, providing a constant magnetic field in a region 20 cm

[1]courtesy of Prof. K. Kuroda

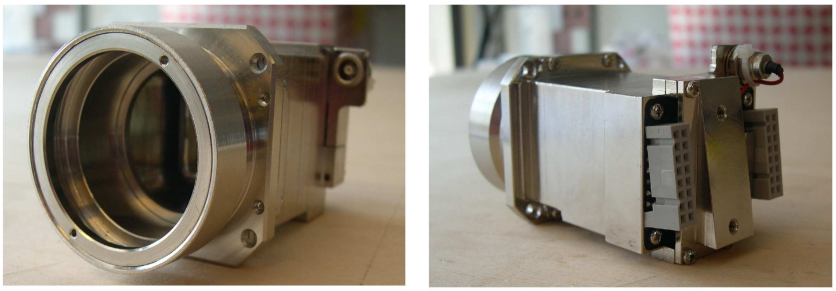

Figure 5.5: Left: frontal view of the magnetic shield, the cylindrical end-cap, working as a lens holder, used to complete the closing of the field line is clearly visible. Right: side back view of the shield case, the bleeder circuit and the analog output connection are housed on the same circuit fixed on the Armco case. The resulting structure is compact and robust.

long. It has been possible to test the magnetic field intensity within the shield case in different positions along its axis, for different values of the external field. The residual field measured in the central region, where the photomultiplier is installed, ranges between 0.5 (z=0 mm) to 2 mT (z=±2 mm) (see fig. 5.6), a value that ensures a stable output for the photomultiplier tube operating in proximity to the fringe magnetic field, as established by the studies described in section 5.5.3.

5.5.3 Threshold scan

The MAPMT type R7600-03-M16 is sensitive to magnetic fields: in presence of a non zero field a reduced response is observed, in principle due to the combination of two possible effects: (i) more photoelectrons do not enter the multiplication chain (about 70% are accepted when there is no magnetic field) and (ii) the gain is reduced. For the detection of single photons, effect (i) results in a net decrease of the detection efficiency, while effect (ii) can be tolerated, provided that the gain reduction is limited. In the COMPASS application, MAPMTs have to operate in a region with magnetic field up to 20 mT, with its main component parallel to the MAPMT axis, due to the fringing field of the open H-shaped spectrometer magnet placed a few metres upstream of the RICH-1 counter. The single photoelectron response of the MAPMT in presence of low magnetic field have been performed. The magnetic field has been generated with the Helmholtz coil previously described. The MAPMTs have been read out using the digital electronics system described in sec. 4.5. The characterisation studies have been performed illuminating the MAPMT photocathodes with light pulses attenuated so to provide single photoelectron conditions. To guarantee this condition the following quantity $\mu = \frac{N_{signals}}{N_{triggers}}$ (multiplicity is moni-

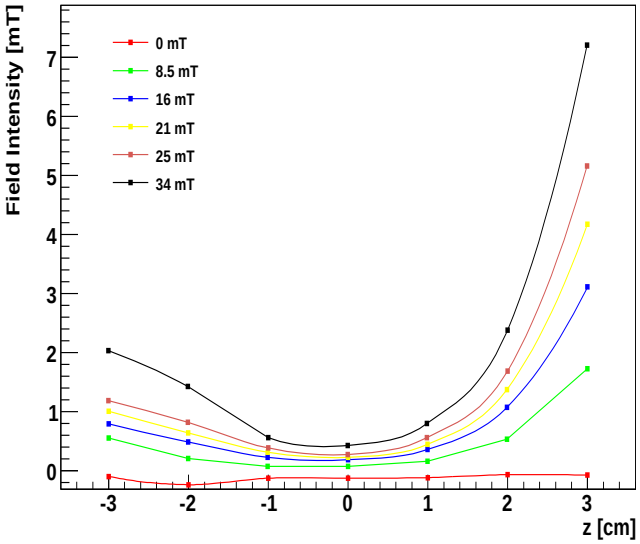

Figure 5.6: Magnetic field intensity inside the shield case, along the MAPMT axis measured with Hall probe as function of the longitudinal position, for different external magnetic field values. The nearly central position in the range [-1.8,0] cm is occupied by the MAPMT.

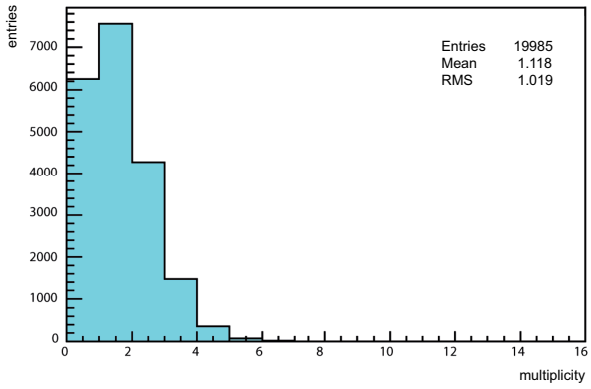

Figure 5.7: Multiplicity spectra of the detected photons. The distribution follows the Poissonian statistics.

tored during the whole test and an average value near 1 guarantee the probability to have more than a single photon converted at the same time by the same anode to be negligible. Typical multiplicity is shown in figure 5.7 which corresponds to the previously defined probability of 0.23%. The light pulses are provided by an commercial 470 nm LED powered with reversed bias, so to be able to obtain short pulses (typical pulse length: ∼20 ns), the same signal used to drive the LED is also the trigger signal. Threshold curves, as those shown in fig. 5.8, are taken in different field conditions: the plateau value, normalised to the value obtained with no magnetic field, provides the relative efficiency variation. The error associated to the measure is just the statistical propagated error on the number of detected photons. The x-axis scale correspond to the ADC channels of the DAC: each channel is 0.4 fC. Repeated measurements with no magnetic field indicate that the overall stability of the results obtained with this method is at a level better than 3%. The threshold scan consists of taking 20K triggers for each of the selected threshold values. The resulting curve will be called *threshold curve* (see fig. 5.8). As it can be noticed from the curve tree different zones can be easily recognised: a first zone of noise at low threshold values till ∼2fC characterised by an exponential shape; a subsequent cross talk region extending over the range between 8 and 16 fC, and the plateau region corresponding to the range in which variations of the threshold does not affect the multiplicity values. The stability response region of the system is defined as the one where the point of maximum multiplicity μ differs less than 3% from its minimum one, in this specific case between 16 and 80 fC.
Due to the pretty simple light source setup several test have been performed to check the stability in time of the system led+MAPMT before starting the measurements with magnetic field: to avoid biasing the result the overall system stability has been

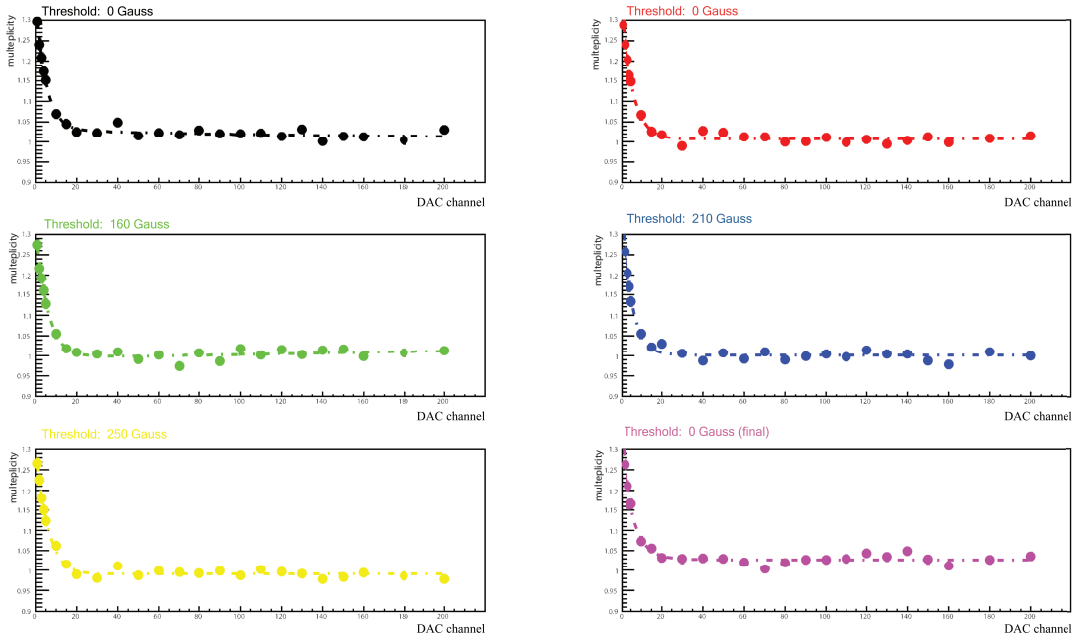

Figure 5.8: Threshold curves for one of the 16 anodes of a MAPMT in different magnetic field conditions. The channel multiplicity is plotted versus threshold setting in DAC units (200 units correspond to 90 fC). The illumination conditions are constant during the measurement. Different colours correspond to different threshold scans for different field values: black 0 mT, red 8.5 mT, green 16 mT, blue 21 mT, yellow 25 mT, pink 0 mT. The stability scan curves illustrate a reduction for the average multiplicity with the magnetic field increase.

kept under continuous monitoring repeating the null field threshold curve at the end of the set of measurement and detecting possible deviation from the single photon emission configuration via the average multiplicity results (see as example first and last curve of fig. 5.8). After the measurement with null field the threshold scan measure has been repeated with different field values: 8.5,16,21,25 mT. The result is shown in figure 5.8. From the results in presence of the magnetic field it is possible to define a stability region (between 16 and 80 fC) where no multiplicity reduction is observable as for the null magnetic field value for all the tested values of the magnetic field at variance with the result obtained with the MAPMT not shielded[137].

It has been seen that the pixels in a row exhibit a very similar response variation in magnetic field: in fig. 5.9 the response from the pixel of a same column are averaged, the response averaged over the whole set of 16 pixels of a MAPMT is also shown. The plot in fig. 5.9 (a) clearly indicates a drastic decrease of the efficiency averaged over the whole set of 16 pixels outside the magnetic field range ± 2 mT; in

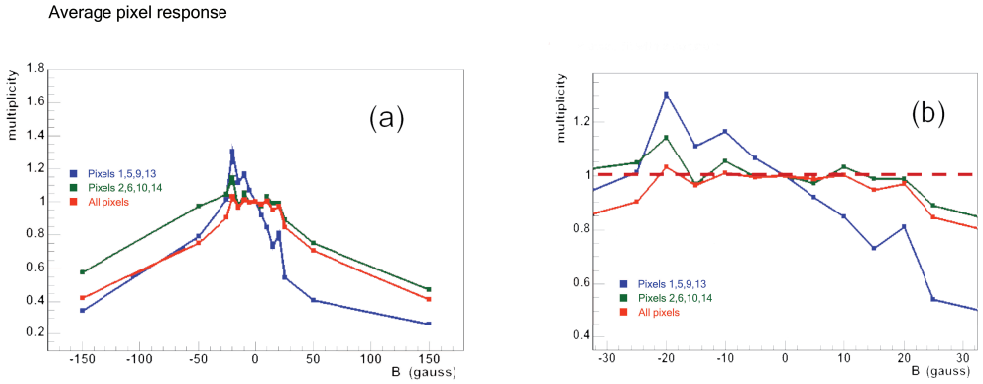

Figure 5.9: Multiplicity response of MAPMT pixels versus magnetic field, averaged for different pixel groups: a column of external pixels, namely pixels 1, 5, 9, and 13; a column of internal pixels, namely pixels 2,6, 10, 14; all 16 pixels. The magnetic field is parallel to the MAPMT axis and oriented from the photocathode towards the anodes. The plot in (b) is a zoom of the central portion of the plot in (a).

fig. 5.9 (b) a zoom of the central portion of the same plot is shown: also for the pixels of one of the two central columns (pixels 2, 6, 10 and 14) the efficiency is constant in the range -2 mT to +2 mT, while for the external column (pixels 1, 5, 9 and 13) there is an efficiency increase between -2 mT and zero field and a corresponding decrease between zero field and +2 mT. A similar behaviour is seen for the other two columns, provided that the magnetic field orientation is reversed. As example figure 5.10 illustrates the reduction of efficiency for the two external columns of pixels when the magnetic field is reversed. In the range -2 mT to +2 mT the effect of the magnetic field is too feeble to modify the acceptance of the MAPMT multiplication chains, in particular in the external pixel columns, with a substantial constancy of the global efficiency. Outside the region ±2 mT, there is a net reduction of the acceptance of the multiplication chain resulting in an important reduction of the single photoelectron detection efficiency. In our application we can tolerate a small acceptance shift, caused by the presence of the magnetic field, but not an efficiency decrease: the MAPMT magnetic shielding must ensure to expose the MAPMT at a magnetic field with intensity below 2 mT as guaranteed by the individual soft iron boxes used to enclose the MAPMTs.

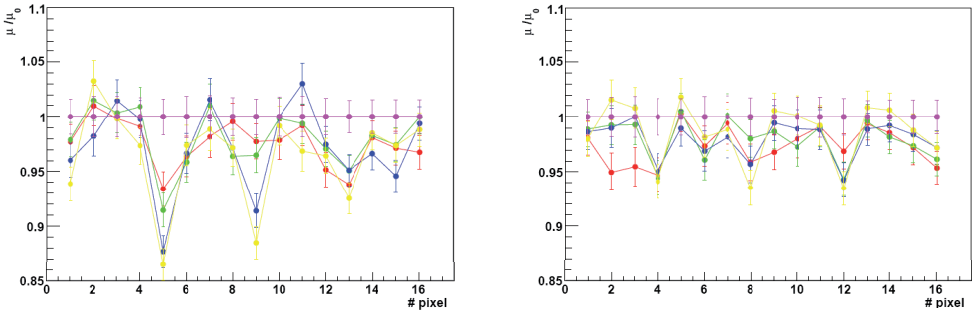

Figure 5.10: Left: ratio of the curves in figure 5.8 normalised to the multiplicity value with null field as function of the pixel number. A clear multiplicity reduction effect is clearly visible for pixel 1,5,9,13. Right: ratio of the curves as in figure 5.8 normalised to the multiplicity value with null field as function of the pixel number but with opposite $\vec{B}$ field direction. A multiplicity reduction effect is visible for pixel 4,8,12,16. Field values are: red 8.5 mT, green 16 mT, blue 21 mT, yellow 25 mT, pink 0 mT.

5.5.4 Spatial Uniformity

Although the focusing electrodes of a photomultiplier tube are designed so that electrons emitted from the photocathode or dynodes are collected efficiently by the first or following dynodes, some electrons may deviate from their desired trajectories causing lower collection efficiency. The collection efficiency varies with the position on the photocathode from which the photoelectrons are emitted and influences the spatial uniformity of a photomultiplier tube. The spatial uniformity is also determined by the photocathode surface uniformity. A dedicated test has been performed to scan the anodic MAPMT surface both in horizontal (x) and vertical (y) directions. To perform the test a halogen lamp emitting in the wavelength range between 310 and 150 nm has been used. Emitted light is guided to the MAPMT surface by an optical fibre and collimated via a pin hole of 100μm. The distance from the surface is chosen in order to have one single anode illuminated. Light intensity is adjusted to be in single photoelectron configuration via the use of optical filters. The average multiplicity is $\mu = 0.03$ corresponding to a probability of 0.04% of detecting two photons in a single pulse. The light spot is moved in x or y direction using a 2-axis stepping motor system which allows 1μm resolution. The MAPMT is placed, as in the previously described tests, inside the Helmotz coils but without the magnetic shield.
The measurement has been done first without magnetic field and then generating a 1 mT field.

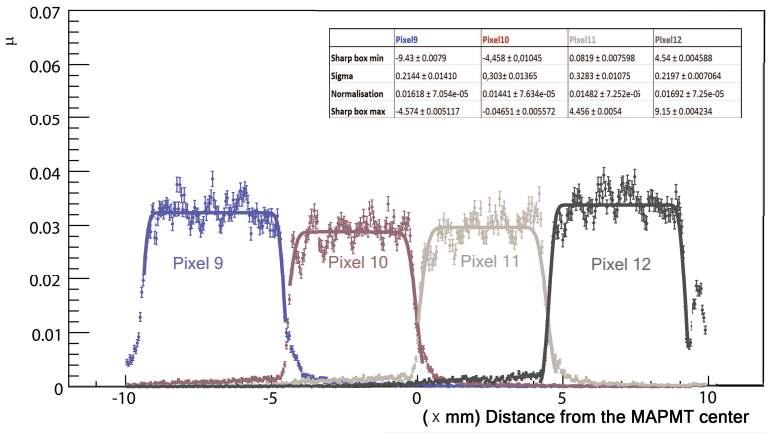

Figure 5.11: Spatial scan of 0.05 mm step of the MAPMT central raw (pixel 9,10,11,12). Different colours correspond to the response of different channels: blue:pixel 9, red:pixel 10, light gray: pixel 11, dark Gray: pixel 12.

The first step has been the measurement of the light source dimension. This has been performed applying an opaque slit of known width (1.12 mm) in vertical position at the centre of an anodic column of the MAPMT and scanning horizontally the surface with 0.05 mm step detecting the average multiplicity for 20k events. The output curve will be fitted by the convolution of a "box" function parameterising the slit and a Gaussian function parameterising the light intensity distribution assumed Gaussian. The $Box(x)$ function is equal to 0 outside its limits (x_{min}, x_{max}), the Gaussian function is characterised by its standard deviation. The result of the fit gives: $\sigma = 0.056 \pm 0.003$ mm and $slit = 1.135 \pm 0.004$ mm. The last values comes as a confirmation of reliability of the fit. The horizontal scanning has been performed sampling the anodes number 9,10,11,12. The scan range has been extended over the -9mm to 9mm active surface range as given by the Hamamatsu data-sheet. The scanning step applied is 0.05 mm. The result is illustrated in figure 5.11 in which the response on the 4 MAPMT anodes is visible. The tail visible at low multiplicity values is related to a small tilt in the positioning of the optical fibre with respect to the MAPMT surface. The multiplicity peak on the very left is due to light reflected by the external metallic surface on the MAPMT box[138]. The regular pattern, observable as oscillations of the multiplicity value for each anode is due the the absorption of electrons from the metallic wires, which focalises the photoelectrons onto the first stage dynode. Moreover the average multiplicity for the central pixels (9,12) is lower that the external one. For each data set, corresponding to a pixel, the curve is fitted with function which is also in this case a convolution of a box and

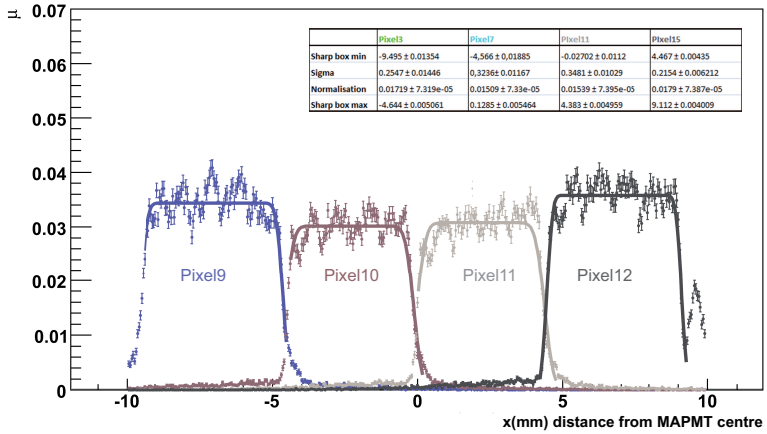

Figure 5.12: Spatial scan of 0.05 mm step of the MAPMT central raw (pixel 9,10,11,12) with a magnetic field of 1 mT. Different colours correspond to the response of different channels: blue:pixel 9, red:pixel 10, light gray: pixel 11, dark gray: pixel 12.

a Gaussian. The results from the fit are in table 5.2: pixel 10 and 11 have a 10% greater active surface respect to the Hamamatsu detasheet, pixels 9 and 12 have a even greater active surface with a more defined edge shape. The behaviour can be easily explained assuming a good electric field collection efficiency of the photons converted near the edge of the pixel. The second step for the complete characterisation of the horizontal scan consisted in repeating the same measurements in presence of a magnetic field of 1mT intensity along the MAPMT axis.The complete setup remains so unchanged. From the result of the threshold scan test in presence of the magnetic field a systematic shift of the pixel position is expected. This behaviour is in fact supported by figure 5.12. The pixel dimension extracted from the fit is unchanged while all the centres are shifted of 0.08 mm towards the right side.

To evaluate the behaviour of the MAPMT along the vertical (y) axis the pixel column (3,7,11,15) has been sampled. The fibre is centred horizontally respect the pixel area. Since the sampling direction is along the focalisation wires no oscillations of the multiplicity inside the pixel is expected. No horizontal shift due to the magnetic field should be observed. Moreover from a visual inspection of the MAPMT surface the vertical separation of the pixels is wider that the horizontal one. The result of the test is illustrated in figure 5.13. The long multiplicity tails extending towards the right side of the figure are given by a small tilt of the optical fibre which is not exactly perpendicular to the MAPMT surface[138]. The edges of pixel 3 and 15 present a smoother slope, anyhow in a range outside the nominal active surface

B=0mT					B=1mT						
pixel	min	max	width	σ	min	max	width	σ	Δwidth	Δ min	Δmax
9	-9.43	-4.57	4.86	0.21	-9.5	-4.64	4.85	0.25	-0.01	-0.06	-0.07
10	-4.46	-0.05	4.41	0.3	-4.57	-0.13	4.44	0.32	0.03	-0.11	-0.08
11	0.08	4.46	4.37	0.33	-0.03	4.38	4.41	0.35	0.04	-0.11	-0.07
12	4.54	9.15	4.61	0.22	4.47	9.11	4.65	0.22	0.04	-0.07	-0.04

Table 5.2: Fit parameter of the central row and resulting pixel dimension, without any magnetic field and in presence of a 1 mT field along the MAPMT axis On the right side the corresponding pixel variation is reported, and the movement of the pixel due to the field. Measured values are in mm, the associated error is ± 0.01.

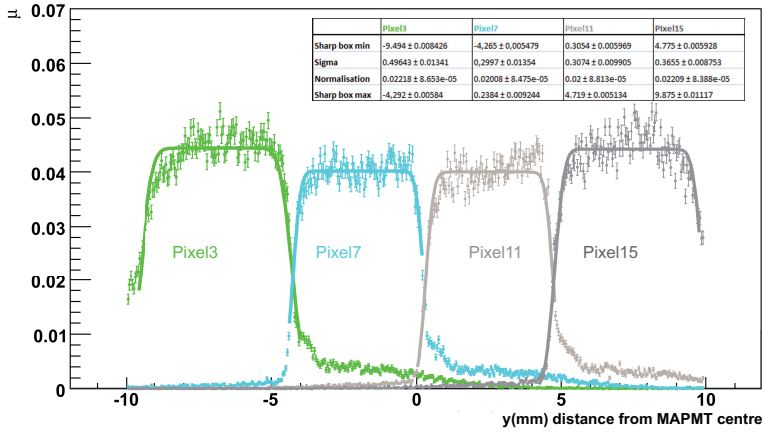

Figure 5.13: Spatial scan of 0.05 mm step of the MAPMT column made by pixel 3,7,11,15. Different colours correspond to the response of different channels: green:pixel 3, cyan:pixel 7, light gray: pixel 11, dark gray: pixel 15.

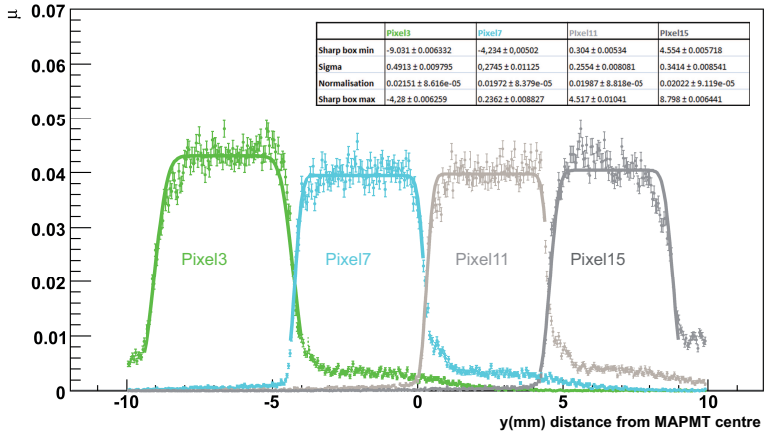

Figure 5.14: Spatial scan of 0.05 mm step of the MAPMT column made by pixel 3,7,11,15 with a magnetic field of 1 mT. Different colours correspond to the response of different channels: green:pixel 3, cyan:pixel 7, light gray: pixel 11, dark gray: pixel 15.

of the MAPMT. The regular pattern of oscillation has disappeared as expected, the effective active length of pixels 3 and 15 is wider than the one of the central pixels and they present grater multiplicity. Results are reported in table 5.3. The external pixels presents higher values of σ (0.46 mm pixel 3, 0.36 mm pixel 15 while 0.30 for pixels 7,11). There is compatibility between the result of the fit in the horizontal case and vertical case only for the central pixels while for the external ones the behaviour is opposite.
The test has been repeated also in this case in presence of the same magnetic field (1mT). As expected (see fig. 5.14) there is no effect of the field for the vertical structure if the central pixels are taken into account. For the external pixel, namely 3 and 15 the net result of the presence of the field is a focalising effect resulting in a reduction of 0.45 mm and 0.86 mm of the effective vertical size of the pixel. Fit parameter are reported in table 5.3.

5.5.5 Amplitude spectrum

A detailed analysis of the analog output of a MAPMT anode in single photo-electron mode shows several components. A rich set of spectra is available as a by-product of the MAPMT quality control procedure described in section 5.7.
A typical amplitude spectrum, obtained with a supply voltage of 900 Volt is shown in figure 5.15: at very small amplitudes, the tail of the pedestal signal distribution is visible, mainly due to noise signals, which is followed by two signal peaks. The signal peak at larger amplitudes corresponds to the single photoelectrons that have been multiplied by the whole 12-dynode chain of the MAPMT while the peak at smaller amplitude is contributed both by photons converted at the first dynode or by photoelectrons from the photocathodes directly impinging on the second dynode of the chain. The typical mean amplitude value of the two peaks at 900 V is $\sim 8 \times 10^5$ and $\sim 4 \times 10^6$ electrons respectively. The population of the first peak is always an important fraction of the total population. A description of the fit algorithm is given in section 5.5.6. The detection of both the components of the signal is of the utmost importance for this particular type of application. This task is possible thanks to the high sensitivity electronic MAD4-Chip adopted. As also small amplitude can be detected, it is possible to recover for the different gain of the signals forming the two peaks of the amplitude spectra to recover for the spread in gain among the MAPMT channels (the 16 anodes of each MAPMT have 16 independent dynodic structures).

This is demonstrated in fig. 5.16. Left figure is the normalised integral of the global fit shown in fig. 5.15 versus the lower limit of the integration range, which corresponds to the threshold setting of the digital electronics. In fig. 5.16 right, a zoom of the first portion of the integral spectrum is given and the range of the threshold adjustment is also shown. The typical threshold setting is about 40 fC. This value assures the rejection of the pedestal as well as of the cross-talk signals

B=0mT					B=1mt						
pixel	min	max	width	σ	min	max	width	σ	Δwidth	Δ min	Δmax
3	-9.49	-4.29	5.2	0.46	-9.03	-4.28	4.75	0.49	-0.45	0.46	0.01
7	-4.27	0.24	4.5	0.3	-4.23	0.24	4.47	0.27	-0.03	0.03	0
11	0.31	4.72	4.41	0.31	0.3	4.52	4.21	0.26	-0.2	0	-0.2
15	4.78	9.88	5.1	0.37	4.55	8.8	4.24	0.34	-0.86	-0.22	-1.08

Table 5.3: Fit parameter of the central column and resulting pixel dimension, without any magnetic field and in presence of a 1 mT field along the MAPMT axis On the right side the corresponding pixel variation is reported, and the movement of the pixel due to the field. Measured values are in mm, the associated error id ± 0.01.

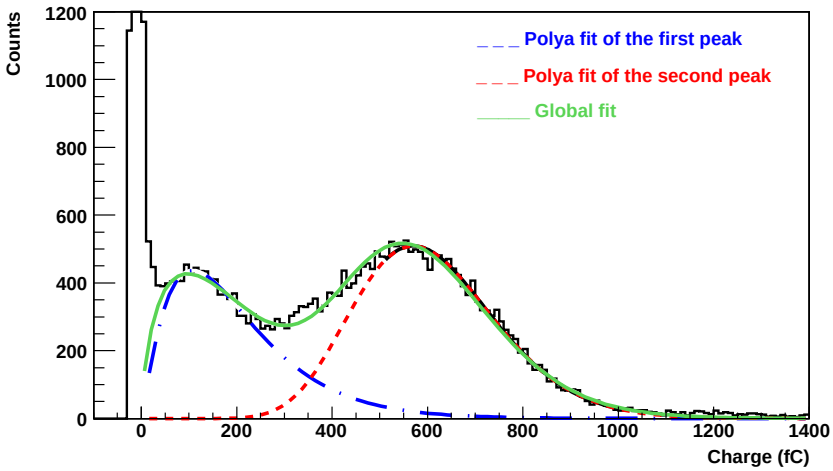

Figure 5.15: Typical amplitude spectrum obtained with a MAPMT R7600-03-M16 by Hamamatsu at 900 V illuminating the photo-cathode in single photo-electron mode. The noise pedestal is visible, as well as two signal peaks, the lowest one corresponding to photo-electrons skipping a multiplication stage. The dashed curves are individual fits of the two peaks with Polya functions; the solid curve is a global fit with a sum of two Polya functions.

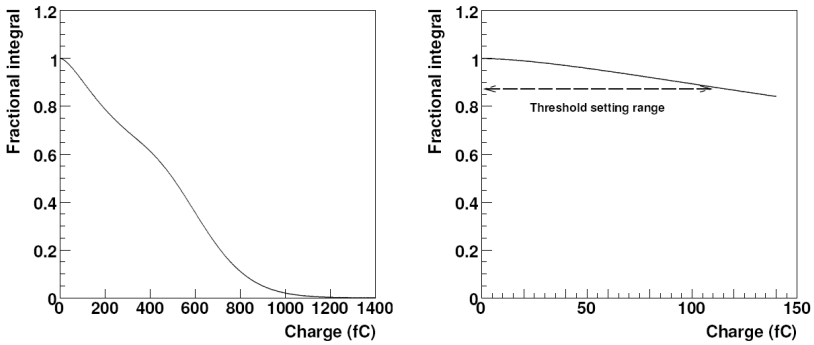

Figure 5.16: Left: Normalised integral of the function obtained with the global fit of the amplitude spectrum of fig. 5.15 versus the starting point of the integration range. Right Zoom of the integral spectrum of the left figure; the region of the front-end threshold range is indicated.

with extremely limited efficiency losses ($\sim 10\%$).

5.5.6 The fitting algorithm for the double peak Polya distribution.

As explained in section 5.2.1 the spectrum distribution for a PMT follow the Polya statistic. Due to the shape of our MAPMT spectrum which presents a double peak structure a double Polya fit has been implemented. The task to obtain a stable automated system has revealed harder than expected due to the extreme sensitivity of the minimisation routine to the fit parameters starting point. The necessity of an automated routine is due the high number of fits to be performed: nearly 600 MAPMT with 16 channels each for two different wavelength configurations times 5 different HV working points leads to ~ 96000 fits. Several test have been performed analysing the behaviour of the fit upon the different starting parameters and output fitted values of the algorithm. The optimum procedure has been found in a multi step fit algorithm with several cuts on the fitted parameters to guarantee the fit goodness. The preliminary step consists in fitting the tail of the noise spectrum with a Gaussian distribution to acquire the parameters of the noise distribution, which are used, if necessary, to modify the fit range. Due to the high stability of the Gaussian fit the following step consists in fitting the two ADC amplitude with two independent Gaussian distributions whose parameters are stored and are used as starting point for the fit with two independent Polya functions as eq. 5.15.

$$Polya(x, A, \theta, \bar{n}, x_0) = A \cdot \frac{(\theta+1)^{(\theta+1)}}{\bar{n} \cdot \Gamma(\theta+1)} \cdot \left(\frac{(x-x_0)}{\bar{n}}\right)^{\theta} \cdot e^{-(\theta+1)\cdot\frac{(x-x_0)}{\bar{n}}} \qquad (5.15)$$

Finally the output parameters of the independent fit of the two distributions are used as starting point for the fitting function of the double peak distribution. All the parameters with the subscript $1s$ or $2s$ refer respectively to the fit of the first and second peak of the amplitude spectra with the two independent distribution functions, while the subscript $g1$ or $g2$ refer to the fit of the first and second peak of the ADC spectra with a single distribution function (global fit). Before storing the final result a final check on the fit output values is performed to exclude fits that could be not reliable. In particular a fit is accepted if:

1 the mean value of the Gaussian fitted noise is ≥ 2 and ≤ 3 ADC channels;

2 the σ value of the Gaussian fitted noise is ≤ 0.20 and ≥ 0.06 ADC channels;

3 χ^2_{1s} is ≤ 3;

4 χ^2_{2s} is ≤ 3;

5 χ^2 of the global fit is ≤ 3;

6 θ_{1s} is ≥ 0.1;

7 $\theta_{g1}$is ≥ 0.3;

8 the Ratio $R = A_{g2}/A_{g1}$ is >0 and ≤ 20.

Where A_i is the population of the corresponding Polya, and θ is the parameter in equation 5.15. All the extracted quantities (fitted values) and their correlation with others have been plotted before and after applying the previous set of cuts in order to estimate the efficiency of the method and to observe if, in case of possible anomalous behaviour of the fit, the result is rejected. The whole procedure has been repeated for the 16 anodes and for all the HV settings and for the two wavelength $\lambda = 360,\ 480\ m$ of the light source. As example only figures for a single anode and a single set of HV (910 V) and λ (360 nm) will be illustrated.
The effect of the cuts is checked and illustrated in figure 5.17: each point of the histograms is the percentage of accepted events applying the corresponding cut described above. In this case the cut number 7 is the most restrictive since is

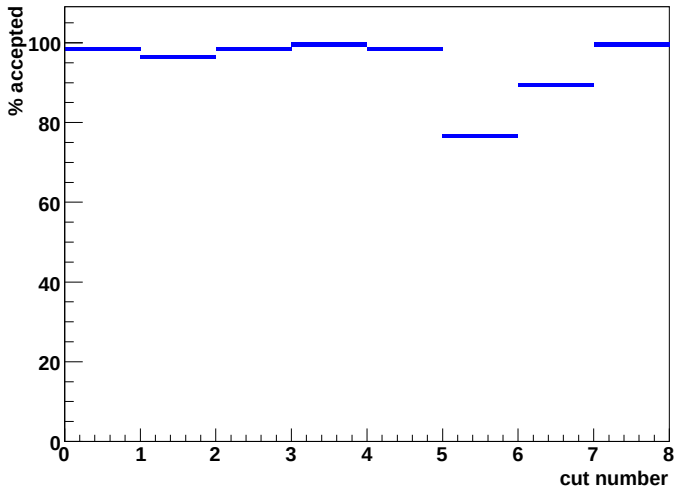

Figure 5.17: Impact of the cut number in rejecting a fit as function of the cut applied. Each entries stands for the percentage of accepted fits for the corresponding cut (x entry) described before.

rejecting $\sim 20\%$ of the fits. The monitor, while fine tuning the parameters for the cut has been used to check the sensitivity of the cut itself on the rejection of a bad fit leading finally to the previously selected values of the cuts, later to check if

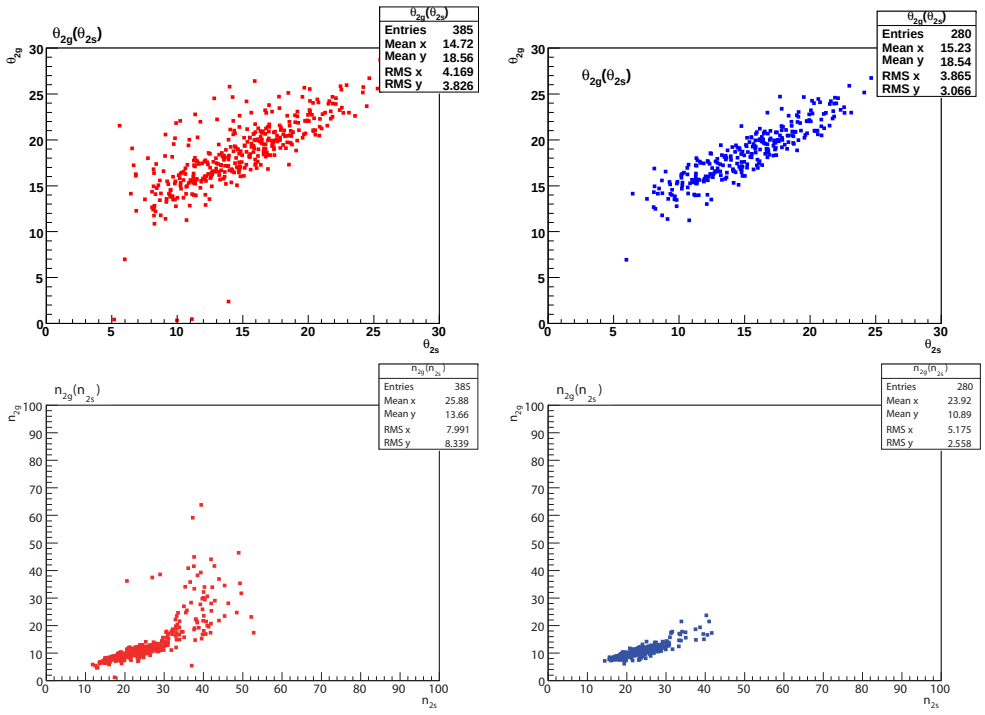

Figure 5.18: Top: correlation plot of $\theta_{2g}(\theta_{2s})$. On the right the distribution before the cuts, on the left the distribution after the cuts. The RMS of the distribution is reduced thanks to the rejection of badly fitted histogram. Bottom: correlation plot of $n_{2g}(n_{2s})$. On the right the distribution before the cut, on the left the distribution after the cut.

any anomalous behaviour of the procedure was present. The impact of this set of cuts, as already mentioned, is controlled by a set of correlation plots, in particular the following correlation plots were produced: $\chi^2_{1s}(\chi^2_{2s})$, $\theta_{1g}(\theta_{1s})$, $A_{1g}(A_{1s})$, $n_{1g}(n_{1s})$, $\theta_{2g}(\theta_{2s})$, $A_{2g}(A_{2s})$, $n_{2g}(n_{2s})$, $A_{1s}(n_{1s})$, $A_{1g}(n_{1g})$, $\theta_{1s}(A_{1s})$, $\theta_{1s}(A_{1s})$, $n_{2g}(n_{2s})$. Figure 5.18 illustrates the effect of the cut set just for two of the previously mentioned correlation plots. The plots of the rejected fits show the reason of the fit rejection, which is mainly due to the fact the parameters used as starting point for the global fit are wrongly computed; in few cases the histograms was empty. The final result has been an extremely reliable, quite flexible, procedure with the drawback of an efficiency ranging from $\sim 65 \div 85\%$. This stability of the procedure is illustrated as example in figure 5.19 where the spectra of all the 16 anodes of a MAPMT are fitted (yellow curve) with the global Polya function.
The parameters distribution of the Polya fit can be used to investigate the behaviour of the MAPMT globally or anode by anode.

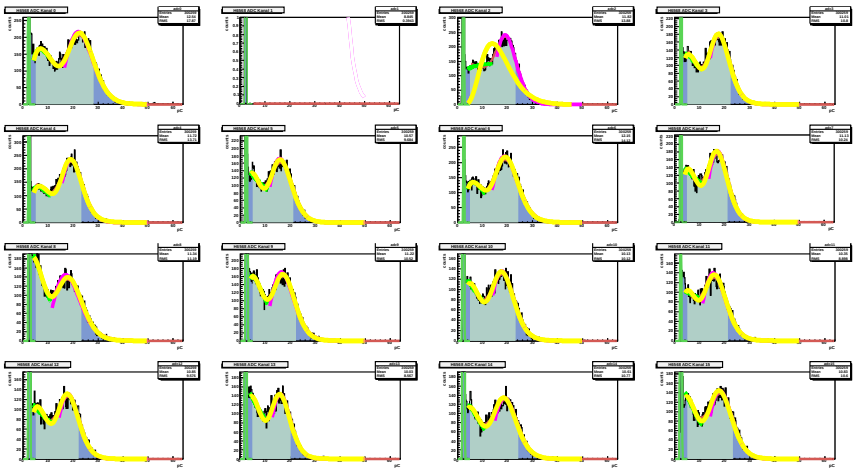

Figure 5.19: A full spectrum view for all the 16 anodes of a MAPMT with superimposed the fitting curves. In this particular case the second anode is not providing any signal.

One of the most interesting quantity is the ratio A_{g2}/A_{g1} for each PMT anode and of course the mean value for all the anodes as function of the HV and of the wavelength. This quantity is sensitive to the signal sharing between electrons that are converted on the photocathode or on the inner metal structure of the MAPMT and give rise to the firs peak in the distribution. Analysing the figure in 5.20 it is clear this phenomenon depends on the specific anode, and this consideration is true for all the HV values tested, since the shape of the curve is the same for all the HV values. There is also a clear dependence on the HV applied. This is visible in the same figure, on the bottom, where the ratio of the two population integrated over the anode number is plotted. Going to higher values of the voltage applied means increasing the gain but also increasing the focalising power of the MAPMT wire grid placed just below the photocathode surface, so that the probability for a photo-electron to escape a multiplication stage should be lower. The effect is there for the first three points, then the curve becomes flat. It has already been mentioned that two are the possible sources of the double peaked spectra: the conversion of a photon after the photocathode window by the inner metal structure of the MAPMT or photoelectron skipping a multiplication stage. The last hypothesis is supported by the HV dependence of the ratio A_{g2}/A_{g1} just illustrated, the population of the first peak decreases with the increase of the HV meaning less and less electrons escape. In principle it should also be possible to check if there is any dependence on the wavelength, or in other words on the quantum efficiency of the photoconverter

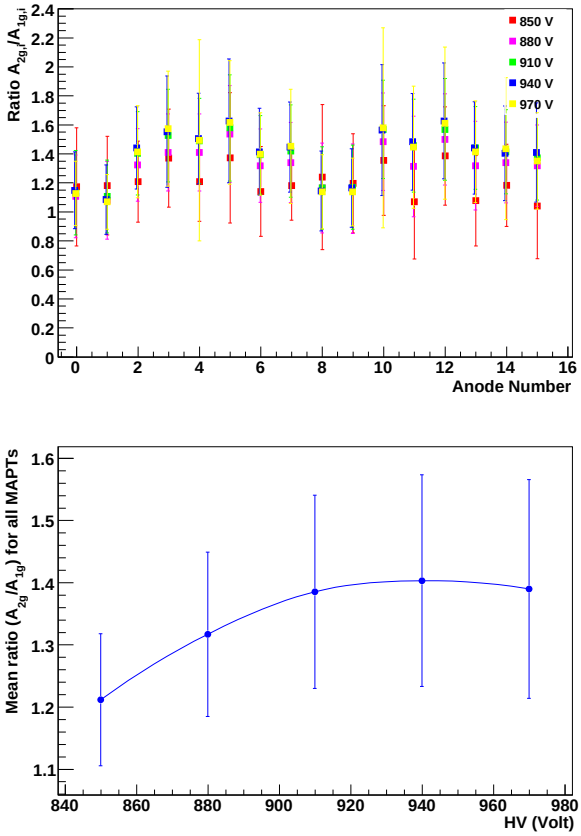

Figure 5.20: Top: A_{g2}/A_{g1} as function of the HV applied and of the anode number. Bottom: A_{g2}/A_{g1} integrated over the anode number($\sim$ 500 MAPMTs, statistical error only).

material, by comparing the the plot of A_{g2}/A_{g1} for the two different wavelength. No dependence from the led wavelength can be observed as shown id figure 5.21. Naïvely in case of $\lambda = 480$nm a lower QE of the photocathode would result in a greater number of photons that can be converted by the metal and so to lower value of A_{g2}/A_{g1} which is observed (excluding the first point at 850 V). So also this phenomenon could contribute to the shaping the ADC spectrum. Unfortunately the LEDs used are commercial ones, and their characteristic spectrum is not known enough in detail to draw a final conclusion.

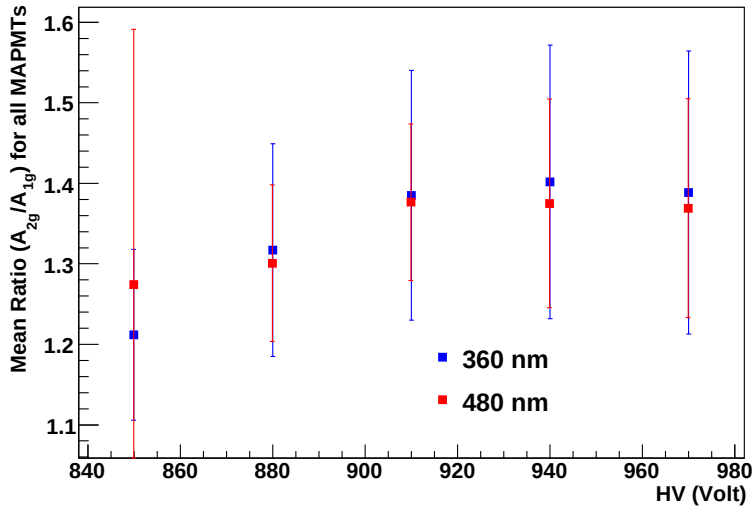

Figure 5.21: Left: A_{g2}/A_{g1} as function of the HV applied for the two different light wavelengths: 360 nm blue, 480 nm red.

5.6 MAPMT uniformity characteristics

Each of the MAPMT ordered to Hamamatsu is identified by its unique serial number. It is also accompanied by a data-sheet in which several characteristics quantities, as measured by Hamamatsu laboratories are reported, in particular:

Relative spatial uniformity.

Cathode luminous sensitivity ^{74}W lamp 2856 K.

Cathode luminous sensitivity with corning CS 5-58 filter ^{74}W lamp 2856 K.

Anode luminous sensitivity ^{74}W lamp 2856 K.

Dark Current as measured at 800 Volt.

Gain measured at 800 V.

The very first information about the photomultipliers quality is provided by analysing the data from the individual data-sheet accompanying each MAPMT.
Spatial uniformity has been introduced in section 5.5.4, it is defined as the variation of the output signal with respect to the photocathode position. Anode output uniformity is thought to be the product of the photocathode uniformity and the

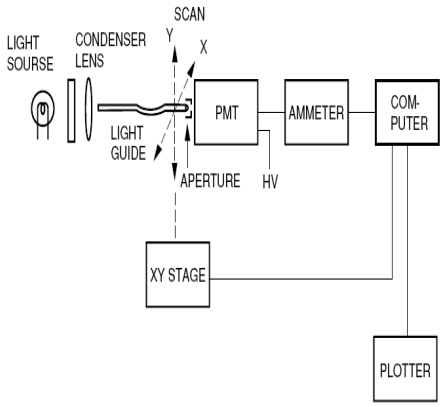

Figure 5.22: Schematic diagram for spatial uniformity measurement.

electron multiplier (dynode section) uniformity. In general, both photocathode uniformity and anode uniformity deteriorate as the incident light shifts to a longer wavelength, and especially as it approaches the long-wavelength limit. This is because the cathode sensitivity near the long-wavelength limit greatly depends on the surface conditions of the photocathode and thus fluctuations increase. To measure spatial uniformity, a light spot is scanned in two-dimensions over the photocathode of a photomultiplier tube and the variation in output current is graphically displayed. Figure 5.22 shows a schematic diagram for the spatial uniformity measurement. Hamamatsu data-sheet reports only the spatial uniformity for the 16 anodes of each PMT relative to an anode giving the maximum value, which is defined as the reference: this anode has the uniformity value equal to 100% by definition. Figure 5.23 is obtained taking for each PMT the ratio of the minimum among the 16 PMT anodes relative spatial uniformity with the reference one. It illustrates the relative anodic uniformity for the PMT set. Clearly all PMT satisfy the uniformity requirement 3:1 except for one that has been replaced. The distribution of the spatial uniformity, plotted anode by anode, presents a interesting behaviour. First it is possible to see how all the corner anodes present a clear peak in the distribution at 100% suggesting a wider effective area of these pixels. The effect is less evident for the upper and lower rows of pixels (2,3 and 14,15) and it results mainly in a shift of the distribution toward higher values rather than a peak. While the lateral pixel 5,9 and 8,12 are characterised by a quite symmetric narrow Gaussian distribution, the four central pixels have the most spread distribution of values. This is more evident, if the entries when a 100% spatial uniformity value is found is plotted against the pixel number (see fig. 5.25). **Cathode luminous sensitivity** is the photoelectric current from the photocathode per incident light flux (10^{-5} to 10^{-2} lumens) from a tungsten filament lamp operated at a distribution temperature of

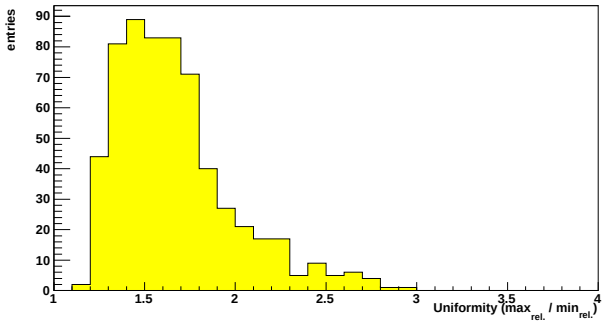

Figure 5.23: Relative uniformity distribution (all anodes) for the Hamamatsu PMT as derived from the data-sheets.

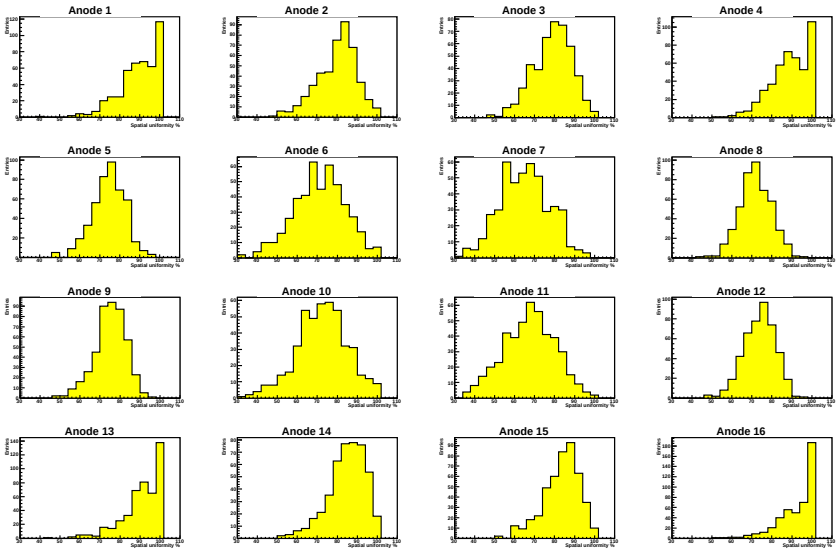

Figure 5.24: Relative uniformity distribution (all anodes) for the Hamamatsu PMT as derived from the data-sheets data.

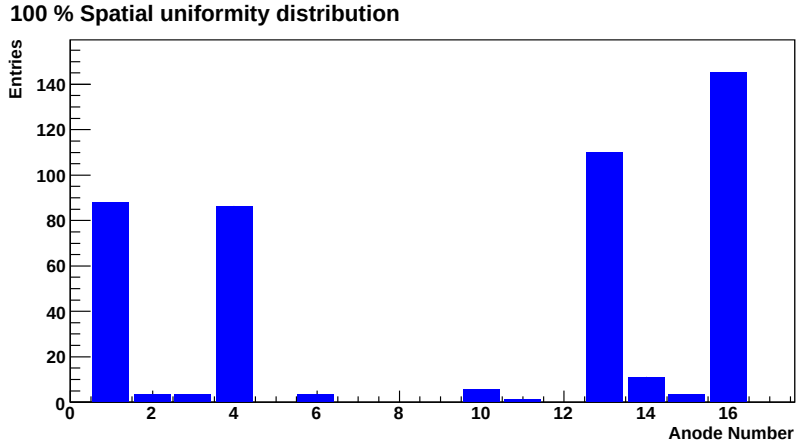

Figure 5.25: 100% relative uniformity distribution for the Hamamatsu PMT as derived from the data-sheets data.

2856K. The cathode luminous sensitivity is expressed in $\mu A/lm$ (microamperes per lumen). Typical values range around 80 $\mu A/lm$, as illustrated by figure 5.26. The minimum value accepted to fulfil our requirements is 60 $\mu A/lm$ which is satisfied by all the MAPMT batch. A further measurement for the cathode luminous sensitivity is performed interposing a Corning filter between the MAPMT and the light source shifting the light wavelength to 400 nm. In this case the value for a MAPMT not to be rejected is 6.5 $\mu A/lm$ condition satisfied also in this case (see fig. 5.26). The **anode luminous sensitivity** is the anode output current amplified by the secondary emission process per incident light flux (10^{-5} to 10^{-2} lumens) on the photocathode, it is expressed in A/lm (amperes per lumen). The minimum allowed value is set to 70 A/lm, condition well satisfied by the MAPMT batch as illustrated in figure 5.28. The **Gain** requirement to be greater than $1 \cdot 10^6$ at 800 Volt was satisfied by all MAPMTs. A consideration: the cathode luminous sensitivity illustrates the average homogeneity of the PMT sample: since no amplification is applied it is sensitive to the photoconverter material deposition and to the geometry of the photocathode. Also the analysis of the anode spectral sensitivity (fig. 5.28) is sensitive to the geometry of the photocathode but now the distribution is convoluted with the gain distribution of each single channel. The global effect is a spreading of the original distribution of cathode luminous sensitivity which suggests the possibility of very different behaviours among the MAPMTs channels.

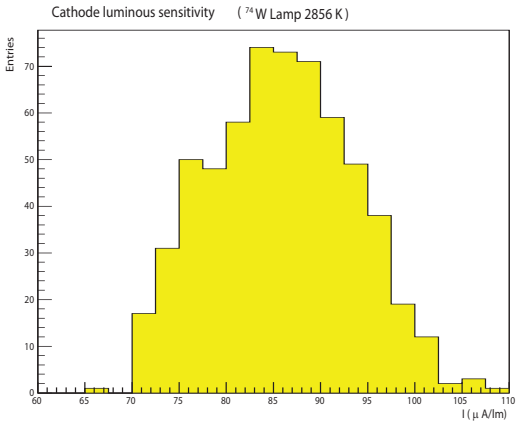

Figure 5.26: Cathode luminous sensitivity from a tungsten filament lamp operated at a distribution temperature of 2856K.

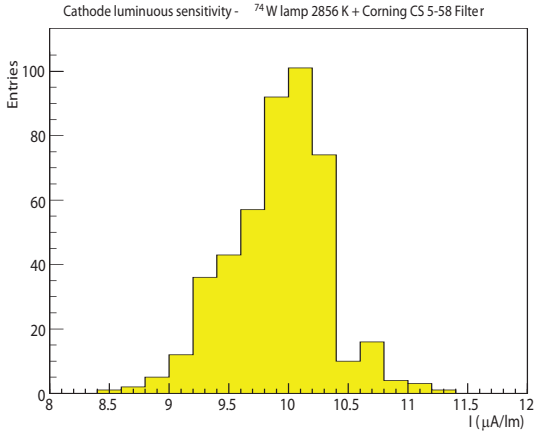

Figure 5.27: Cathode luminous sensitivity from a tungsten filament lamp operated at a distribution temperature of 2856K with Corning Filter

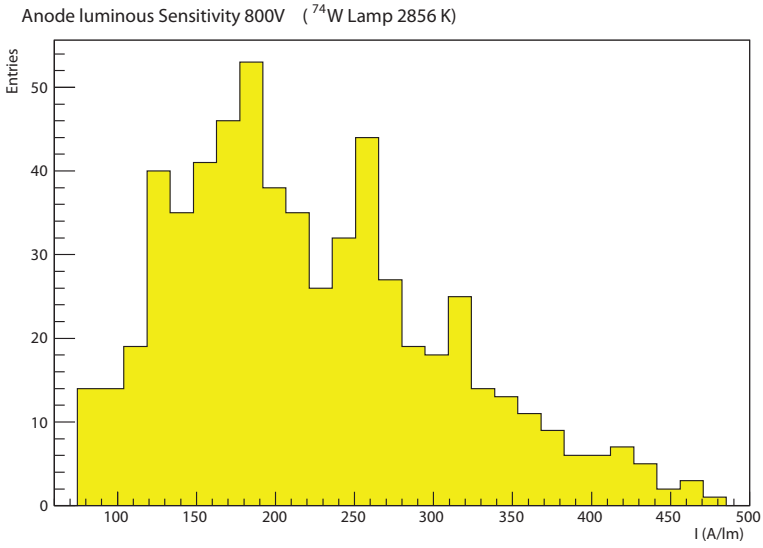

Figure 5.28: Anode luminous sensitivity from a tungsten filament lamp operated at a distribution temperature of 2856K.

5.7 The Quality Control of the multianode photomultiplier tubes for the upgrade of COMPASS RICH-1

To guarantee that the complete set of 576 MAPMTs, used in the upgraded RICH-1 detector, fulfils all specified parameters and that all the 9216 channels are operated at the optimum working point, a fully automated test-setup was designed and assembled.

5.7.1 Mechanical properties

Grid alignment

The first check operated on the MAPMT was about the correct alignment of the dynodic structure with respect to the external case. This is obtained taking a high resolution image of the frontal view of the MAPMT. The image is then imported by Autocad[2] software. Possible misalignments are then detectable via the embedded software toolkit. Misalignments greater than 2 mrad are tolerated, only one in our sample of $\sim$ 600 MAPMTs presented a clear misalignment, that required its replacement.

5.7.2 Functional parameters

Setup description

A LED pulsing system illuminates homogeneously the photocathode of the MAPMT and concurrently generates a trigger signal as gate for the charge-to-digital converter (QDC). The frequency of the LED pulses can be adjusted from 1 Hz up to 2 MHz. To study single photon response, polarisation filters placed directly in front of the LED are used. The MAPMT output signals are amplified by a factor of ten by LeCroy PMA 612A modules and then digitised by CAMAC charge sensitive ADCs of type LeCroy 2249A (10 bit, 0.25 pC per bin). The data acquisition system is based on CAMAC (CC16 by Wiener). The trigger rate is 1 kHz. The high voltage for the MAPMT is provided and monitored by a four channel HV power supply by WENZEL. Dark current measurements by a Keithley picoamperometer model 6485, and signal inspection at the scope are performed upstream of the PMA stage and a 16-fold Relays circuit allows to switch among different channels and measurements.

[2]Copyright 2007 Autodesk, Inc. All rights reserved, http://autodesk.com

The measurement protocol

The measurement protocol of each MAPMT lasts two hours and it includes: the recording of QDC spectra at five different high voltage values (from 850 V to 970 V in steps of 30 V) for two different wavelength values each (360 nm and 480 nm), recording of oscilloscope images, and the analysis of the amplitude spectra of all the channels at maximum high voltage level. Right before and after data recording, the dark current of all 16 channels is measured. During each test, no significant ambient room temperature changes occurred. The measurement procedure is immediately followed by data analysis, determining uniformity, relative quantum efficiency and gain. More than 600 MAPMTs (576 plus spares) were characterised in terms of all relevant parameters.

Dark Current

In Cherenkov image application mainly single photoelectrons have to be detected. It is therefore extremely important to study the MAPMT dark noise at very low threshold levels. It is well known in fact that a small amount of current flows in a photomultiplier tube even when the tube is operated in a completely dark state. This output current is called the anode dark current (DC), and the resulting noise is a critical parameter in determining the lower limit of light detection, since this source of noise can not be eliminated.
Major sources of dark current may be categorised as follows:

1. The materials of the photocathode emit tiny quantities of thermionic electrons even at room temperature. Most dark currents originate from the thermionic emissions, especially those from the photocathode since they are successively multiplied by the dynodes.

2. Residual gases inside a photomultiplier tube can be ionised by collision with electrons. When these ions strike the photocathode or earlier stages of dynodes, secondary electrons may be emitted. These secondary electrons result in relatively large output noise pulses. These noise pulses are usually observed as after-pulses following the primary signal pulses and may be a problem in detecting short light pulses.

3. When electrons deviating from their normal trajectories strike the glass envelope, scintillations may occur and a dark pulse may result.

4. Leakage current resulting from imperfect insulation of the glass stem base and socket may be another source of dark current. Also contamination from dirt and moisture on the surface of the tube stem, base or socket may increase the leakage current.

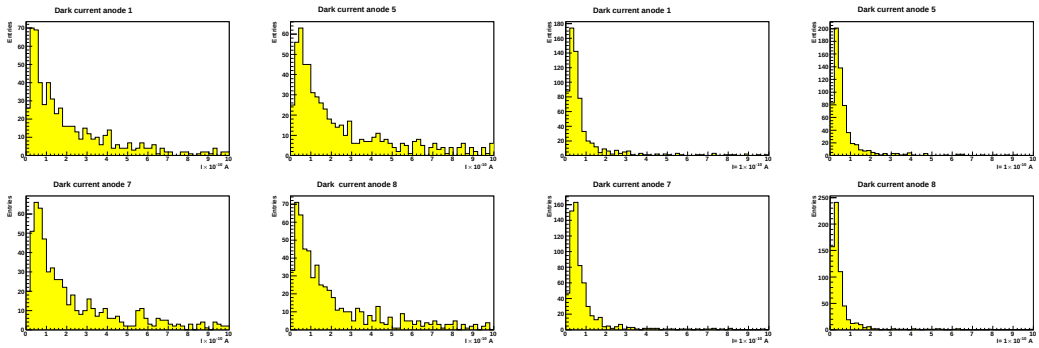

Figure 5.29: Dark current measurement immediately after HV powering (left); after 20 minutes in dark state at 970 Volt (right). Only four anode distributions are shown.

5. When a photomultiplier tube is operated at a voltage near the maximum rated value, electrons might be emitted from electrodes by the strong electric field and cause dark pulses.

For the dark current quality checks the tubes under test are kept in the dark, the dark current is measured at 800 V and then the measurement is repeated after 20 minutes. The anode dark current decreases within time, after the tube is placed in a dark state. In this analysis also the time stability of the picoamperometer has been verified after and before each measurement which showed to be stable during the dark current measurement. All tested photomultiplier tubes apart 20 units accomplished all test criteria. Twenty MAPMTs did not fulfil the dark current limit of less then 2 nA for each individual channel, exhibiting at most 2 out of 16 channels with higher dark current: typical values ranging from 6 till 55 nA. In general, the dark current registered at the end of the two hour measurement protocol, is an order of magnitude less than specified in table 5.1.

The comparison between figures (left-right) in 5.29 shows a clear and strong reduction of the DC values after the conditioning, in fact the ratio between the mean of the distribution is ≥ 2 or more.

Gain

The gain optimisation has been performed studying each MAPMT powered at different voltages (850, 870, 910, 940, 970 Volt) using two different set of led (360 nm and 480 nm) and measuring the ADC distribution for each of the 16 anodes of a tube as is illustrated in fig. 5.15 (left side). Figure 5.15 shows one of the typical single photon QDC distributions obtained. Mean value and standard deviation of each contributing peak is determined by a double Gaussian fit. A MAPMT gain

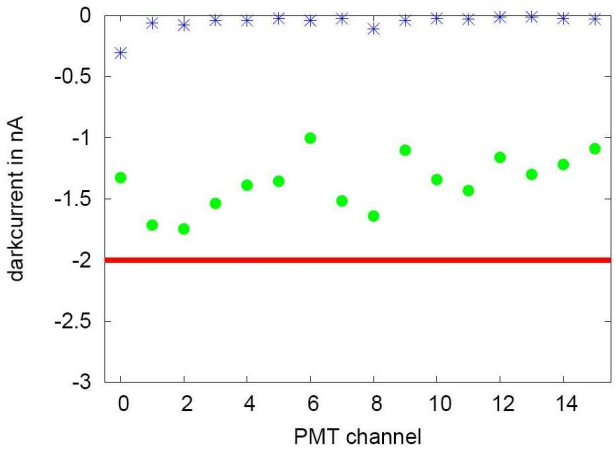

Figure 5.30: Dark current measurement immediately after HV powering (green circles) and after 20 minutes conditioning (blue stars) for the final selected set of MAPMTs. Clearly the DC level is much below the required threshold at 2 nA.

lower than $1 \cdot 10^6$ at 800 Volt leads to the MAPMT rejection, event which never happened. The ideal high voltage setting for each MAPMT is the minimum value which guarantees at least 95% efficiency for all the MAPMT channels coupled to the Front End readout chain, based on the MAD4 discriminator boards [79]: 1.7 pC (gain$\sim 10^7$). The HV setting is deduced from an exponential best fit of the measured gain data. Figure 5.31 shows the calculated high voltages for a subsample of 556 MAPMTs. These values are Gaussian distributed around 890 V with a standard deviation of $\sim$40 V. The central value corresponds pretty well to the typical value given by Hamamatsu ($\sim$910 V for an amplification of $\sim 10^7$).

Uniformity response

The uniformity response has been defined in 5.6. From the parameters of the fit, described in the previous section 5.7.2, it is also possible to monitor the uniformity response of the MAPMT. In particular the measured pulse height distribution, called the Single Electron Response (SER) of the photomultiplier, can be used to plot for each MAPMT (see fig. 5.32): the Single Electron Response (SER) mean charge distribution as function of the anode number, the corresponding sigma, the SER uniformity and the normalised Integral peak.

The obvious use of the monitored quantities stays in the discovering of a possible anomalous behaviour of the MAPMTs or of devices showing a behaviour not satisfying our quality criteria.

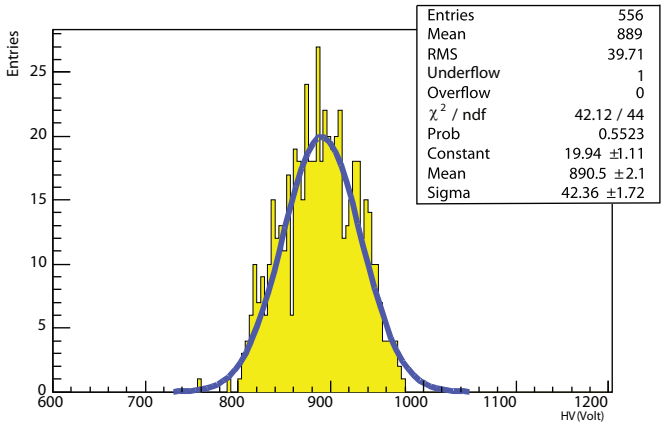

Figure 5.31: Distribution of the high voltage value needed to get a minimum output charge of 1.7 pC for a sample of 556 MAPMTs.

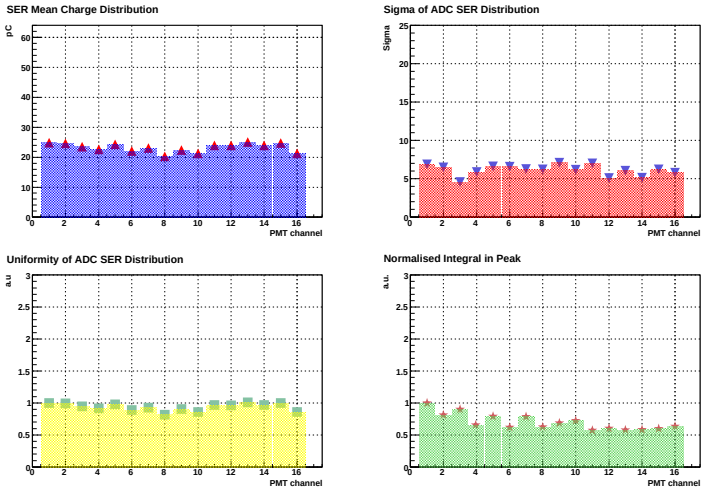

Figure 5.32: MAPMT characteristic parameters extracted via the fitted values as described in 5.7.2: SER mean charge distribution number, the corresponding sigma, the SER uniformity and the normalised Integral peak as function of the anode are illustrated.

5.7.3 Consideration on the upgraded hardware.

This section concludes the description of the work done to characterise the MAPMT. The studies on the data sheet information, the detailed study of the output statistics via the Polya fit, the rigorous quality control and the studies to find the ideal working point of each MAPMTs are the basis for a very accurate understanding of the upgraded detector response.

5.8 Pushing even more the performances of upgraded RICH-1

In section 4.6 the improvement due to the upgrade of the RICH-1 counter have been widely described: the standard deviation of the measured Cherenkov angle changed from 0.6 mrad to less than 0.3 mrad. But there is still some potential to increase the accuracy of the measurement by improving the information about the mirror alignment. In RICH detectors, such as RICH-1, with extended gas radiators, image focusing is obtained by large reflecting surfaces formed by mirror segments of smaller size (see, for instance, [68, 70, 139, 140]). The extended mirror walls are included in the gas vessel and they are sitting in the acceptance region of the experimental setup. These architectural aspects dictate specific requirements for all the components of the mirror systems. They must be compatible with the required purity of the radiator gas, as pollutants can reduce the radiator transparency, particularly for UV photons. The amount of material must be minimised. Moreover, the mirror sets are not accessible during detector operation. The mirror elements must be very accurately aligned so to form a single smooth reflecting surface. In fact, their misalignments result in poorly focused images, directly affecting the detector resolution. The most critical parameter is the relative angular alignment. It is often not possible to recover for the resolution degradation even if the misalignments themselves are precisely determined. In fact, offline corrections are only partially effective. The Cherenkov photons hit the reflecting surface in a pseudo-circular region and the reflection point of each individual photon is not known because the photon emission point is randomly distributed along the particle path in the radiator. If the disk is entirely included in a single mirror element, the correction is fully effective. If the disk is shared among several adjacent mirror elements, the correction can be applied only on a statistical base: it can result in a limited or null improvement. The fraction of images that can be effectively corrected depends on the ratio between the mirror element surface and the disk surface and it increases for larger values of this ratio. On the other hand, the size of the mirror elements is limited because of the total amount of material tolerable, the optical quality requirements and economic considerations. Relative mirror misalignments can be determined from the collected

data (see, for instance, [141], from surveying procedures with direct access to the mirror setup performed when the detector is not in operation (see, for instance, [72]) or via optical monitoring [142, 58, 143]). The first approach has the disadvantage that monitoring the mirror alignment using the reconstructed data is only marginally effective, mainly due to the non-availability of statistically meaningful samples of data collected within a few hours: no more than about one quarter of the mirrors, those sitting in the most populated areas, can be monitored with this approach. The second approach, besides the fact it can only be done when the detector is not in data taking mode, is extremely time consuming: in the specific case of the COMPASS RICH-1 it takes between 1 to 2 months. A different method, based on online optical monitoring, has been implemented and put in operation for the RICH-1. It is presented in the next section.

5.8.1 Continuous Line Alignment Monitoring method (CLAM)

The possibility to have an on online optical monitoring system offers several advantages: the information can be obtained during the detector operation almost in real time and no integration over long time intervals is needed, making possible a true monitoring of the alignment evolution. The basic idea of this method is simple[142, 58]. A rectangular grid, placed near the focal plane of the mirror wall inside the detector vessel, is formed with reflecting strips. It is illuminated by high luminosity LEDs. The images of this grid, reflected by the spherical mirrors, are collected by four high resolution cameras, pointed to the spherical mirrors. The rectangular grid image is observed by the camera as a set of intersected conics. If some mirrors are tilted respect to the neighbouring ones, the images of the grid points are shifted, and the conics lines appear to be broken. This observed shift of the line images provides the direction and amount of the mirror tilt (see figure 5.33). Pictures have been collected at different times, before and during the 2007 COMPASS data collecting period, which was 6 month long. The comparison of pictures, taken during the run, and analysed via dedicated software, shows that some mirrors exhibit a slow continuous motion, characterised by a typical tilt of 0.05 mrad in the horizontal and 0.11 mrad in the vertical direction. Some mirrors reach a stable position after 2 months of run. Further analysis has demonstrated that the continuous line alignment monitoring method can trace relative mirror tilts in the RICH-1 detector during the run, with a precision better than the required value of 0.1 mrad. Presently this value is 0.04 mrad[58]. The CLAM method, much faster than the surveying procedure with direct access to the mirrors [72] can be used for the correction of the mirror position before closing the vessel.

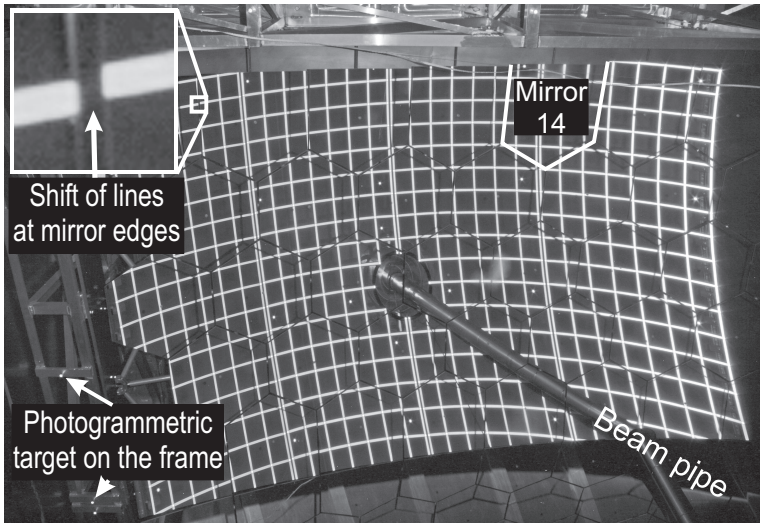

Figure 5.33: A picture collected by the CLAM system: a zoom of a tilted mirror is visible as the reflected grid line is discontinuous between two separate mirrors.

5.8.2 Remote Alignment of large mirror array for RICH detectors

The obvious complement of the online monitoring of the mirror alignment is a system making possible quasi online adjustment of the alignment: this adjustment, to be performed during detector operation periods, requires remote control, solving the problem of the opening of the RICH-1 vessel structure. Systems for remotely control adjustment of large mirror arrays have already been implemented, for instance in large Cherenkov telescope for the cosmic gamma-ray spectroscopy. In the MAGIC experiment, an Active Mirror Control (AMC) system [144] provides fast correction of the global mirror shape: each of the 241 mirror panels is controlled by laser spot monitoring and is adjustable through a pair of mechanical actuators moved by stepping motors. The implementation of an adjustment system in a gaseous RICH counter must satisfy the requirements concerning material budget and gas pollution. A original system matching these requirements, well suited for the COMPASS RICH-1 mirror system is now presented.

Adjusting the mirror system of COMPASS RICH-1

The RICH-1 mirror system has already been described in 4.2.2. We recall here those features of this huge mirror wall [72], which are relevant for the adjustment system we propose. The mirror system is formed by 116 spherical VUV reflecting units, about 3 kg each, supported by a lightweight mechanical structure so to form two

Figure 5.34: Mirror wall rear face, detailed view: the mechanical arrangement for the angular adjustment of an individual mirror element is visible.

spherical surfaces (R = 6600 mm). The image dispersion due to the mirror optical imperfections results in a contribution to the error on the measured Cherenkov angle of 0.1 mrad; the error contribution caused by the misalignment adds in quadrature. It is therefore reasonable to require angular misalignments of the same order of magnitude at most.

The centres of the two spherical surfaces lie well outside the vessel volume and are not accessible to align the mirrors by standard Foucault procedure; a different procedure based on the use of the theodolite in auto-reflection mode was adopted, able to provide the absolute mirror alignment with 0.1 mrad accuracy. The mirror orientation can then be corrected acting manually on the individual mechanical actuators on the mirror element rear face (fig. 5.34). The adjustment is obtained rotating around two orthogonal axes: the translational push (or pull) of a micrometric screw (pitch 0.5 mm) against one end of a rigid bar (200 mm long) is converted into a rotation at the other end of the bar constrained to a pivot anchor; the angular resolution is 2.5 mrad/turn with very good linearity, practically no hysteresis and a negligible (0.01 mrad) cross-talk.

In practice, the minimum correction that can be applied is about 0.1 mrad. The unit weight of these support and adjustment elements is 112 g.

The mirror rear faces are reachable removing a large panel (3×4 m^2) closing the vessel volume. The procedure is time consuming; moreover, it requires both accessing the vessel and removing part of the vessel walls: it must be performed outside data taking periods. In year 2001, the whole mirror wall was aligned and the measured residual misalignments showed a standard deviation of 0.06 mrad. Later, the mirror alignment was measured several times between the experiment data taking periods, typically once or twice per year, and misalignments with a random distribution in the range 0-1 mrad have been observed, with a few elements exhibiting misalignments up to 1.5 mrad. The source of the misalignments developed

Figure 5.35: Piezo actuator NexLine® N-110.

after the initial alignment procedure is not known. Some information about the mirror alignment during detector operation is obtained from the collected data and it provides information averaged over long time intervals.

Remotely controlled positioning actuator

Piezo micrometric actuators can be chosen to adjust the individual mirror inclination: they can be remotely controlled, are compatible with the radiator gas purity and are light-weighted devices: they can be locally mounted, as they do not represent an important increase of the material budget of the mirror system. A major problem for standard piezoelectric actuators is their lifetime when high voltage is applied to keep the desired position: keeping the mirror correctly aligned, in our application. Typical values range around 100 days, fully incompatible with the life of an experiment like COMPASS: COMPASS data taking period extends over typically five-six months per year over about a decade. Short lifetime is due to metal diffusion from the electrodes used to apply the supply voltage to the ceramic insulator: eventually this results in a high leakage current and finally into the reduced capability or impossibility of actuator movements. Moreover, if the mirrors are kept aligned by the voltage supply, an accidental power cut will result in the loss of the whole mirror wall alignment. The new principle applied in the NexLine® miniature High-Load piezo nanopositioning devices by PI[3] is based on the combination of the feed forward and the clamping cycles to provide push/pull forces: it looks the natural answer to the difficulty previously discussed.

A piezo actuator NexLine® N110 is shown in fig. 5.35. The device keeps the full holding force available when no voltage is supplied, even during a movement cycle: the application of long-term offset voltages, which limit the lifetime, is avoided. The

[3]Physik Instrumente (PI) GmbH and Co. KG Auf der Römerstr. 1 D-76228 Karlsruhe,Palmbach, Germany, http://www.pi.ws

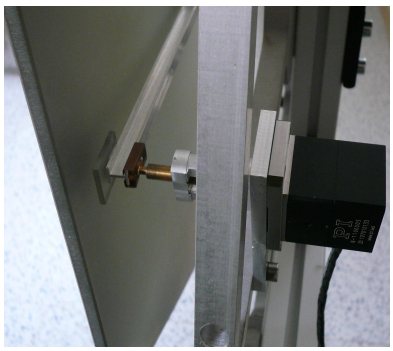

Figure 5.36: Laboratory setup, the mirror rear side: the piezo actuator replaces one of the micrometric screws.

main characteristics of this device are summarised in Table 5.4. The travel range is wide enough to guarantee a reasonable range for mirror angular adjustment: for example, if coupled to the present mechanical arrangement of the COMPASS RICH-1 mirror wall, the angular adjustment range would be about 15 mrad. The forces that can be applied are also adequate for this application.

Table 5.4: Summary of the main characteristics of the piezo actuator NexLine® N110.

characteristic	value	Unit
Travel range	3	mm
Max step size	1.5	μm
Max freq.	100	Hz
Max speed	0.15	mm/s
Resolution	< 0.1	nm
Holding f. (passive)	> 50	N
Push/Pull f. (active)	30	N
Stiffness	15	N/μm
Max operating V.	250	V
L×W×H	46.6× 28× 35.5	mm^3
Mass	131.0	g

The zero voltage stand-by condition offers further advantages. A single power supply and a single control unit are required even for an extended system: both high voltage and control signal can be provided via a multiplexer device, thus reducing the costs, the cable layout and the maintenance requirements.

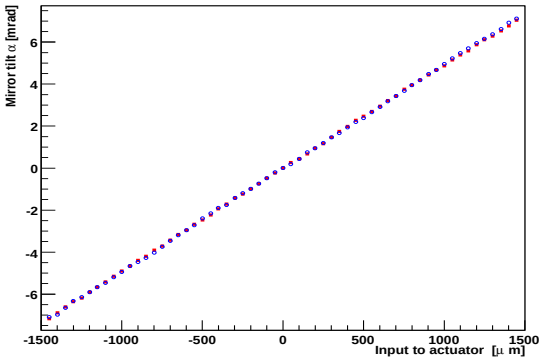

Figure 5.37: Mirror rotation versus the input value to the NexLine® N110 actuator, full actuator travel range. Two sets of points are plotted (open circles and solid squares), obtained moving the actuator in the two opposite directions: the two sets result superimposed.

The feasibility of the application proposed has been tested in a laboratory exercise. A RICH mirror element is mounted on a holder identical to the RICH-1 ones. The mirror rotations are measured by a laser beam spot reflected by the mirror and collected at 12.45 m distance, resulting in a resolution of 40 μrad. The angular adjustment is performed replacing one of the two micrometric screws with a piezo actuator NexLine® N110 (fig. 5.36). The result of the test is presented in fig. 5.37. The adjustment resolution is improved at least by 2 orders of magnitude respect to what obtained with the micrometric screws. Within the measurement resolution, no hysteresis or non-linearity have been observed exploring the whole 3 mm long travel range.

Considerations

Complementing the on-line measurement of the relative mirror misalignments with a system for the online adjustment of their position via remotely controlled piezoelectric actuators can enhance COMPASS RICH-1 performances by increasing the resolution of the measured Cherenkov angle: the residual mirror misalignments can be made totally negligible. The possibility to adjust the mirror alignments without accessing the radiator vessel has other remarkable advantages: the vessel can remain always closed, so that the mirrors can be constantly kept in a dry, clean atmosphere, thus preventing the degradation of the reflecting surface by moisture and dust. The technological aspects of the proposed system have been reviewed and its technical feasibility has been discussed and checked. The open question is the cost of the

system itself, related to the cost of the actuators; the total number of actuators required for RICH-1 is $232 = 116 \times 2$ (the number of the mirror elements $\times$ the number of the angular degrees of freedom per element). The technology considered is pretty young; fast technological development can result in a reduction of the costs. Actuators with less pushed resolution can be considered. Both these elements could make the implementation of this system economically affordable in the next future.

Data analysis

The previous chapter closes the section of this thesis dedicated to the *hardware activities*.
In the next to chapters the focus is moved on the *data analysis* from the 2007 transverse run at COMPASS with a polarised proton target.
The main goal of this analysis is

- the extraction of the Collins and Sivers from the unidentified hadron sample,
- the extraction of the Collins and Sivers asymmetries from the identified hadron sample using the upgraded RICH-1,
- the evaluation of the systematics affecting the result,
- the comparison with the existing results from the HERMES experiment,
- the comparison with some theoretical predictions.

All the listed topics are discussed in the next chapters.

Summary table of the COMPASS spectrometer relevant parameters for 2007 transverse data taking.

Spectrometer		
	Setup	Two stage spectrometer (LAS+SAS)
	Luminosity	$5 \cdot 10^{32}\ cm^{-2} \cdot s^{-1}$
	x range	$0.003 < x < 0.5$
	Q^2 range	$10^{-3}\ \div\ \sim 10\ (GeV/c)^2$
Beam		
	Particles	μ^+
	Momentum	160 GeV/c
	Flux	$2 \cdot 10^8\ \mu^+$/spill
	Dimension	$\sigma_x \times \sigma_y = 0.8 \times 0.8\ mm^2$
	Angular divergency	$\sigma_{\theta_x} \times \sigma_{\theta_y} = 0.5 \times 1\ mrad^2$
	Duty cicle	4.8s/16.2s
Target		
	Material	Ammonia, (NH_3)
	Setup	Three cells (60+120+60) cm
	Acceptance	$\pm$ 180 mrad
	Average polarisation	90%
RICH		
	Radiator	C_4F_{10}
	Acceptance	$\sigma_x \times \sigma_y = 250 \times 200\ mrad^2$
	PID	$2\sigma\ \pi\ K$ separation up to 43 GeV/c
Cuts for data analysis		
	Q^2	greater than 1 $(GeV/c)^2$
	W	grater than 5 GeV/c^2
	y	0.1$\div$0.9
	z	greater than 0.2
	P_t^h	greater than 0.1 GeV/c
	Hadron minimum E deposit in Calorimeters	4$\div$5 GeV

Chapter 6

Collins and Sivers asymmetries

The extraction of the Collins and Sivers Single Spin Asymmetries from the 2007 transverse data is the main topic of this chapter.
First the data sample on which asymmetries are extracted is introduced, then a short description of the necessary resources for data processing and some useful definition are given in section 6.2. In section 6.3.1, the transverse polarisation values of the NH_3 target cells are reported. The different target cell combinations used to extract the asymmetries are discussed within the notation that will be used throughout the chapter, finally closing the introductory section. The focus will move on data analysis (section 6.4.1): first the criteria which are used to select SIDIS events and hadrons are presented, then data stability (section 6.5) is introduced: a detailed description of the different tests performed and their outcome is given, bringing us to the final statistics sample used for the asymmetry extraction (section 6.5.5).
Different methods have been developed and tested to extract the asymmetries (section 6.6), the results obtained on the same data sample have been compared and analysed in order to select the most suitable method to use.
The Collins and Sivers asymmetry results are then illustrated in section 6.7 which is followed by a complete and detailed analysis of the systematics checks preformed (section 6.8).

6.1 2007 transverse run

In 2007 COMPASS took data with a proton target (NH_3) and a 50% sharing between longitudinal and transverse target configuration, accumulating $\sim 40 \cdot 10^{12}$ and $\sim 42 \cdot 10^{12}$ μ^+ on tape respectively. The transverse run, which started May 18^{th} 2007 and ended November 11^{th} 2007, has been divided in 12 "periods" (or weeks), each of them corresponding to about 5 full days of data taking. Consecutive periods correspond to opposite polarisation of each of the three target cells as illustrated in figures 3.1 and 6.4. Data taking periods and the target polarisation are reported

in table 6.1. Almost all the data collected in the transverse polarisation of the target have been analysed a first time. The preliminary results are illustrated hereafter.

6.2 Data taking during transverse run: event size and resources for processing

The nominal proton flux delivered to the T6 **Be** target is 1.2×10^{13} p per SPS cycle. Each cycle lasts 16.8 seconds, only during the first 4.8 seconds protons are extracted (spill). This corresponds to a flux up to 2×10^8 μ^+ on the COMPASS polarised target. See also section 3.3 for further details. Figure 6.1 (left side) illustrates the

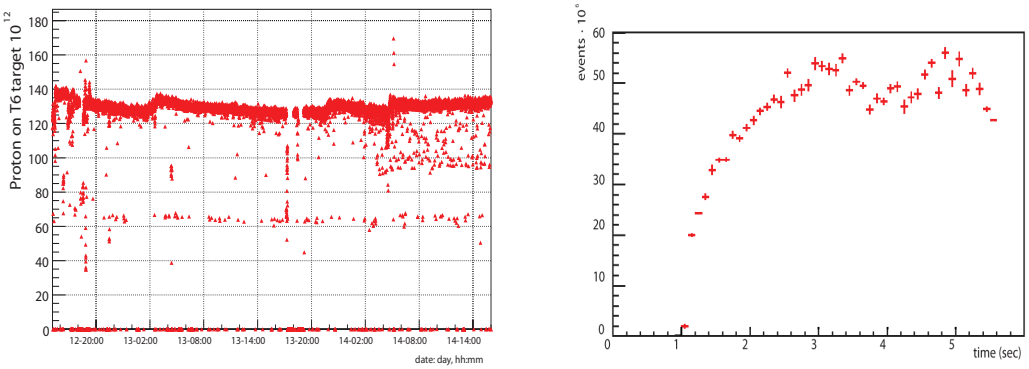

Figure 6.1: Left:SPS proton current on T6 target. Right: muon spill structure in the COMPASS hall on the polarised target.

measured proton SPS current intensity on the T6 target for about three days of data taking, while figure 6.1 (right side) describes the spill structure during the extraction: the muon intensity increases during the first time-second reaching a plateaux which lasts for the remaining time of the spill, finally after 4.8 seconds the intensity rapidly drops. With an average event size of ∼35 KB (see fig. 6.2) and a trigger rate of ∼18 kHz, the data acquisition system digests about 180 MB/s of raw detector information, (the so called raw-data) averaged over the SPS spill cycle. Data collected for 200 continuous spills are grouped together defining a *run*. The data are buffered locally on disk arrays with a combined size of 12 TB before being sent to the tape libraries at the CERN central data recording CDR[145]. The daily average transfer rate to CASTOR is: 4.8 TB/day. About 20 runs/day are collected. During the 2007 transverse run 0.49×10^3 PB were stored. Raw data reconstruction is done via CORAL[66] as described in 3.10, in particular for the transverse target

data about 25 kSI2K[65] for a 200 spill run (about 400 chunks) are needed. Roughly 1 chunk takes 4 hours to be processed.

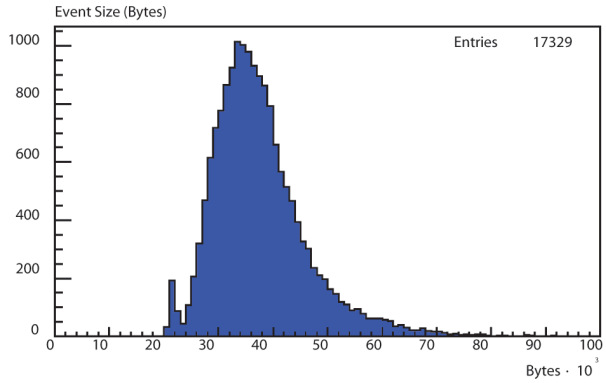

Figure 6.2: Event size distribution for a 200 spill run. Data is expressed in KB.

6.3 Target in transverse polarisation mode

6.3.1 Polarisation measurement

A direct measurement of target polarisation at COMPASS is not possible in transverse mode[146], because the Nuclear Magnetic Resonance (NMR) process can not be performed with the magnetic field in transverse direction. For this reason the polarisation is measured in the longitudinal 2.5 T field at the beginning and the end of each transverse data acquisition period. It is measured independently for the three target cells via 15 coils. The polarised cells (see figure 6.4, namely Upstream (U), Central (C) and Downstream (D) house 5 coils each. Target database values storing the measured polarisation were used to compute for each cell the polarisation value as the mean of the corresponding coils measurement. The run-by-run value of the polarisation is calculated using the relaxation time of the material and it is extracted from the measured starting and ending values of the polarisation of the period (see fig. 6.3 and table 6.1).

6.3.2 Target cell configuration: definitions

The spin orientation of the polarisation of the COMPASS target cannot be flipped by inverting the magnetic field, because the target acceptance would change. Moreover

Week	Upstream (%)	Central (%)	Downstream (%)	Polarisation sign
25	89.87	90.35	85.38	-+-
26	85.07	86.82	78.44	+-+
27	83.58	83.94	79.76	-+-
28	90.56	89.58	86.11	+-+
30	88.31	86.83	81.84	-+-
31	84.57	87.53	76.09	+-+
39	95.68	92.65	94.26	+-+
40	85.58	89.96	84.89	-+-
41	90.09	91.84	86.93	-+-
42	91.11	89.89	89.39	+-+
43	73.54	87.88	76.63	-+-

Table 6.1: The average values of the target polarisation for the three different target cells as a function of the different data taking weeks for the 2007 transverse run. The target polarisation indicated as + - + is related to the spin vector direction of the target material $\vec{s}$: a positive sign corresponds to an upward pointing of $\vec{s}$ a negative sign to a downward direction. The first sign stands for the first target cell (U), the second for the central (C), the third for the last target cell (D). See also figure 6.4 for further details

since the spectrometer acceptance and efficiency are unknown, they have to be compensated in the data analysis, taking into account that they differ between the target cells. To compensate for the acceptance effects, the measurement is always split in two periods: period$_k$ (p_k) and period$_{k+1}$ (p_{k+1}), characterised by opposite spin orientation, and physical asymmetries are extracted comparing data belonging to the periods p_k and p_{k+1}. The polarisation reversal is done by exchanging the microwave frequencies of the cells in the target. The duration of this process is typically two days in order to achieve $\geq 70\%$ polarisation. Once the target is polarised the data is taken for several days (typically 5 days) before a polarisation reversal is done. Data is taken again with the target polarised after a spin flip for 5 more days.
In figure 6.4 the polarisation configuration for the tree target cells is illustrated. The central cell for the period p_k, $C_{p_k} = C_{1,p_k} + C_{2,p_k}$ has opposite polarisation with respect to the upstream (U_{1,p_k}) and the downstream one (D_{1,p_k}). Consecutive data taking periods, p_k and p_{k+1} are characterised by opposite polarisation direction for all the cells, as indicated by the arrows in the same figure. The central cell can also be thought as the sum of two virtual sub cells C_{1,p_k} and C_{2,p_k}.
If not specified differently in the following sections $N_u^{\uparrow}$ stands for the sum of the number of produced hadrons from quarks belonging to the cells D_{1,p_k} and U_{1,p_k}, $N_d^{\downarrow}$ the sum of the number of produced hadrons from quarks belonging to the central

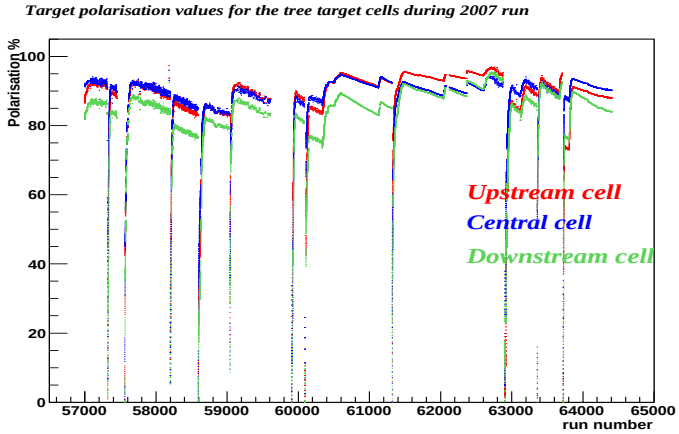

Figure 6.3: Polarisation value for the tree target cell as function of the run number.

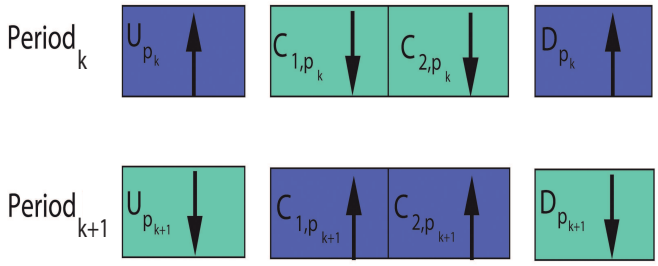

Figure 6.4: Schematic illustration of the target cells in transverse mode. The longitudinally polarised muon beam impinges from the right. The different spin orientations in the upstream, central and downstream target cells are represented by the arrows. The polarisation is reversed in all cells between periods, p_k and p_{k+1}.

cell C_{1,p_k} and C_{2,p_k}, coherently $N_u^{\downarrow}$ and $N_d^{\uparrow}$ are the same quantities but for the period p_{k+1}.

6.4 Analysis

6.4.1 Event reconstruction and selection

The following sections describe the criteria applied to reconstruct and select the SIDIS events.
In the event reconstruction, a track reconstructed before the target is assumed to

be an incoming muon (μ) if:

- The momentum is reconstructed by the BMS.
- The momentum is below 200 GeV/c
- The BMS and trigger time are, when calculated at the same position within 3 ns interval.
- The associated track must have a reduced $\chi^2_{red} = \chi^2/Ndf = \frac{\chi^2_{tot}}{N_{hits}-5} < 10$.

If several valid BMS-tracks are compatible with the track time, a back-tracking algorithm is used to resolve ambiguities.
The scattered muon (μ') is defined as a positively charged outgoing track reconstructed after SM1 magnet and with a momentum larger than 1 GeV/c. All the triggers are used in the analysis (see section 3.8) even if the event contribution is different for each of them due to the different Q^2 kinematic region covered. For all triggers based on the hodoscope information, the track must be compatible with the hodoscope hits as given in the trigger matrix. In the case of a calorimetric trigger, a minimal number of hits is required in the muon walls and the amount of material traversed in the spectrometer must be larger than 66 and 74 radiation lengths for tracks reconstructed in the first and in the second spectrometer stage respectively. The muon interaction point, the so-called primary vertex, is defined by the intersection of the tracks of one beam particle and one scattered muon. The event reconstruction can result in more than a single primary vertex, due to different reconstructed beam muons or scattered muons. If more primary vertexes are found the one with more outgoing track is selected and flagged as the Best Primary vertex. In case of more vertexes with the same number of outgoing tracks the vertex associated with smaller χ^2 is taken. After the Best Primary Vertex identification, to the μ' the following quality criteria are applied: $\chi^2_{red} \leq 10$ and a penetration length $nXX_0 > 30$.
To ensure the position of the primary vertex is inside of the target material the coordinates are checked to be inside the target region: $-62.5cm \leq z_{vtx} \leq +67.5cm$), rejecting Primary vertex events in between the target cells ($-32.5 < z_{vtx} < -27.5$ cm and $32.5 < z_{vtx} < 37.5$ cm). A radial cut $r_{vtx} \leq 1.9$ cm is finally applied ending the primary vertex selection. A further cut is applied to ensure identical beam intensity for the three target cells discarding all the events where the projection of the incoming muon lies outside the most upstream (z=-62.5cm) and the most downstream limit (z=+67.5cm) of the target cells. The resulting distribution of the primary vertex z_{vtx} coordinate is shown in fig. 6.5.

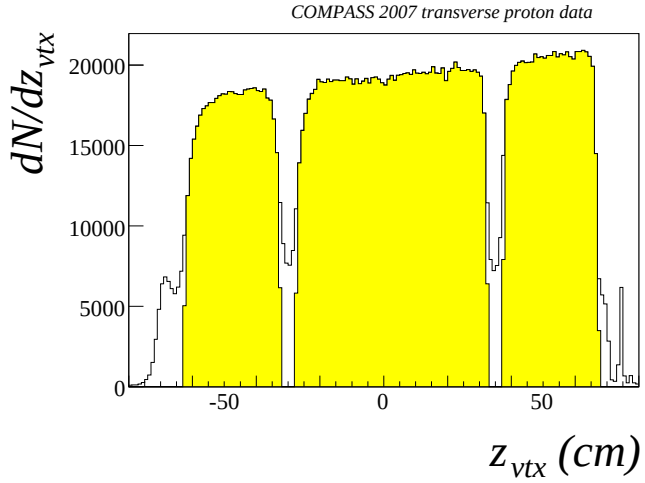

Figure 6.5: Primary vertex z_{vtx} coordinate distribution (z_{vtx}) for the final sample. The increase of events with the increasing of z_{vtx} coordinate is due to the different target cell geometrical acceptance.

6.4.2 DIS event selection

The previous selection is based only on tracks parameters. The main focus of this analysis is on the distribution of hadrons produced in the hadronisation of the struck quark from DIS events. The selection of the hadron sample is therefore based on: standard DIS cuts:

- $Q^2 > 1$ (GeV/c)^2 to guarantee the deep inelastic scattering regime.
- $0.1 < y < 0.9$ in order to to reduce radiative effects which are more important at the sides of the y distribution.
- $W > 5$ GeV/c^2 so to avoid the region of the resonances.

Figure 6.6[1] illustrates the $Q^2 - x$ phase-space covered by the COMPASS experiment. As it can be seen the high energy of the muon beam (160 GeV/c) allows to reach the low x region, covering at the same time a wide range in x. It can be noticed also that most of the statistic is located at low x values: $0.008 \div 0.02$.
Figure 6.7 illustrates the distributions of the event variables Q^2 and W^2. For the last one the effect of the cut $W > 5$ is visible (white portion of the right plot).

[1]The plot is obtained from all the 2007 data sample used for the asymmetries extraction.

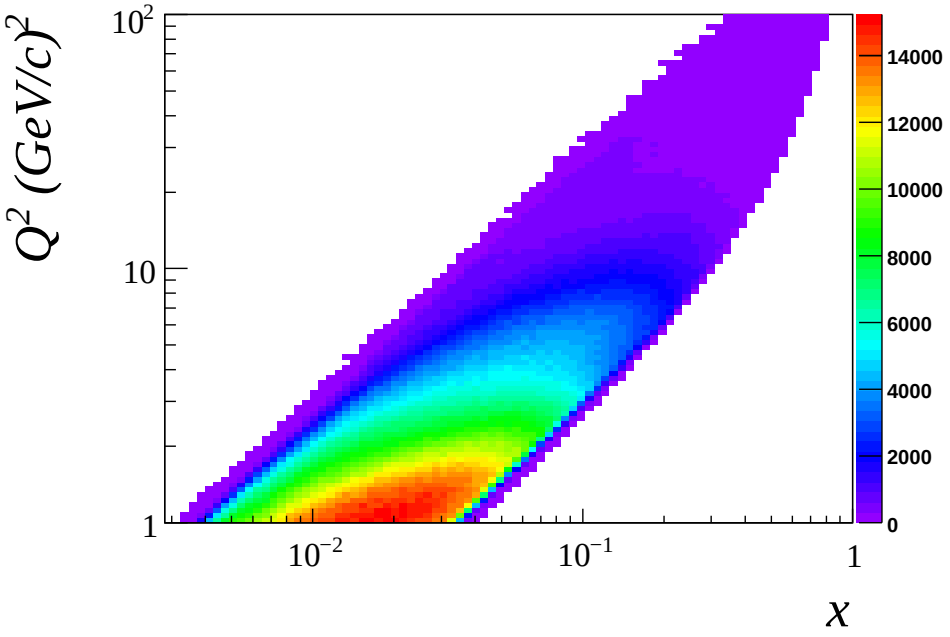

Figure 6.6: Scatter plot of Q^2 as function of x for the events after all the kinematic cuts. Most of the statistics is concentrated at low x values.

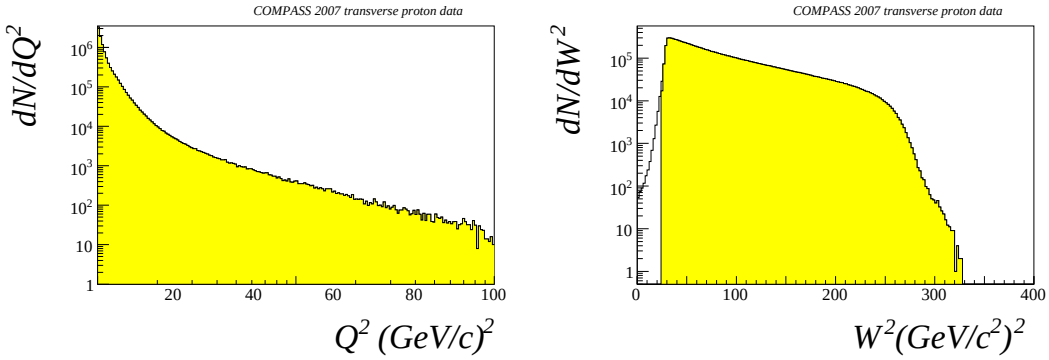

Figure 6.7: Event variables distributions, left Q^2, right W^2: the Q^2 distribution reaches the 100(GeV/c)^2 region. For the W^2 distribution the effect of the cut is clearly visible as the withe area of the distribution plot.

Hadron definition

An outgoing track from the best primary vertex is defined as hadron if it is not the flagged μ'. A general condition applies, that every track must have at least one hit after the magnet SM1, to reject tracks reconstructed only in the fringe field. This condition is satisfied by a cut on the last measured coordinate ($Z_{last} > 350\ cm$). In addition the hadron must satisfy the following criteria:

- $\chi^2_{red} < 10$.
- $Z_{first} < 350$ cm, to allow for momentum computation.
- $nX/X_0 < 10$.
- A minimum energy deposition in the cluster associated with the hadron track in HCAL1 and HCAL2: the requirement is $E^{HCAL1} > 4$ GeV or $E^{HCAL2} > 5$ GeV. Hadrons with no associated cluster are NOT discarded.
- Tracks with associated clusters in both hadronic calorimeters are discarded.

As described in [147], there is a peak present at high y in the y distribution of the positive hadrons appearing in the last z bin ($0.8 < z < 1$). The peak is also visible in the distribution of the energy of positive hadrons at high z, and in the distribution of the momentum of the scattered muon. None of these peak problems appeared in negative hadrons. The previously preformed studies have shown the origin of the y-peak in the hadron distribution is due to the scattered muon which is identified as a positive hadron, because it goes through the holes in the muon absorbers and therefore the associated amount of radiation lengths passed by the tracks is to small to allow for identification as muon, or a positive muon from the primary vertex which is wrongly identified as scattered muon. The reconstruction of these events is wrong and they have to be rejected following the method suggested in [148].
The following cuts are also applied for the hadrons:

- $z > 0.2$ to assure that we are dealing with hadrons from the current fragmentation region.
- $P_t^h > 0.1$ GeV/c in order to have a good resolution on the hadron azimuthal angle.

Figures 6.8 show the distribution of the hadron variables and the effect of the mentioned cuts (yellow part of the plot). Among them the effect of the z cut is clearly visible and has a strong impact on the statistic accepted.

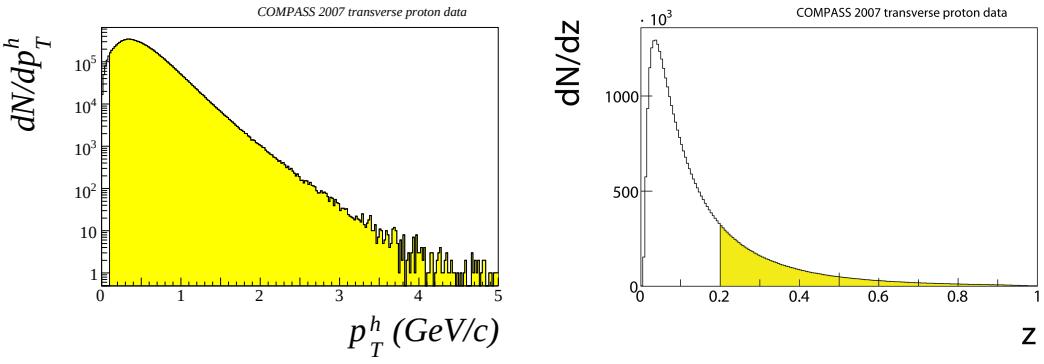

Figure 6.8: Hadron variable distributions, left P_t^h, right z, the cut $z \geq 0.2$ effect is clearly visible as the white area in the distribution plot.

6.5 Data selection criteria: data stability

Stable data taking conditions in time are a mandatory requirement to measure small effects, such in COMPASS case, of the order of 10^{-4} as cross section spin asymmetries. In particular, for the transversity measurements, it is important to assure the data stability both inside each period and between the two consecutive periods used to extract the asymmetries. In a complex apparatus as COMPASS, there are many redundancies and several sources of possible instability in the data. It is not always possible to identify them during the data taking time. Therefore an offline analysis of the data is necessary in order to test the data stability versus time and reject from the physical analysis runs or spills showing instability, and that could introduce false asymmetries. The quality criteria are the topic of the following sections: they can be divided into event selection and subsequent hadron selection. The full complete chain adopted to reject instabilities consist of several steps to be performed in a precise order: first global variables will be taken into account to isolate unstable spill, then the K^0 test is performed. Possible instabilities from the trigger system are investigated and finally the checks move to precise set of kinematic variables. The idea is to use a step by step procedure refining more and more the stability of the data sample:

1. Bad spill rejection;
2. Bad run rejection on reconstructed K^0 mass basis;
3. Bad Trigger rejection;
4. Kinematic stability within each week;
5. Kinematic stability between coupled weeks;

Before applying the complete procedure, runs or groups of runs with evident problems reported in the COMPASS e-logbook[2] were rejected.

6.5.1 Bad spill rejection

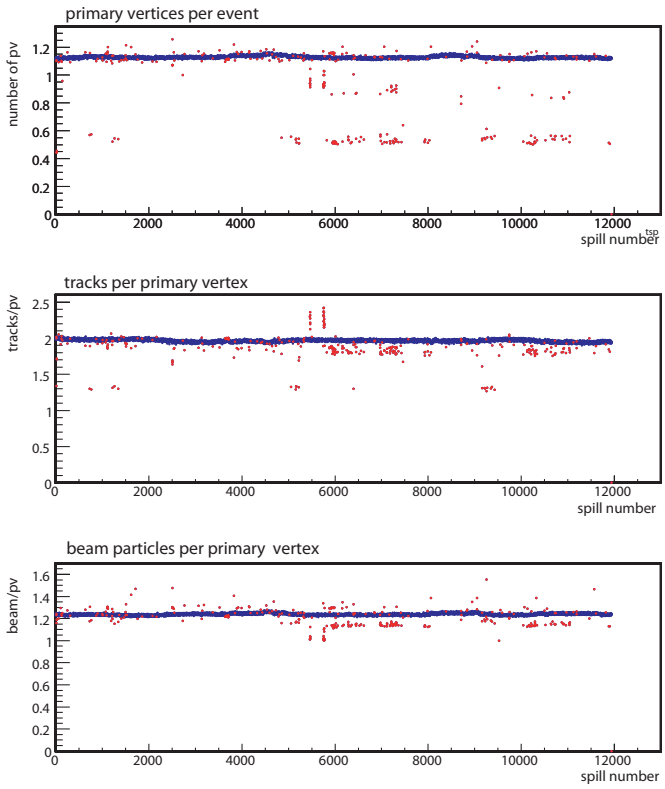

Figure 6.9: Bad spill variables monitored as function of the spill number: number of primary vertexes per event, number of tracks per primary vertex and beam particles per vertex. The red points are the spills excluded by the algorithm.

The first step to check the data stability is via bad-spill identification. This procedure allows in fact to identify

- low intensity spills or aborted spills due to instabilities in the beam line, such as magnet problems.
- spill affected by DAQ problems, such as loss of synchronisation between the Front End and the CATCH.

[2]The COMPASS electronic logbook storing the informations written by the shift crew while spectrometer is in data taking operation.

- spill affected by detector problems, such as trips of some detector which require several seconds to be back in full operative condition i.e. MicroMegas, DC.

To accomplish this task 3 variables were monitored on a spill-by-spill level searching for instabilities (see figure 6.9):

- number of beam particles per vertex
- number of tracks per primary vertex
- number of primary vertexes per event

The three variable distributions are expected to be constant in time if no problems occurred. To reject spills which deviate in at least one of the three variables the following method was applied. For each spill the number of neighbours is defined counting the number of spills whose variables lie within a certain box around the values of the regarded spill. To define the size of the box the RMS of each of the three distributions was computed and a 3 RMS box was chosen. A spill is defined as bad if it has less than 600 neighbours both to its left and its right. Spills with less than $75 \cdot 10^6$ muons were classified as bad and got zero neighbours by definition. Since the calorimeters are used to reject muons the method was also applied to control their stability. The counting of neighbours was done separately for the electromagnetic and the hadronic calorimeters. As final criterion a spill was rejected if it was classified as bad in at least one of the spill lists. On average a 5% spill rejection was obtained.

6.5.2 K^0 invariant mass and multiplicity test

The K^0 reconstruction is a very sensitive tool to test the stability of the spectrometer: it tests the quality of the alignment[3] and more generally of the track reconstruction via the dependence from the momenta and from the opening angle of the pions produced in the decay.
In this test the mass of the K^0 is reconstructed from the $\pi + \pi-$ decay. V_0 secondary vertexes[4] are searched at least 20 cm downstream the end of the target, and the invariant K^0 mass is calculated. The relevant parameters for the stability of the data are the mass shift between the mean value of this distribution and the literature PDG value[149], the mass resolution and the number of the produced K^0 per primary vertex. For the last one the distribution for every period was plotted and

[3] An alignment file contains all the detector coordinates with respect to a defined reference system, its information are needed to know the relative position of detectors and compute correctly for example the track parameters. A new alignment file is needed every time a detector is moved in the COMPASS hall.

[4] V_0 secondary vertex are given by the decay of a neutral particle into 2 charged daughters.

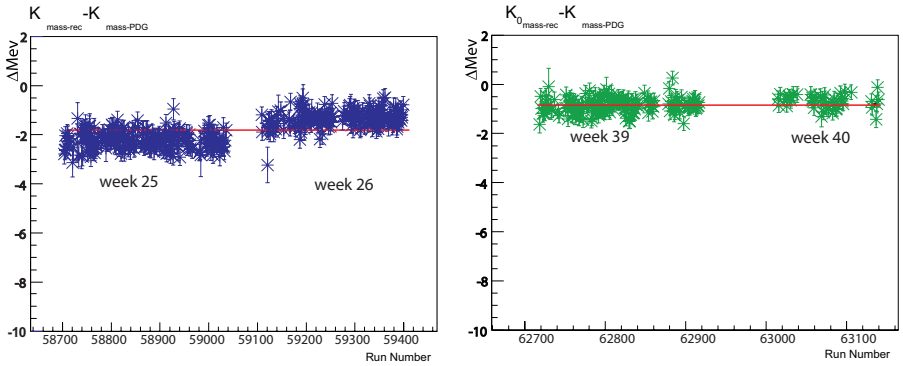

Figure 6.10: Left: the K_0 difference between the K_0 mass reconstructed and the corresponding PDG value as function of the run number for the week 25 and week 26, on the right the same distribution for week 39 and 40.

fitted with a Gaussian. The runs for which the number of K^0 per primary vertex were more than 3σ away from the mean value were tagged as bad and excluded. Only from this test over all periods in 2007 the rejection was 2.8 % of the runs.
The stability of the three parameters for the weeks to be combined for the asymmetries extraction were examined together as shown in figure 6.10: on the left the K^0 difference between the reconstructed mass and the corresponding PDG value is plotted as a function of the run number for weeks 25 and 26, clearly the jump between the two weeks is symptomatic of a problem, most probably a bad alignment file. The situation is clearly good for the data of week 39 and 40 (right figure).

6.5.3 Bad trigger rejection

All the triggers are used to select events entering the analysis. Different triggers are obtained using the signal of the different hodoscopes as illustrated in section 3.8. A source of possible instabilities can be searched in the trigger apparatus, since a modification of the trigger conditions between two coupled period (p_k and p_{k+1}) can bias the asymmetry extraction. An important tool to monitor both the absolute and the azimuthal stability of the apparatus allowing the identification of possible trigger malfunctioning is given by the so called R test where the number of events belonging to the different cells are used to build the ratio $R(\Phi)$:

$$R_j(\Phi) \quad = \quad \left(\frac{N_u^{\uparrow}(\Phi) N_d^{\downarrow}(\Phi)}{N_u^{\downarrow}(\Phi) N_d^{\uparrow}(\Phi)} \right)_j , \quad \Phi = \Phi_C, \Phi_S \tag{6.1}$$

Using equation 2.48, the Φ distribution of the number of events for each cell and for each polarisation state can be written as

$$N^{\pm}_{j,k}(\Phi_j) = \mathfrak{F}^{\pm}_k \, n_k \, \sigma \cdot a^{\pm}_{j,k}(\Phi_j) \cdot (1 \pm \epsilon^{\pm}_{j,k} \, \sin\Phi_j), \tag{6.2}$$

where $j = C, S$, and $\mathfrak{F}$ is the muon flux, n the number of target particles, σ the spin averaged cross-section, and a_j the product of angular acceptance, trigger efficiency and efficiency of the spectrometer and ϵ_j are the Collins and Sivers asymmetries. Introducing equation 6.2 in 6.1 the $\sin\Phi_j$, assuming the absolute value of the target polarisation to be the same in each cell before and after reversal, at first order it is

$$R_j(\Phi_j) \;\simeq\; \frac{\mathfrak{F}^+_u \cdot \mathfrak{F}^-_d}{\mathfrak{F}^-_u \cdot \mathfrak{F}^+_d} \cdot \frac{a^+_{j,u}(\Phi_j) \cdot a^-_{j,d}(\Phi_j)}{a^-_{j,u}(\Phi_j) \cdot a^+_{j,d}(\Phi_j)} \,. \tag{6.3}$$

In the very likely case in which $a^+_{j,u}(\Phi_j)/a^-_{j,d}(\Phi_j) = a^-_{j,u}(\Phi_j)/a^+_{j,d}(\Phi_j)$ it is

$$\begin{aligned} R_j(\Phi_j) \;&\simeq\; \frac{\mathfrak{F}^+_u \cdot \mathfrak{F}^-_d}{\mathfrak{F}^-_u \cdot \mathfrak{F}^+_d} \cdot \left(\frac{a^+_{j,u}(\Phi_j)}{a^-_{j,u}(\Phi_j)} \right)^2 \\ &\simeq\; \frac{\mathfrak{F}^+_u \cdot \mathfrak{F}^-_d}{\mathfrak{F}^-_u \cdot \mathfrak{F}^+_d} \cdot \left(\frac{a^-_{j,d}(\Phi_j)}{a^+_{j,d}(\Phi_j)} \right)^2 . \end{aligned} \tag{6.4}$$

The $\sin\Phi_j$ modulation cancels out, thus the constancy in Φ_j of $R_j(\Phi_j)$ implies for each cell the ratio of the acceptances before and after the reversal to be constant in Φ_j. This test reveals to be a stringent test, as function of the trigger selected, on the stability of the apparatus and in particular to the acceptances constancy in the different periods p_k and p_{k+1}, since deviation of statistical significance is therefore given by instabilities in the spectrometer during the data taking.
The ratio R has been calculated for each bin of x, z, p^h_T for the Collins and Sivers angles for all positive and negative hadrons; the distribution R was fitted with a constant and the corresponding χ^2 of the fit computed. As already said this operation was repeated trigger by trigger.
Any deviation of statistical significance is therefore given by instabilities in the spectrometer during the data taking. The goal of the test is the identification of events selected by one particular trigger which had to be excluded. Figure 6.11 illustrates the R test result for the Sivers angle for the 9 bins in x for negative hadrons just for the Outer triggered events (for positive hadrons the situation is identical). The χ^2 distribution obtained from the fit is expected to follow the theoretical black curve in figure 6.12. Since the data points are not constant in the different x bins, (see fig. 6.11) the χ^2 data distribution from the fit results shifted towards higher values 6.12 than expected[5]. The criterion which was followed is to reject the data

[5]The mean value of the distribution is expected to be 15: the numbers of degrees of freedom is given by $16 - 1$ where 16 are the angle bins and 1 is the fit parameter.

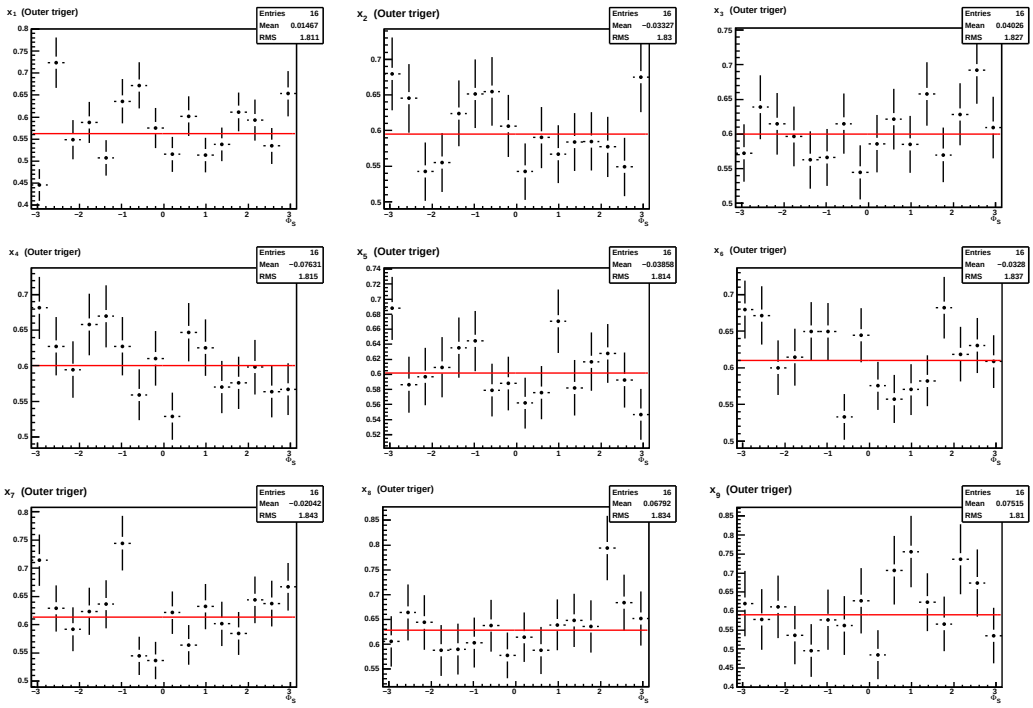

Figure 6.11: A sub sample of plots of the R test result for the Sivers angle for the 9 different bins in x for week 41 and week 42a, limited to Outer triggered events. Lines are fit with a constant.

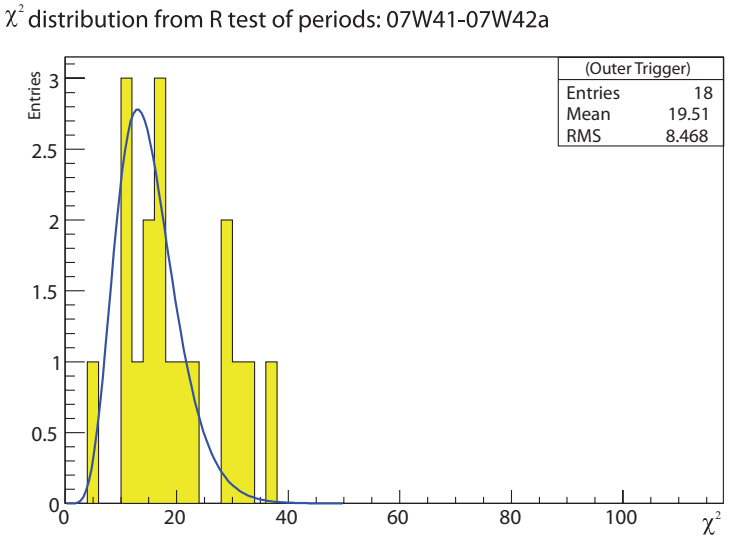

Figure 6.12: The χ^2 distribution of the values from the R test with the theoretical χ^2 curve for 15 degrees of freedom superimposed, only for the Outer triggered events, both for positive and negative hadrons.

associated with a particular trigger when the C.L. associated to the χ^2 value of the R-test is smaller than $\sim 10^{-4}$.
As an example of good R test, related to the Outer trigger the χ^2 distribution for the period week 42b and week 43, both for positive and negative hadrons, is reported in figure 6.13, where the agreement with the expected distribution is good. The final outcome of this test is the rejection of Calorimetric Trigger and High Q^2 trigger from week 25 and 26, the Ladder trigger for week 27 and 28, the Outer trigger for week 41 and 42a. We can also conclude that for the non rejected triggered events, for each cell the ratio of the acceptances in period p_k and after the spin reversal in p_{k+1} results to be constant in Φ_j; this important result will be used later when the double ratio method for the asymmetry extraction will be introduced.

6.5.4 Kinematic stability

The analysis of the kinematic stability of the acquired data is the next step to remove possible instabilities to which the other tests could not be sensitive. For example the bad spill analysis could result insensitive to modifications in the x distribution since it is monitoring macro variables that could not be affected modification for example of x. To accomplish this task a set of variables, chosen since strongly correlated to the quantities entering the asymmetry extraction have been selected and

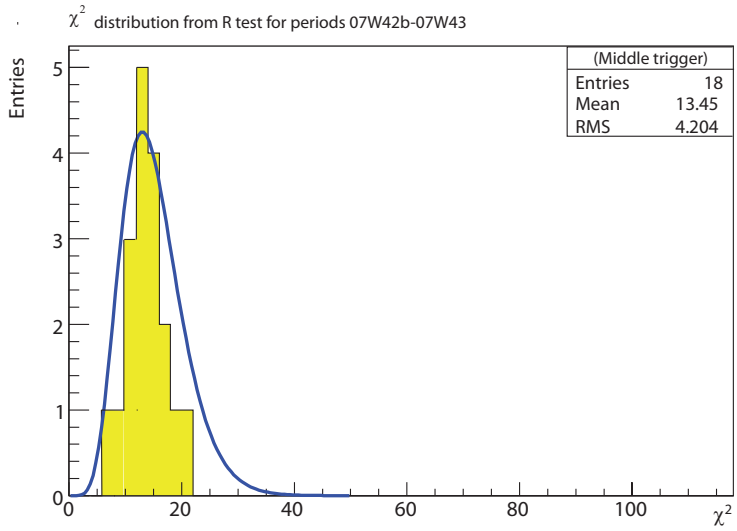

Figure 6.13: The χ^2 distribution of the values from the R test with the theoretical χ^2 curve for 15 degrees of freedom superimposed for week 42b and week 43 related to the middle triggered events.

monitored. The test is divided into a first step, consisting in verifying the variable stabilities for all the runs belonging to the same week (p_k), followed by a similar procedure but developed to check the stability of the same quantities between the two different periods (p_k and (p_{k+1}); since as already mentioned asymmetries are extracted combining data of both the periods.
The list of variable used is:
- z_{vtx}: the primary vertex distribution,
- Q^2: the virtuality of the interaction,
- W: the invariant mass,
- x: the x Bjorken variable,
- y: the fractional energy transfer,
- $E_{\mu'}$: the energy of the scattered muon,
- $\theta_{\mu'}$: the scattered muon polar distribution in the laboratory system,
- P_h^T: the hadron transverse momentum in the GNS,
- $\phi_{had_{LAB}}$: the hadron azimuthal distribution in the laboratory system,
- $\theta_{had_{LAB}}$: the hadron polar distribution in the laboratory system,
- $\phi_{had_{GNS}}$: the hadron azimuthal distribution in the GNS system,
- $\phi_{Spin_{GNS}}$: the nucleon spin azimuthal distribution in the GNS system.

The total distribution for each variable v and for the period p_k: $\mathscr{D}_{k,v}$ is defined

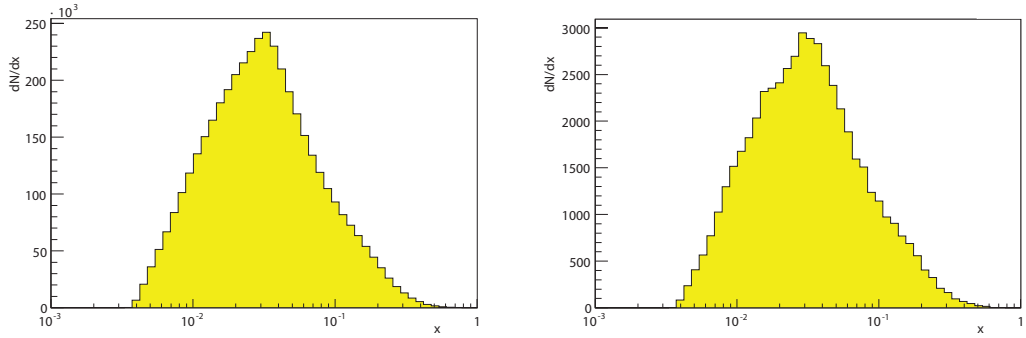

Figure 6.14: Left side: total x distribution. Right side: x distribution for a single run.

as the sum of the distributions of the same variable $\mathscr{D}_{k,v,i}$ of each of the runs (i) belonging to the period p_k: $\mathscr{D}_{k,v} = \sum_i \mathscr{D}_{k,v,i}$, clearly $\mathscr{D}_{k+1,v} = \sum_i \mathscr{D}_{k+1,v,i}$.

Kinematic stability within one period

The goal of this the procedure is the identification for each data taking week of the problematic runs which present anomalous distribution for the mentioned variables. The idea of the method is simple: for each of the previously listed variables the ratio between the variable distribution of a run $\mathscr{D}_{k,v,i}$ and the total distribution $\mathscr{D}_{k,v}$ (see fig 6.14) is computed $\mathscr{R}_{k,v} = \dfrac{\mathscr{D}_{k,v,i}}{\mathscr{D}_{k,v}}$. This ratio is expected to be constant in the whole kinematic range if no problems occurred during the data taking week. $\mathscr{R}_{k,v}$ is fitted with a constant function (see fig 6.15) and the corresponding χ^2_{Ndf} of the fit is extracted. This operation is repeated for all the runs i and results in plots (see fig. 6.14) in which the reduced chi square (χ^2_{Ndf}) versus run number is plotted. If evident problematic runs (i.e. giving very high χ^2_{Ndf}) are detected they are removed by hand after checking in the e-logbook if any problem was reported, then the procedure is repeated excluding them. This is the case of the the hadron azimuthal distribution in the laboratory system in figure 6.16. The deviation of the first runs resulted to be related to a movement of the beam veto.

The χ^2_{Ndf} mean value of the distribution for each kinematic variable ($\langle\chi^2_{Ndf}\rangle_i$) is expected to be centred at 1. During the data analysis it has been notice that the average value of the reduced χ^2 distribution for several kinematic variables is shifted from to a higher value, for example this can be noticed looking at the fit with a constant function intercept (black line) reported on the left side of figure 6.17. The run selection is based on the request that all the χ^2_{Ndf} values, for each variable, must lie within a $3\sigma_i$ interval with respect to the mean of the distribution, right side of figure 6.17. To take into account the shift of the average value of the

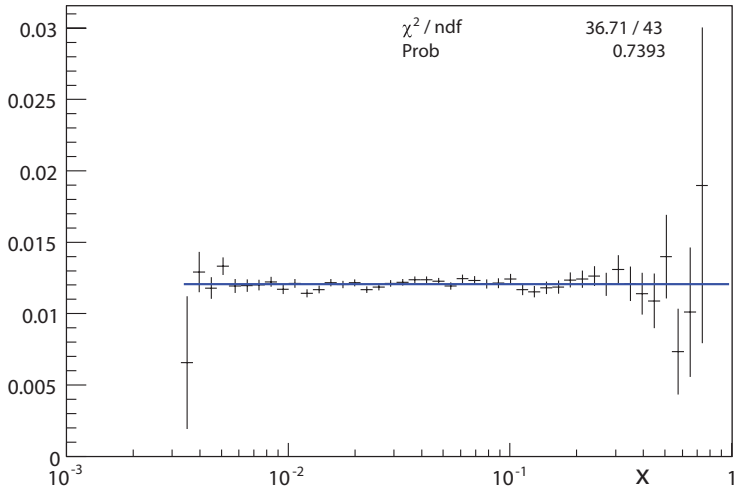

Figure 6.15: Ratio of the two distributions of figure 6.14 and the corresponding fit with a constant function. The χ^2, Ndf and the probability of the fit are shown in the upper part of the plot.

reduced χ^2 the σ_i extracted from the Gaussian fit is scaled for a factor C, where $C = \sqrt{\langle \chi^2_{Ndf} \rangle_i}$.
The presence of at least one values outside the $3\sigma_i$ interval is enough to reject a full run. This operation is repeated for all the available statistics week per week. The result of the procedure is a set of runs for each data taking week in which good homogeneity between the variables distribution of the runs within a single week is guaranteed.

Kinematic stability for coupled periods

The method illustrated in the previous section does not guarantee homogeneity among the several monitored distributions between the two coupled periods, p_k and p_{k+1}. For this reason a nearly identical procedure to the one illustrated before has been applied again, but computing first the ratio $\mathscr{R}_{k,v} = \dfrac{\mathscr{D}_{k,v,i}}{\mathscr{D}_{k,v}}$ then $\mathscr{R}_{k+1,v} = \dfrac{\mathscr{D}_{k+1,v,i}}{\mathscr{D}_{k,v}}$. The comparison between the two different periods, using the same variables, and in particular those which could be different for physics reasons is possible because the physics modulations are much more smaller than the fluctuation given by the statistics. For this reason the same set of kinematic quantities

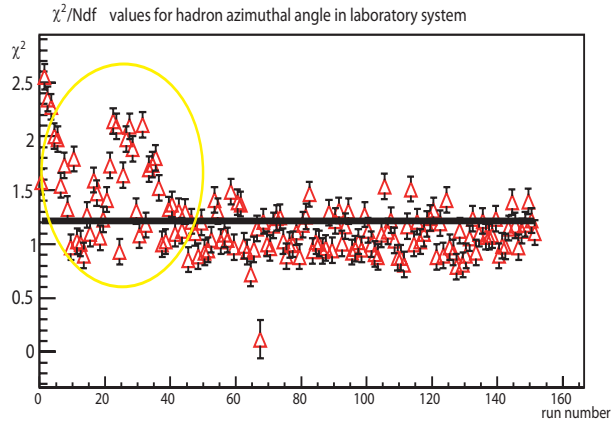

Figure 6.16: χ^2_{Ndf} distribution for the hadron azimuthal angle in the laboratory system for week 27. The first data taking period, nearly 30 runs, has been affected by a beam veto movement as clearly identified by the high values of the reduced χ^2.

were taken into account and the procedure was applied employing the set of runs resulting from the test illustrated in the previous section. Again the resulting distribution of the reduced χ^2 from the fit with a constant function, were fitted with a Gaussian to reject problematic runs. The final result of the full procedure chain of the stability checks is a subsample of the full data suited to be used for the asymmetries extraction. Finally it can be noticed looking at table 6.2 and taking into account the mentioned rejection rate for the other test that this last procedure results to be the most stringent.

6.5.5 Final statistics

Table 6.2 summarises the final rejection rates as % on the total number of hadrons. The asymmetry presented in this thesis are extracted using only the second half of data taking, namely from week 39 to week 43. Due to the fact that the processing of the raw data for the first data taking period was required quasi-online not all the final alignment and calibration constant for the detectors were available at the time. This data before being used need to be reprocessed. This operation requires long time to be performed due to the reduced availability of computing power of the CERN farm, presently nearly 100% dedicated to the 2008 COMPASS hadron run processing. Therefore it has been decided not to use the first half of datataking until a new re-process of the raw data and a full data stability chain will be performed again.

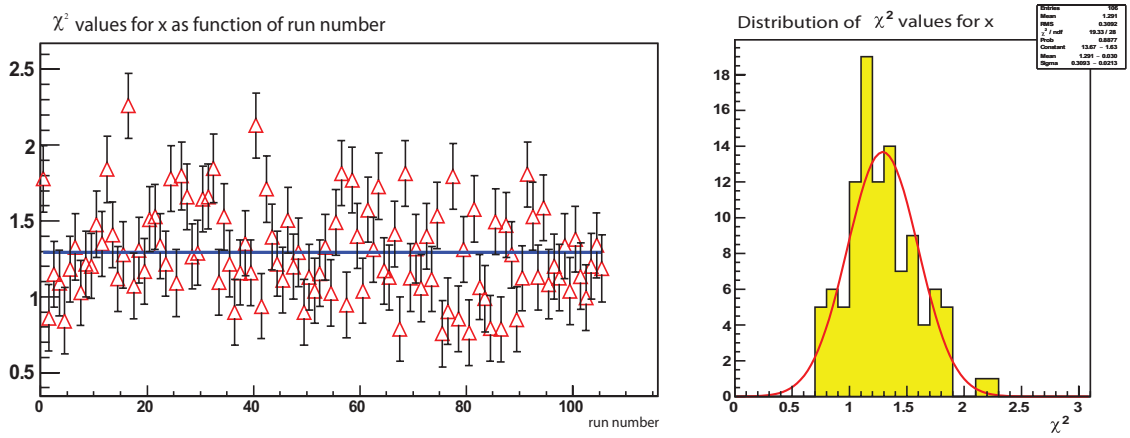

Figure 6.17: Left side: the χ^2_{Ndf} values from the fit with a constant as a function of the run number for the variable x. Right side: the corresponding χ^2_{Ndf} distribution with the Gaussian fit superimposed.

Table 6.3 summarises the statistics entering the analysis for these periods, separately for both charges of the hadron sample.

6.5.6 RICH-1 Particle Identification

The sample of charged hadrons selected so far consists mainly of pions and kaons. To identify them, the Ring Imaging Cherenkov detector RICH-1 is used. A dedicated class of CORAL[66], named RICHONE [150] allows to reconstruct the physical interesting quantities using as input the hits from the photon detectors of the RICH-1 as well as the particle trajectories of the given events. Particle identification using the RICH detector is performed using a Likelihood method. The reconstruction of the RICH data starts with a clustering procedure which is used only for the MWPC part of the detector. This procedure combines individual hits from the photon detectors to clusters, which are expected to correspond to the real photon impact point. A transformation of the cluster coordinates to the $\phi - \theta_{Ch}$ plane is performed, where θ_{Ch} is the polar (Cherenkov) and ϕ the azimuthal angles of the photon relative to the particle trajectory. In this plane the clusters from a given particle distribute along a fixed θ_{Ch} uniformly in ϕ, thus the ring search in the detector plane is equivalent to searching for a peak in the θ_{Ch} projection.
The likelihood is constructed for five mass hypotheses, namely electron, muon, pion,

Week	#runs	hadrons [%]	rejected trigger
25	120	70.6	CT, HQ^2T
26	94	67.4	
27	206	83.5	LT
28	156	96.8	
30	90	31.5	
31	136	39.2	
39	140	39.0	
40	44	25.3	
41	99	39.9	OT
42a	98	52.8	
42b	37	67.7	
43	44	52.5	

Table 6.2: Final rejection rates starting from all produced runs. The events corresponding to some triggers have been discarded as indicated in the last column.

Period	Positive hadrons	Negative hadrons
W39/40	2742704	2149343
W41/W42a	2199513	1752684
W42b/W43	761014	603061
Sum	5703231	4505088

Table 6.3: Final statistics for the 2007 periods used for this analysis.

kaon, and proton:

$$L_N^i = \prod_{k=1}^{N} \left[(1-\eta)G(\theta_k, \phi_k, \theta_i^{Th.}) + B(\theta_k, \phi_k)\right] i \quad \in\ e,\ \mu,\ \pi,\ K,\ p, \tag{6.5}$$

where the product runs over all N photons associated to the track, θ_k is the angle of the k-th photon, $\theta_i^{Th.}$ is the expected Cerenkov angle for a given mass hypothesis i. η is the probability of loosing a photon due to the dead zones of the detector, $G(\theta_k, \phi_k, \theta_i^{Th.})$ and $B(\theta_k, \phi_k)$ parametrise the signal and background contributions respectively. The mass assignments are then done on the basis of the largest likelihood probability among the different mass hypothesis.
The signal contribution to the likelihood $G(\theta_k, \phi_k, \theta_i^{Th.})$ can be conveniently described as a Gaussian centred at the expected angle $\theta_i^{Th.}$ with a spread $\sigma_\theta(\phi_k)$. The advantage of using a likelihood method is that it takes into account the background contribution explicitly. Except for the central upgraded part of the RICH-1 detector, possible contributions to the background are electronic noise, photons from other particles belonging to the same event, but also photons from particles belonging to different events.

Particle Identification: cuts on likelihood

To guarantee a good identification, some cuts on the hadron momentum and on the distribution $\frac{LH}{LH_{2nd}}$ have to be applied.

Cut on momentum

Corresponding to the 1.5σ separation between K and π, an upper limit for accepted momenta of 50 GeV/c has been chosen. A cut is applied above the Cherenkov threshold (p_{th}) to reject particles with no Cherenkov photons. The Cherenkov threshold p_{th} is calculated for a particular particle mass with the corresponding refractive index with the formula:

$$p_{th} = \frac{m}{\sqrt{n^2 - 1}} \tag{6.6}$$

The threshold is computed on a run-by-run basis using the information of the refractive index of the radiator gas. This cut is applied separately for pions and kaons.

Cut on Likelihood variables

The variable $\frac{LH}{LH_{2nd}}$ is the ratio between the highest likelihood, after the identification is performed, with the second highest likelihood for a different mass hypotheses. It indicates the distinction between two different mass hypothesis: if this variable is

near 1, it means that the likelihood of the identified particle and that of the second particle have almost the same value, implying that the distinction between these two particles can be ambiguous. The cuts on this distributions are tuned finding a good compromise in term of purity and efficiency of the sample as illustrated in figure 6.18. For the pions the following cuts are applied:

- p$\geq p_{th}$
- $\frac{LH}{LH_{2nd}} \geq 1.02$

while for identification of kaons:

- p$\geq p_{th}$
- $\frac{LH}{LH_{2nd}} \geq 1.06$

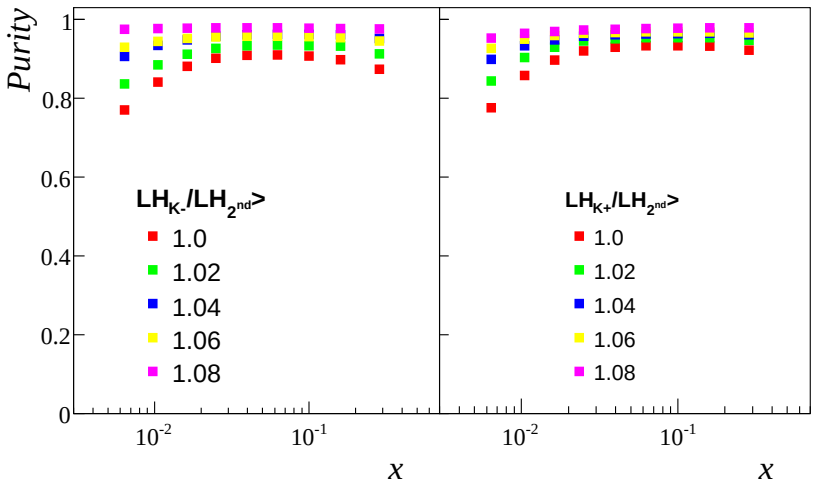

Figure 6.18: Positive and negative Kaons purity as function of the cut $\frac{LH}{LH_{2nd}}$.

Final data sample for RICH identified pions and kaons

Table 6.4 shows the final statistics entering the analysis after all the above cuts were applied, for the periods entering the analysis in 2007 (week 39÷ week 43), for positive and negative pions and kaons.

	Positive	Negative	Sum
Pions	3810915	3305232	7116147
Kaons	706467	433933	1140400
Non identified	545419	403704	949123

Table 6.4: Identified particle sample for all the statistic entering the analysis, on the left side for the positive particles, on the right for the negative.

6.6 Asymmetries extraction

In this section the experimental extraction of raw asymmetries using methods based on the double ratio product, which will be defined in the next section, is explained within the discussion on how the raw asymmetries are corrected with the relevant scaling factors to give physics asymmetries. A special place is occupied by the Unbinned Maximum Likelihood method which is not based on the double ratio product.
The double ratio based extraction methods compare the event yield coming from cells with opposite polarisation in one period $N_u^{\uparrow}$ and $N_d^{\downarrow}$ with the corresponding ones in the period p_{k+1}: $N_u^{\downarrow}$ and $N_d^{\uparrow}$. At least 2 cells with opposite polarisation are required. The presence of tree cells in the target, whose the central one has the double length of the external ones, if split into two virtual sub cells theoretically allows to combine them so that the asymmetry could be calculated just from one data taking period. Several tests have been performed in this direction and the conclusion is that the extraction of asymmetries just from one single period is subject to systematic effects coming from the different acceptances of the cells. For this reason, the asymmetries extraction from the data of one single period have been given up and the extraction is done aways using at the same time the informations coming from cells in two consecutive periods with opposite configuration. A last remark all the binned methods require a correction due to the finite bin size which is discussed in section 6.6.1.
Different methods have been used to extract the asymmetries. The assumptions, the advantage and disadvantages of each of these methods will be shortly described in the following.

6.6.1 Double ratio based methods

All the methods which rely on the use of the double ratio products present several advantages, in particular:

- cancellation of acceptance corrections in the reasonable assumption;

- cancellation of beam flux variations;
- cancellation at first order of spin independent asymmetries;

All the mentioned advantages are cleared up and illustrated in the next sections.

Calculation of the raw asymmetries with the 1-dimensional method

As it has been shown in equation 2.48, and in sections 2.7.2 and 2.7.3 the single spin asymmetries have been defined comparing the cross section on the two different spin target configuration; in particular, in eq. 2.58 and 2.63 it is shown as looking for different azimuthal modulations in the cross section, the Collins and Sivers contributions can be accessed. The hadron yield in both effects, Collins and Sivers, depends on an azimuthal angle, $\Phi_{C,S}$ in the following way:

$$N(\Phi_{C,S}) = \mathfrak{F} n\sigma\, a(\Phi_{C,S})(1 + A^{raw}_{C,S} sin(\Phi_{C,S})); \tag{6.7}$$

where $\mathfrak{F}$ is the muon flux, n the number of target nucleons, σ the spin averaged cross-section, $A^{raw}_{C,S}$ the Collins and Sivers asymmetry and $a(\Phi_{C,S})$ the product of the angular acceptance and the efficiency of the spectrometer. If the angles are always calculated assuming spin up, we get two different rate distributions depending on the real spin direction, This assumption introduces a phase of π in the angle definitions:

$$N^{\uparrow}(\Phi_{C,S}) = \mathfrak{F} n\sigma a^{\uparrow}(\Phi_{C,S})(1 + A^{raw}_{C,S} sin(\Phi_{C,S})); \tag{6.8}$$

$$N^{\downarrow}(\Phi_{C,S}) = \mathfrak{F} n\sigma a^{\downarrow}(\Phi_{C,S})(1 - A^{raw}_{C,S} sin(\Phi_{C,S})). \tag{6.9}$$

To extract the asymmetries with the double ratio method the following ratio is built

$$\mathcal{G}(\Phi) \;=\; \frac{N_u^{\uparrow,p_{k+1}}(\Phi) N_d^{\uparrow,p_k}(\Phi)}{N_u^{\downarrow,p_k}(\Phi) N_d^{\downarrow,p_{k+1}}(\Phi)}; \tag{6.10}$$

here Φ stands for $\Phi_{C,S}$. Writing explicitly the event yield dependence on Φ:

$$\begin{aligned}
\mathcal{G}(\Phi) &= \frac{\mathfrak{F}_{p_{k+1}} n_u \sigma a_u^{\uparrow p_{k+1}}(\Phi)(1 + A^{raw}_{C,S} sin(\Phi)) \mathfrak{F}_{p_k} n_d \sigma a_d^{\uparrow p_k}(\Phi)(1 + A^{raw}_{C,S} sin(\Phi))}{\mathfrak{F}_{p_k} n_u \sigma a_u^{\downarrow p_k}(\Phi)(1 - A^{raw}_{C,S} sin(\Phi)) \mathfrak{F}_{p_{k+1}} n_d \sigma a_d^{\downarrow p_{k+1}}(\Phi)(1 - A^{raw}_{C,S} sin(\Phi))} \\
&= D \frac{a_u^{\uparrow p_{k+1}}(\Phi) a_d^{\uparrow p_k}(\Phi)}{a_u^{\downarrow p_k}(\Phi) a_d^{\downarrow p_{k+1}}(\Phi)} \frac{(1 + A^{raw}_{C,S} sin(\Phi))(1 + A^{raw}_{C,S} sin(\Phi))}{(1 - A^{raw}_{C,S} sin(\Phi))(1 - A^{raw}_{C,S} sin(\Phi))} \\
&\approx D \frac{a_u^{\uparrow p_{k+1}}(\Phi) a_d^{\uparrow p_k}(\Phi)}{a_u^{\downarrow p_k}(\Phi) a_d^{\downarrow p_{k+1}}(\Phi)} \cdot (1 + 4 A^{raw}_{C,S} sin(\Phi))
\end{aligned} \tag{6.11}$$

at the first order in $A^{raw}_{C,S}$. The projection of the data only on the angle of interest (Collins, Sivers) is possible since all the modulation in the equation 2.48 are linearly independent.

The ratio is calculated in 16 equal bins over the range of $\Phi_{C,S}$ and plotted against $\Phi_{C,S}$. The statistical error on the ratio is estimated from eq. 6.10 as:

$$\sigma^2_{\mathcal{G}(\Phi)} = [\mathcal{G}(\Phi)]^2 \cdot \left[\frac{1}{N_u^{\uparrow,p_{k+1}}} + \frac{1}{N_d^{\uparrow,p_k}} + \frac{1}{N_u^{\downarrow,p_{k+1}}} + \frac{1}{N_d^{\downarrow,p_k}}\right]. \tag{6.12}$$

The ratio values as a function of $\Phi_{C,S}$ are fitted with a sin amplitude with two free parameters, $par(0) \cdot (1 + par(1)sin(\Phi))$; from $par(1)$ the asymmetry is extracted as $A^{raw}_{C,S} = par(1)/4$.
We assume the assumption to hold:

$$\frac{a_u^{\uparrow p_{k+1}}(\Phi) a_d^{\uparrow p_k}(\Phi)}{a_u^{\downarrow p_k}(\Phi) a_d^{\downarrow p_{k+1}}(\Phi)} = const, \tag{6.13}$$

or

$$\frac{a_u^{\uparrow p_{k+1}}(\Phi)}{a_d^{\downarrow p_{k+1}}(\Phi)} = const \frac{a_u^{\downarrow p_k}(\Phi)}{a_d^{\uparrow p_k}(\Phi)}. \tag{6.14}$$

In this way we can assume the asymmetry extraction via equation 6.12 is not biased by a modulation dependence on Φ originating from the term factorising $(1+4A^{raw}_{C,S} sin(\Phi))$ in the same equation. In section 6.5.3 the assumption of constant spectrometer acceptance has been verified. The main disadvantage of this method is that the integration on all other angles appearing in the 2.48 introduces a correlation due to the acceptance between the extracted asymmetry amplitudes.

Calculation of the raw asymmetries with the 2-dimensional method

Instead of projecting the data on the angle of interest (Collins, Sivers) a second approach consists in building a matrix of counts as a function of the two azimuthal experimental angles ϕ_h and ϕ_s and fit the ratio given by equation 6.10, with a function which incorporates all the relevant modulation present in the cross-section, i.e.:

$$\begin{aligned}\mathcal{G}(\phi_h, \phi_S) = A_0 \cdot (1 + 4(&A_1^{raw}\, sin(\phi_h + \phi_S - \pi) + A_2^{raw}\, sin(3\phi_h - \phi_S) \\ &A_3^{raw}\, sin(\phi_h - \phi_S) + A_4^{raw}\, cos(\phi_h - \phi_S) + A_5^{raw}\, sin(\phi_S) + \\ &A_6^{raw}\, sin(2\phi_h - \phi_S) + A_7^{raw}\, cos(\phi_S) + A_8^{raw}\, cos(2\phi_h - \phi_S)).\end{aligned} \tag{6.15}$$

The raw asymmetries are obtained from the fitted parameters after correcting for the bin width (see section 6.6.1). The eight term entering the fit function expression are nothing else than the 8 independent modulations in the cross section for transversely polarised target described in equation 2.48.
The main advantage of this method with respect to the 1-dimensional fit, which

projects over one of the angles, is that the correlations introduced by the apparatus acceptance are taken into account. The disadvantage related to the statistics entering the matrix of counts since sometime the number of counts within one bin is too small and the errors in the double ratio are no longer Gaussian.

Calculation of the raw asymmetries with a modified version of 1-dimensional method

This method is a modified version of the 1-dimensional fit in which the correlation between the different asymmetries introduced by the spectrometer acceptance are expected to cancel. The main idea is to build a 8 x 8 grid in (Φ_j, ϕ), where Φ_j is the angle corresponding to the asymmetry one wants to measure (Collins, Sivers, ...) and ϕ is any independent angle (typically ϕ_h or ϕ_s). The ratio products quantities $A_j(\Phi_j, \phi)$ are evaluated in each of the 64 bins. Then the arithmetic mean of the 8 quantities corresponding to the same value of Φ_j are evaluated to get the values of the ratio products $A_j^M(\Phi_j)$ in the 8 Φ_j bins. Finally, 1D fits with the same functions used in the 1D method are done to extract the raw asymmetries. The correction due to the Φ_j bin width, which can be not negligible, has been applied (see section 6.6.1). This method has the following advantages:
- with respect to the previous 1D method, the integration on all the other angles is avoided, thus preventing the introduction of correlations due to the acceptance, since the quantities $A_j(\Phi_j, \phi)$ are evaluated on the 2D grid;
- with respect to the 2D method, allows to reduce the effect of the overlapping of the bins when calculating the Collins or Sivers or the other relevant angles starting from the central values in each (ϕ_h, ϕ_s), which, strictly speaking, can be corrected only if the acceptance is flat;
- uses the ratio products, which have the advantages described before.

Calculation of the raw asymmetries with 2-Dimensional Fit to Counts

When using the double ratio method in the one or two dimensional case, the errors on the extracted asymmetries are determined assuming Gaussian distributions of the counts in each bin and Gaussian error propagation[151]. However, the distribution of the double ratio does not have to follow a Gaussian distribution. This is especially true in the case of a low number of counts, where even the Gaussian assumption for the individual factors does not hold anymore. One possibility is to leave out such bins in the fit. A different approach for the calculation of asymmetries is a fit of count rates in bins of ϕ_h and ϕ_s [152]. Using a two dimensional binning in ϕ_h and ϕ_S, the number of counts in a given bin j can be described by

$$N_{j,\mathrm{u,d}}^{\uparrow\downarrow} = \mathfrak{F}_{\mathrm{p}_k,\mathrm{p}_{k+1}} n_{\mathrm{u,d}} \sigma a_{j,\mathrm{u,d}}^{\uparrow\downarrow} \left(1 \pm \sum_i A_i^{raw} \sin(\Phi_j^i)\right). \tag{6.16}$$

Where all the quantities entering equation 6.16 have been defined in 6.6.1. The bin number is $j = \{1, 2, ..64\}$ for an eight by eight binning. A_i^{raw} and Φ_j^i correspond to the eight modulations of the cross-section evaluated for the bin j in equation 2.48. The sign of the polarised amplitude is positive or negative depending on the polarisation in the corresponding cell and period. Since from the number of counts one cannot isolate $n_{\mathrm{u,d}}$, σ and $a_{j,\mathrm{u,d}}^{\uparrow\downarrow}$, all these terms are reabsorbed in the following way: $a_{j,\mathrm{u,d}}^{\uparrow\downarrow} = n_{\mathrm{cell}}\sigma\tilde{a}_{j,\mathrm{u,d}}^{\uparrow\downarrow}$. The total number of free parameters left is $4m^2 + 12$ for a m by m binning with $4m^2$ data points. Extra constraints, needed to solve the equation, come from the acceptances relations in each bin given by the assumption in equation 6.13. Since the flux parameter is linear dependent on the other parameters, four equations are left to describe the number of counts for the two cells in each polarisation state.

$$\begin{aligned} N_{ju}^{\uparrow} &= D\frac{a_{jd}^{\downarrow}a_{ju}^{\downarrow}}{a_{jd}^{\uparrow}}\left(1 + \sum_i A_i^{raw}\sin(\Phi_j^i)\right) \qquad N_{jd}^{\downarrow} = a_{jd}^{\downarrow}\left(1 - \sum_i A_i^{raw}\sin(\Phi_j^i)\right) \\ N_{ju}^{\downarrow} &= a_{ju}^{\downarrow}\left(1 + \sum_i A_i^{raw}\sin(\Phi_j^i)\right) \qquad N_{jd}^{\uparrow} = a_{jd}^{\uparrow}\left(1 \sum_i A_i^{raw}\sin(\Phi_j^i)\right) \end{aligned} \tag{6.17}$$

Where D is a constant factor coming from equation 6.13. Eq. 6.17 is a nonlinear system of equations. A well known way to find a solution of these is the Levenberg-Marquardt (LM) algorithm [153][154]. The LM-algorithm solves the problem of minimising $\|\vec{H}(\vec{a})\|^2$, with respect to the vector of arguments $\vec{a}$ of the general function $\vec{H}(\vec{a})$. This is done iteratively by solving the linearised version of the problem

$$\min_{\vec{a}} \|\vec{H}(\vec{a}_k)J(\vec{a}_k)(\vec{a} - \vec{a}_k)\|^2. \tag{6.18}$$

Here J denotes the Jacobian of H. A solution can be found by rearranging eq. 6.18 to

$$J^T J(\vec{a}_k - \vec{a}) = J^T H(\vec{a}_k). \tag{6.19}$$

The choice of H has to be taken, such that a solution of 6.18 is also a solution of 6.17, in the maximum likelihood sense. Let N_j be the number of counts in one bin and the fit function evaluated in that bin $h_j(\vec{a})$, the target function is chosen as

$$H_j = (N_j - h_j(\vec{a}))/\sigma_j, \tag{6.20}$$

where σ_j is the error on the number of counts N_j. If the number of counts is too low to make the Gaussian assumption so that the error can be approximated by $\sigma_j = \sqrt{N}$, the derivation of the H_j has to be made with the Poisson probability. This is given for bin number j as

$$P(\vec{a}) = \frac{e^{-h_j(\vec{a})}h_j(\vec{a})^{N_j}}{N_j!}. \tag{6.21}$$

Computing the log likelihood with this probability distribution leads to the minimisation of the corresponding function given by:

$$\sum_j 2(h_j(\vec{a}) - N_j) + 2N_j \ln(N_j/h_j(\vec{a})). \tag{6.22}$$

The target function H_j was always derived with the Poisson probability:

$$H_j = \sqrt{2}\sqrt{h_j(\vec{a}) - N_j + N_j \ln(N_j/h_j(\vec{a}))}. \tag{6.23}$$

The advantage of this method is the same as described before for the 2-dimensional method, avoiding also the Gaussian assumption in case of low statistics.

Corrections due to Finite Bin Size

For any binned method, that is a method that uses a binned histogram to which the azimuthal modulations are fitted, one has to account for effects due to the finite bin size [155]. Because the fit is done to the value at the centre of the bin or at the centre of gravity, one has to compare the mean value of the fit function over the bin range with the value of the function at the point of evaluation. Alternatively the value of the integral of the fit function can be fitted to the value of the bin. But since the relation of the integral to the value of the function in the middle of the bin can be determined analytically the added complexity can be avoided by correcting the obtained amplitudes with the true value of the function at the point of evaluation divided by the mean value. The true value is chosen such that the integral over the bin equals the bin content. For the one dimensional case this approach can be illustrated by considering the function

$$f(\Phi) = 1 + a\cos(\Phi) + b\sin(\Phi) \tag{6.24}$$

The mean value of $f(\Phi)$ in a bin (Φ_i, Φ_{i+1}) is

$$\langle f(\Phi)\rangle_{i,i+1} = \frac{1}{\Delta\Phi}\int_{\Phi_i}^{\Phi_{i+1}} f(\Phi)d\Phi. \tag{6.25}$$

For n bins, the bin width is $\Delta\Phi = 2\pi/n$. The standard fit is done to the mean value of $f(\Phi)$ at the centre of the bin. But the true value of the function at the centre of the bin is given by

$$f(\Phi_i + \Delta\Phi/2) = 1 + a\cos(\Phi_i + \Delta\Phi/2) + b\sin(\Phi_i + \Delta\Phi/2). \tag{6.26}$$

The two values $\langle f(\Phi)\rangle_{i,i+1}$ and $f(\Phi_i + \Delta\Phi/2)$ are not equal. Their difference depends on the number of bins. For the limiting case $n \to \infty$ the difference vanishes and for

the other cases the relation between the real amplitudes, a and b, and the amplitudes as extracted from the fit, a_{fit} and b_{fit}, can be analytically determined to be:

$$a_{\text{fit}} = a\frac{2}{\Delta\Phi}\sin\frac{\Delta\Phi}{2} \qquad b_{\text{fit}} = b\frac{2}{\Delta\Phi}\sin\frac{\Delta\Phi}{2}. \tag{6.27}$$

Evaluating these relations leads to a correction factor $a_{\text{fit}}/a = b_{\text{fit}}/b$ in the one dimensional case with 16 bins of 0.9936. Albeit the correction is very small, it is different for the two dimensional fits presented in sec. 6.6.1. Here, due to the higher overall bin number, the number of bins in each direction is chosen as eight. This corresponds to 64 bins overall. Then the amplitudes given in the full cross-section in eq. 2.48 can be described in the general form [155]

$$f(\Phi_h, \Phi_S) = 1 + \sum_{k=-1}^{3} (a_k \sin(k\Phi_h - \Phi_S) + b_k \cos(k\Phi_h - \Phi_S)). \tag{6.28}$$

Using the same logic as before the correction factors can be extracted as

$$\begin{aligned} a_{k,\text{fit}} &= a_k \frac{2}{k\Delta\Phi_h}\sin\frac{k\Delta\Phi_h}{2}\frac{2}{\Delta\Phi_S}\sin\frac{\Delta\Phi_S}{2} \\ b_{k,\text{fit}} &= b_k \frac{2}{k\Delta\Phi_h}\sin\frac{k\Delta\Phi_h}{2}\frac{2}{\Delta\Phi_S}\sin\frac{\Delta\Phi_S}{2}. \end{aligned} \tag{6.29}$$

For the eight times eight binning used in the following, the correction factor for extracting Collins or Sivers evaluates to 0.87735. A last remark, the correction due to the finite bin size is included in ROOT package[156].

6.6.2 Unbinned maximum likelihood estimator

A special place is dedicated to the unbinned maximum likelihood since it has all the advantages of the previously described fit methods and due to its general approach can be used also when the statistical sample is quite poor. The likelihood technique is based on the evaluation of the probability, for a given set of parameters, of observing the particular data set measured. The best combination of the parameters is then chosen as that which maximises the probability. In our measurement, for each x, p_T, z bin of interest, we have N hadrons and we consider the variables (ϕ_S, ϕ_h). The probability of observing the set of N variables (ϕ_S, ϕ_h) for a set of parameters $a_1, \cdots, a_m$ is given by the product of the probability for each hadron:

$$\mathcal{L} = \prod_{i=0}^{N} p(\phi_S^i, \phi_h^i; a_1, \cdots, a_m) \ ; \tag{6.30}$$

where the probability density p is normalised to unity in the (ϕ_S, ϕ_h) range:

$$\int p(\phi_S, \phi_h; a_1, \cdots, a_m) d\phi_S d\phi_h = 1 \ . \tag{6.31}$$

The probability p contains two parts, the acceptance $\mathcal{A}$ and the cross section σ:

$$p(\phi_S, \phi_h; a_1, \cdots, a_m) \propto \mathcal{A}(\phi_S, \phi_h; a_1, \cdots, a_l) \cdot \sigma(\phi_S, \phi_h; a_{l+1}, \cdots, a_m) \tag{6.32}$$

the two parts depending on different parameters. More precisely, the acceptance is described with a Fourier series:

$$\mathcal{A}(\phi_S, \phi_h; a_1, \cdots, a_l) \propto 1 + \sum_{j,k} (c_{jk}\, cos(j\phi_S \pm k\phi_h) + s_{jk}\, sin(j\phi_S \pm k\phi_h)); \tag{6.33}$$

where the free parameters are now indicated as c_{jk} and s_{jk}. The cross section contains both the unpolarised and the polarised part[6]:

$$\begin{aligned} \sigma \propto 1 + U_1 cos(\phi_h) + U_2 cos(2\phi_h) \pm (\epsilon_1 sin(\phi_h + \phi_S - \pi) + \epsilon_2 sin(3\phi_h - \phi_S) + \\ \epsilon_3 sin(\phi_h - \phi_S) + \epsilon_4 cos(\phi_h - \phi_S) + \epsilon_5 sin(\phi_S) + \\ \epsilon_6 cos(2\phi_h - \phi_S) + \epsilon_7 cos(\phi_S) + \epsilon_8 sin(2\phi_h - \phi_S)) \ ; \end{aligned} \tag{6.34}$$

U_1 and U_2 are the unpolarised asymmetries ($\cos\phi$ is the so called "Cahn" effect), while $\epsilon_1 \cdots \epsilon_8$ are the single spin asymmetries measurable with a transverse polarised target. In particular, ϵ_1 is the Collins asymmetry and ϵ_3 is the Sivers asymmetry. In order to obtain the parameters of interest, the likelihood has to be maximised; what is done is to minimise the expression:

$$-ln(\mathcal{L}) = -\sum_{i=0}^{N} ln(p(\phi_S^i, \phi_h^i; a_1, \cdots, a_m)); \tag{6.35}$$

using the Minuit program.
In order to provide a good description of the acceptance and on the same time to avoid a large number of parameters, some preliminary fits of the acceptance have been performed. An example of acceptance description is in given fig. 6.19. The effectiveness of the likelihood fit has been tested using MC samples. In the MC, (ϕ_S, ϕ_h) values have been generated with an acceptance function similar to the real one and with different asymmetries values. The fit has always converged, and the resulting values have been found distributed in a Gaussian way around the values used at generation level.
Several test have been performed to compute the asymmetries also from real data from two coupled periods. The result obtained are very promising since all possible combination of data from the cells such as the asymmetries extraction from a fit of all the events coming from the 3 cells and the asymmetries evaluated as the weighted mean from 3 independent fits on the 3 cells showed to be in very good agreement.

[6]The equation is another way of writing the formula 2.48

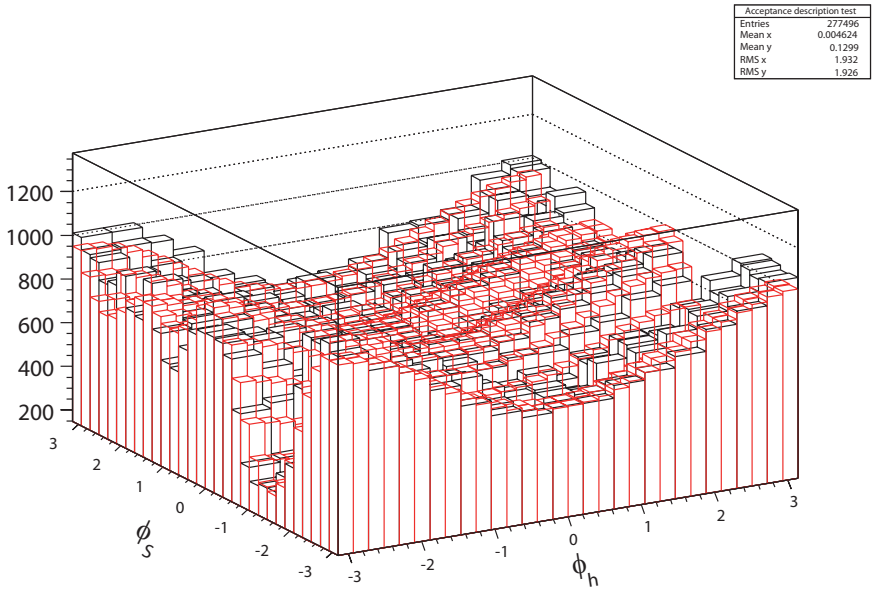

Figure 6.19: Example of (ϕ_S, ϕ_h) distribution in one x bin with superimposed the acceptance curve obtained with the likelihood fit.

6.6.3 From experimental to final asymmetries

The final Collins and Sivers asymmetries are related to the raw asymmetries via their respective scaling factor. The Collins asymmetry is extracted from the raw asymmetry through the expression:

$$A_{Coll} = \frac{A_C^{raw}}{D_{NN} \cdot f \cdot P_T}. \tag{6.36}$$

The depolarisation factor $D_{NN} = \frac{2(1-y)}{1+(1-y)^2}$ is calculated from the kinematics of each event; it is evaluated in each bin for all the events entering in the asymmetry extraction and the mean value for each bin is taken. The dilution factor is taken constant as $f = 0.15$. The values of target polarisation are reported in table 6.1.
The Sivers asymmetry is extracted from the raw asymmetry through the expression

$$A_{Siv} = \frac{A_S^{raw}}{f \cdot P_T}\ ; \tag{6.37}$$

in the Sivers case D_{NN} is equal to 1, since the photon couples to an unpolarised quark in a transversely polarised nucleon.

x	z	P_T^h
$0.003 < x < 0.008$	$0.20 \leq z < 0.25$	$0.10 < P_T^h \leq 0.20$ GeV/c
$0.008 \leq x < 0.013$	$0.25 \leq z < 0.30$	$0.20 < P_T^h \leq 0.30$ GeV/c
$0.013 \leq x < 0.020$	$0.30 \leq z < 0.35$	$0.30 < P_T^h \leq 0.40$ GeV/c
$0.020 \leq x < 0.032$	$0.35 \leq z < 0.40$	$0.40 < P_T^h \leq 0.50$ GeV/c
$0.032 \leq x < 0.050$	$0.40 \leq z < 0.50$	$0.50 < P_T^h \leq 0.60$ GeV/c
$0.050 \leq x < 0.080$	$0.50 \leq z < 0.65$	$0.60 < P_T^h \leq 0.75$ GeV/c
$0.080 \leq x < 0.130$	$0.65 \leq z < 0.80$	$0.75 < P_T^h \leq 0.90$ GeV/c
$0.130 \leq x < 0.210$	$0.80 \leq z < 1.00$	$0.90 < P_T^h \leq 1.30$ GeV/c
$0.210 \leq x < 1.000$		$1.30 < P_T^h$

Table 6.5: Bins in x, z, and P_T^h.

6.7 Results

The results for the Collins and Sivers asymmetries from the 2007 data for unidentified hadrons are shown in figure 6.20 and in figure 6.21 respectively for positive and negative hadrons. The method used for the extraction is the fit to counts described in 6.6.1. The errors bars are the statistical errors only, the systematic error evaluation will be described in section 6.8. The overall asymmetries are the result of a weighted mean of the asymmetry measured for each transversity data taking period. The Collins and Sivers asymmetries were evaluated as a function of x, P_T^h, and z integrating over the other two variables; the binning chosen is shown in table 6.5.
The Collins asymmetry (figure 6.20) is small, statistically compatible with zero up to $x = 0.05$ while a signal is visible in the last points, the asymmetry then increases in module up to 10% with opposite sign for positive and negative hadrons. For P_T^h and z the asymmetry amplitude is compatible with zero due to the fact that most of the statistical sample is in the low x region.
At variance with A_{Coll}, the Sivers asymmetry (figure 6.21) is small and statistically compatible with zero for both positive and negative hadrons over all the measured x range. Moving to identified hadrons in figure 6.22 the Collins (top) and the Sivers (bottom) asymmetries are shown for identified pions. As expected the behaviour of the asymmetry is similar to the non identified hadron one, since nearly 80% of the hadrons are pions.
The PID allows to extract the asymmetries also for the positive and negative kaons sample. In figure 6.23 and 6.24 even with limited statistics, (see table 6.4) The Collins and the Sivers asymmetries for the positive and negative kaons are shown.

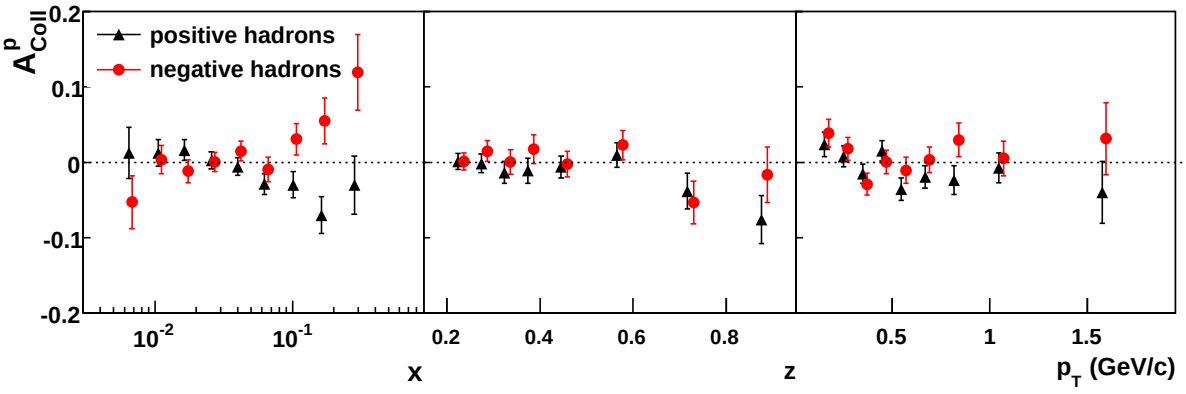

Figure 6.20: Collins asymmetries for positive unidentified hadrons (triangles) and for negative unidentified hadrons (circles) as function of x, P_T^h, and z.

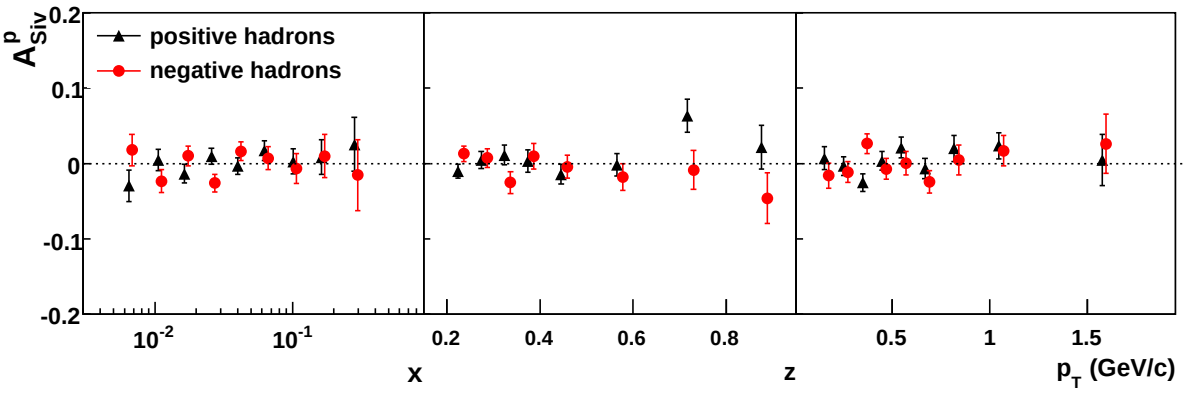

Figure 6.21: Sivers asymmetries for positive unidentified hadrons (black) and for negative unidentified hadrons (circles) as function of x, P_T^h, and z.

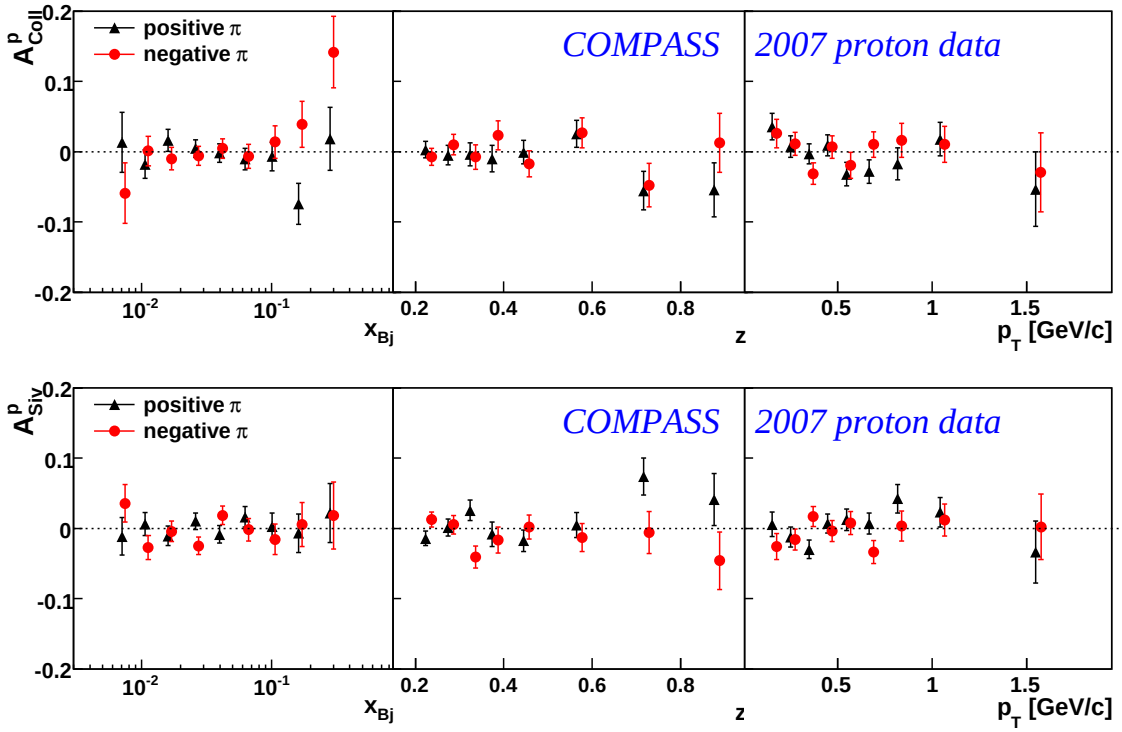

Figure 6.22: Top: Collins asymmetries for positive pions (triangles) and for negative pions (circles) as function of x, P_T^h, and z. Bottom: Sivers asymmetries for positive pions (triangles) and for negative pions (circles) as function of x, P_T^h, and z.

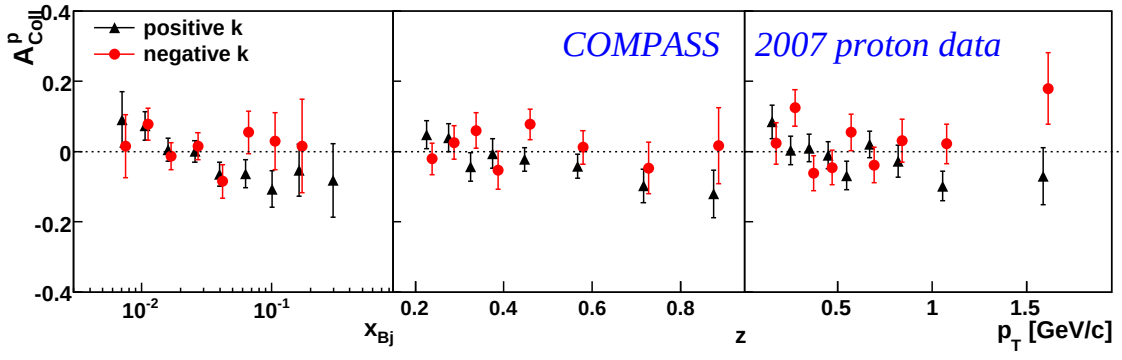

Figure 6.23: Collins asymmetries for positive kaons (triangles) and for negative kaons (circles) as function of x, P_T^h, and z.

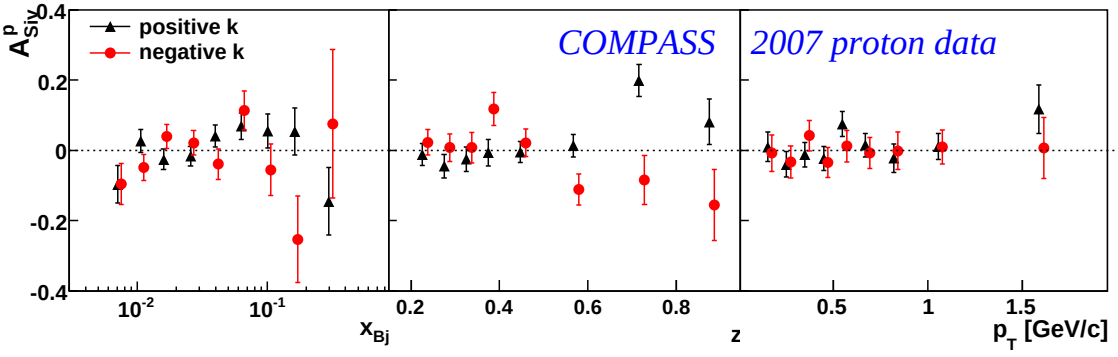

Figure 6.24: Sivers asymmetries for positive kaons (triangles) and for negative kaons (circles) as function of x, P_T^h, and z.

6.8 Systematic studies

Several tests were performed to investigate possible systematic effects affecting the result. The main task of this analysis is to quantify the size of the systematic errors. The tests performed are:

- False asymmetry evaluation.
- Compatibility of the results for the different periods.
- Dependence of the result on the target cell splitting.
- Dependence of the result on the vertex position.
- Effect of different estimators.

In order to evaluate possible false asymmetries many tests were done on the unidentified sample hadron sample from 2007 data. In particular asymmetries expected to be zero have been built splitting the central target cells in two parts and combining the data from the same cell or scrambling randomly the data collected.

6.8.1 Target configuration definitions

The middle cell of the target was split in two parts in order to work with four different cells. With these cells four different *configurations* can be defined, referring to figure 6.4 and 6.25: $conf_0$ is built using cells $(U_j, C_{1,j})|_{j=p_k,p_{k+1}}$, $conf_1$ with $(C_{2,j}, D_j,)|_{j=p_k,p_{k+1}}$ and are used to calculate the physics asymmetries by combining the events of two consecutive weeks with opposite target polarisations. Configurations $conf_2$ and $conf_3$ couple cells with the same sign of polarisation: $(U_j, D_j)|_{j=p_k,p_{k+1}}$,

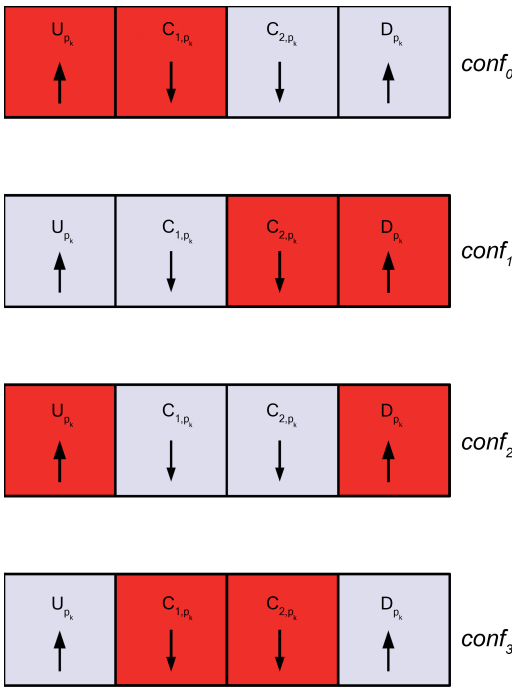

Figure 6.25: Target configurations: the red marked cells are used for the analysis. The configuration names are on the right side, the corresponding cells for the period p_{k+1} have been omitted.

$(C_{2,j}, C_{1,j})|_{j=p_k,p_{k+1}}$. Assuming the wrong sign of the polarisation in one of the two cells the false asymmetries measured by combining the events of two consecutive weeks, are used to investigate systematics. Finally configuration $conf_4$ was built as a combination of $conf_0$ and $conf_1$ by summing the data of all four cells. $conf_4$ was also used as an alternative way to evaluate the physics asymmetries $(U_j + D_j, C_{2,j} + C_{1,j})|_{j=p_k,p_{k+1}}$.

6.8.2 False asymmetry results

The results for the false Collins asymmetry, measured with conf_2, for positive and negative hadrons and for all periods are shown in figure 6.26. In Figure 6.27 the results for the false Sivers asymmetry measured with the different combination conf_3 for positive and negative hadrons are shown. Given the fact that we are calculating an asymmetry using data from cells with the same spin orientation, obviously the sign of the asymmetry, not defined by the physics, is a matter of choice. In the calculation the upstream cell U_{p_j} was always assigned with the correct polarisation and the cell C_{1,p_j} with the opposite. All the extracted false asymmetries, using

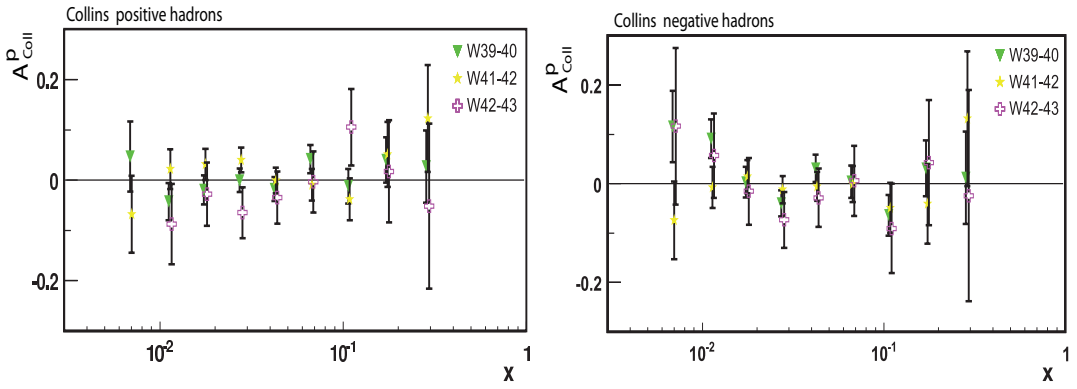

Figure 6.26: False Collins asymmetries for positive unidentified hadrons (left) and for negative unidentified hadrons (right) as function of x for all the 2007 data taking periods with target conf_2.

both the configuration conf_2 and conf_3 resulted to be small and compatible with zero.

6.8.3 Compatibility of the measurements

The measured asymmetries are given by the weighted mean of the asymmetry results obtained from the used data taking periods. The statistical compatibility among the periods have been checked by looking at the distribution of the following quantity:

$$f_i = \frac{A_i - \langle A \rangle}{\sqrt{\sigma_i^2 - \sigma_{\langle A \rangle}^2}} \qquad i = 1, 3 \tag{6.38}$$

where A_i are the asymmetries of each x, P_T^h, z bin and $\langle A \rangle$ is the corresponding weighted mean. In the denominator the difference of the variances takes into account the correlation between A_i and $\langle A \rangle$. This distribution has been calculated for different subsamples, i.e. separately for Collins and Sivers asymmetries and for positive and negative hadrons. In the case of the Collins asymmetry, both for negative and positive hadrons the distributions are as expected, i.e.: mean values compatible with zero and RMS values close to unity (see fig. 6.28), and this is true also for Sivers asymmetries.

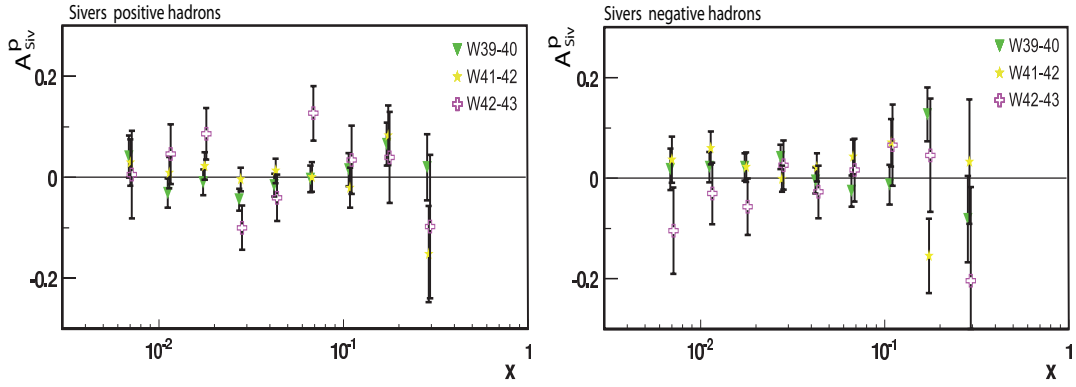

Figure 6.27: False Sivers asymmetries for positive unidentified hadrons (left) and for negative unidentified hadrons (right) as function of x for all the 2007 data taking periods with target conf_3.

6.8.4 Dependence on the target cells configurations conf_0 and conf_1

Due to the splitting of the middle cell two configurations both conf_0 and conf_1 contain the same physical asymmetries (figure 6.25). To check the dependence from the target cell the pulls between the asymmetries extracted from these configurations have been computed:

$$g_i = \frac{A_{conf_0} - A_{conf_1}}{\sqrt{\left(\sigma^2_{conf_0} + \sigma^2_{conf_1}\right)}} \tag{6.39}$$

for all the points in x, z and P_T^h. In this case the samples are independent and so we have the sum of the variances at the denominator. Results are shown in figure 6.29.

On the top row the distributions calculated for the Collins asymmetries, while in the bottom row the same plots for the Sivers asymmetries are shown. The sigmas of both distributions are compatible with one, however the mean value of the negative hadrons distribution is shifted by -0.19 in terms of sigma [7]. For positive hadrons no shift is observed. In the bottom part of the same figure the the corresponding pulls for the Sivers asymmetry are shown. The sigmas of both distributions are compatible with one. However the mean value of the negative hadrons distribution is shifted by -0.29 in terms of sigma, for positive hadrons -0.17 in terms of sigma. The contribution to the systematic error for each of the sources has been obtained as mean value between its positive and its negative terms.

[7] $\sigma = \sqrt{\left(\sigma^2_{conf_0} + \sigma^2_{conf_1}\right)}$

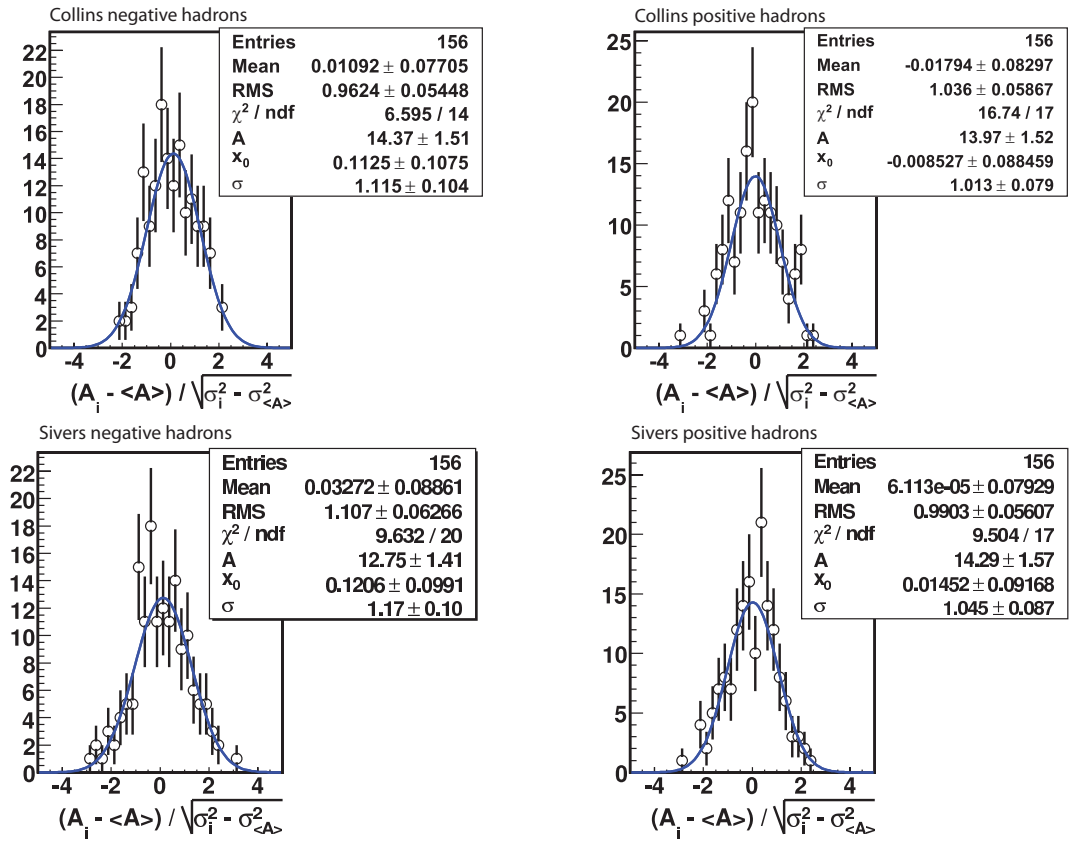

Figure 6.28: Top: f_i as defined in equation 6.38 for the Collins asymmetry: On the left side for negative hadrons, on the right for the positive ones. Bottom: f_i for Sivers asymmetry on the left for negative hadrons, on the right for positive hadrons. All the distributions show no deviations within statistics from the expected values.

6.8.5 Dependence on vertex position

To check if the measured asymmetries depend on the transverse position of the primary vertex the target was divided into segments, as shown in figure 6.30. The red coloured regions indicate the parts of the target used in the calculation. The pulls h_i between the two measurements obtained using the different target sector (Seg_i) have been computed for all the asymmetries in x, z and P_T^h:

$$h_{i,j} = \frac{A_{Seg_i} - A_{conf_j}}{\sqrt{\left(\sigma^2_{Seg_i} + \sigma^2_{Seg_j}\right)}} \tag{6.40}$$

where the indexes i, j stand respectively for Seg_1 and Seg_2 or Seg_3 and Seg_4. The so called conf_4 defined in section 6.8.1 has always been used in this particular test.

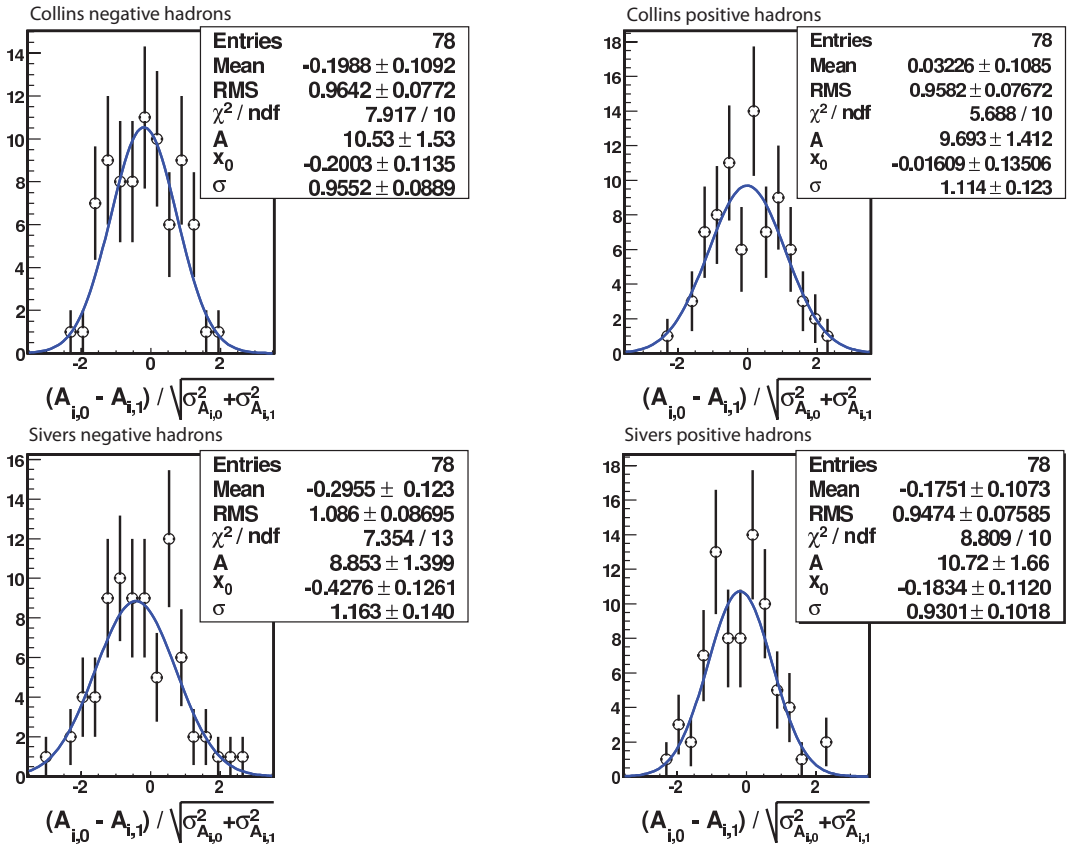

Figure 6.29: Top: pulls for Collins for conf_0 minus conf_1. Left negative hadrons, right positive. Bottom: pulls for Sivers for conf_0 minus conf_1. Left negative hadrons, right positive.

Figure 6.31 shows the results for the Collins asymmetry for negative and positive hadrons. Referring to equation 6.40: on the top the distributions $h_{i,j}$ are shown for i, j=Seg_1, Seg_2 (left and right segments) for positive hadrons on the left side and for negative hadrons on the right one. The bottom part of the same figure show the results for $h_{i,j}$ with i, j=Seg_3, Seg_4 (top and bottom segments) again for both the hadron charges. All the four distributions show the expected statistical behaviour: mean compatible with zero and RMS compatible with one. In the same way figure 6.32 shows the pulls for the Sivers asymmetry: on the top for i, j=Seg_1, Seg_2 (left and right segments) positive hadrons on the left, negative hadrons on the right; on the bottom the results for i, j=Seg_3, Seg_4 (top and bottom segments).
The pulls distribution for positive hadrons between Seg_1, Seg_2 shows a RMS value

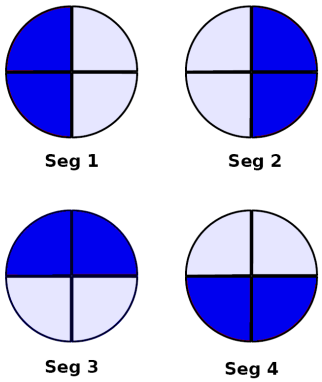

Figure 6.30: Definition of target sector, left $\equiv Seg_1$ right $\equiv Seg_1$, top $\equiv Seg_3$ bottom $\equiv Seg_4$ which have been used in the systematic studies.

compatible with one, however the mean value is shifted by a factor 0.47σ [8]. For the Seg_3, Seg_4 check only the distribution of negative hadrons shows a shifted mean of 0.37σ even if the RMS is still compatible with one. The remaining distributions show, within the statistical error, the expected behaviour.

6.8.6 Comparison of asymmetries extracted using different methods

In order to evaluate the systematic effect introduced by the extraction method the result of the different methods have been compared building the following distribution Δ_i:

$$\Delta_i = \frac{A_{method-i} - A_{2D}}{\left(\sigma_{method-i} + \sigma_{2D}\right)/2}$$

The 2-dimensional method has been taken as reference Separated distributions of pulls have computed for A_{Coll} and A_{Siv}, for positive and negative hadrons. The Δ-distributions for the 1-dimensional method and the two-dimensional fit to counts are shown, as example in figure 6.33, while for the 1-dimensional method modified are shown in figure 6.34. From the figure it is clear that the first method differs from the 2D by $10\% \div 20\%$ of the statistical error, while for the 1-dimensional and 1-dimensional modified methods the RMS is about 0.4 and 0.5 respectively. At the time of the release the Unbinned likelihood was not tuned and so it was not taken into account, the most recent Δ-distributions obtained are shown in figure 6.36; still this method needs more test before being used.

[8] $\sigma = \sqrt{\left(\sigma^2_{Seg_i} + \sigma^2_{Seg_j}\right)}$

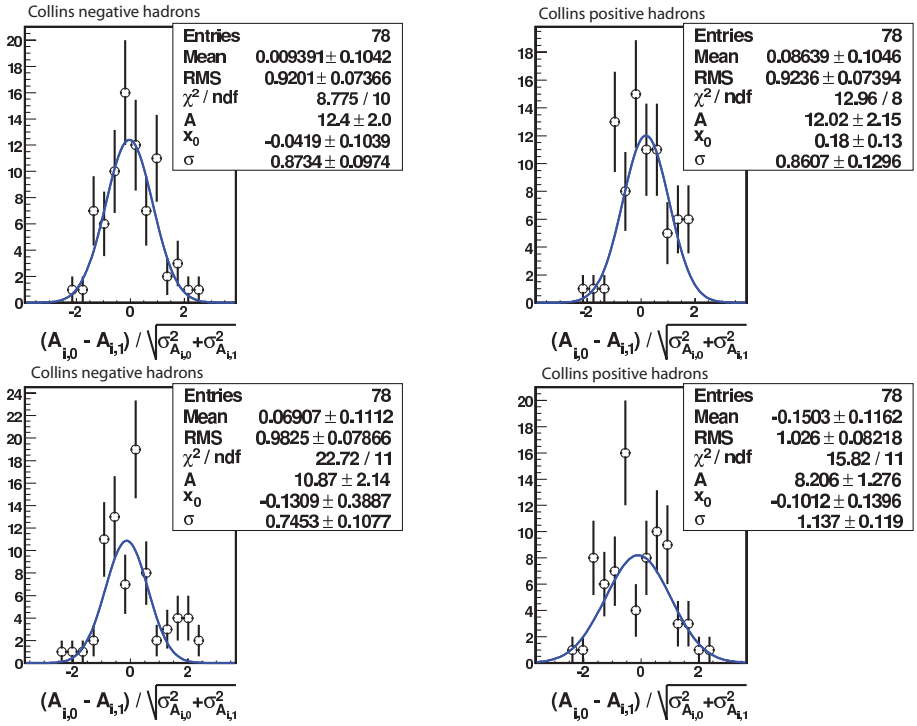

Figure 6.31: Top: pulls ($h_{i,j}$) for Collins for segments Seg_1, Seg_2. On the left negative hadrons, on the right for positive hadrons. Bottom: pulls for Collins for segments Seg_3, Seg_4. Again on the left for negative, on the right for positive hadrons. As mentioned in the text the conf_4 has always been used.

Considering the results obtained comparing the methods it was decided to compute the average value of the previous listed contribution and to assign a conservative error of 0.3σ as systematic error due to the asymmetry estimator. Finally due to the fact the 2 dimensional and the 2 dimensional fit to counts methods are strongly correlated and the statistical data sample to compute the asymmetries is somehow limited the last method[9] is chosen to extract the asymmetries.

6.8.7 Summary of the systematic studies

In this preliminary analysis to evaluate the total systematic error to be associated to the measurement of the Collins and the Sivers asymmetries the previously listed sources of error (see tab. 6.6) have been added in quadrature.
It is known that they are not independent, the target polarisation and the target density for example occur in all of them. For this reason the results are *"preliminary"*

[9] 2 dimensional fit to counts

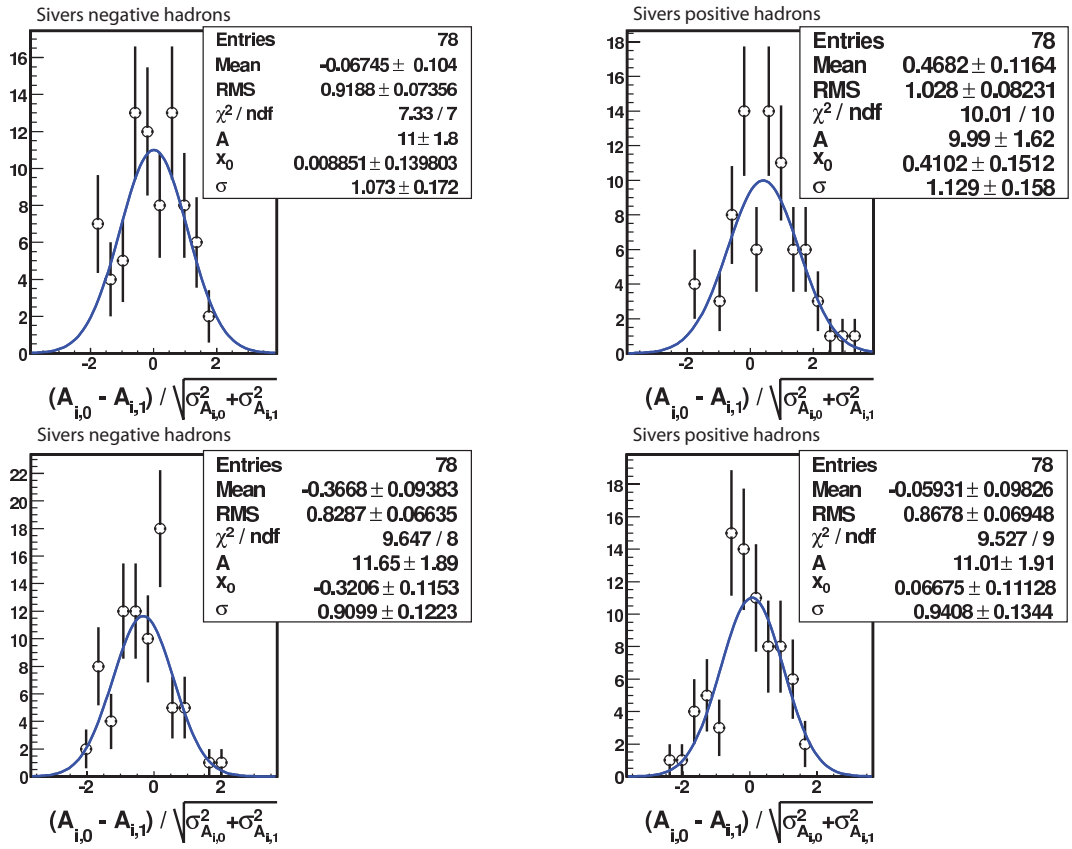

Figure 6.32: Top: pulls ($h_{i,j}$) for Sivers asymmetry for segments Seg_1, Seg_2. On the left negative hadrons, on the right for positive hadrons. Bottom: pulls for Sivers asymmetry for segments Seg_3, Seg_4. Again on the left for negative, on the right for positive hadrons. As mentioned in the text the conf_4 has always been used.

since the evaluation of the systematic error is not definitive: a careful analysis is in fact ongoing to evaluate the correlation among them. This analysis is not yet over. Therefore for this thesis the preliminary systematic errors has been evaluated to be $0.3\,\sigma_{stat}$ for the Collins asymmetries and $0.5\,\sigma_{stat}$ for the Sivers asymmetries.

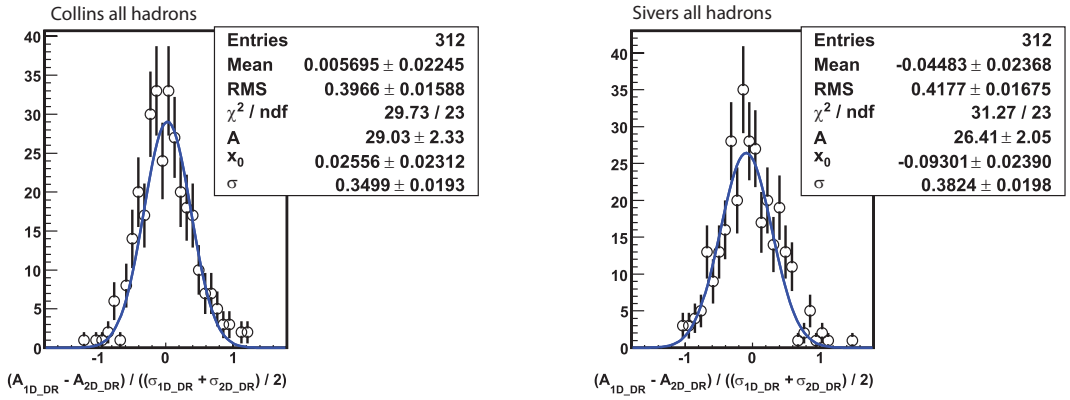

Figure 6.33: Δ distribution obtained from the 1-dimensional method and the 2-dimensional method. Δ for Collins (left) and Sivers (right) asymmetries.

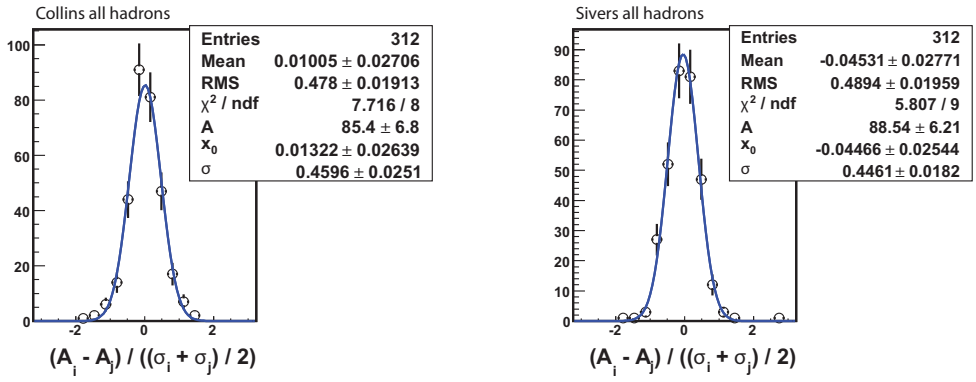

Figure 6.34: Δ distribution obtained from the new 1-dimensional method modified and the 2-dimensional method. Δ for Collins (left) and Sivers (right) asymmetries.

Source	Collins	Sivers
Cell combinations		
$conf_0/conf_1$	0.1	0.23
Transverse Vertex position		
left/right	0	0.24
up/down	0.08	0.19
Extraction Method	0.3	0.3
Overall	0.3	0.5

Table 6.6: Summary of the systematic error in unit of σ_{stat}.

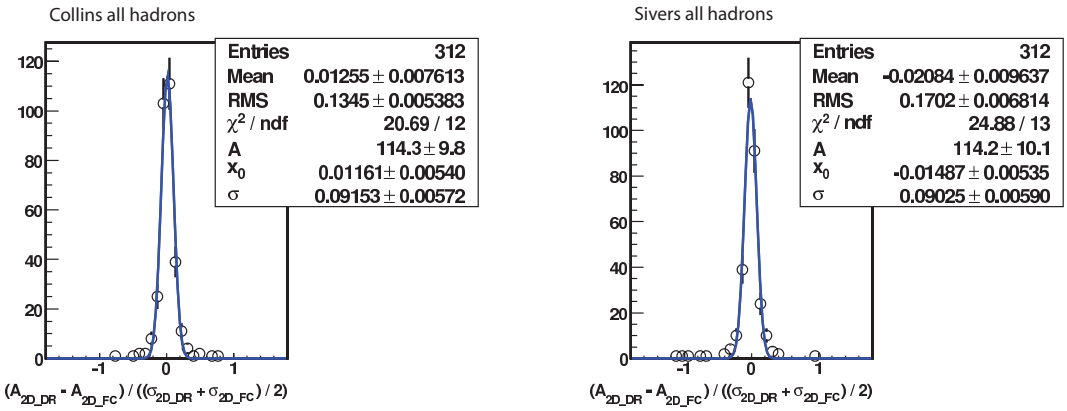

Figure 6.35: Δ distribution obtained from the 2-dimensional fit to counts method and 2-dimensional method. Δ for Collins (left) ans Sivers (right) asymmetries.

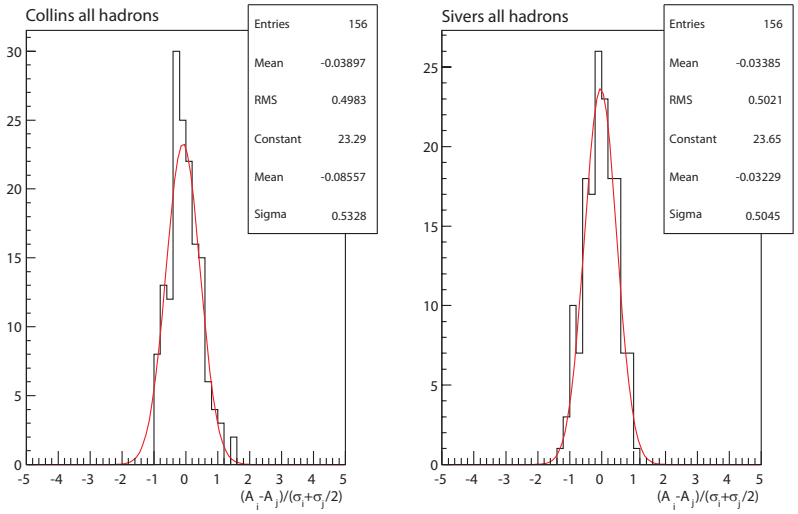

Figure 6.36: Δ distribution obtained for the Collins (left) and Sivers (right) asymmetries extracted with Unbinned maximum likelihood and with the 2-dimensional fit to counts method.

Chapter 7

Interpretation of the results

7.1 Comparison with models

In the previous chapter 6 the results for the Collins and Sivers asymmetries for unidentified hadrons and for identified pions and kaons have been presented. In this chapter a comparison of the extracted asymmetries with the existing results from HERMES and with some theoretical predictions are shown.
When comparing the results for the Collins asymmetry from COMPASS with those from HERMES a remark is necessary. The Collins asymmetry has been written in equation 2.58 where at variance with the Sivers case, the integrals over y in the denominator and numerator do not cancel out. In the analysis of the COMPASS data, the asymmetries have been extracted factorising out the term $D_{NN} = (1 - y + y^2/2)/(1 - y)$ (see section 6.6.3), so the contribution of the y integrals to the asymmetries can be neglected. In the first HERMES analysis, the approach is different: in ref. [29, 157], two types of asymmetries were presented: the "virtual-photon" and the "lepton-beam" asymmetries. The lepton-beam and virtual-photon asymmetries differ by a factor:

$$\frac{1-y}{\frac{1+R_{SIDIS}}{1+\gamma^2}(1-y)+y^2/2} \tag{7.1}$$

where R_{SIDIS} is the ratio of cross sections for longitudinally and transversely polarised virtual photons on an unpolarised target, and $\gamma = \frac{2Mx}{Q}$. The difference with the asymmetries shown by COMPASS is the presence of the R and the γ^2 terms. Both terms can be neglected at first order; moreover the R term is not measured and its relevance in the formula is not clear. In the new HERMES data [44] formula 7.1 is no longer used since only the lepton-beam asymmetries are presented, so when comparing them only the D_{NN} term must be taken into account. To have an idea of the impact of this extra term the D_{NN} average value is computed from the 2007 proton data and plotted in figure 7.1. When the COMPASS asymmetries are scaled

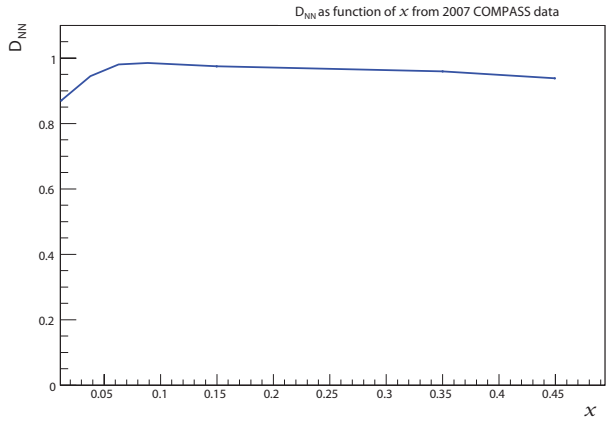

Figure 7.1: D_{NN} as function of the x variable computed from the 2007 COMPASS proton data as the average D_{NN} for different x bins.

for this factor the resulting effect is an increase of the asymmetry value around 10%. Finally due to a difference in the definition of the Collins angle, also a change of sign for the asymmetry value must be taken into account.

7.1.1 Collins asymmetry

In the previous chapter it has been shown that the Collins asymmetry results to be small, compatible with zero up to $x = 0.05$ while a signal is visible in the last points. It has been noticed that for P_T^h and z the asymmetry amplitude is compatible with zero due to the fact that most of the statistical sample is in the low x region. To select the valence quark contribution and to check the dependence on x for z and P_T^h, an event subsample where $x > 0.05$ has been selected. The asymmetry signal becomes now more evident both in P_T^h and z bins as shown in fig. 7.2, and from the figure it seems that there is not an appreciable z or P_T^h dependence. Figure 7.3 shows the model expectations of the Collins asymmetries in the COMPASS kinematic range[53] both for positive and negative hadrons. The predictions are obtained from a global analysis of the HERMES[43] data, COMPASS [84] deuterium data and the BELLE e^+e^-[51] data. The good agreement with the measured asymmetry is clear in the figure.
The HERMES measured non zero Collins asymmetry on the proton has provided convincing evidence that both the transversity distribution $\Delta_T u(x)$ and the Collins mechanism $\Delta_T^0 D_u^h(z)$ are not zero [43, 44, 52]. Independent evidence that the Collins mechanism is a real measurable effect has come from the recent analysis of the BELLE Collaboration [51]. The recent result of COMPASS for the Collins asym-

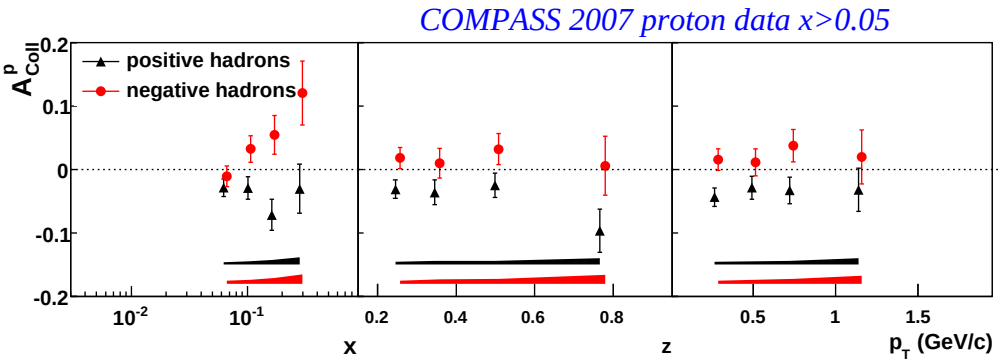

Figure 7.2: Collins asymmetries for positive unidentified hadrons (triangles) and for negative unidentified hadrons (circles) with the cut $x > 0.05$ as function of x, P_T^h, and z. Systematic error is also displayed by the coloured bands.

metry on proton data comes as a further confirmation of the previous results. What is important to stress is that both the sign and the size of the asymmetries are comparable in the two experiments and that the effect are still there at a different kinematic regime.

Our preliminary Collins asymmetries for identified charged kaons are shown in figure 7.4, together with the corresponding asymmetries measured by HERMES. The Collins asymmetries as function of x from the HERMES and COMPASS experiments both for the positive and for the negative kaons are in good agreement. The agreement is also good for z and P_T^h. Still in both the cases the associated statistical error limits somehow the significance of the result.

7.1.2 Sivers asymmetry

At variance with the Collins case the Sivers asymmetry shown in the previous chapter is small and statistically compatible with zero for both positive and negative hadrons over all the measured x range. The result for positive hadrons is at variance from what has been measured by HERMES [43, 44], and the two data samples are marginally compatible as shown in figure 7.5. Considering the identified positive kaons sample a similar trend seems to be present (see fig. 7.5): for positive kaons the COMPASS Sivers asymmetry seems to be systematically lower than the HERMES one: in particular for z and P_T^h the HERMES Sivers asymmetry is different from zero while this happens in COMPASS only for the very last points.
Very muck like for the negative hadron sample there is quite good agreement for the

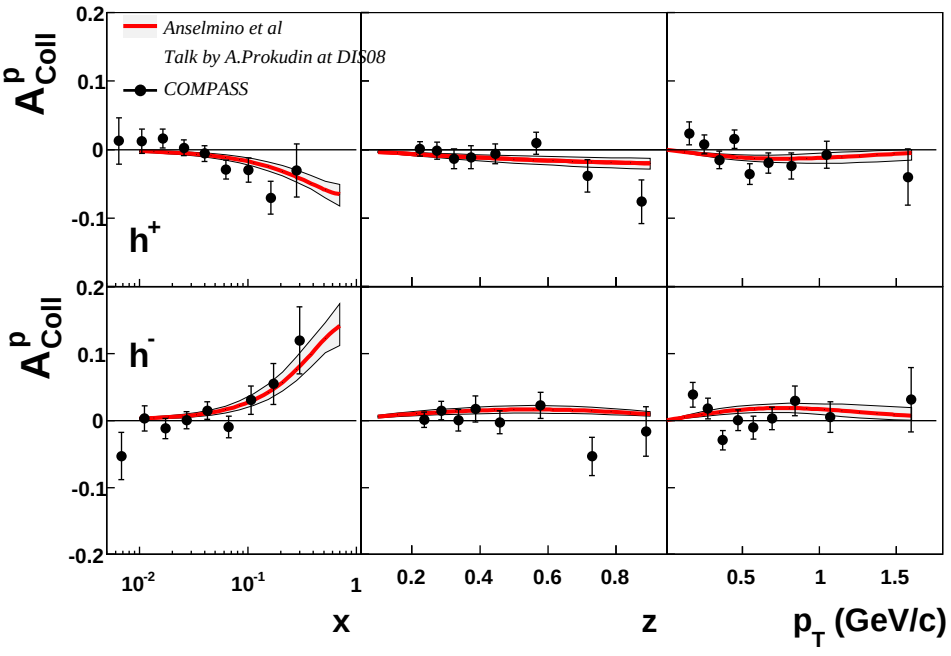

Figure 7.3: COMPASS preliminary Collins asymmetries on proton with the latest prediction of Anselmino et *al*[59].

Sivers asymmetry for negative kaons. As further test, to check the compatibility of the results between the two experiments a cut $x \geq 0.05$ has been applied and the Sivers asymmetry has been computed again. The combined effect of low statistics to begin with, and the extra cut applied reduces furthermore the data sample so the comparison is not particularly enlightening. The COMPASS data with the cut $x \geq 0.05$ are shown in 7.7 with the HERMES data. A mild enhancement of the signal versus z and P_T^h can be noticed but again the low statistical sample strongly reduces the significance of the result. Anyhow it must be remembered that this is the first extraction of asymmetries for identified hadrons in COMPASS, so it is far from being to be definitive.

Figure 7.8 compares the COMPASS Sivers asymmetry on proton data for positive and negative hadrons with the latest prediction of Anselmino et *al*[59]. The agreement for positive hadrons is not satisfactory. However it must be taken into account that the predictions are driven by the HERMES proton data, but magnitude is given by COMPASS deuteron data.

Other theoretical models, as for example the one proposed by S. Arnold et *al*[158], show the same disagreement for the Sivers results (see fig. 7.9).

As possible explanation of the barely compatible results with the predictions, the

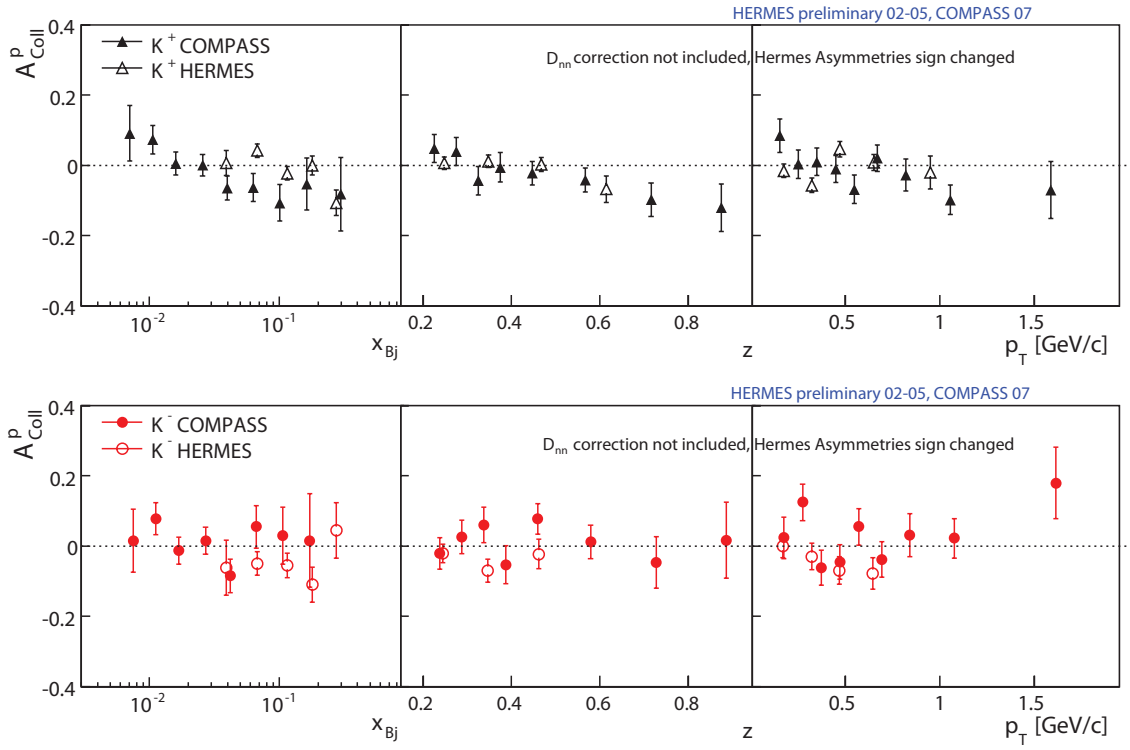

Figure 7.4: Top: Collins asymmetries for positive kaons, solid triangles, for COMPASS and in open triangles for HERMES, as function of x, P_T^h, and z. Bottom: Collins asymmetries for negative kaons, solid red circles, for COMPASS and in open circles for HERMES, as function of x, P_T^h, and z.

group of Arnold et *al* has pointed out that when averaged over the respectively covered kinematic regions, COMPASS and HERMES have a comparable $\langle Q^2 \rangle \sim$ (2-3) GeV/c^2. At fixed x, however, Q^2 can vary in these experiments. For example,

$$\begin{aligned} \text{HERMES:} \quad & \langle x \rangle = 0.115\,, \quad \langle Q^2 \rangle = 2.62\,\text{GeV/c}^2, \\ \text{COMPASS:} \quad & \langle x \rangle = 0.1205\,, \quad \langle Q^2 \rangle = 12.9\,\text{GeV/c}^2, \end{aligned} \tag{7.2}$$

A priori, power corrections should not be important if the Sivers effect observed by HERMES is indeed due to the leading-twist contribution. In this case the Q^2 dependence should be small. Otherwise power corrections could came into play:

$$A_{UT\,\text{measured}}^{\sin(\phi-\phi_S)} = \Big\{ \text{'twist-2 Sivers effect'} \Big\} + C(Q)\,\frac{M_N^2}{Q^2} \tag{7.3}$$

where the coefficient $C(Q)$ could be flavor-dependent, dependent on x, z, ... etc.. and depending on scale logarithmically.

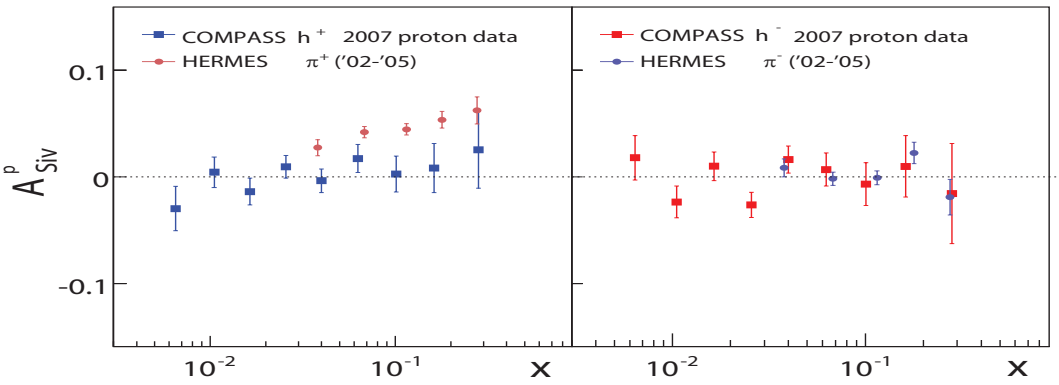

Figure 7.5: Preliminary results for Sivers asymmetry for positive (left) and negative (right) hadrons compared to the results of HERMES (02-05) sample.

A particularly interesting aspect is that the Sivers functions are not universal in the usual sense, i.e., they are not the same in each hard-scattering process. This makes the study of these functions very interesting, as the non universality has in fact a clear physical origin, and its closer investigation has turned out to be an extremely important and productive development in QCD. We have already mentioned that, in order to be non-zero, the Sivers functions require an additional final/initial-state interaction, represented by the gauge-link that makes the function gauge-invariant. This may be viewed as a re scattering of the parton in the colour field of the nucleon remnant. Depending on the process, the associated colour Lorentz forces will act in different ways on the parton. In DIS, so far explored experimentally, the final-state interaction between the struck parton and the nucleon remnant is attractive. In contrast, for the Drell−Yan process it is repulsive and is an initial state interaction. Therefore, the Sivers functions contribute with opposite signs to the single-spin asymmetries for these two processes [159]. This is a remarkable and fundamental prediction that really tests all concepts we know when analysing hard-scattering reactions in strong interactions. It awaits experimental testing.
It has been pointed out that the Sivers effect involves a k_t unintegrated quark distribution function in a transversely polarised proton. This dependence on the intrinsic quark transverse momentum means that the Sivers process is related to quark orbital angular momentum [160]. The result of non zero Sivers asymmetry at HERMES for positive hadrons has been interpreted as experimental evidence for orbital angular momentum $L_q \neq 0$ of quarks, but a quantitative contribution of L_q to the nucleon spin is still unclear [29, 43], result that opens the way to the use of the more sophisticated theory of GPDs. The possible role of quark orbital angular momen-

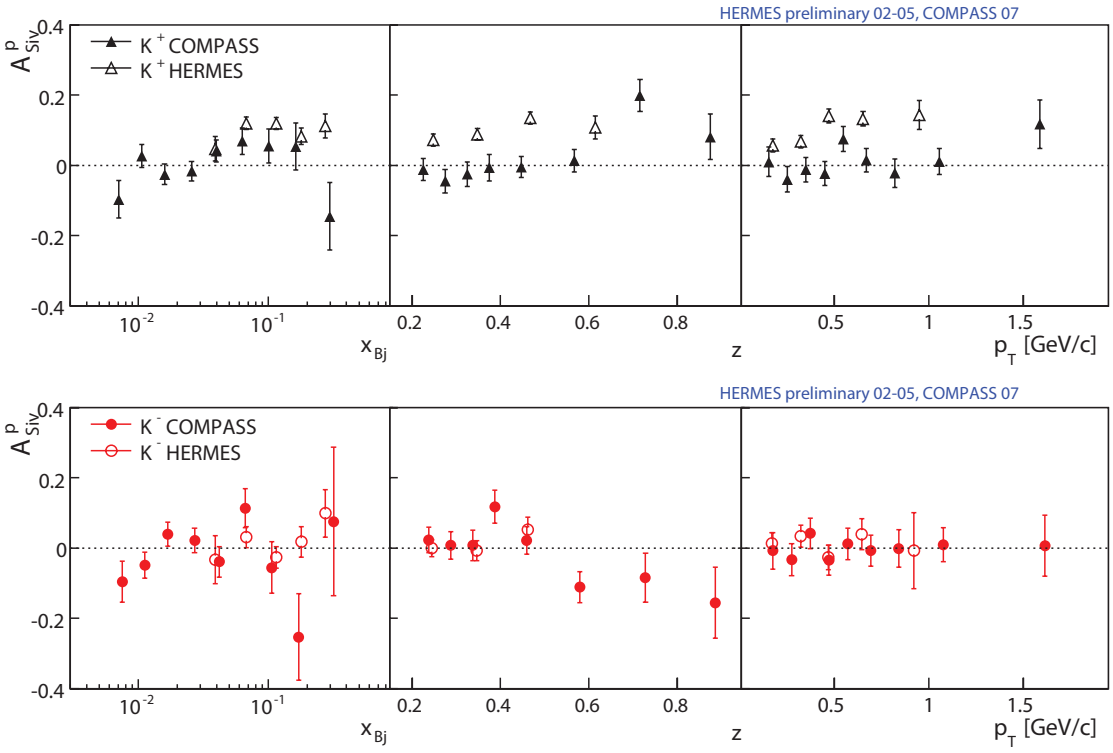

Figure 7.6: Top: Sivers asymmetries for positive kaons (full triangles) for COMPASS and in open triangles for HERMES, as function of x, P_T^h, and z. Bottom: Sivers asymmetries for negative kaons (full red circles) for COMPASS and in open circles for HERMES, as function of x, P_T^h, and z.

tum in understanding single spin asymmetries is also discussed in [161] where, as a consequence of the almost exact cancellations between the u and d-quark Sivers functions, the smallness of the COMPASS Sivers asymmetry on deuteron has been interpreted as evidence for the absence of large gluon orbital angular momentum in the nucleon.

7.2 Conclusion

In the last 10 years a huge progress has been made in understanding the transverse spin and the transverse structure of the nucleon: theoretically, the relevance of the "transversity" PDFs has been firmly established. The first moments of the transversity PDFs are related to both the nucleon transverse spin and to the tensor charge which is being calculated on the lattice. Their properties, will very likely allow some

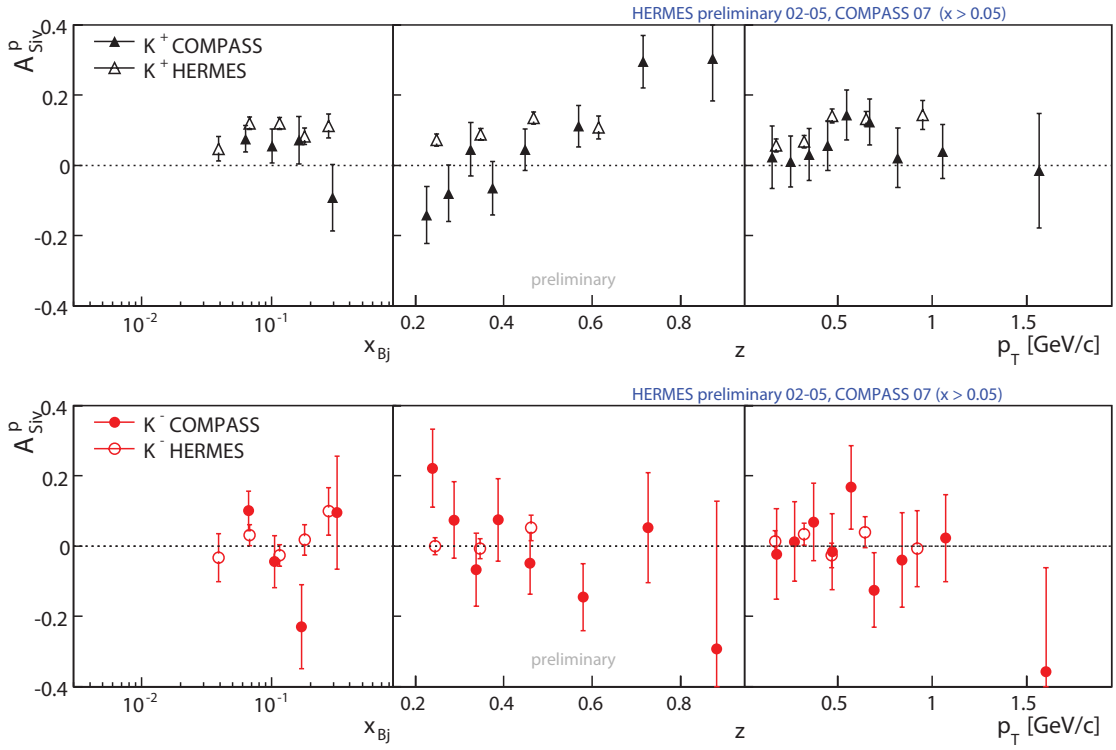

Figure 7.7: Top: Sivers asymmetries for positive kaons for COMPASS after the $x \geq 0.05$ cut and superimposed to the HERMES results, in function of x z and P_T^h. Bottom: Sivers asymmetries for negative kaons for COMPASS after the $x \geq 0.05$ cut and superimposed to the HERMES results, in function of x z and P_T^h.

progress in the understanding of the spin *puzzle* and of QCD in the non-perturbative domain. In parallel, TMD phenomena have also been investigated opening a new field. New TMD PDFs have been introduced which could explain several transverse spin phenomena observed since a long time and not yet explained. The most famous and the most studied TMD PDF is the Sivers PDF, which is related to the quark angular momentum. The theoretical and experimental effort has led to a much more solid and complete picture than the one of the times of the COMPASS proposal. The contributions provided up to now by HERMES and COMPASS are of the utmost importance, giving for the first time evidence that the foreseen new properties of matter are real.

In this pretty new field several issues like evolution, factorisation and universality, need further theoretical investigation and, of course, precise measurements.

In this thesis the preliminary result both for the Collins and Sivers asymmetry have been presented. The 2007 proton transverse data has been deeply scrutinised, via

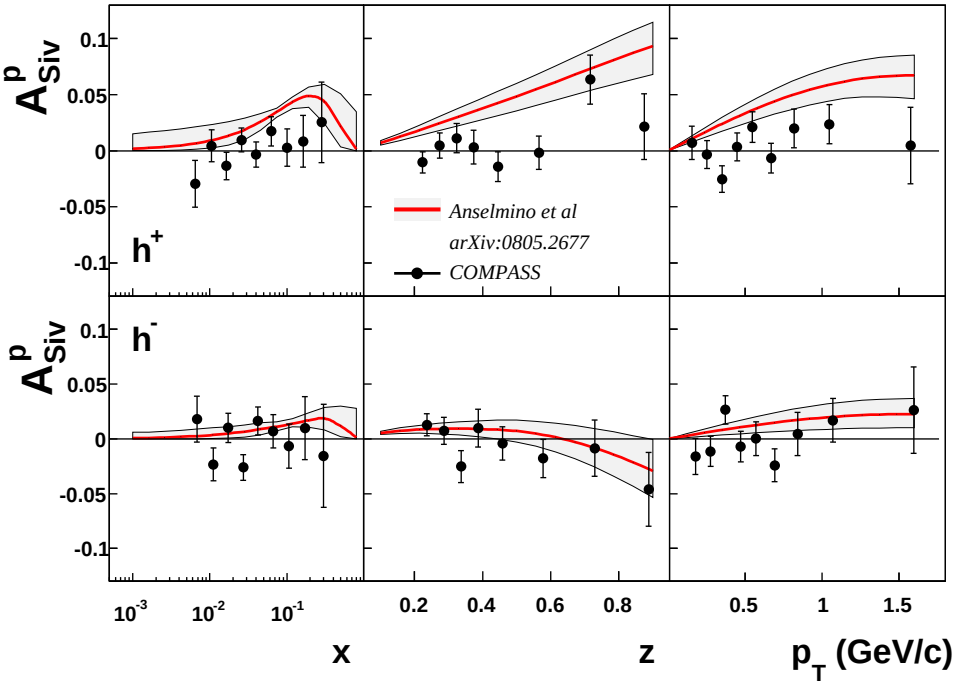

Figure 7.8: COMPASS Sivers asymmetry on proton for positive and negative hadrons, with the latest prediction of Anselmino et *al.*

the stability tests which have been described in chapter 6. The quality criteria have allowed the identification of single runs or periods of data taking not satisfactory for the extraction of the physic asymmetries. Finally the estimation of the systematic contribution to the measurement have been performed. It is necessary to remark that the evaluation of the systematic error is not the final one.
For the Collins effect COMPASS confirms the possibility to measure this tiny modulation, and that transversity gives rise to sizable effects. The result is of fundamental importance since the effect is present also at high energies, in a different kinematic range than the HERMES one.
The work on COMPASS 2007 proton transverse data has just started: this analysis includes about 20% of the whole data accumulated in 2007. As mentioned, data reprocessing is awaited to increase the statistic sample. A reduction up to a factor of 2 of the statistical error is expected if all data would be included after reproduction, although a more conservative estimate suggests up to a factor of 1.4.
The good agreement with the previously seen effect at HERMES and the good agreement with the theoretical predictions are very rewarding. A detailed study of this effect is now a mandatory step in the process of our comprehension of the nucleon

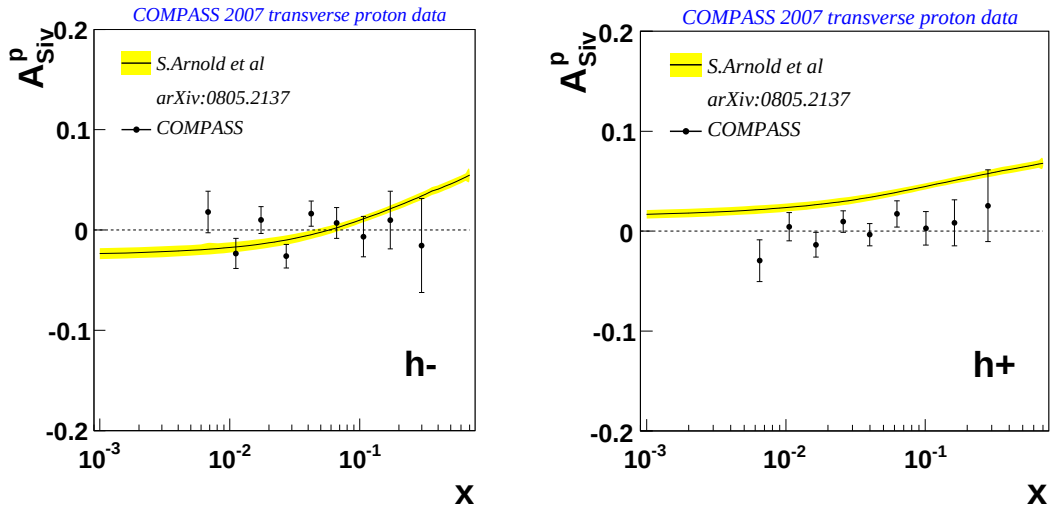

Figure 7.9: COMPASS Sivers asymmetry on proton for positive and negative hadrons, with the prediction of Arnold et *al.*

spin structure.
The extraction of the Collins asymmetries on the identified K and π sample which have been illustrated will allow to perform flavour separation, necessary to measure the first moments. The presented new result will contribute, in the framework of a global analysis as the one presented in this chapter, to the reduction of the uncertainty band for the transversity and Collins functions.
As presented in chapter 2.7.4 the HERMES Collins moments are compatible within the statistical accuracy for π^+ and K^+, while are of opposite sign for π^- and K^-. However, there is no reason to expect a similar amplitude for π^- and K^-, being the K^- most likely produced in the fragmentation of sea quarks ($K^- \equiv \bar{u}s$). Also in this case COMPASS will help to unveil the role of the sea quark contribution as soon as the new data will be included in the analysis to reduce the statistical error of the preliminary result presented here. It is worth to remark that COMPASS is a running experiment and thanks to its unique muon beam line it allows to access the measurement, in a wide x range, of the Q^2-Collins effect dependence at high energies when COMPASS results are combined with HERMES and JLab ones.
For what concerns the Sivers asymmetries the marginal compatibility of the result for positive pions illustrated in this thesis with the HERMES one and with the theoretical prediction is not clear. The asymmetry is not expected to depend on the energy, nor on W, and the dependence on Q^2 should be weak.
The clarification of this unexpected result require necessarily more data, possibly in

parallel to a systematic study of the Sivers asymmetry dependence on these quantities. This would be fundamental to unveil the origin of the disagreement, and this is feasible at COMPASS. If in the future COMPASS will confirm the smallness of the Sivers asymmetry as compared to the values measured by HERMES, the present understanding of the Sivers effect should be revisited.
However only with a careful comparison of all (present and future) data from COMPASS, HERMES and JLAB it will be possible to shed some light on the possible size of power corrections.
Moreover the amplitude for Sivers asymmetry as measured by HERMES for K^+ is roughly twice as big as that for π^+. Since the content of these two mesons differs only in the anti-quark involved, the result suggests a not null Sivers function for the strange sea quarks. Adding the COMPASS result presented here for the identified kaons can help to understand the role of the sea quark contribution to a non-zero orbital angular momentum of the quarks within the nucleon, which is one of the still unmeasured possible candidates to the nucleon spin. As for the Collins case the new result will reduce the uncertainty band for the Sivers function in a global analysis work.
The results here presented, both for Collins and Sivers, can also be used to release some of the constrains imposed to the models inferred by theoreticians as described in paragraph 2.7.4.
Very interesting results have been obtained, the comparison with the predictions is pointing out that we are deepening our knowledge on the nucleon spin structure, but we are, probably, far from a complete understanding. For the transverse spin case, the statistics collected in 2007 is probably not enough for some key topics like the detailed study of the Q^2, x, z_h, and P_T^h dependence of the Collins asymmetry[162]. A proposals to CERN SPSC to resume data taking with a muon beam and with a transversely polarised proton target to improve the 2007 precision of the measurement is in preparation and is almost ready for submission.

Chapter 8

Acknowledgements

The time I spent in the Trieste group of the COMPASS collaboration has been a great experience for me, I'm grateful to all the Trieste members and to all the remaining COMPASS members.
I would like to thank Dott. Silvia Dalla Torre who was the first to believe in me and gave me this unique opportunity and Prof. Franco Bradamante who has introduced me the extraordinary field of Spin physics with his clear explanations, his enthusiasm and his patience too.
It has not always been an easy task to accomplish all the work I had to, but I would like to remark that this result, this thesis and "what" is in, is the result of a group, of a strong collaboration with colleagues.
Nor I can forget Prof. Anna Martin who also helped me with her supervision during my analysis work offering me her assistance and help, and Prof Paolo Schiavon for his suggestions about RICH-1 and his sincere and useful advices.
I'd like to thank Fulvio Tessarotto from whom I learned a lot, for being all the time ready to explain me and to clarify in such an enthusiastic ways what I had not understood. I'd like to thank Andrea Bressan for the useful conversation we had, for the help he gave me during my first year I spent at CERN, for the suggestions when I moved to the data analysis.
I'm indebted to all my four colleagues with whom I shared room 216: Federica Sozzi, Giulia Pesaro, Giulio Sbrizzai and Vinicio Duic. I would like to tank Federica for her help and for the useful discussions, for helping me when I started my analysis work, Giulia for offering me her software assistance and sharing with me her knowledge. I thank Giulio for his help and for the funny situations we created to release the tension, Vinicio who clarified and answered to all my doubts software related, for his useful Perl scripts, Renato Birsa for his support on Sun machines, Benigno Gobbo for his help and support on C++, his assistance when using the Trieste farm. I would like to thank Elena Rocco who introduced me to Trieste when I arrived here in 2006 and gave me her support when I was at CERN.

I would like to express my gratitude also to Piero Ciliberti and a sincere thank to all the people with whom I spent days and nights at CERN trying to be on schedule "all" the time: Aldo Zanetti, Claudio Azzan, Giorgio Menon, Livio Rinaldi, Mauro Gregori, Mauro Bari, Roberto Baccomi, Stefano Reia, Veronica Diaz.
I would like to thank Prof. E. De Sanctis who has dedicated his time to the reading of this thesis.
My deepest gratitude goes to my wife who supported me all these tree year long experience and who has gave me the invaluable joy of being father, I thank finally all my relatives.

Bibliography

[1] F. Bradamante, QCD@WORK 2007 Martina Franca (Italy). 16 - 20 june 2007. Vol. 964, pp. 162-173 (2007).

[2] P. L. Anthony *et al.*, Phys. Lett. **B493**, pp. 19-28, (2000).

[3] F. Bradamante, A. Magnon, G. Mallot, CERN COURIER. vol. 46N6, pp. 15 (2006).

[4] G. Baum *et al.* [COMPASS Collaboration] CERN-SPSLC-96-14, CERN-SPSLC-P-297, (1996).

[5] Elliot Leader, Spin in particle physics, Cambrige University Press (2001).

[6] S. Chekanov *et al.* [ZEUS Collaboration], Eur. Phys. J. C **21**, 443 (2001)

[7] C. Adloff *et al.* [H1 Collaboration], Eur. Phys. J. C **21**, 33 (2001)

[8] L. W. Whitlow, E. M. Riordan, S. Dasu, S. Rock and A. Bodek, Phys. Lett. B **282**, 475 (1992).

[9] A. C. Benvenuti *et al.* [BCDMS Collaboration], Phys. Lett. B **223**, 485 (1989).

[10] M. R. Adams *et al.* [E665 Collaboration], Phys. Rev. D **54**, 3006 (1996).

[11] M. Arneodo *et al.* [New Muon Collaboration], Nucl. Phys. B **483**, 3 (1997)

[12] W. M. Yao *et al.* [Particle Data Group], J. Phys. G **33**, 1 (2006).

[13] J. Ashman *et al.* [European Muon Collaboration], Nucl. Phys. B **328**, 1 (1989).

[14] P. L. Anthony *et al.* [E142 Collaboration], Phys. Rev. D **54**, 6620 (1996)

[15] K. Abe *et al.* [E143 collaboration], Phys. Rev. D **58**, 112003 (1998)

[16] K. Abe *et al.* [E154 Collaboration], Phys. Rev. Lett. **79**, 26 (1997)

[17] P. L. Anthony *et al.* [E155 Collaboration], Phys. Lett. B **463**, 339 (1999)

[18] X. Zheng *et al.* [Jefferson Lab Hall A Collaboration], Phys. Rev. C **70**, 065207 (2004)

[19] A. Airapetian *et al.* [HERMES Collaboration], Phys. Lett. B **442**, 484 (1998)

[20] B. Adeva *et al.* [Spin Muon Collaboration], Phys. Rev. D **58**, 112002 (1998);

[21] E. S. Ageev *et al.* [COMPASS Collaboration], Phys. Lett. B **612**, 154 (2005)

[22] X. Artru, [arXiv:hep-ph/0207309] (2002)

[23] J. P. Ralston and D. E. Soper, Nucl. Phys. B **152**, 109 (1979).

[24] X. Artru and M. Mekhfi, Z. Phys. C **45**, 669 (1990).

[25] R. L. Jaffe and X. D. Ji, Phys. Rev. Lett. **67**, 552 (1991).

[26] G. Bunce *et al.*, Part. World **3**, 1 (1993).

[27] B. Vuaridel *et al.*,[HELP Collaboration] CERN reports LEPC 93-14, LEPC/P7 (1993).

[28] V. Barone, A, Drago, and P. G. Ratcliffe, Phys. Rept., **359**, 1 (2002).

[29] A. Airapetian *et al.*, Phys. Rev. Lett., **94**, 012002 (2005).

[30] V. Y. Alexakhin *et al.*, Phys. Rev. Lett., **94**, 202002 (2005).

[31] A. Afanasev *et al.*, (2007).

[32] J.C. Collins, Nucl. Phys., B **396**, 161 (1993).

[33] A. Bacchetta, M. Diehl, K. Goeke, A. Metz, P. J. Mulders and M. Schlegel, JHEP **0702**, 093 (2007)

[34] V. Barone, P. G. Ratcliffe, Transverse spin physics, World Scientific (2003).

[35] D. W. Sivers, Phys. Rev., D **41** 83 (1990).

[36] G. Bunce *et al.*, Phys. Rev. Lett. **36**, 1113 (1976).

[37] D.L.Adams *et al.*, FNAL E704 Collaboration, Phys. Lett., B **261**, 201, (1991). D.L.Adams *et al.*, FNAL E704 Collaboration, Phys. Lett., B **264**, 462, (1991).

[38] J.Adams *et al.*, [STAR Collaboration], Phys. Lett., B **92**, 17180, (2004)1.

[39] J. Qiu and G. Sterman, Phis. Rev., D **59** 014004 (1999).

[40] S. S. Adler *et al.*, [PHENIX Collaboration], Phys. Rev. Lett., **95** 202001 (2007).

[41] M. Anselmino *et al.*, Phys. Rev. Lett., D **70** 074025 (2004).

[42] J. H. Lee and F. Videbaek, Proceeding of the 17th Spin Physics Simposium (SPIN2006) Kioto, Japan AIP conf. proc 915.533, (2006)

[43] M. Diefenthaler [HERMES Collaboration], proceedings of DIS 2007, p. 579. (2007) [arXiv:hep-ex/0706.2242].

[44] L. L. Pappalardo, [HERMES Collaboration], Eur. Phys. J. A 38, 145148 (2008).

[45] E. S. Ageev *et al.* [COMPASS Collaboration], Nucl. Phys. B **765** 31 (2007)

[46] V. Y. Alexakhin *et al.* [COMPASS Collaboration], Phys. Rev. Lett. **94** (2005) 202002

[47] W. Vogelsang and F. Yuan, Phys. Rev. D **72**, 054028 (2005)

[48] A. V. Efremov, K. Goeke and P. Schweitzer, AIP Conf. Proc. **915** 579 (2007)

[49] J. C. Collins, A. V. Efremov, K. Goeke, S. Menzel, A. Metz and P. Schweitzer, Phys. Rev. D **73**, 014021 (2006)

[50] M. Anselmino, M. Boglione, U. D'Alesio, A. Kotzinian, F. Murgia, A. Prokudin and C. Turk, Phys. Rev. D **75**, 054032 (2007)

[51] A. Abashian *et al.*, [BELLE Collaboration]: Nucl. Instr. Meth., A **479** 117 (2002).

[52] F. Bradamante, Prog. in Part. and nuc Phy. vol. 61, p. 229 (2008).

[53] A. Prokudin , presentation at DIS 2008, (2008).

[54] J. Soffer, Phys. Rev. Lett., **74**, 1292 (1995).

[55] A. V. Efremov, K. Goeke, and P. Schweitzer, Phys. Rev., **D73**, 094025 (2006).

[56] A. Bacchetta, L. Gamberg, G. R. Goldstein, A. Mukherjee PLB659, 234-243, (2008).

[57] A. Ogawa *et al.*, [BELLE Collaboration] AIP Conf.Proc.915:575-578, (2007).

[58] M. Alexeev *et al.*, Nucl. Instr. and Meth. **595** A (2008).

[59] M. Anselmino *et al.*, Eur. Phys. J. A **33** (2008) 145.

[60] F. Gautheron [COMPASS Collaboration], AIP Conf. Proc. **915** (2007) 961.

[61] T. Schmidt, PhD Thesis, A common readout driver for the COMPASS Experiment, Univerisitat Freiburg (2001).

[62] A. Grenemaier, Eine universelle Ausleseschnittstelle fur das COMPASS Experiment, PhD Thesis, Universitat Freiburg (2002).

[63] B. Grube, PhD Thesis, A trigger control system for COMPASS and a measurement of the Transverse Polarisation of L and X Hyperons from Quasi-Real Photo Production, Technishe Universitat Munchen (2006).

[64] CASTOR - CERN Advanced STORage system web page, http://castor.web.cern.ch/castor/ .

[65] Standard Performance Evaluation Corporation, http://www.spec.org/ http://www.spec.org/cpu2000/CINT2000/

[66] The COMPASS Reconstruction and AnaLysis Program (CORAL), COMPASS Collaboration. Available at: http://coral.cern.ch.

[67] RD26 Collaboration at CERN.

[68] P. Abbon, *et al.*, Nucl. Instr. and Meth., A **589** (2008) 362.

[69] M. J. French, *et al.*, Nucl. Instr. and Meth., A **466** (2001) 359.

[70] E. Albrecht *et al.*, Nucl. Instr. and Meth., A **553**, 215 (2005), and references therein.

[71] E. Albrecht *et al.*, Nucl. Instr. and Meth., A **502**, 266 (2003).

[72] E. Albrecht *et al.*, Nucl. Instr. and Meth., A **502**, 236 (2003).

[73] E. Albrecht *et al.*, Nucl. Instr. and Meth., A **502**, 112 (2003).

[74] E. Albrecht *et al.*, Nucl. Instr. and Meth., A **518**, 586 (2004).

[75] F. Sozzi, Diploma thesis, University of Trieste (Italy), (2003).

[76] J. Seguinot, G. Charpak, Y. Giomataris, V. Peskov, J. Tischhauser and T. Ypsilantis, Nucl. Instr. Meth. A **297**, 133 (1990).

[77] G. Malamud, P. Mine, D. Vartsky, B. Equer, A. Breskin and R. Chechik, Nucl. Instr. Meth. A **343**, 121 (1994).

[78] J. C. Santiard *et al.*, GASSIPLEX: 6^{th} Pisa Meeting on Advanced Detectors, La Biodola, Isola d'Elba, Italy (1994).

[79] P. Abbon *et al.*, Nucl. Instr. and Meth., A **587** (2008) 371.

[80] I. Ariño *et al.*, Nucl. Instr. and Meth., A **516** (2004) 445.

[81] The LHCb Collaboration, LHCb Technical Design Report, CERN/LHCC/2000-37; E. Albrecht, *et al.*, Nucl. Instr. and Meth., A **488** (2002) 110.

[82] G. Ingelman, *et al.*, Comput. Phys. Commun., **101** (1997) 135.

[83] GEANT-detector description and simulation tool, CERN Program Library Long Writeup W5013, http:wwwasdoc.web.cern.ch/wwwasdoc/geanthtml3/geantall.html .

[84] P. Abbon *et al.* [COMPASS Collaboration], Nucl. Instr. Meth. A **577**, 455 (2007)

[85] D. Kramer, Diploma thesis, Technical University of Liberec (Czech Republic), (2005).

[86] D.R. Broemmelsiek, Nucl. Instr. and Meth., A **433** (1999) 136.

[87] P. Abbon *et al.*, Czech. J. Phys. **56** (2006) F 323.

[88] F. Gonnela, M. Pegoraro, CERN-LHCC-2001-034, p. 204.

[89] H. Fischer, *et al.*, Nucl. Instr. and Meth., A **461** (2001) 507.

[90] H. C. van der Bij, *et al.*, IEEE Trans. Nucl. Sci., NS-44 (1997) 398.

[91] TDC-F1 Functional description, ACAM Messelektronik, D-76297 Stutensee, www.acam.de .

[92] R. Hagemann, Diploma Thesis, University of Freiburg, (2007).

[93] T. Ypsilantis, J. Seguinot, Nucl. Instr. and Meth., A **343**, 30 (1994).

[94] F. Sozzi, Nucl. Instr. and Meth., A **595**, pp. 233-236, (2008)

[95] P. A. Cherenkov, Phys. Rev., **52** (1937) 378.

[96] A. Buys , Nucl. Instr. and Meth., A **371** (1996) 1.

[97] S. Stone, Nucl. Instr. and Meth., A **433** (1999) **293**; Forty R., Nucl. Instr. and Meth., A **502** (2003) 275

[98] H. Herts, Ann Physic, **31**, 983 (1887).

[99] W. Hallwacks, Ann. Physik **33**, 301 (1888).

[100] J. Elster and H. Geitel, Ann. Physic, **38**, 497 (1889).

[101] A. Einstein, Ann. Phisik, **17** 132, (1905).

[102] L. Koller Phys. rev, **36** 1639 (1930).

[103] N.R. Campbell, Phil. Mag., **12**, 173 (1931).

[104] P. Gorlich, Z. Physik, **101**, 335 (1936).

[105] A. H. Sommer, US patent **2**, 285, 062, Brit Patent 532,259.

[106] A. H. Sommer, Rev. Sci. Instr., **26** 725 (1955).

[107] A. H. Sommer, Appl. Phys. Lett., **3**, 62, (1963).

[108] A. N. Arsenova-Geil and A. A. Kask, Soviet Phys. Solid State, **7**,952 (1965).

[109] A. N. Arsenova-Geil and Wan.Pao Kun: Soviet Phys. Solid State, **3**, 2632 (1962).

[110] DJ. Haneman, Phys. Chcm. Solids, II, **205** (1965).

[111] G. W. Goheli and P. O. Allen, Phys. Rev., **137**, 245 A (1965).

[112] D. O. Fisher, R. E. Enstrom, J. S. Escher. H. F. Gosscnberger, IEEE Trans. Elect. Devices, Vol ED 21. No. 10, 641 (1974).

[113] C. A. Sanford and N. C. Macdonald, J. Vac. Sci. Techiiol, B **8** (6), (1990).

[114] D. G. Fisher and G. H. Olsen, Journal Appl. Phys., **50** (4), 2930 (1979).

[115] J. L. Bradshaw, W. J. Cnoyke and R. P. Devaty, Journal Appl. Phys., **67**(3), 1483 (1990).

[116] H. Bruining, Physics and applications of secondary electron emission, McGraw-Hill Book Co., Inc. (1954).

[117] H. E. Iams and B. Salzberg, Proc. IRE, **23**, 55 (1935).

[118] V. K. Zworykin, G. A. Morton, and Malter: Proc. IRE, **24**, 351 (1936).

[119] V. K. Zworykin and A. Rajchman, Proc. IRE, **27**, 558 (1939).

[120] G. A. Morton, RCA Rev., **10**, 529 (1949).

[121] G. A. Morton, IRE Trans. Nucl. Sci., **3**, 122 (1956).

[122] GARFIELD - simulation of gaseous detectors. http://garfield.web.cern.ch/garfield/

[123] M. C. Teichand R. Y. Yen, IEEE Trans. Aerosp. Electron. Syst 1972, AES-8, 13-18.

[124] J. R. Prescott, Nucl. Instr. Meth., **39**, 173-179 (1966).

[125] A. Dietz, Rev. Sci. Instr., **38** 1332-1333 (1967).

[126] B. Leskovar, IEEE Trans. Nucl. sci., NS-59,50-62, (1972).

[127] Hamamtsu Photonic K K Central Research Laboratory / Research Administration Division 5000, Hirakuchi, Hamakita-ku, Hamamatsu City, Shizuoka Pref., 434-8601, Japan

[128] J. Engelfried *et al.*, Nucl. Inst. Meth. A, **502** (2003) 285 and references therein.

[129] D. P. Morrison *et al.*, Nucl. Phys. A, **638** (1998) 565.

[130] B. N. Ratcliff, Nucl. Inst. Meth., A **371** (1996) 309.

[131] H. E. Jackson *et al.*, Nucl. Inst. Meth., A **502** (2003) 36.

[132] Y. Fukuda *et al.*, Phys. Lett., B **433** (1998) 9.

[133] Bernardini E., Amsterdam-Netherlands, Proceedings of VLVNT 5-8 October 2003, pp. 17-20.

[134] T. Lohse *et al.*, Proposal for HERA-B, DESY PRC-94/02, May 1994.

[135] Hamamtsu Photonic K K, Products catalog and datasheet, http://www.hamamatsu.com/ Japan.

[136] M. Alekseev *et al.*, Nucl. Instr. and Meth., A **553** (2005) 53; P. Abbon *et al.*, Nucl. Instr. and Meth. ,A **567** (2006) 114; P. Abbon *et al.*, Nucl. Instr. and Meth., A **572** (2007) 419; P. Abbon *et al.*, Studies for a fast RICH, World Scientific ISBN 981-256-798-4, Singapore, (2006), p. 103; P. Abbon *et al.*, Nucl. Instr. and Meth., A **580** (2007) 906; P. Abbon *et al.*, Nucl. Phys. B, Proc. Suppl., **172** (2007) 75; P. Abbon *et al.*, Czech. J. Phys., **56** (2006) 318; P. Abbon *et al.*, Czech. J. Phys., **56** (2006) 327; P. Abbon *et al.*, Czech. J. Phys., **56** (2006) 333; P. Abbon *et al.*, Nucl. Instr. and Meth., A **581** (2007) 419.

[137] E. Rocco, Diploma Thesis, Studio e caratterizzazione di un sistema di rivelazione di fotoni con MAPMT per il RICH di COMPASS, (2005).

[138] G. Pesaro, Diploma thesis, Messa a punto e Caratterizzazione del RICH veloce dell'esperimento COMPASS (2006).

[139] H. W. Siebert *et al.*, Nucl. Instr. and Meth., A **343** 91994 60 (1994).

[140] I. Ario *et al.*. Nucl. Instr. and Meth., A **516** (2004) 445.

[141] A. Gorišek *et al.*, Nucl. Instr. and Meth., A **433** (1999) 408; M. Starič and P.Križan, Nucl. Instr. and Meth., A **586** (2008) 174.

[142] S. Costa *et al.*, Nucl. Instr. and Meth., A **553** (2005) 135.

[143] M.Sannino, Nucl. Instr. and Meth. A **595** (2008).

[144] A. Biland *et al.*, Procs. ICRC 2007, [astro-ph/0709.1574], (2007).

[145] R. Kuhn, T. Nagel, R. Konopka, S. Paul, L. Schmitt, Design and performance of the COMPASS online event filter, Nuclear Science Symposium Conference Record, (2007). NSS apos; 07. IEEE Volume 3, Issue , Oct. 26 2007-Nov. 3 2007 pp. 1733 - 1736.

[146] J. Ball, Nucl. Instr. and Meth., A **526**, Issues 1-2, pp. 70-75, (2004).

[147] A. Bressan, Origin and cure of the peak in y, Compass Note, 3 Apr 2007.

[148] A. Korzenev, mail to the COMPASS collaboration, Sunday, 9 Mar 2008.

[149] W. M. Yao *et al.*, Rev. of Part. Physics, Journal of Physics, G **33**, (2006). http://pdg.lbl.gov.

[150] G. Baum *et al.*, Nucl. Instr. and Meth., A **502**, 315 (2003).

[151] A. Vossen, PhD thesis, Transverse Spin Asymmetries at the COMPASS Experiment, Physikalisches Institut Albert-Ludwigs-Universitat Freiburg, (2008). Abbon:2007pq

[152] Principle of a bias-free "2D" transverse asymmetry fit, COMPASS Analysys meeting, August 2007.

[153] D. Levenberg, Quart. Appl. Math. 2, pp. 164-168, (1944).

[154] D. Marquardt, SIAM J. Appl. Math., **11** 431-441, (1963).

[155] A. Kotzinian (on behalf of the COMPASS collaboration), Workshop on Deep-Inelastic Scattering and Related Subjects. (2007)[hep-ex/arXiv:0705.2402]

[156] ROOT manual: ftp://root.cern.ch/root/doc/FittingHistograms.pdf

[157] L. Pappalardo [HERMES Collaboration], Prepared for 14th International Workshop on Deep Inelastic Scattering (DIS 2006), Tsukuba, Japan, 20-24 Apr 2006; proceedings World Scientific (2007), 667.

[158] S. Arnold, A. V. Efremov, K. Goeke, M. Schlegel and P. Schweitzer, Sivers effect at HERMES, COMPASS and CLAS12, [arXiv:hep-ph/0805.2137], (2008).

[159] S. J. Hwang D S and I. Schmidt Phys. Lett., B **530** 99 (2002); S. J. Brodsky , D. S. Hwang and I. Schmidt, Nucl. Phys., B **642** 344 (2002); J. C. Collins, Phys. Lett., B **536** 43 (2002). X. Ji and F. Yuan Phys. Lett., B **543** 66 (2002).

[160] M. Burkardt, Phys. Rev, D **66** 114005 (1988).

[161] S. J. Brodsky, and S. Gardener, [hep-ph/0608219], (2008).

[162] F. Bradamante, Nucl. Phys., B **154**, pp. 86 (2006).